UNIVERSITY OF SOUTHAMPTON

FACULTY OF ENGINEERING and THE ENVIRONMENT

Energy Technology Research Group

UV radiation resistant polyimide based composites reinforced with nanostructured titanate particles: preparation and properties

by

Christian Harito

Thesis for the degree of Doctor of Philosophy

October 2017

UNIVERSITY OF SOUTHAMPTON

<u>ABSTRACT</u>

FACULTY OF ENGINEERING AND THE ENVIRONMENT

<u>Energy Technology Research Group</u>

Thesis for the degree of Doctor of Philosophy

UV RADIATION RESISTANT POLYIMIDE BASED COMPOSITES REINFORCED WITH NANOSTRUCTURED TITANATE PARTICLES: PREPARATION AND PROPERTIES

by Christian Harito

Ultraviolet (UV) exposure is one of the most deleterious threats to polymers. UV light may alter chemical bonds, leading to discoloration of the polymer and even degradation of its properties. Polyimide (PI) is a well-known polymer in electronic devices, filtration and as components for spacecraft and satellites. PI has desirable properties as a lightweight material, which is flexible and resistant to heat and chemicals. This work is focused on protection of polyimide from UV damage by incorporating titanate nanostructures. The effects of titanate particle incorporation within a PI based polymer on mechanical and thermal properties are discussed.

Addition of titanate nanosheets (TiNS) (2 wt%) to a polyimide precursor enhanced the hardness (by 90%) and modulus (by 103%) due to the high aspect ratio ($l/h = 133.33$) and aligned orientation of the TiNS, observed by TEM and SAXS. In contrast, 2 wt% titanate nanotubes (TiNT) increased the hardness and modulus by 91% and 165%, respectively; these values are higher than theoretical predictions using TiO_2 properties, indicating TiNT may have higher mechanical properties than TiO_2. Small additions of TiNT (0.1 wt%) to polyimide, either by an *in-situ* or *ex-situ* method, increased its T_g by *ca.* 69 °C, probably due to strong bonding between TiNT and PI.

The incorporation of TiNT protected functional groups of polyimide (e.g., C=O and C-F) from UV light. Long cracks and degradation of mechanical properties were not observed in TiNT-PI samples. The protection of PI from UV exposure was similar to the exsisting polyhedral oligomeric silesquioxane (POSS). A novel characterisation method of polymer UV degradation by methylene blue adsorption was developed. Methylene blue reacted with moieties created from UV damage. Changes in its concentration indicated degradation.

Table of Contents

List of Tables

List of Figures

DECLARATION OF AUTHORSHIP

I, Christian Harito, declare that this thesis entitled

UV radiation resistant polyimide based composites reinforced with nanostructured titanate particles: preparation and properties

and the work presented in it are my own and has been generated by me as the result of my own original research.

I confirm that:

1. This work was done wholly or mainly while in candidature for a research degree at this University;
2. Where any part of this thesis has previously been submitted for a degree or any other qualification at this University or any other institution, this has been clearly stated;
3. Where I have consulted the published work of others, this is always clearly attributed;
4. Where I have quoted from the work of others, the source is always given. With the exception of such quotations, this thesis is entirely my own work;
5. I have acknowledged all main sources of help;
6. Where the thesis is based on work done by myself jointly with others, I have made clear exactly what was done by others and what I have contributed myself;
7. Parts of this work have been published as:

(Papers submitted to peer-reviewed journals)

1. Christian Harito, Ruben Porras, Dmitry V. Bavykin, Frank C. Walsh, Electrospinning of *in situ* and *ex situ* synthesized polyimide composites reinforced by titanate nanotubes, *Journal of Applied Polymer Science,* 2017, 134, 44641.
2. Christian Harito, Dmitry V. Bavykin, Mark E. Light, Frank C. Walsh, Titanate nanotubes and nanosheets as a mechanical reinforcement of water-soluble polyamic acid: Experimental and theoretical studies, *Composites Part B*, 2017, 124, 54-63.

3. Christian Harito, Dmitry V. Bavykin, and Frank C. Walsh, Incorporation of titanate nanosheets to enhance mechanical properties of water-soluble polyamic acid, submitted to *Polymer-Plastic Technology and Engineering* as suggested from IPST 2016 conference.

4. Christian Harito, Dmitry V. Bavykin, and Frank C. Walsh, Inhibition of polyimide photodegradation by incorporation of titanate nanotubes into the composite, to be submitted in *Journal of Physical Chemistry C*.

(Papers submitted in collaborations with colleagues)

1. Alysson S. Martins, Christian Harito, Dmitry V. Bavykin, Frank C. Walsh, and Marcos R. V. Lanza. Insertion of nanostructured titanates into the pores of an anodised TiO_2 nanotube array by mechanically stimulated electrophoretic deposition, *Journal of Materials Chemistry C*, 2017, 5, 3955-3961. Contributions: titanate nanosheets synthesis, brush design, SEM, TEM, Raman spectroscopy, and contact angle measurement.

(Papers presented at conferences)

1. C. Harito, R.P. Ortigosa, D.V. Bavykin, A. Nuruddin, and F.C. Walsh, Electrospinning of *in-situ* and *ex-situ* polyimide reinforced by titanate nanotubes, *Electrospin 2016*, Otranto, June 2016.

2. C. Harito, D.V. Bavykin, and F.C. Walsh, Incorporation of titanate nanosheets to enhance mechanical properties of water-soluble polyamic acid, *IPST 2016*, Medan, November 2016.

3. C. Harito, D.V. Bavykin, and F.C. Walsh, Inhibition of polyimide photodegradation by incorporation of titanate nanotubes into the composite, *Nanomaterials: from theory to applications*. Manchester, May 2017.

Signed: ....

Date: 14 July 2017 ....

Acknowledgements

List of Abbreviations

6FAP	1,4-bis(4-amino-2-trifluoromethylphenoxy)benzene
6FBAB	4,4'-bis(4-amino-2-trifluoromethylphenoxy)biphenyl
6FDA	4,4'-(hexafluoroisopropylidene)diphthalic anhydride
6FDAm	2,2'-bis(4-aminophenyl)hexafluoropropane
10DAD	1,10-diaminodecane
APTES	3-aminopropyltriethoxysilane
atm	Atmosphere
BOCA	Bicyclo[2.2.2]oct-7-ene-2,3,5,6-tetracarboxylic dianhydride
BPDA	3,3',4,4'-biphenyltetracarboxylic dianhydride
BTDA	3,3',4,4'-benzophenone-tetracarboxylic dianhydride
BHDA	Bicyclo[2.2.1]heptane-2,3,5,6-tetracarboxylic dianhydrides
BODA	Bicyclo[2.2.2]octane-2,3,5,6-tetracarboxylic dianhydrides
BBH	Bis(aminomethyl)bicyclo[2.2.1]heptane
TFDB	2,2'-bis-trifluoromethyl-4,4'-diaminobiphenyl
CTC	Charge transfer complex
PCP	*p*-chlorophenol
CHDA	1,2,4,5-cyclohexanetetracarboxylic dianhydride
DFT	Density functional theory
DMF	N,N-dimethylformamide
DNDA	(4arH,8acH)-decahydro- 1t,4t:5c,8c-dimethanonaphthalene-2t,3t,6c,7c-tetracarboxylic 2,3:6,7-dianhydride

DMAc	N,N-dimethylacetamide
DMSO	Dimethyl sulfoxide
EDX	Energy dispersive X-ray spectroscopy
FESEM	Field emission scanning electron microscopy
T_g	Glass transition temperature
HRTEM	High resolution transmission electron microscopy
MMCA	4,4'-methylene bis(2-methyl cyclohexylamine)
MCA	4,4'-methylene bis(cyclohexylamine)
NMP	N-methyl-2-pyrrolidone
MB	Methylene blue
NT	Nanotubes
NSp	Nanospheres
NS	Nanosheets
NF	Nanofibres
ODPA	4,4'- oxydiphthalic anhydride
ODA	4,4'-oxydianiline
PI	Polyimide
PEI	Polyethyleneimine
PAA	Polyamic acid
PAAS	Polyamic acid salt
PMDA	Pyromellitic dianhydride
PDA	*p*-phenylenediamine
MPD	*m*-phenylene

PPD   *p*-phenylenediamine

PEO   Polyethylene oxide

PI   Plasticity index

SAXS   Small-angle X-ray scattering

STiNS   Scrolled titanate nanosheets made by hydrothermal method

TOF-SIMS Time-of-flight secondary-ion mass spectroscopy

TiO_2 Titanium dioxide

TiNS   Titanate nanosheets made by Sasaki's method

TiNT   Titanate nanotubes made by hydrothermal method

TEM   Transmission electron microscopy

TBA   Tetrabutylammonium

TBAOH   Tetrabutylammonium hydroxide

TMA   Tetramethylammonium

TMAOH   Tetramethylammonium hydroxide

TEA   Triethylamine

TIP   Ti(IV)isopropoxide

THF   Tetrahydrofuran

UV   Ultraviolet

UV-vis   Ultraviolet-visible

vol%   Volume percentage

wt%   Weight percentage

WAXS   Wide-angle X-ray scattering

XPS   X-ray photoelectron spectroscopy

List of Symbols

Symbols	Units	Descriptions
A	mm^2	Projected contact area between indenter and specimen at maximum depth
A_f	dimensionless	Filler aspect ratio
A_g	dimensionless	Area under the Raman curve for a particular functional group (e.g., C=O, C-F) with respect to the baseline (after UV exposure)
$A_g{}^0$	dimensionless	Area under the Raman curve for a particular functional group (e.g., C=O, C-F) with respect to the baseline (before UV exposure)
A_{ph}	dimensionless	Area of the reference Raman peak of aromatic C=C bond at wavenumber of $\approx$1618 cm^{-1} (after UV exposure)
$A_{ph}{}^0$	dimensionless	Area of the reference Raman peak of aromatic C=C bond at wavenumber of $\approx$1618 cm^{-1} (before UV exposure)
C	dimensionless	Calibration factor of Ostwald viscometer
c_o	mol L^{-1}	Initial concentration
c	mol L^{-1}	Concentration that will be measured by UV-vis spectroscopy
E_c	GPa	Young's modulus of composite
E_f	GPa	Young's modulus of filler
E_i	GPa	Young's modulus of indenter
E_m	GPa	Young's modulus of matrix
E_s	GPa	Young's modulus of spesimen
H_c	GPa	Hardness of composite

H_f	GPa	Hardness of filler
H_m	GPa	Hardness of matrix
h	nm	Nanosheets thickness or nanotubes diameter
l	nm	Nanosheets or nanotubes length
m	g	Mass of the film sample
N	dimensionless	Number of nanosheet stacks
n	dimensionless	The number of chemical bonds in one repeating unit of 6FDA-ODA PI
S	N mm^{-1}	Stiffness
s	nm	Spacing between nanosheets
t	nm	Thickness of a single nanosheet
$tan\,\delta$	dimensionless	Dielectric loss
V_f	dimensionless	Volume fractions of filler
V_m	dimensionless	Volume fractions of matrix
ν	cSt	Kinematic viscosity
ν_i	dimensionless	Poisson's ratio of indenter
ν_s	dimensionless	Poisson's ratio of specimen
W_p	nJ	Plastic work
W_e	nJ	Elastic work
α	mol g^{-1}	The specific amount of methylene blue absorbed on the sample after irradiated by UV
α_0	mol g^{-1}	The specific amount of methylene blue absorbed on the sample before irradiated by UV
β	dimensionless	Parameter which depends on indenter geometry

ΔA	dimensionless	The change of Raman absorbance in a particular functional group
ε	L mol^{-1} cm^{-1}	Molar absorptivity of a solution
ε'	dimensionless	Relative permittivity
η	dimensionless	Geometric factor
μ	mPa s	Shear viscosity
ρ	g L^{-1}	Density of solution
Φ_f	dimensionless	Volume fractions of filler
χ_f	dimensionless	Particle strengthening factor

Chapter 1:   Introduction

1.1   Background and motivation

The term "polymer" derives from the ancient Greek word πολύς (polus, meaning "many, much") and μέρος (meros, meaning "parts"). It refers to multiple repeating units that build up a polymer. Since the discovery of synthetic polymers in 1900s, which is a thermosetting phenol–formaldehyde resin as known as Bakelite, they have become very popular up to this day due to their unique properties [1]. Polymers are mainly lightweight, flexible, and easy to process compared to steel or aluminosilicate. They have a wide variety of properties and applications. The polymer industry exceed steel as a widely used material per unit volume and now it has complementary to steel, aluminium, and copper. It could be find in tyres, electrical insulators, bottles, pipes, packaging, toys, electronic devices, aircrafts, bulletproof vests, and even for space applications, such as satellites [2–4].

This work will focuses on polyimide which is a common polymer for space applications due to its high temperature stability [5]. Unfortunately, polyimide is susceptible to ultraviolet (UV) radiation. Free radicals can be created due to UV attack on the chain structure of polymers [6]. This can change the polyimide properties, leading to discoloration and degradation of its mechanical properties. Physical break-up such as cracking and disintegration can occur due to prolong UV exposure. To lengthen the life of polyimide in space, additives or fillers are needed to protect polyimide from UV radiation since there is strong and harsh UV radiation outside of the Earth's protective atmosphere.

There are two types of UV blockers that are mainly used in polymers which are organic and inorganic UV blockers. Compared to organic UV blockers such as oxybenzone or octyl methoxycinnamate, inorganic UV blockers (e.g., titania or titanate) are preferable due to its unique features such as non-toxicity and chemical stability under high temperature. It may also be used to improve the mechanical properties of the polymer.

For polyimide, titania [7] and polyhedral oligomeric silesquioxane (POSS) [8] are often used to prevent degradation caused by UV exposure and its combination with atomic

oxygen erosion in outerspace condition. Polyimide were coated by titania using liquid phase deposition method. However, coating method may rise problems such as imperfect coating, poor adhesion, thermal expansion mismatch between the coating and the substrate [9]. Incorporation of POSS into polyimide may solve these problems but it may also decrease the thermal properties of polyimide such as glass transition temperature [8]. Alternative materials needed to address these problems.

This thesis examines and develops several techniques to fabricate UV radiation resistant polyimide based composites reinforced with nanostructured titanate particles. The work focuses on the preparation, mechanical, optical, thermal and chemical properties of composites. Hydrothermal, sol-gel, and solid-state synthesis method of titanate nanostructure preparation are deployed. Bearing hydroxyl groups on the surface of titanate nanotubes, hydrothermally synthesised titanate nanotubes may creates network with polyimide strengthening its thermal properties. The effect of the shapes of titanate such as nanotubes and nanosheets on the mechanical properties of polyimide is evaluated.

The inhibition of UV degradation of polyimide by titanate nanostructures is studied using Raman, UV-vis spectroscopy, optical microscope, and nanoindentation. Electron spin resonance (ESR) is usually used to determine UV degradation in polymer. However, titanium oxide in the polymer may disturb the signal of the degradation products of polymer [10]. Hence, the degradation products of titanate/polyimide composites are determined by methylene blue uptake in this work. The exposure of UV upon polyimide may creates moieties that have affinity towards methylene blue. The adsorption of methylene blue on polyimide after irradiated with UV implies the exsistence of the moieties. The procedure is supported with other characterisation such as Raman spectroscopy, optical microscope, and nanoindentation.

Besides ultraviolet exposure, polyimide, as a polymer that is widely used in satellite and spacecraft, is also facing other threats such as atomic oxygen erosion, vacuum ultraviolet and space debris [8]. This thesis is limited to the preparation of titanate/polyimide composites, its mechanical, thermal, chemical properties, and ultraviolet resistance.

1.2   Aims and objectives

The aim of the project is to develop several synthetic routes for titanate nanostructures, embedding and controlling dispersion of nanostructured titanate within the polyimide matrix, study the mechanical, optical and UV resistance properties of produced composites. The effect of the morphology of nanostructured titanate (nanotubes and nanosheets) on the above properties is investigated. Therefore, this research pursued the following objectives:

- development of several synthesis method of titanate nanosheets to create different type of nanosheets

- fabrication of several polymer such as non-soluble, organo-soluble, water-soluble polyimide based polymer to be incorporated with titanate nanostructures

- preparation of titanate/polyimide composites using several synthesis techniques such as *in-situ*, *ex-situ*, and solution mixing.

- investigation of the effect of titanate morphology (nanosheets, nanotubes, and scrolled nanosheets) on mechanical properties of polymer composite using nanoindentation. Small-angle X-ray diffraction (SAXS) and transmission electron microscopy (TEM) are deployed to detect the orientation and agglomeration of nanostructures.

- utilisation of titanate nanostructures to inhibit photodegradation of polyimide.

- characterisation of the UV degradation of the titanate/polyimide composites using methylene blue uptake method, Raman spectroscopy, optical microscopy, and nanoindentation.

1.3 Thesis outline

This report is divided into literature review, methodology, experimental works, conclusions and future work. Chapter 2 consists of a thorough literature review of of titanate nanostructures, polyimide and composites, from the synthesis, properties, chemical and physical characteristics towards its behaviour upon UV irradiations. Electrospinning of polymer composites fibre is also discussed in this chapter. This encompass the introduction of electrospinning, the synthesis and the properties of polyimide, the electrospinning parameters and the effect of incorporation of filler.

The experimental work is emphasized in different approaches to synthesis titanate nanosheets, polyimide, and polyimide nanocomposites (film and fibre) which is described in Chapter 3. In Chapter 4, the discussion of several synthesis methods of titanate nanosheets and its properties are provided. The effect of titanate nanostructures on the mechanical properties of polyimide precursor is shown in Chapter 5. The preparation of polyimide films and fibres is provided in Chapter 6, as well as the incorporation method of titanate nanotubes. Inhibition of polyimide UV irradiation by titanate nanostructures is also presented in Chapter 7. The method to determine of the UV degradation of polyimide and its composites by methylene blue uptake is described in this chapter. The works are concluded in Chapter 8 and suggestions for further work are outlined.

Chapter 2: Literature Review

This chapter provides definition of titanate nanostructures, especially nanosheets, followed by its synthesis methods and properties. Conventional procedure as well as recent methods to synthesis polyimide is described. The polyimide properties and its degradation mechanism under UV exposure is covered. Strategies to utilise nanostructures for inhibition of UV degradation of polymer is reviewed alongside with the mechanical reinforcement of polymer composites. Lastly, the electrospinning of polyimide and the effect of filler in electrospun polymer fibre are provided.

2.1   Titanate nanostructures

Definition of titanate in this thesis refers to inorganic compounds composed of titanium oxide (e.g., H_2TiO_3, $H_2Ti_3O_7$) while the commonly known titanium oxide stuctures, titanium dioxide (TiO_2), is denoted as titania. The name "nano" in nanostructures refers to their characteristic size of 1-100 nm. The structures are widely varied from zero (spheres, cubes, and polyhedrons), one (rods, fibres, tubes), two (sheets, discs, plates) dimensional, and complex shapes (flower, leaf, etc.) [11] (Figure 2.1). Nanospheres, nanofibres, nanorod, nanotubes, and nanosheets are common morphologies of synthetic nanostructures.
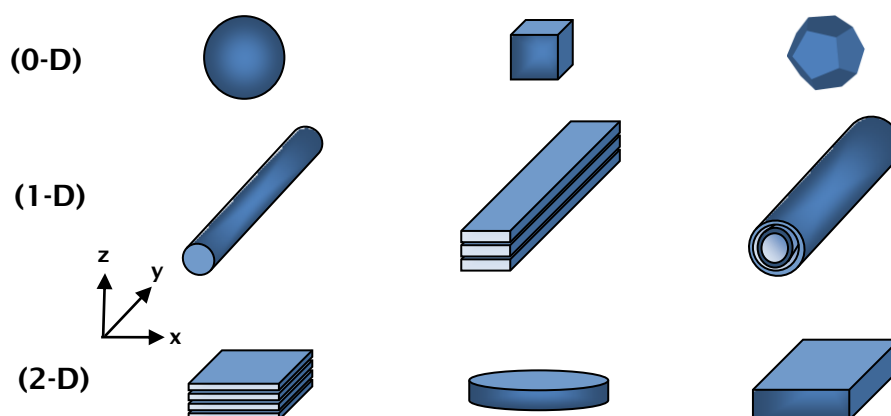
Figure 2.1. Morphologies of synthetic nanostructures (from left to right): (0-D) nanospheres, nanocube, nanopolyhedron; (1-D) nanorod, layered nanofibres, nanotubes; (2-D) nanosheets, nanodisc, nanoplate [12].

In this thesis, nanosheets (e.g., graphene) is defined as a 2 dimensional layered compound of single nanosheets with ≈1-2 nm thickness (typical thickness (z) of nanosheets), which has similar value of x and y. The difference between nanofibres and nanosheets is on the ratio of x and y. The length of y of the nanofibres is much larger than the length of x. The definitions of nanosheets, nanoplate are vague because each of them has similar shape. Nanoplates are thicker than nanosheets which have typical thickness (z) ≈5-100 nm such as bismuth vanadate ($BiVO_4$) nanoplate [13].

2.1.1   Synthesis of single-layer titanate nanosheets

The titanium oxide nanosheets can be categorized into three type of sheet such as facet-controlled TiO_2 nanosheets, multi-layered nanosheets and single/mono-layered nanosheets. The growth of TiO_2 in solution can be controlled by capping agent (e.g., HF) exposing one of its facet such as {001}. Highly exposed {001} facet of anatase TiO_2 (>70%) may produce sheet-like structure with thickness up to 2 nm [14]. However, its crystallographic structure is still in three dimensional orders which is anatase. In this thesis, the nanosheets are defined as a two dimensional sheet-like structure containing several or single atomic or molecular layer thickness. Many studies have been done for the synthesis of multi-layered nanosheets (solid-state synthesis [15–22], hydrothermal method [23–28], sol-gel method [29,30], solvothermal synthesis [31], chemical vapour deposition [32]) but there are only a few papers about single/mono-layered nanosheets. Single/mono-layered nanosheets became popular by Sasaki (1998) [33] who prepared a single nanosheets with chemical exfoliation of lepidocrocite-like titanate. This type of titanate has been discovered by Grey (1987) [34] with solid-state reaction.

Solid state reaction is a reaction of a close union of solid starting/precursor materials which usually occurs at high temperature (800-1500 ºC) [35]. Homogeneous and intimate mixture is a prerequisite for insuring uniform reaction. The powder precursors are usually mixed and ground with mortar and pestle (for larger quantities, ball milling is usually employed). In some cases, sufficient amount of volatile organic liquid (preferably acetone or alcohol) is added to help homogenisation. Later, the liquid will evaporated after mixing. To increase the area of contact between precursors, pelleting of samples is preferred prior to heating. There are several factors such as temperature, structural properties, surface area, and reactivity of the reactants which are affecting the

rate of solid-state reaction. Fine-grained materials are preferable since an increase in surface area enhances the rate of reactions.

The nature of products depends on the selection of the precursors and the reaction conditions (temperature and duration). Synthesis of titanate by solid-state reaction of alkali salt (e.g., $CsNO_3$, Cs_2CO_3, and K_2CO_3) and titania powder usually produce fibrous-like structure but with certain composition and condition it can be a unique structure, such as lepidocrocite-like titanate. The crystal structure and SEM images of fibrous-like titanate and lepidocrocite-like titanate is provided in Figure 2.2.
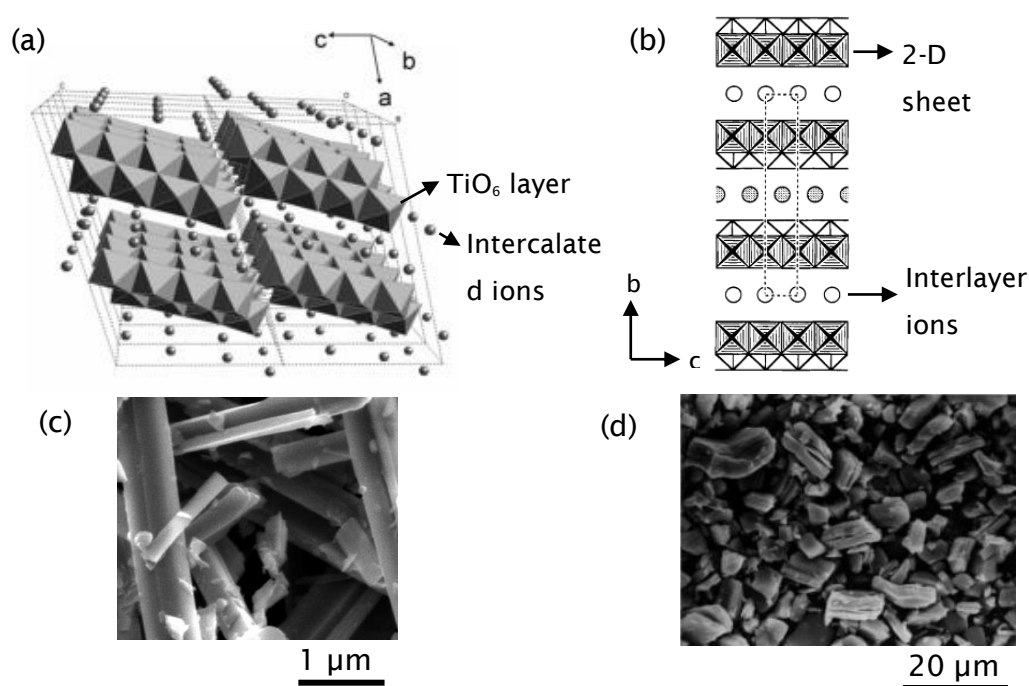
Figure 2.2. (a) Crystal structure of fibrous-like titanate (monoclinic) [36]; (b) Crystal structure of lepidocrocite-like titanate (orthorhombic) viewed down along a-axis [37]; (c) FESEM image of fibrous-like titanate [37]; (d) FESEM image of lepidocrocite-like titanate [15].

The first lepidocrocite-like titanate was created by solid-state reaction of TiO_2 and $CsNO_3$ with controlled ratio (Molar ratio TiO_2 : $CsNO_3$ = 1 : 2.8-3.2), temperature (800-1050 ^{o}C), and duration (0.5-20 hr). The resulting product is a white powder of lepidocrocite-like caesium titanate, $Cs_xTi_{2-x/4}\square_{x/4}O_4$ (x ≈0.61-0.65; $\square$ = titanium vacancy). Sasaki *et.al.* has been adapted the method by adjusting molar ratio of Cs_2CO_3 to TiO_2 (molar ratio 1: 5.3) and successfully synthesised new lepidocrocite-like

nanosheets [37]. Large lepidocrocite-like titanate has also been fabricated, using potassium carbonate and lithium carbonate as an alkali precursor in a K_2MoO_4 molten salt flux by slow-cooling method [38]. The molten flux serves as good heat transfer medium facilitating contact between alkali salt and titania, which ultimately enhancing the growth condition of titanate. This combination of flux and slow-cooling method is also a known method to grow fibrous titanate [39,40]. The resulting lepidocrocite-like titanate has average lateral size of 4 mm while usual lepidocrocite-like titanate has ≈0.1 mm lateral dimension.

The general chemical formula for lepidocrocite-like nanosheets which created by Sasaki's method are $Cs_xTi_{2-x/4}\square_{x/4}O_4$ (x ≈0.7; $\square$ represents titanium vacancy [41,42]) and $A_xTi_{2-x/3}Li_{x/3}O_4$ (x ≈0.7 for A = Cs, x ≈0.75 for A = Rb, and x ≈0.8 for A = K) [33]. The detailed crystal structure of Sasaki's nanosheets is presented in Figure 2.3.
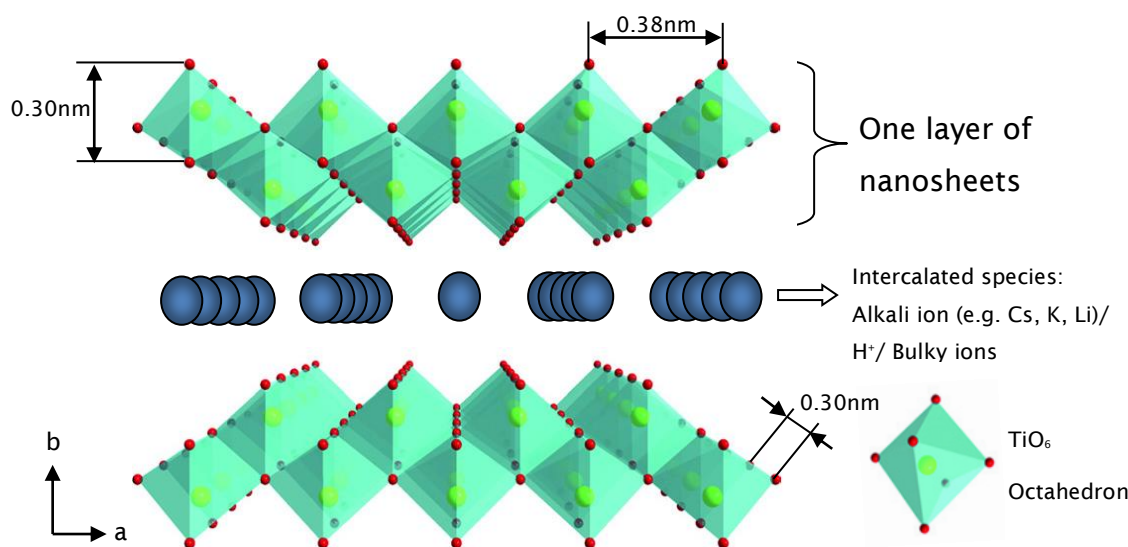
Figure 2.3. The polyhedral representation of crystal structure of lepidocrocite-like titanate nanosheets viewed down along the c-axis [43].

Lepidocrocite-like potassium-lithium titanate is different with lepidocrocite-like caesium titanate in terms of structural arrangement of interlayer ions (blue dot in Figure 2.3) due to the size of potassium ion is smaller than caesium [44] (see Figure 2.4). By modifying the precursor, other structures such as $Na_2Ti_3O_7$, $A_xTi_{2-x/2}M_{x/2}O_4$ (A = Cs, Rb or K; M= Mg, Fe, Co, Ni, Cu, or Zn) and $A_xTi_{2-x}M_xO_4$ (A = Cs, Rb or K; M= Mn(III), Fe(III), Sc, or Al) can be produced [43,45].
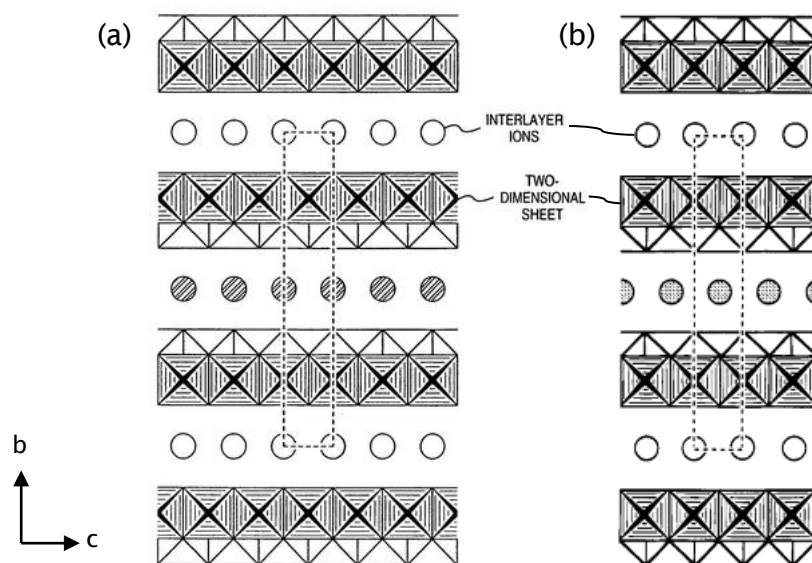
Figure 2.4. Crystal structure of lepidocrocite-like titanate projected on the (100) plane: (a) potassium-lithium titanate; (b) caesium titanate (area surrounded by the dotted line corresponds to orthorhombic unit cell) [44].

To create the single-layer nanosheets, Sasaki *et.al.* exfoliate lepidocrocite-like nanosheets by filling the interlayer of titanate with some bulky molecule. Intercalation of bulky molecules into the lepidocrocite-like titanate cannot be achieved in one step. Sasaki used two-step ion-exchange intercalation to exfoliate the lepidocrocite-like nanosheets. First step is an acid intercalation of H^+ ion by acid solution, replacing alkali ions and producing a smectite-like protonated titanate. H^+ ions are replenished by changing the used acid solution into a pristine acid solution, which is known as decantation. Repeated decantation is necessary for complete removal of alkali ions. According to Sasaki *et.al.* [36], Cs^+ ions will be exponentially decreased and replaced by H^+ ions (Figure 2.5). After three cycles of acid decantation, caesium ions are almost fully extracted ($\approx$98% removal achieved). The resulting state of titanate have high cation-exchange capacity and it is similar to smectite clay minerals (e.g., montmorillonite, saponite, hectorite) which its interlamelar structure possess unique hydration activity that can be swollen as molecule fills the interlayers.
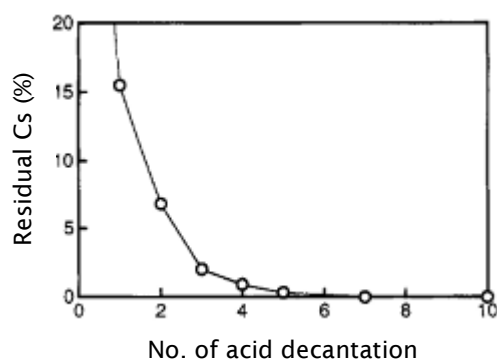
Figure 2.5. Caesium ion removal by acid decantation [36].

Next step is exfoliation by bulky ions molecules. There are three possible outcomes depending on the concentration of bulky ions (e.g., tetrabutylammonium (TBA$^+$) and tetramethylammonium (TMA$^+$) ion), which are intercalation of ions, exfoliation, or swelling [33]. The schematic representation of Sasaki's method to synthesis single-layer titanate nanosheets is shown in Figure 2.6.
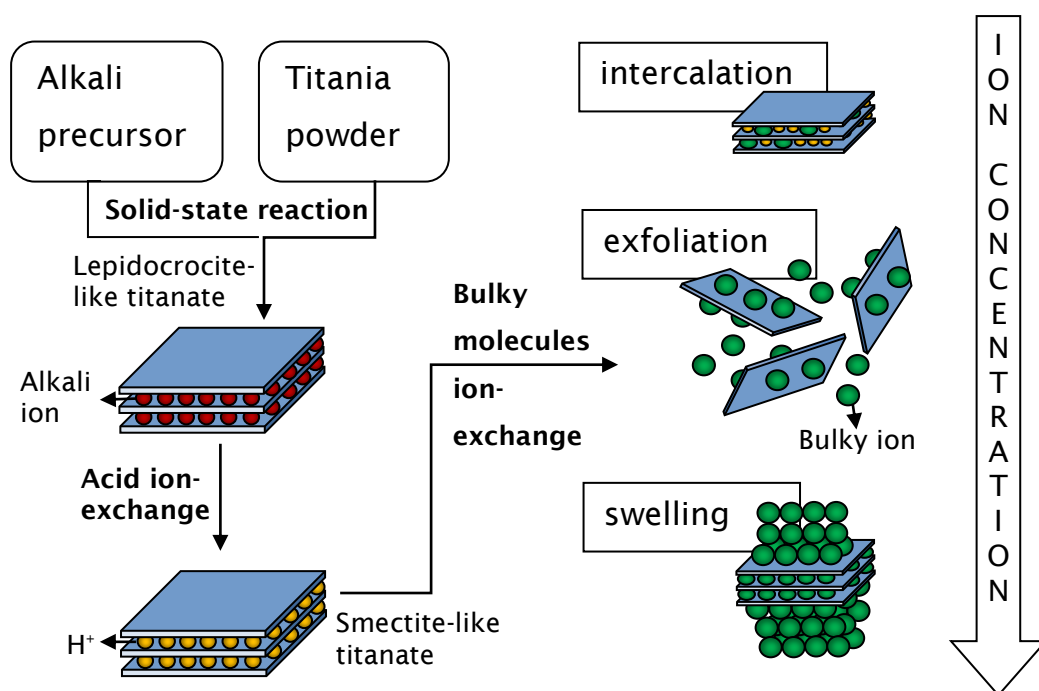
Figure 2.6. Schematic representation of Sasaki's method to synthesis single-layer titanate nanosheets.

The amount of bulky ions is critical to exfoliate the acid titanate (Figure 2.6). Intercalation, exfoliation, and swelling can be controlled by adjusting mole ratio of TBA^+ to H^+. For caesium route nanosheets, intercalation can be detected by small-angle X-ray scattering (SAXS), if the ratio of TBA^+/H^+ below 0.5. Interlayer spacing of nanosheets increases as the amount of bulky ions increases. Exfoliation (infinite interlayer spacing) occurs with the ratio of TBA^+/H^+ of 1-5 when the concentration of TBA^+ ions are high enough to fully cover the surface of nanosheets. At a greater amount $(TBA^+/H^+ > 5)$, some nanosheets start to form a multilayer arrangement of nanosheets (osmotic swelling). Further addition of bulky ions leads to fully swelling state and interlayer spacing of nanosheets become closer (coagulation). The osmotic swelling nanosheets can be exfoliated with agitation and coagulated if those are settled for certain period of time. This ratio of TBA^+/H^+ depends on the stoichiometry of the smectite like-materials [38,46,47].

Other methods of exfoliation such as supercritical fluid exfoliation [48] and combination of bulky molecules exfoliation and ultrasonication [49] have been investigated. By applying ultrasonic wave in a solvent, cavitation bubbles are generated and collapse into high energy jets thus breaking up layered nanosheets. Ultrasonication accelerates the synthesis of single nanosheets yet the lateral size reduction of nanosheets is inevitable. The exfoliation can also occur by putting layered titanate nanosheets in supercritical fluid of dimethylformamide. A supercritical fluid is any compound at a temperature and pressure above its critical point, where intermediate phase, that can effuse through solids like a gas and dissolve materials like a liquid, occurs. Effusion is a movement of gas molecules through a hole smaller than its mean free path. In this case, the supercritical fluid rapidly intercalates the layered nanosheets. By applying thermal stress to the intercalated nanosheets, the nanosheets are exfoliated and the single-layer nanosheets are formed. When the fluid is cooled down, some of the single-layer nanosheets restack to reform layered nanosheets. The yield of single-layer nanosheets made by supercritical fluid exfoliation depends on the cooling rate. Faster cooling rate is more favourable for single-layer nanosheets formation. However, the highest yield of this method, without stabilisation of single nanosheets, was estimated only 10%.

Other researchers have tried to make single nanosheets by bottom-up approaches such as sol-gel [50,51] and electron beam deposition of titania and oxygen atoms [52]. Some sol-

gel synthesis, by reacting titanium precursor (e.g., TiF_4, $(NH_4)_2[TiO(C_2O_4)_2]$) with aqueous alkaline solution such as KOH, NaOH, create small multi-layered nanosheets thus it still require bulky molecules (e.g., TBAOH, TMAOH) to exfoliate into single nanosheets [53,54]. By refluxing titanium isopropoxide (TIP) with excess of tetramethylammonium hydroxide (TMAOH) aqueous solution, high yield of diamond shaped single-layered nanosheets can be produced [50]. Nevertheless, this approaches usually produce relatively small (<50 nm) single-layer nanosheets. Some researchers considered the products as a nanodot, 0-D nanostructure [50]. Ban *et.al.* [55] successfully created large diamond shaped titanate nanosheet (*ca.* 100 nm) using organic ligand by consecutive sol-gel and dialysis. Aqueous solution of TIP, $(N(C_2H_4OH)_3$ or lactic acid (organic ligand), and tetrabutylammonium hydroxide (TBAOH) heated in autoclave at 80 °C for 1-7 days for crystallization of titanate nanosheets. The organic ligand adsorb on titanate layers retarding crystal nucleation promoting growth in lateral direction. To prevent restacking of titanate nanosheets, removal of interlayer cation was performed by dialysis. The schematic representation of the synthesis method is provided in Figure 2.7.
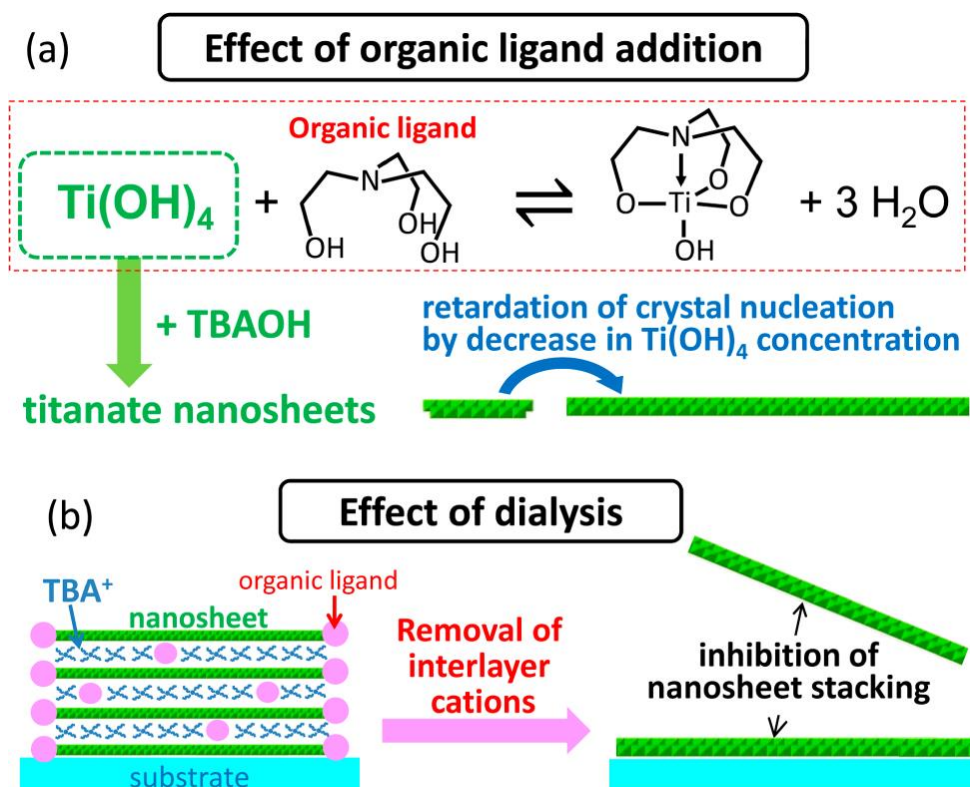
Figure 2.7. The illustration of (a) the effect of the organic ligand in crystallisation of the titanate nanosheets and (b) inhibition of nanosheets restacking by dialysis.

12

Sol-gel synthesis at ice/hexane interface may also produce large nanosheets [51]. The idea of this method is to confine the growth of TiO_2 within ice and organic solvent interface thus creating 2-D TiO_2 structure. The sol-gel formation of 2-D TiO_2 by this method is illustrated in Figure 2.8.

Figure 2.8 Schematic illustration of 2-D TiO_2 formation on ice interface [51].

These nanosheets are unique because they are made up of several nanodiscs ($\approx$5-15 nm) instead of diamond shape, which are agglomerated horizontally in Figure 2.9. The ultra-thin thickness ($\approx$0.5-1 nm) measured by atomic force microscopy (AFM) indicating the single-layered nanosheet structure. The crystal structure of this nanosheets is akin to anatase TiO_2 structure which characterised by X-ray diffraction (XRD).
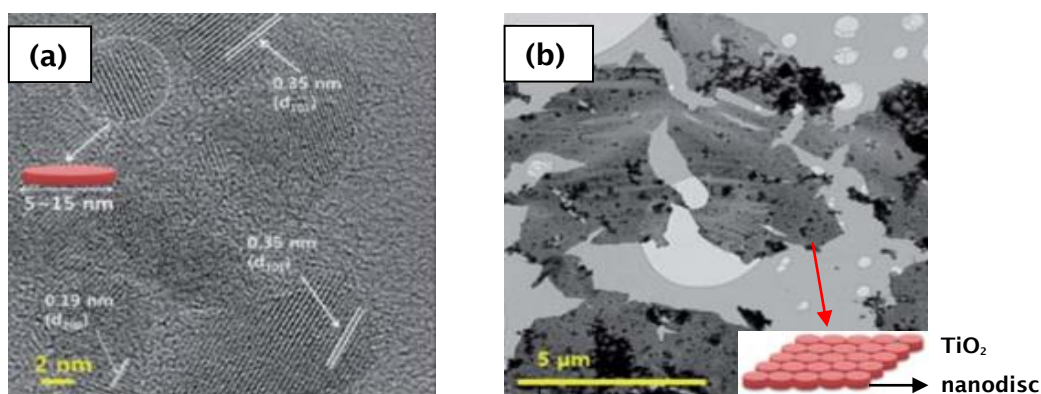
Figure 2.9. TEM images of a nanosheet consisting of horizontally agglomerated TiO_2 nanodiscs [51]: (a) HR-TEM image of nanodiscs, (b) TEM image of nanosheets.

Summary of synthesis methods for single-layer titanate nanosheets is presented in Table 2.1. The schematic of several routes to create single nanosheets are illustrated in Figure 2.10. Sasaki's method remains popular among other methods because its simplicity to create large nanosheets. Due to the titanium vacancies, Sasaki's titanate nanosheet has a net negative charged on the nanosheet surface providing stability in basic solution (pH $\geq$10) [56]. Alkali metal ions such as K^+ or Cs^+ may intercalates the interlayer of titanate nanosheets to balance the charges. By treating the titanate nanosheets in acid solution, these alkali metal ions can be replaced by protons. The ion exchange capability of titanate nanosheets evokes the possibility to modify the chemical properties of titanate nanosheets.

The electronic band structure of titanate nanosheets ($Ti_{0.91}O_2$) is slightly larger than anatase titania, TiO_2. Electrochemical studies was performed by applying a negative bias of -1.3 V to a 10 layers films of the $Ti_{0.91}O_2$ nanosheets stacked on indium-doped tin oxide (ITO) glass, along with *in-situ* UV−vis absorption measurement at the wavelength of 323 nm. The band gap energy (E_g) of the $Ti_{0.91}O_2$ nanosheets was estimated at 3.84 eV, which is 0.6 eV larger than anatase TiO_2 [57]. The larger band gap energy of titanate nanosheets may be explained by quantum size effects in two-dimensional structures, considering the fact that the precursor of layered titanate nanosheets has the band gap of 3.24 eV, which is similar to anatase [58]. Stronger UV light is required to activate the photocatalytic capability of titanate nanosheets compare to the anatase TiO_2.

Table 2.1. Summary of synthesis methods for single layered titanate nanosheets.

Top-down approach				
Solid-state reaction				
Synthesis of layered nanosheets	**Exfoliation method and its additive**	**Chemical formula**	**Lateral size**	**Ref.**
$Cs_2CO_3 + TiO_2 \rightarrow Cs_xTi_{2-x/4}\square_{x/4}O_4$ ($x \approx 0.7$; $\square$ = vacancy) Reaction at 800 °C for 20 h (2 times)	Ion-exchange at 25 °C for 2 weeks by 0.00825 to 0.0825 mol L^{-1} aqueous solution of (tetrabutylammonium hydroxide) TBAOH	$Ti_{0.91}O_2^{0.36-}$	$\approx$0.1-1 µm	[33]
$Cs_2CO_3 + TiO_2 + MgO \rightarrow Cs_xTi_{2-x/2}Mg_{x/2}O_4$ ($x \approx 0.7$) Reaction at 800 °C for 1 h followed by 2 times heating at 950 °C for 20 h	Ion-exchange at 50 °C for 1 week by 5 wt% aqueous solution of TBAOH or (tetramethylammonium hydroxide) TMAOH	$Ti_{0.825}O_{1.825}^{0.35-}$	$\approx$0.1-1 µm	[43]
$K_2CO_3 + TiO_2 + Li_2CO_3 \rightarrow K_xTi_{2-x/3}Li_{x/3}O_4$ ($x \approx 0.8$); (with K_2MoO_4 as flux melt) Reaction at 1200 °C for 10 h followed by slow cooling (4 °C h^{-1}) until it reach 950 °C	Ion-exchange at 25 °C for 2 weeks by 0.0125 to 0.025 mol L^{-1} aqueous solution of TBAOH	$Ti_{0.87}O_2^{0.52-}$	10-100 µm; average $\approx$30 µm	[38]

15

Synthesis of layered nanosheets	Exfoliation method and its additive	Chemical formula	Lateral size	Ref.
$Na_2CO_3 + TiO_2 \rightarrow Na_2Ti_3O_7$ Reaction at 900 °C for 24 h	Ion-exchange by methylamine at 60 °C for 6 d followed by propylamine at 60 °C for 6 d	$Ti_3O_7^{2-}$	≈0.1-1 µm (rectangular)	[45]
$Cs_2CO_3 + TiO_2 \rightarrow Cs_xTi_{2-x/4}\square_{x/4}O_4$ (x ≈0.7; $\square$= vacancy); Reaction at 800 °C for 20 h (2 times)	Ion-exchange by TBA$^+$ ion assisted with ultrasonication (60-300 W, 2-30 min)	$Ti_{0.91}O_2^{0.36-}$	≈0.1-0.2 µm	[49]
$K_2CO_3 + TiO_2 + Li_2CO_3 \rightarrow K_xTi_{2-x/3}Li_{x/3}O_4$ (x ≈0.8) (with K_2MoO_4 as flux melt) Reaction at 927 °C for 10 h (Spontaneous cooling)	Supercritical N,N-dimethylformamide (DMF) exfoliation (400 °C, 15 min)	$Ti_{0.87}O_2^{0.52-}$	≈5-20 µm	[48]

Sol-gel followed by ion exchange

Synthesis of layered nanosheets	Exfoliation method and its additive	Chemical formula	Lateral size	Ref.
$(NH_4)_2[TiO(C_2O_4)_2] + KOH \rightarrow K_{1.1}H_{0.9}Ti_2O_5 \cdot 2.6H_2O$ (1 day, 22–80 °C)	Ion-exchange by aqueous solution of TBAOH at 22 °C	$Ti_2O_5^{2-}$	≈10-20 nm	[53]
$TiF_4 + NaOH \rightarrow Na_{0.8}Ti_{1.8}\square_{0.2}O_4 \cdot yH_2O$ (y <1.17) (3 days, 22 °C)	Ion-exchange by aqueous solution of TBAOH at 22 °C	Not available	≈2-5 nm	[54]

Bottom-up approach			
Method	**Chemical formula**	**Lateral size**	**Ref.**
Reflux of Ti(IV)isopropoxide (TIP) + aqueous solution of tetramethylammonium hydroxide (TMAOH); (5 min – 24 h, 100 °C)	$(TMA)_x Ti_{2-x/4} \square_{x/4} O_4$ (x ≈0.7)	Diamond shape with diagonal length (27.3, 19.1) nm to (7.7, 5.5) nm.	[50]
TIP + (N(C$_2$H$_4$OH)$_3$ or lactic acid (organic ligand)+ tetrabutylammonium hydroxide (TBAOH) heated in autoclave at 80 °C for 1-7 days followed by dialysis with water for 2 days	$(TBA, H)_{0.7} Ti_{1.825} O_4 \cdot xH_2O$	Diamond shape with ≈100 nm lateral size	[55]
Sol-gel of hexane + TIP + ice granule interface followed by hydrolysis with HCl	TiO_2	≈5 μm consist of 5-15 nm nanodiscs	[51]
e-beam deposition on (1 × 2)-Pt(110); Ti was deposited at room temperature ($pO_2 = 1\times10^{-4}$ Pa) followed by post-annealing treatment at 700 K and cooling down in oxygen ($pO_2 = 1\times10^{-4}$ Pa)	TiO_2	3.9 × 1.6 nm	[52]
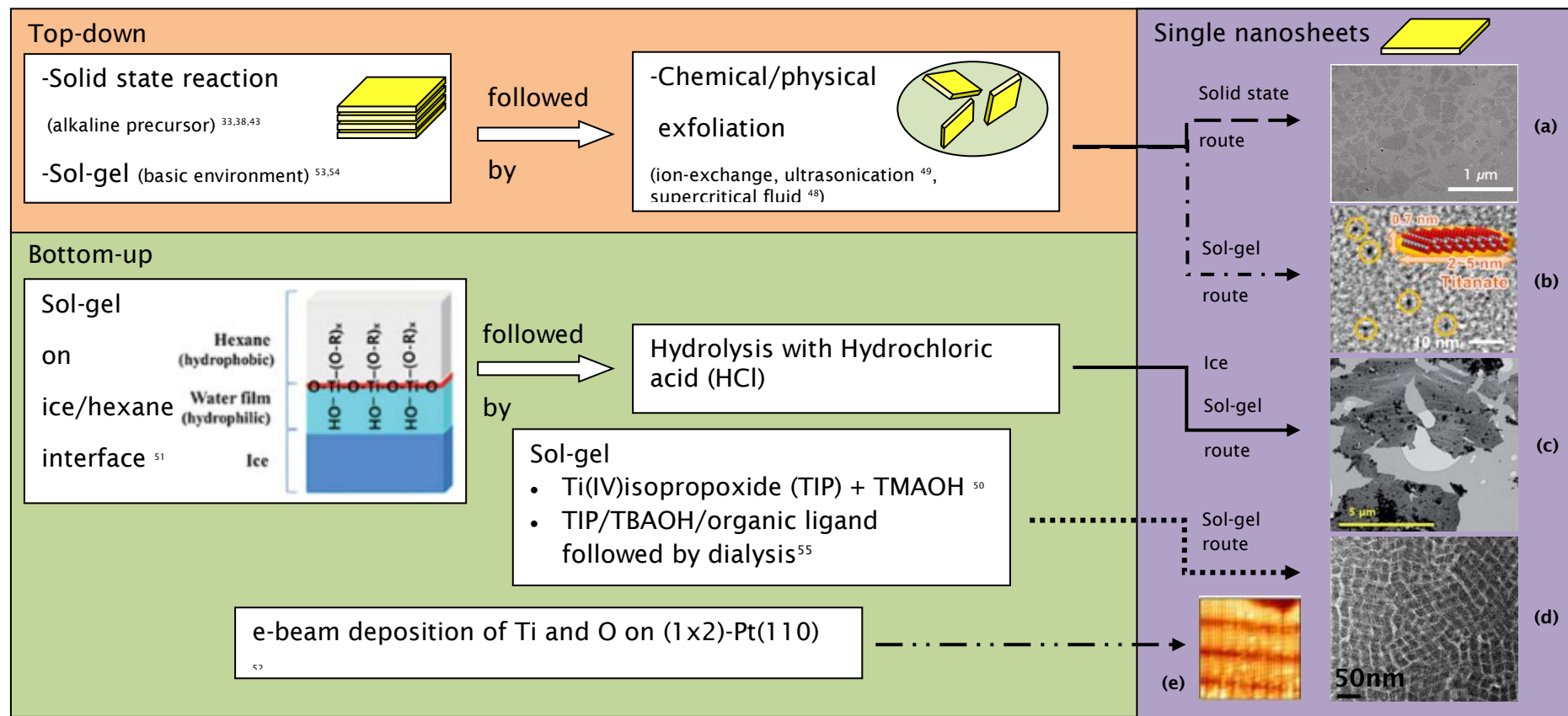
Figure 2.10. Several routes to synthesis single-layer titanate nanosheets: **(a)** TEM image of nanosheets made by solid state route [59], **(b)** Bright-field TEM image of nanosheets made by sol-gel route [54], **(c)** TEM image of nanosheets made by ice sol-gel route [51], **(d)** TEM image of nanosheets made by sol-gel route [50], **(e)** High resolution STM image of nanosheets made by e-beam deposition route (13.6 nm × 13.6 nm; bias voltage = 0.42 V; I_T = 0.9 nA) [52].

18

2.1.2   Other titanate nanostructures

The nanotubes (NT) and nanofibres (NF) are an example of 1 dimesional nanostructure, and nanospheres (NSp) are an example of 0 dimensional nanostructures. Titania nanospheres are commercially available; one of them is available under the brand name "Degussa P25". This has ≈27 nm radius, specific surface area of 50 m^2 g^{-1} with a mixture of 80 % anatase and 20 % rutile.

For titanate nanotubes synthesis, there are three common methods which are template methods, alkaline hydrothermal synthesis, and electrochemical anodizing of titanium [60]. The hydrothermal method is favourable because it is template-less, versatile, and relatively simpler than other methods thus it is suitable for this work. Nevertheless, it has several limitations, such as random orientation of nanotubes.

The mechanism of hydrothermal titanate nanotubes formation can be explained by the scrolling of the titanate nanosheets. There is several therories addressing the driving force for curing of the nanosheets. Zhang *et.al.* [61] argued that the imbalance of H^+ or Na^+ ion concentrations on the two different sides of a single layer nanosheet may cause an excess surface energy and bend the sheet into the shape of a tube. This mechanism is depicted in Figure 2.11 a, where the free surface energy value on each surface denoted as a spring constant (k). In the multi-layered nanosheets, the bending of layered nanosheets may arised from mechanical tensions during the dissolution-crystallisation process in nanosheets [60]. In the most cases of layered chemical compound, the interaction energy between atoms in the same layer is much stronger than the interaction energy between atoms in neighbouring layers. As a result, the imbalance in the rapid growth of each layer during spontaneous crystallisation may creates bending of the layered nanosheets in Figure 2.11 b. On the contrary, flat nanosheets may occur if the interaction energy between atoms in neighbouring layers is much stronger than the interaction energy between atoms in the same layer.
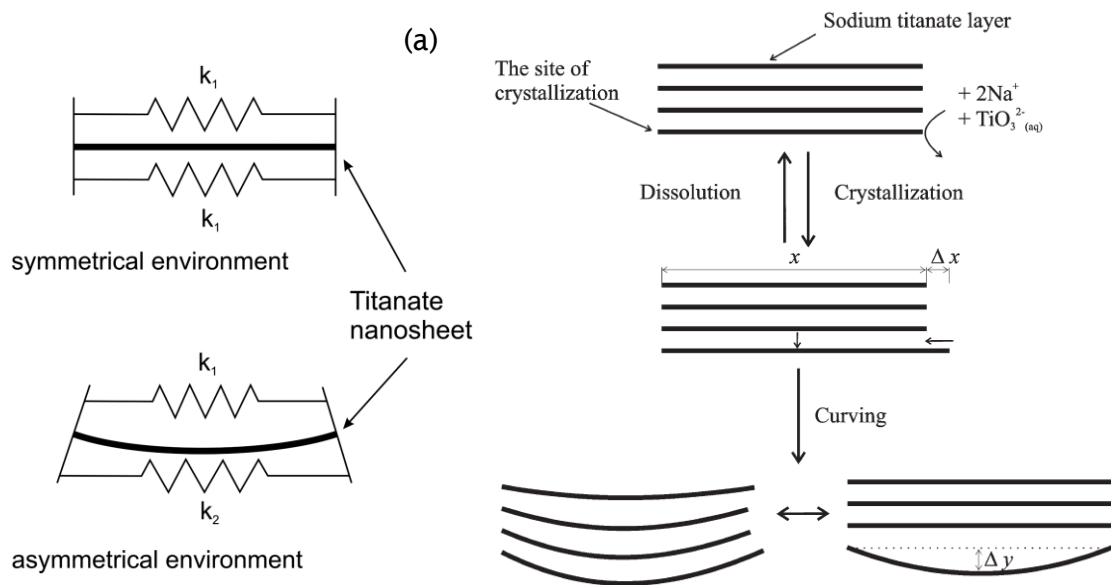
Figure 2.11. The mechanism of the bending of titanate nanosheets with 2 different driving forces; (a) the bending of titanate nanosheets are caused by a difference in surface tension on each side of the nanosheet in an asymmetrical chemical environment; k1 and k2 are the spring constants for each side; (b) The imbalance of layer width (x) shifts and bends the titanate nanosheet layers; Δy is the curving deformation of the layers.

The hydrothermal method is also applicable for the fabrication of nanofibres by changing the processing temperature and/or chemical environment (Figure 2.12). Low temperature process is a favourable condition for the formation of nanosheets while high temperature process is for fabrication of nanofibres. Nanotubes can occur at a certain temperature process between the temperature of nanosheet and nanofibre formation.
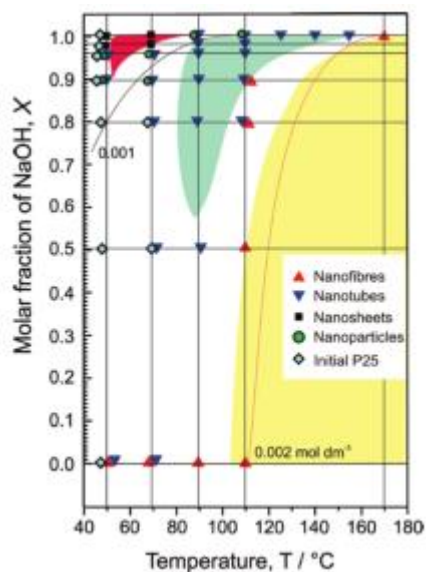
Figure 2.12. The effect of processing temperature and molar fraction of NaOH on the morphology of resulting titanate. Red, blue, and yellow zones are indicating favourable condition for fabricating nanosheets, nanotubes, and nanofibres respectively [24].

Transmission electron microscopy images of an example of titanate nanosheets, nanotubes, nanofibres, and nanospheres are provided in Figure 2.13. The changes in morphology of hydrothermally synthesised titanate corresponds to the processing temperature in which higher temperature is more favourable for one-dimensional titanate.
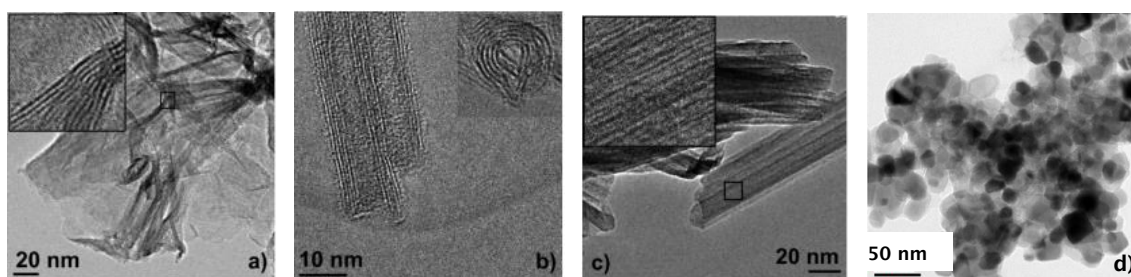
Figure 2.13. TEM images of titanate nanostructures [24]; synthesised by hydrothermal method using NaOH:KOH ratio 25:1 (a) at 50 °C (nanosheets); (b) at 110 °C (nanotubes); (c) at 170 °C (nanofibers); and (d) commercially available titania nanospheres "Degussa P25" [62].

21

The chemical structure of hydrothermally synthesised titanate in protonated form is considered as polytitanic acid ($H_2Ti_nO_{2n+1}$) based on characterisation with X-ray diffraction, selected area electron diffraction, and high-resolution transmission electron microscopy [63,64]. The dissociation of polytitanic acid in an aqueous solution develops a negative zeta potential, for example the titanate nanotubes undergoes following reaction $H_2Ti_3O_7 \rightarrow H^+ + HTi_3O_7^-$ [65]. Owing to the negative surface charge, the titanate nanotubes has the affinity to attracts cations such as cationic dye and metal ions.

The electronic band energy of the titanate nanotubes is similar to Sasaki's flat titanate nanosheets, which is 3.87 eV and 3.84 eV for nanotubes and Sasaki's nanosheets, respectively [66]. The titanate nanotubes may has the similar quantum size effect as flat titanate nanosheets recalling the mechanism of the titanate nanotubes formation is by scrolling of titanate nanosheets. To activate its photocatalytic ability, the large band gap of titanate nanotubes also suggests the utilisation of stronger UV light compared to anatase TiO_2.

2.2 Polyimide

2.2.1 History of polyimide

Polyimide is known as a lightweight material, flexible, resistant to heat and chemicals. It has been used in many applications such as photo-resist, high temperature adhesive, electronic devices (insulating and passivation layer of semiconductor, flexible cable, alignment layers of liquid crystal display), constructive parts (bushings, bearings, sockets), hot gas filtration, reverse osmotic film, sensors, part of spacecraft and satellite [2–4]. Polyimide is often found as a heat and chemical resistant tape in electronic devices (e.g., integrated power electronic module in Figure 2.14 a and b), and duct tape in Figure 2.14 c.
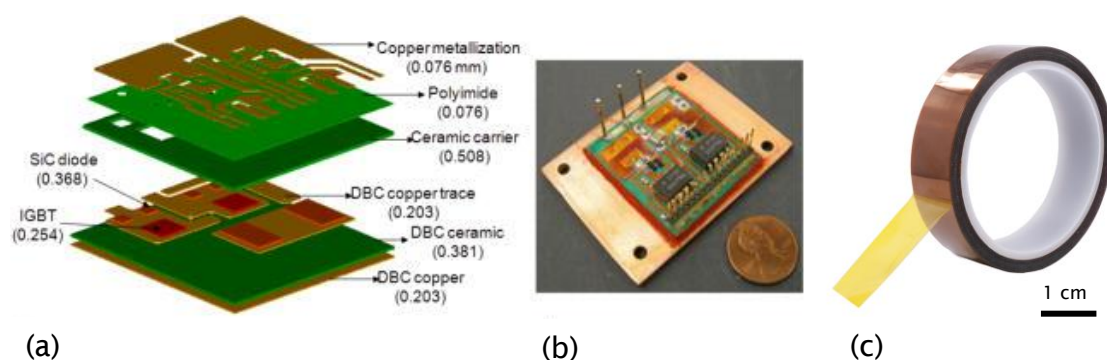
Figure 2.14. Examples of polyimide in everyday life; (a) expanded view of integrated power electronic module (IPEM); all dimension in mm [67]; (b) the overall images of a generation-II (Gen-II) insulated gate bipolar transistor (IGBT) IPEM [67]; (c) polyimide tape [68].

In 1955, the polyimide has been discovered in the DuPont's Film Department laboratory at the Experimental Station in Willmington, USA [5]. Direct melt or solution polymerization of dianhydride and aliphatic diamines or their amine salts was used as a first approach to make polyimide. However, the resulting product was not very useful. John Brill, Director of Research, saw the potential of the polyimide and continued the project with different approach. Later on, the research group focused on aromatic polyimide. They varied the aromatic diamine and developed the polyimide based on three kind of diamines that are m-phenylene diamine (MPD), *p*-phenylene diamine (PPD), and oxy-dianiline (ODA). Polyimides are mainly based on dianhydride and diamine monomers so this thesis will focus on these monomers. Nonetheless, there are other monomers to make polyimide such as di(acid-ester) and diamine [5], amino-anhydride monomers [69], chloral-derived monomers, and trinitrotoluene (TNT) monomers [70].

Finally, DuPont successfully created outstanding aromatic polyimide film based on pyromellitic dianhydride (PMDA) and *m*-phenylene diamine (MPD) via poly(amic-acid) formation (later known as two-step method which become a common method to synthesise polyimide). PMDA-ODA polyimide has received major attention from researchers and industries because its toughness and thermal stability in air and in nitrogen. By the mid-1960s, DuPont had Kapton (film), Vespel (moulding), and Pyre-ML (wire insulation). These three products are their major polyimide products.

Furthermore, many studies have been focused to develop one-step method of polyimide synthesis which is quicker than two-step method [5]. One-step method is also beneficial to synthesis several polyimide because some solvent for two-step method triggers the precipitation of low molecular weight polyimides [71]. The one-step method rapidly becomes popular method apace with two-step method. However, one-step method has several disadvantages such as the use of toxic solvent (e.g. 4-chlorophenol) and broader molecular weight distribution of polyimide compared to two-step method.

This thesis will only use common methods of polyimide synthesis such as two-step method and one-step method. Thus, novel methods such as direct solid-state polymerization [69,72,73], vapour deposition [72,73], and microwave method [72] are not within the scope of this study.

2.2.2 "Classical" two-step method for polyimide synthesis

The classical two steps polycondensation mechanism consists of two major stages that are amic acid formation followed by imide formation (imidization/cyclization). The amic acid formation begins with nucleophilic amine attacks the electropositive carbonyl carbon. The carboxyl remains attached thus resulting in ortho formation of an amide and acid group. The detail mechanism can be seen in Figure 2.15.
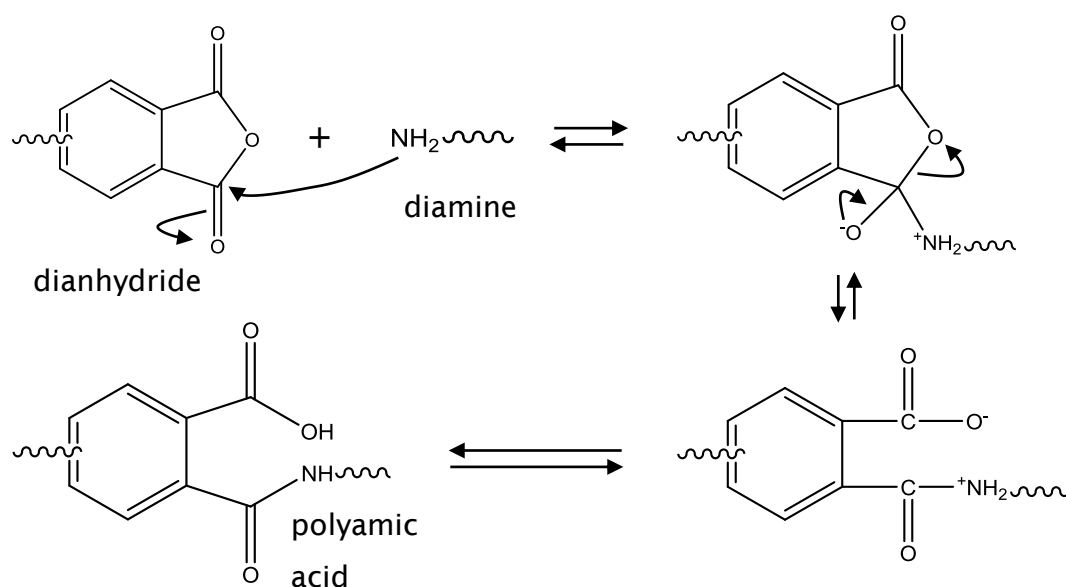
Figure 2.15. The first stage of polyimide synthesis: polyamic acid formation [5].

Some addition of acids can be used as a catalyst of amic acid formation in specific solvent. For example, benzoic acid acts as a catalyst in acetonitrile, N,N-dimethylacetamide (DMAc) and N,N-dimethylformamide (DMF). Acetic acid and N,N-dimethyl-4-amino pyridine are effective catalyst in tetrahydrofuran (THF).

The second stage (imidization) is a condensation reaction between COOH and –NH-groups (see Figure 2.16) which results in imide cyclization. Despite the mechanism of imidization is still debatable, imide formation can be achieved by two different approaches which are thermal imidization and chemical imidization. In thermal imidization, high temperature (≈300 ºC) is needed to achieve fully-cured polyimide. Heat treatment must be done in vacuum chamber to remove the water as by-product of imidization otherwise it will inhibit the imidization process. In chemical dehydration, vacuum chamber is not necessary. Nonetheless, chemical imidization requires dehydrating agent such as acetic anhydride and base catalyst (e.g. pyridine, tertiary amine). Phosphorous pentoxide and phosphorous trichloride were also found to promote polyimide formation. In some cases, polyisoimide are formed instead of polyimide. However, polyisoimide can be converted to polyimide with heating at 200-250 ºC or with base catalyst at temperature below 100 ºC. Schematic representation of two-step process is provided in Figure 2.16.
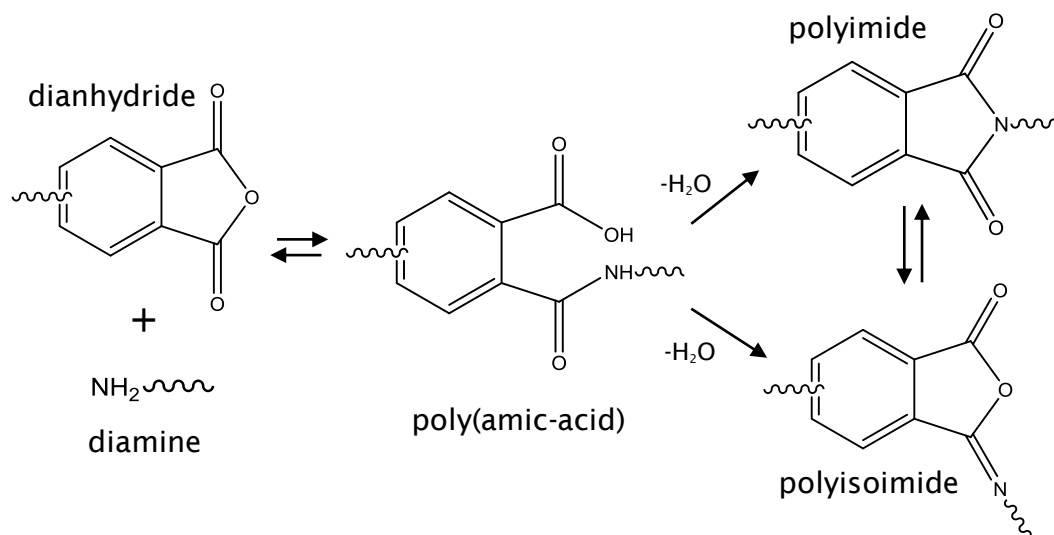
Figure 2.16. Schematic representation of the two-step process for polyimide synthesis.

2.2.3   One-step method for polyimide synthesis

In one-step method, amic acid formation and imide formation happen at the same reaction time. Poly(amic-acid) can rapidly turn into polyimide or revert back into monomers. This reaction occurs in suitable solvent (e.g., *m*-cresol, *p*-chlorophenol (PCP), benzoic acid, salicylic acid) at temperatures in excess of 150 ºC. Higher temperature results in quicker polymerisation. Solvent and water vapour are usually removed from the reactor by inert gas and condensed into gravity separator. Only the solvent is returned into the reactor. As an alternative, 1-cyclohexyl-2-pyrrolidinone (CHP) might be needed as an effective water azeotroping agent for solution imidization. An azeotropic mixture is a mixture of two or more liquids, which exhibits the same fraction of component when those are evaporated and cannot be separated by distillation [74].

The choice of solvent affects the optimum amount of solid content to make the high polyimide molecular weight, hence it is processable to make thick film. If the solid content exceeds the optimum value, gel will be formed decreasing the apparent viscosity. For example, PCP is better than *m*-cresol to make 3,3',4,4'-biphenyl tetracarboxylic dianhydride (BPDA)-ODA aromatic polyimide. The optimum solid content by *m*-cresol is 9.1 wt/vol% while with PCP it can reach 16 wt/vol% without gelation of the solution [75]. Instead of organic solvent, molten acid is often used as a reaction medium. The melt of salicylic acid is better than the melt of benzoic acid. Large amount of solid content (40 wt/vol%) is possible to dissolve in molten salicylic acid whereas it is only 12 wt/vol% for benzoic acid. Isoquinoline and benzimidazole [76] are also often used as a catalyst in molten acid solvent. The catalytic molten acid enables faster reaction (≈2 h) than casual solvent such as *m*-cresol or PCP (≈18 h) [77]. The polymerisation rate is also greatly influence by monomer structure. For example, bulky groups and kinks slow the reaction rate. On the other hand, electron withdrawing groups in dianhydride such as –CF_3 increase the rate of reaction.

One-step method in *m*-cresol or PCP has become a popular research area for semi-aromatic polyimide synthesis especially with aliphatic dianhydrides and aromatic diamines. However, there is a problem with aliphatic diamine in imide formation which impeding the synthesis of fully aliphatic polyimide. Insoluble salt is formed from the reaction of carboxyl group of poly(amic-acid) and excess aliphatic diamine [78]. This

phenomenon does not occur in aromatic diamine due to the difference in basicity. Nevertheless, low molecular weight polyimide still can be formed by adding aliphatic diamine slowly to aromatic dianhydride.

In order to make fully aliphatic polyimide, Ueda *et.al.* used silylated aliphatic diamine to prevent the salt formation, resulting poly(amic-acid) silylester in DMAc (common solvent for two-step process) [79]. The process continued with thermal imidization. This two-step method produced a relatively high molecular weight polyimide.

2.2.4 The properties and applications of polyimide

Polyimide has general chemical characteristic which is repeating unit of imide monomers (Figure 2.17, in the red circle). It can be classified into aromatic, semi-aromatic, fully-aliphatic polyimide according to the main chain composition (Figure 2.17). Aromatic polyimide has aromatic ring in diamine and dianhydride chain. Semi-aromatic polyimide has aromatic structure only in diamine or dianhydride chain while other chain is aliphatic or alicyclic. Fully-aliphatic does not have any aromatic group.
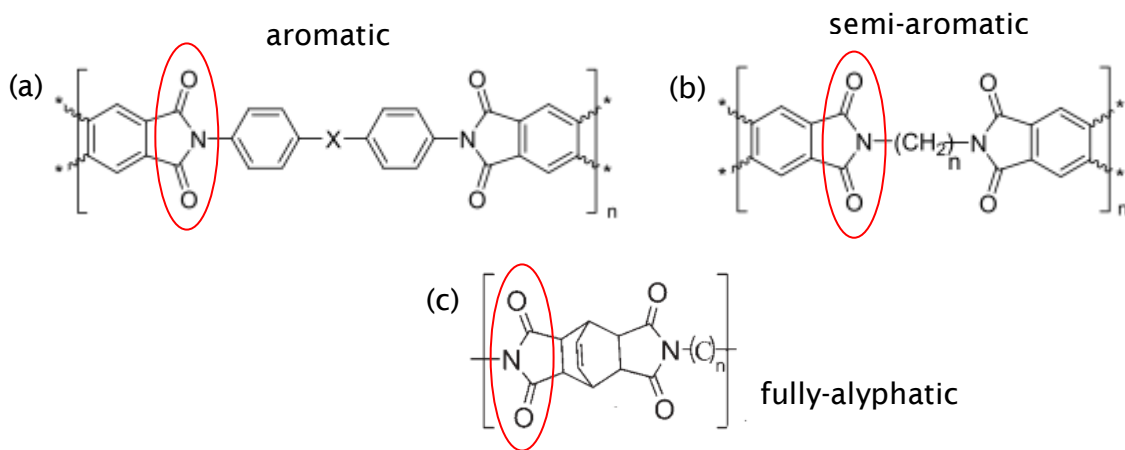
Figure 2.17. Classification of polyimide based on main chain composition; (a) aromatic polyimide [72]; (b) semi-aromatic polyimide [72]; (c) fully-aliphatic polyimide [80] (red circles indicate imide group in polyimide).

The mechanical and thermal properties of polyimide are affected by the degree of imidization, the molecular weight of polyimide, and the structure of the monomers.

These properties increase as degree of imidization and molecular weight increase. Viscosity of poly(amic-acid) can be used as an indicator of polyimide molecular weight. If the viscosity is too low, it will produce brittle material. High viscosity is needed to produce tough polyimide. Aromatic group improves thermal stability of polyimide. For example, aromatic polyimide can withstand up to 400 °C whereas fully-aliphatic polyimide will only survive in the temperature below ≈200 °C [5]. Kapton, which is pyromellitic dianhydride-oxydianiline (PMDA-ODA) polyimide, is one example of aromatic polyimide which has been used for several applications such as space thermal insulators, electrical insulators, and X-ray windows. PMDA-ODA polyimide has high strength (231 MPa), due to its rigid aromatic groups of PMDA, while maintaining high elongation to break (72%) [81]. High elasticity of PMDA-ODA comes from C-O-C angle in oxydianiline segment which is ≈128 ° [82] in Figure 2.18. Oxygen has lone pair of electrons which is repulsive to each other pushing C-O-C bond closer together. This kink structure produces more flexible chain.
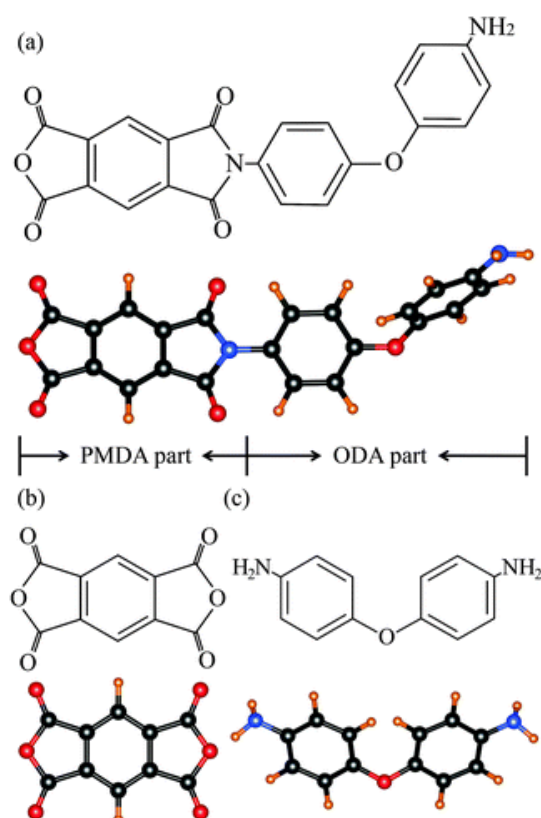
Figure 2.18. Chemical representation of (a) pyromellitic dianhydride oxydianiline (PMDA–ODA) (b) pyromellitic dianhydride (PMDA), and (c) oxydianiline (ODA). The red, blue, black and orange spheres represented oxygen, nitrogen, carbon, and hydrogen atoms, respectively [82].

The visible light absorbance of polyimide depends on three factors which are the charge transfer in the chain sequence, the use of fluorinated monomers, and the use of aliphatic monomers [83]. Charge transfer complex (CTC) of polyimide is related to electron-accepting characteristic of dianhydride and electron-donating properties of diamine which affected intra- and intermolecular interactions. These interactions will strengthen the visible light absorbance. These interactions which related to charge transfer can be lowered by avoiding the use of aromatic monomers and increasing steric hindrance in chains by choosing bulky monomers, kinks, or distorted/flexible chain (e.g., ortho-substituent). Fluorinated monomers usually have bulky substituents such as $-CF_3$ lowering inter-chain interaction which is shown in Figure 2.19. Larger gap between chains indicates the reduction of intermolecular CTC by fluorinated polyimide. The low polarizability of C-F linkage is also diminished interlayer formation energy which weakened the visible light absorbance of polymer.
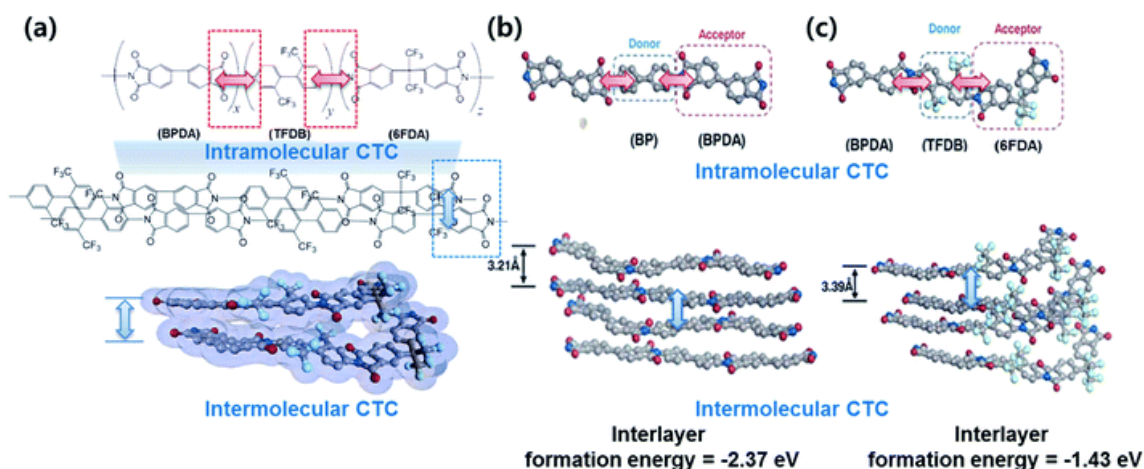
Figure 2.19. (a) An example of intra- (red arrow) /inter- (blue arrow) molecular charge transfer complex (CTC); molecular geometry of (b) non-fluorinated polyimide and (c) fluorinated polyimide using density functional theory (DFT) calculation [84].

By replacing aromatic polyimide to aliphatic polyimide, intramolecular interaction is reduced due to lower electron-donor characteristic. However, non-cyclic aliphatic polyimide should be avoided ascribed to its very low thermo-oxidative stability. Alicyclic (cyclic aliphatic) polyimide can be used as an alternative. Some alicyclic polyimide give very low absorbance of light even in the ultraviolet region [85]. Summary of properties and applications of several polyimide is given in Table 2.2.

Table 2.2. Summary of properties and applications of several type of polyimide.

Aromatic polyimide						
Polyimide	**Young's modulus**	**Elongation at break**	**T_g**	**Colour**	**Applications**	**Ref.**
PMDA-ODA	≈3 GPa	≈60-70%	≈390 ºC	Yellow	Electronic packaging, spacecraft and aircraft insulation, X-ray window	[86]
BPDA-PDA	7.97 GPa	34.5%	≈370 ºC	Yellow	Photosensitive electronic packaging	[87]
BPDA-ODA	≈3.8 GPa	≈70%	325 ºC	Pale yellow	Photosensitive electronic packaging, aircraft insulation	[88,89]
BTDA-ODA	3 GPa	≈23%	280 ºC	Pale yellow	Photosensitive electronic packaging	[88]
ODPA-ODA	≈2.7 GPa	≈20%	≈370 ºC	Pale yellow	Photosensitive electronic packaging, aircraft insulation	[88,89]
6FDA-ODA	1.69 ± 0.05 GPa	10 ± 2%	300 ºC	Pale yellow	Gas separator, low dielectric materials	[90–92]
6FDA-6FDAm	1.75 ± 0.01 GPa	7 ± 1%	320 ºC	Colourless		[90–92]

Semi-aromatic polyimide						
Polyimide	**Young's modulus**	**Elongation at break**	T_g	**Colour**	**Applications**	**Ref.**
BHDA-ODA	1.3 GPa	15%	-	Colourless	Liquid crystal orientation layers, flexible solar cell and organic electroluminescence substrates, light guide, and low dielectric materials	[93]
BODA-ODA	2 GPa	11%	-	Colourless		[93]
DNDA-ODA	2.3 GPa	30%	404 ºC	Colourless		[93]
PMDA-BBH	3 GPa	5%	282 ºC	Colourless		[93]
ODPA-BBH	1.6 GPa	6%	179 ºC	Colourless		[93,94]
BPDA-BBH	1.4 GPa	6.1%	195 ºC	Colourless		[93,94]
CHDA-ODA	2.4 GPa	7.8%	333 ºC	Colourless		[95]
CHDA-TFDB	2.7 GPa	6.6%	370 ºC	Colourless		[95]
CHDA-6FAP	2.2 GPa	9.1%	268 ºC	Colourless		[95]
CHDA-6FBAB	2.3 GPa	11.6%	276 ºC	Colourless		[95]

Fully-aliphatic polyimide						
Polyimide	Young's modulus	Elongation at break	T_g	Colour	Applications	Ref.
BOCA-10DAD	2.1 GPa	4%	219 ºC	Colourless	liquid crystal orientation layers, flexible solar cell and organic electroluminescence substrates, light guide, and low dielectric materials	[96]
BOCA-MCA	2.5 GPa	15%	239 ºC	Colourless		[96]
BOCA-MMCA	2.4 GPa	14.5%	241 ºC	Colourless		[96]
BHDA-BBH	2.1 GPa	6%	297 ºC	Colourless		[93]

Abbreviations : Glass transition temperature (T_g); pyromellitic dianhydride (PMDA); 4,4'-oxydianiline (ODA); 3,3',4,4'-biphenyltetracarboxylic dianhydride (BPDA); *p*-phenylenediamine (PDA); 3,3',4,4'-Benzophenone-tetracarboxylic dianhydride (BTDA); 4,4'-Oxydiphthalic anhydride (ODPA); 4,4'-(hexafluoroisopropylidene)diphthalic anhydride (6FDA); 2,2'-bis(4-aminophenyl)hexafluoropropane (6FDAm); bicyclo[2.2.1]heptane-2,3,5,6-tetracarboxylic dianhydrides (BHDA); bicyclo[2.2.2]octane-2,3,5,6-tetracarboxylic dianhydrides (BODA); (4arH,8acH)-decahydro- 1t,4t:5c,8c-dimethanonaphthalene-2t,3t,6c,7c-tetracarboxylic 2,3:6,7-dianhydride (DNDA); bis(aminomethyl)bicyclo[2.2.1]heptane (BBH); 1,2,4,5-Cyclohexanetetracarboxylic dianhydride (CHDA); 2,2'-bis-Trifluoromethyl-4,4'-diaminobiphenyl (TFDB); 1,4-bis(4-amino-2-trifluoromethylphenoxy)benzene (6FAP); 4,4'-bis(4-amino-2-trifluoromethylphenoxy)biphenyl (6FBAB); bicyclo[2,2,2]oct-7-ene-2,3,5,6-tetracarboxylic dianhydride (BOCA); 1,10-diaminodecane (10DAD); 4,4'-methylene bis(cyclohexylamine) (MCA); 4,4'-methylene bis(2-methyl cyclohexylamine) (MMCA)

2.2.5 The storage of polyimide precursor

Polyimide precursor, namely polyamic acid, is usually stored for a long time before use. Therefore, the stability of polyamic acid during storage needs to be discussed.

The molecular weight of polyamic acid decreased throughout storage time [97]. This is mainly attributable to the hydrolytic instability of amide bonds in polyamic acid, which are attacked by carboxylic acid groups in polyamic acid (see Figure 2.20) reducing the chain length of the polymer. The addition of water increases the number of carboxylic acid enhancing the degradation of polyamic acid.
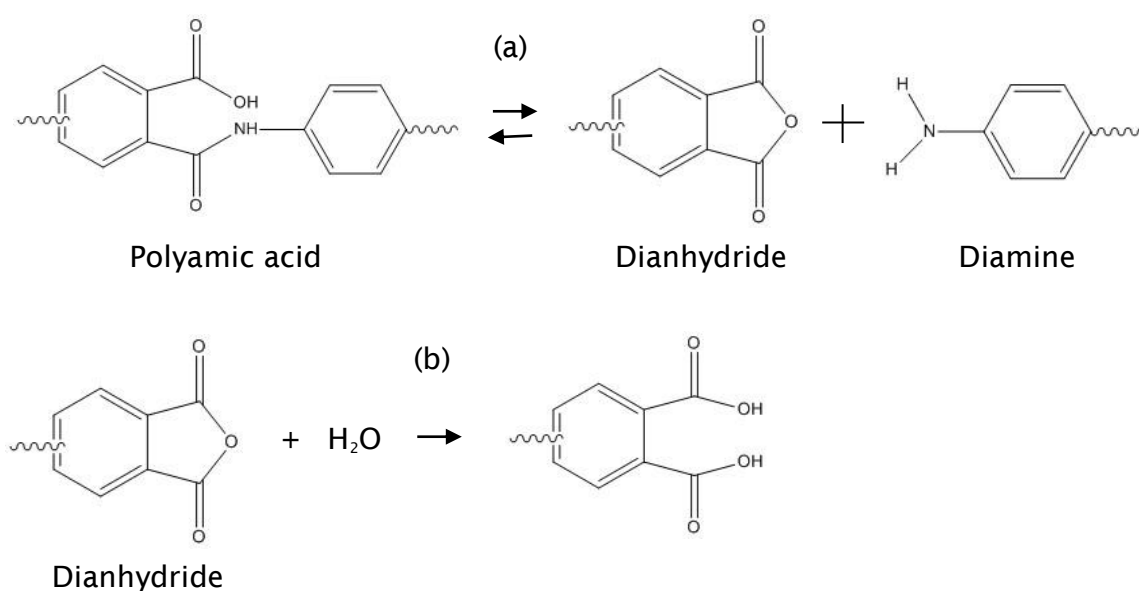
Figure 2.20. The degradation mechanism of polyamic acid. (a) the attack of carboxylic acid group on amide bond in polyamic acid creates dianhydride and diamine; (b) the hydrolysis of dianhydride creates more carboxylic acid [98].

To overcome the problem, Dongdan Cai *et. al.* use triethylamine to cap the carboxyl groups thus it will not attack amide bonds [99]. However, triethylamine becomes volatile during imidization thus diminishing mechanical properties of polyimide as a final product.

The rate of deterioration is determined by concentration, temperature, and humidity. The polyamic acid is less stable in dilute solution and more stable in dry conditions. The

degradation of polyamic acid is indicated by a reduction of its viscosity. The effect of temperature on viscosity of polyamic acid shown in Figure 2.21.
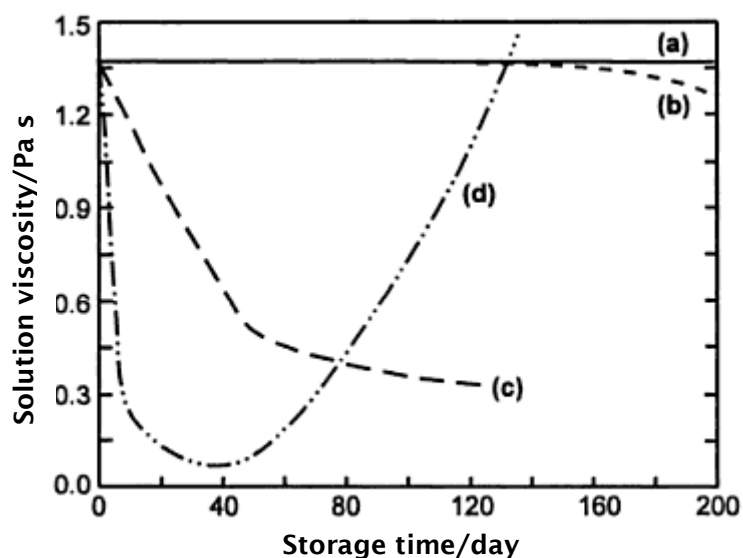
Figure 2.21. Viscosity of 12.5 wt% of polyamic acid solution during storage at different temperature: (a) -20 °C, (b) 4 °C, (c) 25 °C, (d) 50 °C [97].

Even in the room temperature (e.g., 25 °C), the viscosity of dilute polyamic acid solution decreases (Figure 2.21 c). The rate of degradation is even quicker with increasing temperature (Figure 2.21 d). However, if the temperature of storage reaches the imidization temperature, the viscosity will increase after several days of storage because of the presence of polyimide. The viscosity of polyamic acid is more stable at low temperature (Figure 2.21 a and b). For example, one type of polyamic acid is stable for 4 months at 4 °C [97].

The addition of water is also enhanced the degradation of polyamic acid. The water molecule has the ability to attack directly the amide bond of polyamic acid. It is important to control the humidity.

2.2.6   Degradation of polyimide by UV irradiation

Ultraviolet (UV) exposure is one of the most dangerous environmental threads to polymer. The functional groups of the polymer receive energy from ultraviolet light forming unstable photo-excited state [100]. This excited state refers to the movement of electrons to a particular orbital depending on the energy values that the electron received. An orbital is distcrete energy levels in an atom that occupy by a maximum 2 electrons in an opposite spin directions (e.g., up for anticlockwise and down for clockwise).

When two or more atomic orbitals overlap and constrictively interfere to make a covalent bond, a molecular bonding orbital occurs. Depending on the bonding arrangement, it can be categorised as σ and π bonds. The linear interaction of the two bonding atoms along the bonding axis results in sigma (σ) bond, while phi (π) bond occurs when the bonding electrons lies above and below, or in front and behind the bonding axis. When two or more atomic orbitals destructively interfere to separate each other, it creates the opposite of molecular bonding, which is called as molecular antibonding. The arrangement of antibonding are similar to bonding arrangement, which are denoted as sigma star ($\sigma*$) and phi star ($\pi*$). These molecule have high potential energy and less stable than two separated atoms. Besides bonding and antibonding, there is a molecular ortbital which does not involve in bonding and has an energy level between bonding and antibonding. This type of molecular orbital is called non-bonding orbitals and referred as (n). The UV absorption may cause transition of the molecular orbital into less-stable state, for example from n to $\sigma*$, n to $\pi*$, or π to $\pi*$ depending on the energy of incident radiation.

The unstable photo-exicted state may either relax to ground state producing heat or initiate breakdown of chemical bond into free radical [101]. Formation of free radical may cause re-arrangement of molecules, annihilation of small molecules, depolymerisation, crosslinking, or oxidation. These chemical alterations may lead to discolouration of polymer and even degradation of its properties such as mechanical and thermal properties [102]. Characterisation is needed to detect and predict the effect of ultraviolet light on polymers. The photo-degradation mechanism of polyimide has been studied by X-ray photoelectron spectroscopy (XPS) and illustrated in Figure 2.22. Irradiated

PMDA-ODA polyimide produces phenyl isocyanate [103], phenol, amine groups [104], and volatile gases (e.g., CO, CO_2). It shows that the conjugated structure of benzene is stable during UV irradiation whereas some single bonds are susceptible to UV attack.
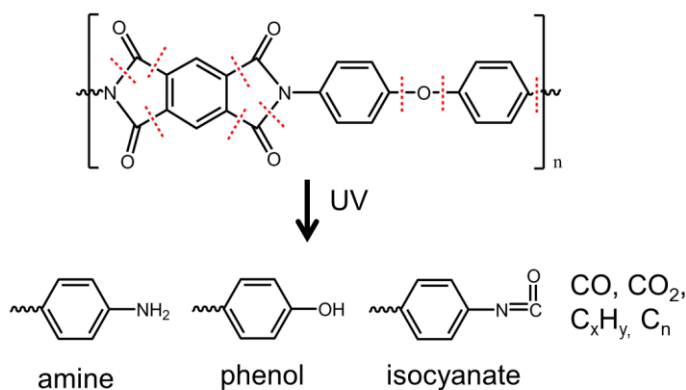
Figure 2.22. Chain scission mechanism of polyimide photo-degradation [6]. Red dots show the chain scission by UV. Black dots indicate the free radicals which generate by UV irradiation.

UV degradation of polymer is more severe in the presence of oxygen or ozone. The oxygen or ozone will react with radicals and generate more radicals [105]. The reaction of photo-oxidation can be written as follows:

Initial step : Polyimide (PH) → P• + P•

Chain propagation : P• + O_2 → POO•

POO• + PH → POOH + P•

POOH → PO• + •OH

2POOH → PO• + POO• + H_2O

PH + •OH → P• + H_2O

Chain termination : POO• + POO• ⎤
                                          ⎬ Crosslinking to non-radical products
POO• + P•

P• + P•

36

where P● = Polymer alkyl radical, PO● = Polymer oxy radical (Polymer alkoxy radical), POO● = Polymer peroxy radical (Polymer alkylperoxy radical), POOH = Polymer hydroperoxide, HO● = hydroxy radical

2.3   Polymer nanocomposites

2.3.1   Fabrication of nanostructure-polymer composites

Nanostructure-polymer composite is often called polymer nanocomposite. It is an incorporation and dispersion of nanosize filler (at least one dimension of at least one filler is ~100 nm or less) into polymer media [106]. Synthesis of polymer nanocomposite can be categorised depending on polymer point of view or filler point of view. In the filler point of view, polymer nanocomposites can be divided by the impregnation of scaffold or by filler mixing [107]. Since polymer nanocomposite in this thesis will be using low content of filler (mainly contain polymer) thus the synthesis of polymer nanocomposites are classified by polymer characteristic. In the polymer point of view, There are three common methods to make polymer nanocomposites which are solution mixing, melt compounding, and *in-situ* polymerization [108] (Figure 2.23.).
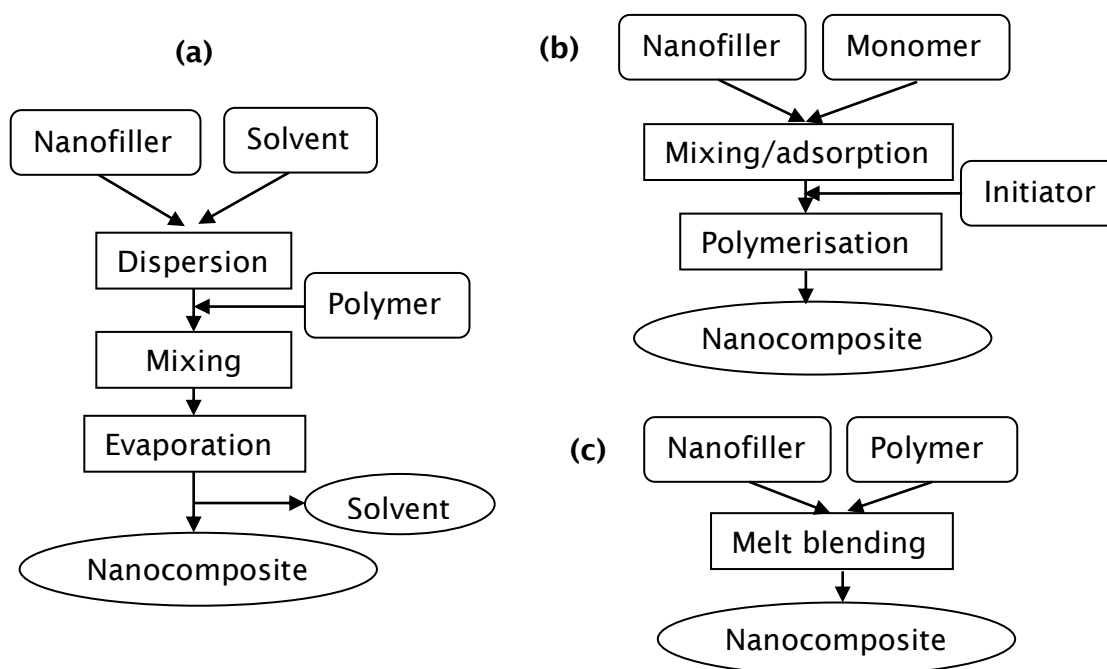
Figure 2.23. The schematic of three categories of nanocomposite fabrication: (a) solution mixing, (b) *in-situ* polymerisation, (c) melt compounding.

In solution mixing, a disperse solution of nanofiller is mixed together with polymer solution. After achieving a homogeneous dispersion of nanofiller in polymer, evaporation of solvent is needed to leave nanofiller intact with the polymer. This method is simple and typically only requires relatively low temperature compare to melt compounding. Nonetheless, this method necessitates an appropriate solvent to adequately disperse the nanofiller and to dissolve the polymer well. The nanofiller can be synthesised in one pot while mixing with the polymer as a template, which can be called as *in-situ* template synthesis. *In-situ* polymerization is the most time-saving method of all. In this technique, nanofillers are directly mixed with monomers solution and disperse while the polymerisation occurs thus reducing the fabrication time of polymer nanocomposites. However, some functional groups of the nanofiller may inhibit polymerisation. Melt compounding is a blending process of nanofiller and polymer melt to manufacture polymer nanocomposite. This method usually requires high temperature to melt the polymer. Although melt compounding needs high processing temperature, it does not require solvent as an intermediate between nanofiller and polymer.

Dispersion of nanofiller and interface between nanofiller and polymer are two major factors that determine the quality (homogeneity and reinforcement) of polymer nanocomposite [109]. Therefore, manipulation of surface chemistry is important to improve dispersion and interfacial bonding. The surface chemistry of nanofiller can be altered by covalent functionalization or non-covalent functionalization (polymer wrapping and surfactant adsorbtion). Covalent functionalization improves the mechanical properties of polymer nanocomposites due to strong interface between nanofiller and polymer. However, it can also damage the nanofiller thus reducing several properties (mechanical, electrical, thermal). Therefore, optimization of covalent functionalization conditions is needed. Mechanical treatment such as ultrasonication, shear mixing, ball milling, calendering, and extruder method is also helpful to improve nanofiller dispersion in a polymer. Ultrasonication and ball milling induced severe damage to the nanofiller while shear mixing, calendering, and extruder have less destructive power.

2.3.2 Nanosheets based polymer composites

The strategies to embed the nanosheets into the polymer can be categorised into 4 types depending on how nanosheets and polymer interacts, that are (1) intercalation of polymer from solution (solution mixing) into the nanosheets, (2) *in-situ* intercalative polymerisation when the polymerisation occur within nanosheets interlayer and (3) polymer melt intercalation/compounding, (4) *in-situ* template synthesis (sol-gel) for layered silicate (synthesis of nanosheets occur on the polymer chain which acts as a template) [110].

There are three categories (Figure 2.24) of the resulting polymer-nanosheets, which are: (1) **phase separated structure (tactoid)**: when the polymer is unable to intercalate inside the layered nanosheets thus phase separation between a bulky layered nanosheets and polymer can be clearly observed. The properties of this polymer nanocomposite are similar to the microcomposite thus it can be categorized as a microcomposite, (2) **intercalated structure**: when some of the polymer chain goes inside the layered nanosheets to create repeating sandwich structure of nanosheets and polymer, and (3) **exfoliated structure**: when single-layer nanosheets are uniformly dispersed inside the polymer matrix [111]. Exfoliated structure provides the best enhancement of polymer properties due to large aspect ratio and surface area of nanosheets.
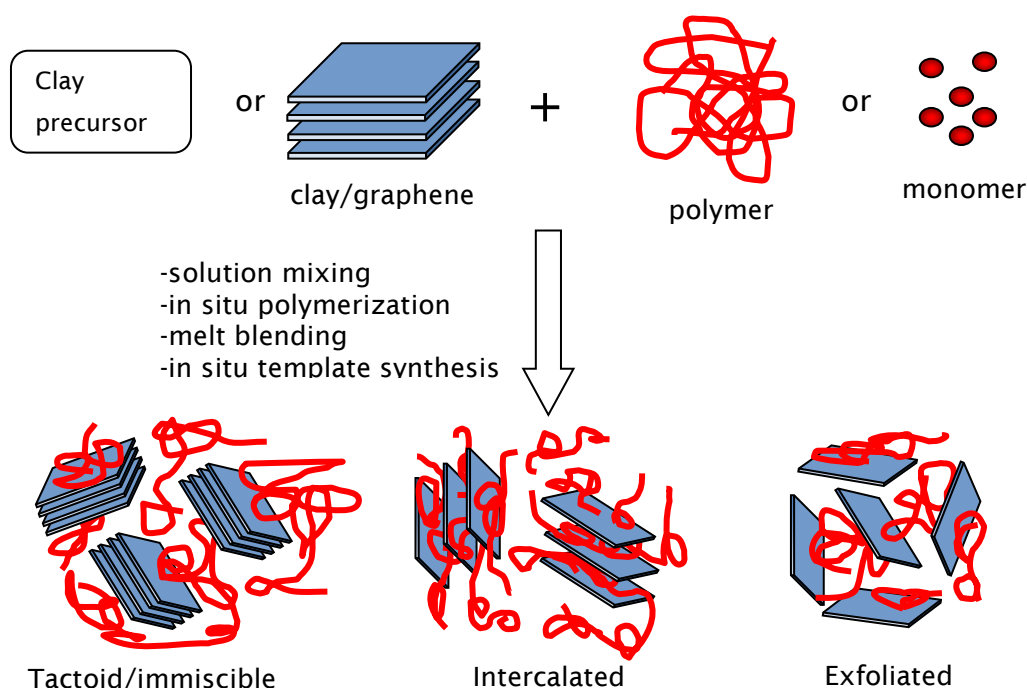
Figure 2.24. The scematic illustration of 3 types of nanosheets polymer composites.

Nanosheets formation within polymer matrix (e.g., tactoid/immiscible, exfoliated, and intercalated) can be characterised using X-ray dispersive spectroscopy (XRD) and transmission electron microscopy (TEM). XRD and TEM results with schematic representation of different nanosheets formation is depicted in Figure 2.25.
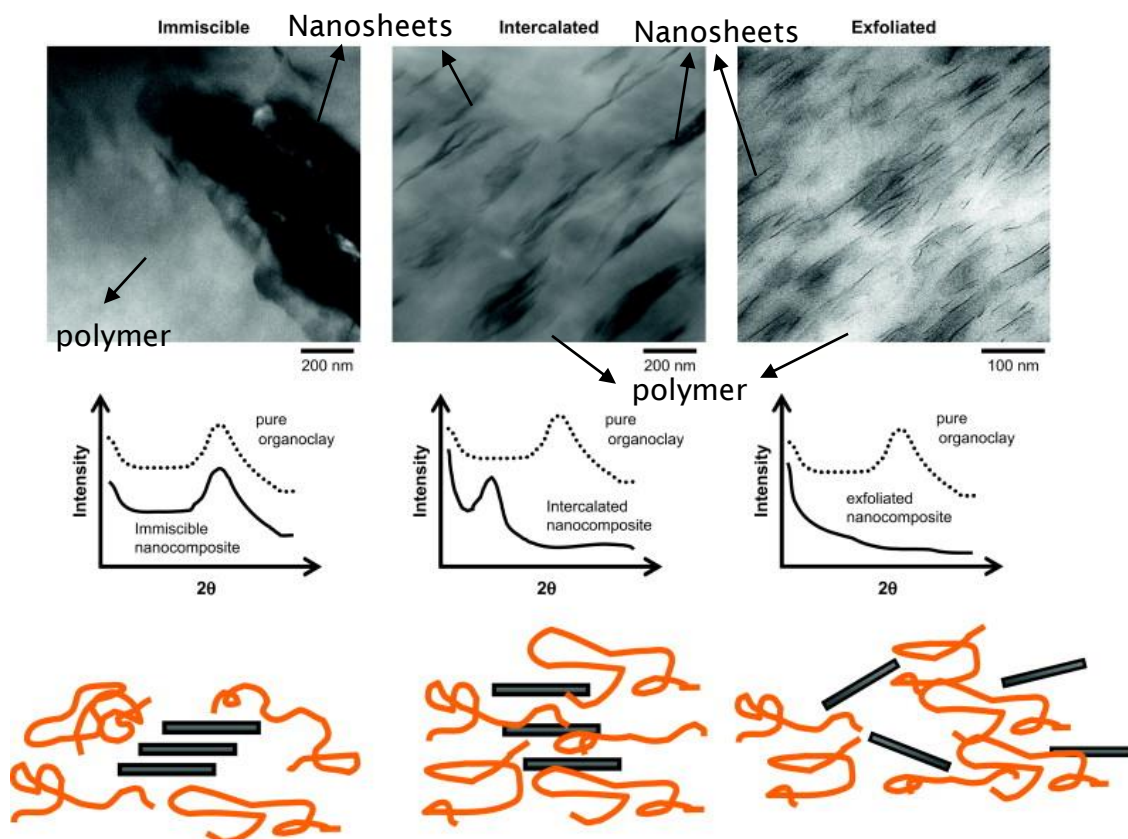
Figure 2.25. XRD and TEM results with schematic representation of different nanosheets formation [112].

Detected peak in XRD corresponds to interlayer spacing between nanosheets layer. Intercalation of polymer into nanosheets layers enlarges the spacing between layers shifting the peak to the left in XRD characterisation. Small-angle X-ray spectroscopy is often needed to be able to characterise peaks in small angle. In TEM, intercalated structures can be identify as elongated or "skewed" agglomerates as the sheets do not stacks perfectly on top of each other. In exfoliated samples, X-ray spectroscopy cannot detect the large distance between each nanosheets which is seen in TEM as a dispersed single layered nanosheets.

Surface treatment plays a big role to avoid tactoid formation of nanosheets in polymer. Intercalation or exfoliation is most likely to happen by changing the surface of nanosheets to organophilic. Toyota Research Group has been introduced the exfoliated clay-polyimide composite via solution mixing with surface-modified montmorillonite as clay [113]. Montmorillonite was modified by ammonium ions (dodecylammonium salt) to disperse it into polyimide solvent (DMAc). Then, organophilic montmorillonite was put into poly(amic-acid) and followed by imidization to produce polyimide-clay composite.

In-situ polymerisation, in which the monomers are mixed with the nanosheets, is favourable to fabricate intercalated nanosheets-polymer composite. A group of researcher alter the clay surface using one of polyimide monomers, namely diamine [114]. By adding the other monomer, namely dianhydride, polimerisation happens inside the organoclay which later continued with thermal imidization. This method produces polyimide intercalated nanoclay. An intercalated, partially exfoliated, or totally exfoliated can be obtained depending on the chain length of the polymer [115]. Longer chain polymers tend to exfoliate the nanosheets. Instead of clay, graphene [116,117] or graphene oxide [118–122], are also able to exfoliate or intercalate inside the polyimide matrix. Graphene, even without surface functional group, can be exfoliated and dispersed within the polyimide by applying mechanical treatment such as ultrasonication [123]. To sum up, a good dispersion, whether it is achieved by chemical or mechanical treatment, is the key to avoid the tactoid formation of nanosheets within the polymer matrix.

2.3.3   Mechanical properties of polymer composites

In the last two decades, nanofillers (e.g. graphene, carbon nanotubes) have become a popular reinforcement to improve mechanical properties of polymer. By adding nanofiller, highest homogeneity and reinforcement are expected due to its scale and extensive interfacial interaction [112]. Mechanical properties of composite improve as the addition of nanofiller up to a certain nanofiller volume fraction. Beyond this critical volume fraction the properties of composites will decreased even below the properties of neat polymer. Generally, a small amount of nanofiller is enough to dramatically increase the properties of polymer nanocomposites [112]. However, polymer nanocomposite has lowest critical volume fraction compared to the other composite

(micro or macrocomposite), due to several problems in dispersion and interfacial strength [124]. A better dispersion and interfacial strength can be achieved by mechanical treatment and modification of surface chemistry as stated in Section 2.3.1.

The mechanical properties of polymer nanocomposites can be characterised by tensile, bending, and compression test either dynamic or static, impact, fatigue, creep test, microhardness, and nanoindentation. Due to the smaller sample size, nanoindentation has become more favourable than other methods. Indentation induces by the loading of indentation tip onto the sample surface by electromagnetic motor [125]. Indentation depth must not exceed 10% of the film thickness of specimen to avoid contribution of substrate mechanical properties [126]. A three-sided pyramid, which is known as Berkovich diamond tip, is often used as an indenter. The load-displacement curve, which recorded during loading and unloading of the Berkovich indenter, is used as base for modulus and hardness calculation. The schematic of nanoindentation on the polymer surface and load-displacement data for viscoelastic-plastic material is given in Figure 2.26.
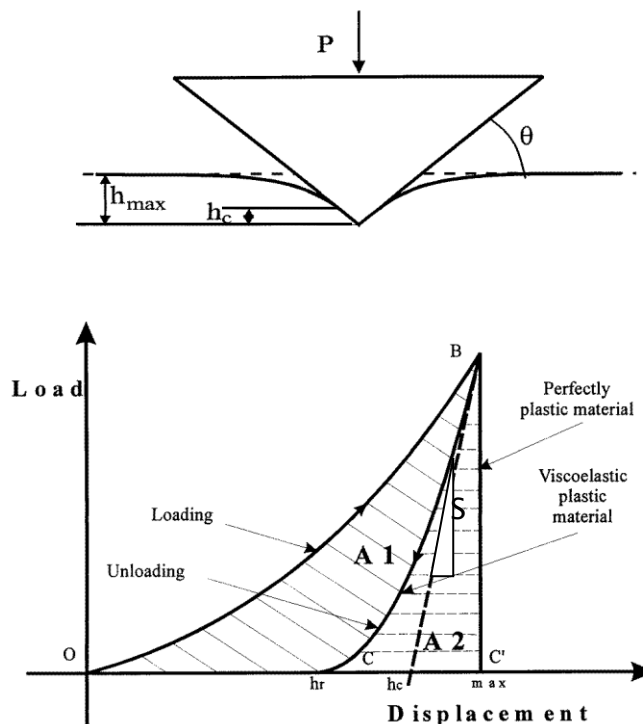
Figure 2.26. Illustration of nanoindentation on the polymer surface and load-displacement data for viscoelastic-plastic material [127]. A1 (OBC) represents to plastic work done on the material and A2 (CBC') corresponds to elastic work recovered during unloading.

P is the applied load, h_{max} is the maximum depth at maximum loading, h_c is the tangent drawn from linear elastic of unloading curve, h_r is the residual or final depth after unloading. The reduced Young's modulus is calculated from the equation [127]

$$E_r = S \frac{\sqrt{\pi}}{2\beta} \frac{1}{\sqrt{A}}$$

(2.1)

where E_r is the reduced Young's modulus, S is the stiffness which calculated from the slope of unloading curve, β is the parameter which depends on indenter geometry ($1 < \beta < 1.034$), and A is the projected contact area between indenter and specimen at maximum depth. The reduced Young's modulus can be converted to the Young's modulus using following formula

$$\frac{1}{E_r} = \frac{1 - v_s^2}{E_s} + \frac{1 - v_i^2}{E_i}$$

(2.2)

where E_s and E_i are the Young's moduli of specimen and indenter. v_s and v_i are the Poisson's ratio of specimen and indenter. Hardness is obtained by the ratio of maximum load (P_{max}) to the surface area of indentation at maximum depth. Young's modulus or modulus of elasticity is a measure of the ability of material to withstand stress and go back to original state without being plasticly deform, which can be expressed as stress divided by strain [128]. Whereas hardness is defined as the material resistance to withstand local plastic deformation.

The Young's modulus and hardness of polymer nanocomposites can be predicted by several theories. The theoretical models used in this thesis are models able to predict composites containing matrix and filler as reinforcements with the basic assumptions of a void free matrix and no residual stress in composites (stress-free state). Modified rule of mixtures, Halpin-Tsai, and Halpin-Kardos were chosen for this purpose.

The rule of mixtures is a well-known model based on the Voigt equation [129] that is used to predict continuous unidirectional fibre composites. This model is also known as the iso-strain model which assumes the filler and matrix have the same elongation when a certain load is applied to the composite. However, it is not suitable for evaluating mechanical properties of some composites as it often overestimates the properties [130,131].

Hence, the modified rule of mixtures, which is a semi-empirical model, is applied [132]. The modified rule of mixtures is:

$$E_c = \chi_f E_f V_f + E_m (1 - V_m)$$ (2.3)

where E_c, E_f, and E_m are the moduli of composite, filler, and matrix, respectively. χ_f is a particle strengthening factor with values between 0 and 1. V_f and V_m are the volume fractions of filler and matrix. This equation can also be applied to estimate the hardness of the composite by substituting the modulus to hardness.

The Halpin-Tsai equation is a model to estimate reinforcement of unidirectional oriented short fibres and has successfully predicted the reinforcement of carbon nanotubes at low filler content (>1 wt%) [133]. It can also be adapted to predict the modulus of polymer nanocomposites with nanosheets (e.g., clay [134] and graphene [135]) as filler. The Halpin-Tsai equation is:

$$\frac{E_c}{E_m} = \frac{1 + 2 A_f \mu \phi_f}{1 - \mu \phi_f}$$ (2.4)

where E_c and E_m are the moduli of the composite and matrix, respectively. A_f is the filler aspect ratio (l/h), in this case (l) is the nanosheets or nanotubes length and (h) is the nanosheets thickness or nanotubes diameter. Φ_f is the volume fraction of filler. η is a geometric factor, given by:

$$\eta = \frac{(E_f/E_m) - 1}{(E_f/E_m) + 2 A_f}$$ (2.5)

where E_f is the modulus of filler. The Halpin-Tsai equation is also able to predict the hardness of micro and nanocomposites by simply exchanging the modulus with hardness [136]. The hardness of the matrix (H_m) is determined by nanoindentation. H_f represents filler hardness.

Originally, the Halpin-Kardos equation was applied to randomly oriented short fibres with a quasi-isotropic laminate assumption involving the $[0/+45/90/-45]_n$ configuration [137]. However, the expression can also be adapted. It has been successfully used to predict the reinforcement of nanosheets (e.g., clay) up to 2 wt% in a polymer blend [134].

The authors argued that the tactoid phase of clay may act in a similar fashion to short fibres. The Halpin-Kardos equation is:

$$\frac{E_c}{E_m} = \frac{3}{8}\left[\frac{1+2A_f\eta_L\phi_f}{1-\eta_L\phi_f}\right] + \frac{5}{8}\left[\frac{1+2\eta_T\phi_f}{1-\eta_T\phi_f}\right] \tag{2.6}$$

where E_c and E_m are the moduli of the composite and matrix respectively. A_f is the aspect ratio of the filler (l/h) where l is the nanosheets or nanotubes length and h is the nanosheets thickness or nanotubes diameter. Φ_f is the filler volume fraction. η_L and η_T can be determined from the following equations:

$$\eta_L = \frac{(E_f/E_m)-1}{(E_f/E_m)+2A_f} \tag{2.7}$$

$$\eta_T = \frac{(E_f/E_m)-1}{(E_f/E_m)+2} \tag{2.8}$$

where E_f is the modulus of filler. To obtain the hardness, this equation was modified by substituting the modulus for hardness. The illustration of Voigt model (rule of mixture), Halpin-Tsai, and Halpin-Kardos model is given in Figure 2.27. Some nanofiller such as titanate nanosheets have anisotropic mechanical properties [138]. Theoretical predictions might give an insight on filler orientation.
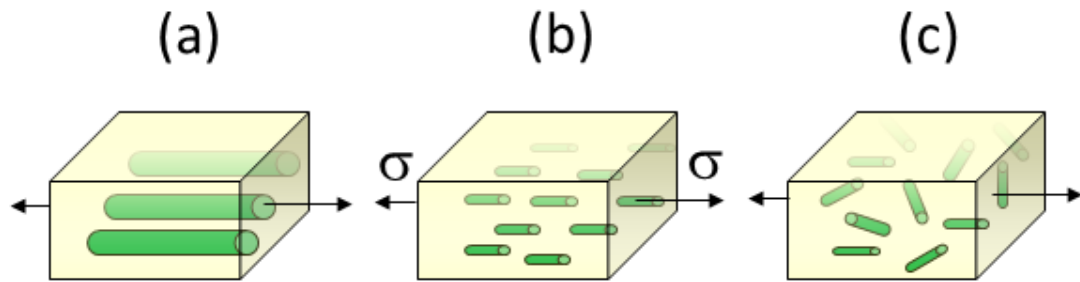
Figure 2.27. The schematic representation of (a) rule of mixture based on Voigt model (continuous and unidirectional filler); (b) Halpin-Tsai model (short and unidirectional filler); (c) Halpin-Kardos model (short and random orientation filler). Arrows indicates stress (σ) direction.

2.3.4   Outline of the inhibition of UV degradation of polymer, aim, and challenges

As mention in Chapter 2.2.6, polymer that exposed to UV irradiation may generates unstable photo-exited state, which leads to radical formation and polymer degradation. UV stabilizer is needed to protect the polymer from UV radiation. There are 5 categories of stabilizer depending on the mechanisms [105]: (1) an ultraviolet reflector, (2) an ultraviolet absorber, (3) an exited-state quencher, (4) a peroxide (from photo-oxidation) decomposer, (5) a free-radical scavenger. Some of the stabilizers have two or more stabilizing actions. For example, carbon black acts as UV reflector by restricting the UV radiation and has the ability to quench the excited state and to trap radicals produced during photo-oxidative process. The stabilizing action is depicted in Figure 2.28.
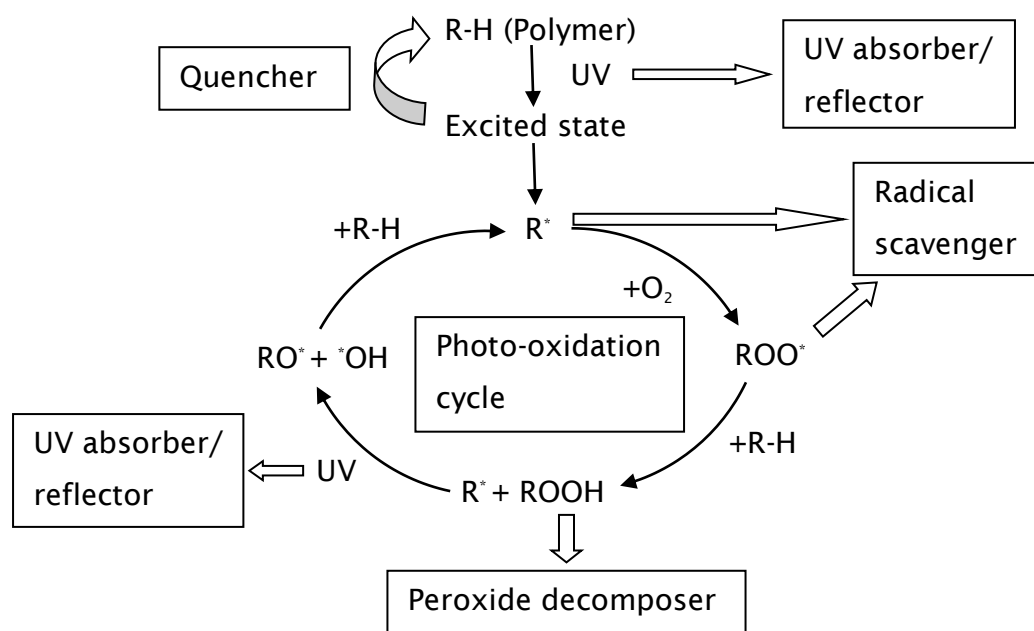
Figure 2.28. Photo-stabilization of common polymer ($\Rightarrow$= terminated by) [105].

In the case of polyimide, inorganic UV absorber such as titania [7] and polyhedral oligomeric silesquioxane (POSS) [8] are often used to inhibit UV degradation. The polyimide can be coated or incorporated with the UV absorber. One group of researcher has studied the effect of titania coating by liquid phase deposition method on the UV protection of polyimide. With an absorption coefficient of $\approx 1 \times 10^6$ cm^{-1} at the UV

wavelength of 200-300 nm [139], a 100 nm thick titanium dioxide coating could almost completely (99 %) block the incident UV light. However, coating method may rise problems such as imperfect coating, poor adhesion, thermal expansion mismatch between the coating and the substrate [9]. Incorporation of POSS into polyimide may solve these problems but it may also decrease the thermal properties of polyimide such as glass transition temperature [8]. Incorporation of inorganic materials is preferred to eliminate the possibility of coating problems while maintaining the glass transition temperature.

Titanate has the suitable band gap (≈3 eV) that corresponds to the absorption of light with wavelength around 200-300 nm. In the most occasion, titanium oxide or titanate is used as a photocatalyst due to the occurrence of the chemical reactions on the surface of titanate when exposed to ultraviolet light irradiation [140]. Titanium oxide absorbs UV photon energy, which excited titanate's electron from the filled valence band of titanate to the conduction band. Electrons (e^-) and holes (h^+) pair are generated as a result. Electrons may react with oxygen creating superoxide radical ($O_2\bullet^-$). This radical can be protonated creating hydroperoxyl radical (HOO$\bullet$). Those radical are able to degrade polymer. Holes is also able to directly degrade polymer and react with water generating hydroxyl radical (HO$\bullet$), which also leads to degradation of polymer.

Photocatalytic ability of titanate can be suppressed by surface treatment of the titanate with non-catalytic inorganic materials such as silica, alumina, and zirconia [141]. By covering the surface of titanate, possible reactions of electrons and holes with oxygen, water, and polymer are eliminated. Alternatively, organic radical scavengers (e.g., hindered amine light stabilizers (HALS)) can be incorporated in polymer to annihilate the generation of radical by the reaction of electrons and holes with oxygen and water [142]. However, the understanding of interaction mechanism of inorganic absorber and organic radical scavengers is still limited.

Instead of adding the organic radical scavenger and the surface treatment of titanate, the photo-catalytic properties of titanate can be modified by simply altering the titanate chemical properties itself, for example by controlling crystallinity and introducing alkali impurities [141,142]. The materials that have low crystallinity or alkali impurities such as sodium have considerable amounts of defects, which can act as a recombination centre of photogenerated electrons and holes. As the both carriers (electron and hole)

annihilate each other, it stops further chemical reaction on the titanate. The hydrothermal reaction of alkali and titania produces titanate nanostructure with a minimum photo-catalytic ability without further treatment, hence it is facile and suitable as inorganic UV absorber.

2.4   Electrospinning of polymer nanocomposite

In 1934, Formalas *et.al.* [143] introduced a new method to produce polymer filaments using an electrostatic force which later on known as electrostatic spinning or electrospinning. It is a practical method to synthesise an ultrafine fibres with diameter reaching nanometres.

Electrospinning machine has three main components which are a capillary tube with small diameter needle, a high voltage supplier, and a metal collector [143]. The process can be divided into two parts. First, polymer inside the tube is pumped until it gets to the end of the needle. Second, the polymer solution or melt is electrically charged by applying high voltage. A critical value of electric field needs to be reached thus the repulsive electrostatic force surpasses the surface tension of the fluid. Then, a stream of liquid forces out from the tip. As the discharged liquid travel in the air, the solvent evaporates (or the liquid solidifies in case of polymer melt) shaping a charged polymer fibres. The schematic diagram of electrospinning machine is shown in Figure 2.29.
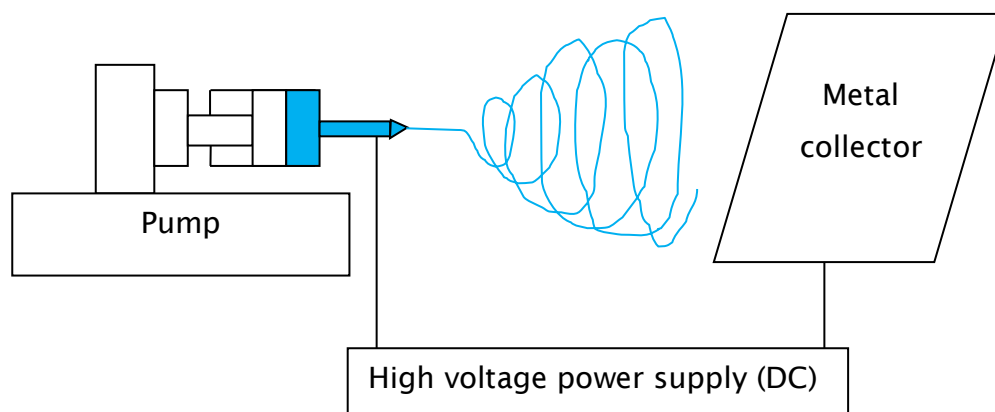
Figure 2.29 Schematic diagram of an electrospinning machine.

2.4.1 The electrospinning of polyimide

Polyimide is a high performance polymer having excellent heat and chemical resistance. Electrospinning can further extend the utilisation of such polymer for many applications such as Li-ion battery separators, fuel cell proton exchange membranes, sensors, high temperature filtration membrane, and polyimide based carbon nanofibers [144]. However, it is difficult to electrospin polyimide due to its resistance to common solvent (e.g., DMF, DMAc, and NMP).

Kapton (PMDA-ODA polyimide), which is a well-known polyimide, is only soluble in concentrated sulfuric acid. Typically, PMDA-ODA polyimide is synthesised by two step method [145]. First, 10 wt% of polyimide precursor (e.g., polyamic acid), made from polymerisation (in N_2 gas) of equimolar pyromellitic dianhydride (PMDA) and oxydianilline (ODA) via organic solvent (e.g., DMF, DMAc, NMP), is electrospun. Second, thermal imidization with a heating sequence (e.g., 80 °C for 2 h, 160 °C for 1 h and at 250, 300 and 350 °C each for 30 min) is performed to convert polyamic acid into polyimide. Chemical imidization can be used instead of thermal imidization by immersion in a mixture of acetic anhydride and pyridine (4:3.5 volume ratio) for 1 min, followed by heating at 120 °C for 1 h [146]. Polyamic acid can be modified using triethylamine or other ammonium ions creating polyamic acid salt which is water soluble. Jiang *et.al.* [147] blended water soluble polyamic acid salt with polyethylene oxide (Mw = 900.000 g mol^{-1}) to assist fabrication of nanofibres. After thermal imidization under nitrogen gas, polyamic acid was converted into polyimide and polyethylene oxide was decomposed. The polyimide nanofibres were used for filtration of Fe_2O_3 particles (d = 1-40 μm) in a hot silicone oil (≈123.5 °C). The modulus of polyimide nanofibers made by water soluble precursor is lower than polyimide (from 428 ± 12 MPa to 132 ± 9 MPa). However, there is no difference in the filtration efficiency between the two types of polyimide nanofibers.

Some aromatic polyimide (e.g., fluorinated polyimide) can be dissolved in organic solvent (e.g., DMF, DMAc, NMP) thus those polyimide solutions can be used directly for electrospinning. Kawakami *et.al.* [148] dissolved 14 wt% of fluorinated polyimide based on 2,2'-bis(3,4-dicarboxyphenyl)hexafluoropropane dianhydride (6FDA) and 2,2'-bis(4-aminophenyl)hexafluoropropane (6FAP) in DMAc and successfully synthesised fibers with diameter of 438 ± 33 nm at 15 kV DC and flow rate of 0.12 mL hr^{-1}. The

humidity greatly affected the diameter of 6FDA-6FAP nanofibers which reduced from 301 ± 19 nm to 109 ± 18 nm for 20 % and 5 % humidity, respectively. The small addition of salt (0.1 wt% of tetrabutyl ammonium bromide) further decreased the diameter to 46 ± 5 nm at 5 % humidity. There are limited publications on semi-aromatic and fully-aliphatic polyimide, probably due to low viscosity of those types of polyimide.

The properties of polyimide nanofibers depend on the structure of its monomers. As stated in Section 2.2.4, the presence of bulky group such as −CF$_3$ hindered the chain packing of polyimide inducing flexibility of chain movement. The mechanical properties of polyimide greatly influence by this chain flexibility. The polyimide nanofibers with high strength and elasticity (high toughness) can be synthesised by electrospinning of the polyamic acid containing rigid monomer such as 3,3',4,4'-biphenyl-tetracarboxylic dianhydride (BPDA) and flexible diamine, 2,2-bis[4-(4-aminophenoxy)phenyl]hexafluoropropane (6FBAPP) [149]. These polyimide nanofibers had tensile strength of 308 ± 14 MPa and 201.9 ± 6.8 % elongation at break. Combination of three monomers (co-polyimide) can also produce high toughness nanofibers. Yao *et.al.* [150] synthesised 10 wt% of polyamic acid solution using 0.01 mol of rigid BPDA, 0.005 mol of rigid *p*-Phenylenediamine (PDA), and 0.005 mol of 4,4'-oxydianiline (ODA) as monomers. The solution was diluted to 4.5 wt% with its solvent (DMF) to achieve homogeneous electrospun nanofibers. The resulting polyimide nanofibers (after thermal imidization) yielded 1040 MPa and 13.5 % for tensile strength and strain at break, respectively. Instead of combination of different characteristic of monomer (rigid and flexible), high toughness polyimide nanofibers can also be achieved by blending rigid polyimide and flexible polyimide. He *et.al.* [151] mixed BPDA-PDA and BPDA-ODA polyamic acid with molar ratio 20:80. Due to high miscibility and high chain interactions between two polymer blends, the polyimide nanofibers mat exhibited tensile strength of 1061.95 MPa and 22.62 % elongation at break. Summary of electrospinning of polyimide is shown in Table 2.3.

Table 2.3. Summary of different type of polyimide preparation and properties.

Type of polyimide	Tensile strength	Elongation at break	Solvent	Number of steps	Ref.
PMDA-ODA	79 ± 3 MPa	22 ± 2.5%	DMF	2	[147]
PMDA-ODA salt + PEO (decomposed)	31 ± 1 MPa	33 ± 4.3%	H_2O	2	[147]
6FDA-6FAP	-	-	DMAc	1	[148]
BPDA-PDA	663.7 MPa	4.9%	DMAc	2	[152]
BPDA-ODA	459 ± 36 MPa	41.3 ± 2.2%	DMAc	2	[153]
BPDA-6FBAPP	308 ± 14 MPa	201.9 ± 6.8%	DMAc	2	[149]
BPDA-PDA-ODA (BPDA:PDA:ODA = 1:0.5:0.5) mol	1040 MPa	13.5%	DMF	2	[150]
BPDA-PDA/BPDA-ODA blend (20:80 mol ratio)	1061.95 MPa	22.62%	DMAc	2	[151]

Abbreviations: pyromellitic dianhydride (PMDA); 4,4'-oxydianiline (ODA); polyethylene oxide (PEO); 3,3',4,4'-biphenyltetracarboxylic dianhydride (BPDA); *p*-phenylenediamine (PDA); 4,4'-(hexafluoroisopropylidene)diphthalic anhydride (6FDA); 1,4-bis(4-amino-2-trifluoromethylphenoxy)benzene (6FAP); 2,2-bis[4-(4-aminophenoxy)phenyl]hexafluoropropane (6FBAPP); N,N-dimethylformamide (DMF); N,N-dimethylacetamide (DMAc)

2.4.2   The electrospinning parameters and the effect of filler incorporation

From electrospinning, one usually wishes to achieve a defect-free and continuous fibre with a desired diameter. Bead shaped fibre is the most common defects in electrospinning. The formation of bead can be controlled by adjusting several factors

such as viscosity, surface tension, surface charge density, and working distance between collector and the tube tip. Increasing the viscosity reduces the number of beads. High viscosity can be achieved by increasing polymer concentration. However, a very high concentration will lead to instability of flow thus the formation of fibres will be less uniform. Reducing the surface tension can also result in fewer numbers of beads. Low surface tension can be achieve by changing the solvent or adding surfactant [154]. In rare cases, a solvent with lower surface tension induces more beads. To address this problem, combination of two solvents is needed to get bead-free fibres. A small amount of salt ($\approx$1 wt%) also decreases the formation of beads [155]. The addition of salt improves the conductivity and surface charge density of polymer solution thus higher elongation forces are applied to the jet of polymer solution. Higher elongation forces reduce the diameter of fibres and diminishing breaded fibres. On the contrary, farther working distance promotes greater number of beads.

To get a desired fibre diameter, one should consider seven parameters that affect it, which are viscosity, polymer concentration, voltage, working distance, ambient temperature, humidity, and the addition of salts. Bigger fibre diameter is attained by increasing viscosity, humidity, or polymer concentration. On the contrary, smaller diameter is obtained by upsurge the voltage, increasing working distance and temperature, or adding salts into the solution. In addition, polymer concentration and voltage need to be within certain range to spin continuous fibres. The working distance should not be too short to allow solidification process of the liquid jet before reaching the collector. Raising the voltage also improves the uniformity of the fibres. However, excessive applied voltage may cause instability in nanofibres formation. Summary of several parameters that affecting fibre quality is shown in Table 2.4.

Table 2.4. Summary of several electrospinning parameters that affecting fibre quality.

Parameters (⇧)	Effects of increasing a parameter
Viscosity	Fibre diameter (⇧) and number of beads (⇩)
Polymer solution	Fibre diameter (⇧) and number of beads (⇩)
Voltage	Uniformity of fibres (⇧) and fibre diameter (⇩)
Addition of salts	Number of beads (⇩) and fibre diameter (⇩)
Surface tension	Number of beads (⇧)
Working distance between collector and the tube tip	Number of beads (⇧) and fibre diameter (⇩)
Ambient temperature	Fibre diameter (⇩)
Humidity	Fibre diameter (⇧)

(⇧) = increasing; (⇩) = decreasing;   The opposite occur when a parameter decreases

This facile method, electrospinning, is beneficial in fabrication of polymer nanocomposites. Electrospinning has been found to enhance the dispersion of nanosilica within the polymer matrix, as well as reduction of nanosilica agglomerates [156]. Electrospinning can also control the alignment of carbon nanotubes inside the polymer matrix [157] (see Figure 2.30 c). Some nanofiller might affect the fibre morphology. Conductive nanofiller improves the solution conductivity, thus has similar effect as salts addition [158], which reduces beads and fibre diameter (Figure 2.30 a and b). Nanofiller may also increase or decrease the viscosity of polymer solution. At high filler concentration, agglomeration may occur which led to bead formation thus good dispersion of filler in the solution is crucial.
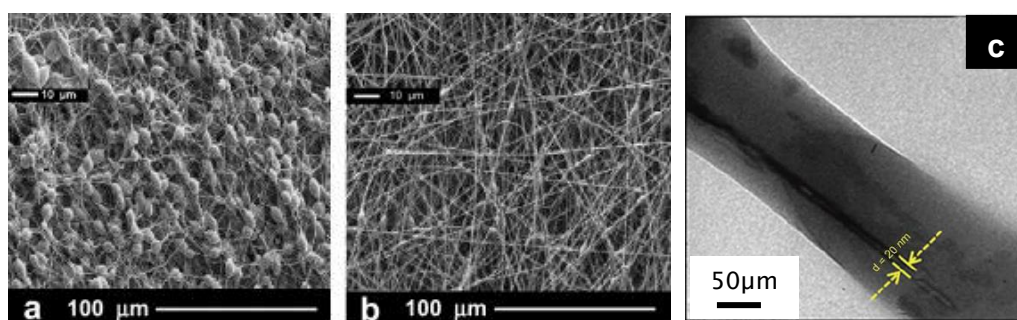
Figure 2.30. (a) SEM images of pure PS fibres; (b) PS with 0.5% MWCNT [158]; (c) TEM image of PVA/1 wt% MWCNT composites fibre [157].

By incorporating a filler into the polymer nanofibre, mechanical, thermal, electrical properties of the nanofibers may increase to broaden its application into membrane, sensor, microelectronics, or high performance fabric materials.

Chapter 3: Experimental Methodology

3.1 Synthesis and characterisation of titanate nanostructures

Several methods to synthesise titanate nanostructures are provided in this chapter. The classical Sasaki procedure for producing single-layer titanate nanosheets (TiNS) is described in Section 3.1.1. The synthesis of scrolled titanate nanosheets (STiNS) and nanotubes (TiNT) by a hydrothermal method is provided in Section 3.1.2. Bottom-up methods, such as sol-gel, are described in Section 3.1.3. The procedures are illustrated in Figure 3.3. The characterisation of titanate nanosheets such as SEM, UV-vis, TEM, and optical characterisation of titanate transparency in solution is outlined in Section 3.1.4.

3.1.1 Sasaki's method to synthesis titanate nanosheets

3.1.1.1 "Caesium" and "potassium-lithium" route for titanate synthesis

A synthesis method for single-layer titanate nanosheets has been adapted from Sasaki *et.al.* [33]. Sasaki's flat single-layer titanate nanosheets (TiNS) are based on two starting material, an alkali precursor (K,Li,Rb,Cs) and TiO_2 powder. This work is based on caesium route and potassium-lithium route. Using the caesium route, TiO_2 (Degussa P25) from Aeroxide and Cs_2CO_3 from Sigma-Aldrich were used without further purification. There are three steps to synthesis single-layer titanate nanosheets. Firstly, solid-state reaction of TiO_2 and Cs_2CO_3 was conducted based on the work of Grey *et.al.* [29]. 1.956 g of Cs_2CO_3 and 2.540 g of TiO_2 (molar ratio 1:5.3) were mixed, grounded, and put into platinum crucible (standard form, capacity 10 mL) or Coors high-alumina crucible (high form, capacity 100 mL) for one hour heating at 800 °C. The mixture was allowed to cool spontaneously. It was ground, followed by two cycles heating at 800 °C for 20 h with grinding at the interval. The resulting product was a white powder of lepidocrocite-like caesium titanate ($Cs_{0.7}Ti_{1.825}\square_{0.175}O_4$).

Second step includes an acid ion-exchange that was performed to create smectite-like acid titanate ($H_{0.7}Ti_{1.825}\square_{0.175}O_4 \cdot H_2O$). 2.4 g of $Cs_{0.7}Ti_{1.825}\square_{0.175}O_4$ was stirred with 96

mL of 1M HCl for 4 days. The acid solution was replaced with a fresh acid solution every day to maintain the amount of H^+ ions for acid leaching of Cs^+ ions. The solution was decanted with deionized (DI) water three times followed by vacuum filtration using 0.2 µm nylon membrane and washed with distilled water until the conductivity around 10 µS cm^{-1}. During third step, exchange of protons with bulky cations was undertaken by stirring (200 rpm) 0.4 g of $H_{0.7}Ti_{1.825}\square_{0.175}O_4 \cdot H_2O$ with 100 mL of aqueous solution of 0.0165 M tetrabutylammonium hydroxide (TBAOH) or tetramethylammonium hydroxide (TMAOH) at 22 °C for 2 weeks. Finally, the exfoliated nanosheets were dispersed in solution.

For potassium lithium route, TiO_2 (Degussa P25) from Aeroxide and K_2CO_3 and Li_2CO_3 from Sigma-Aldrich were used as supplied. The procedure used for lepidocrocite-like potassium-lithium titanate was similar to the work of Sasaki *et.al.* [159]. Firstly, 1.328 g of K_2CO_3, 0.236 g of Li_2CO_3, and 3.324 g of TiO_2 (molar ratio 2.4:0.8:10.4) were mixed, crushed with pestle, and placed in Coors high-alumina crucible (high form, capacity 50 mL) for 30 min heating at 1100 °C. After spontaneous cooling, it was grounded and heating was continued at 1100 °C for 20 h. The resulting product was a white powder of lepidocrocite-like potassium-lithium titanate ($K_{0.8}Ti_{1.73}Li_{0.27}O_4$).

Second, 1.5 g of $K_{0.8}Ti_{1.73}Li_{0.27}O_4$ was stirred with 96 mL of 1 mol L^{-1} HCl for 4 days to leach the K^+ and Li^+ ions. The acid solution was replaced daily with a new acid solution to maintain the amount of H^+ ions. To remove the excess acid solution, the solution was decanted with distilled water three times and followed by vacuum filtration using 0.2 µm nylon membrane and washed with distilled water until the conductivity around 10 µS cm^{-1}. Third, the exfoliated titanate was formed by stirring (200 rpm) 0.4 g of $H_{1.07}Ti_{1.73}O_4 \cdot H_2O$ with 100 mL aqueous solution of 0.025 mol L^{-1} tetrabutylammonium hydroxide (TBAOH) or tetramethylammonium hydroxide (TMAOH) at room temperature (20-25 °C) for 2 weeks. The exfoliation of potassium-lithium nanosheets was based on another Sasaki publication [160].

3.1.1.2   Purification of caesium and potassium-lithium titanate

Alumina or porcelain crucibles are much cheaper than platinum ones. However, the ceramic crucible reacted with alkali salts, such as caesium carbonate, potassium

carbonate, and lithium carbonate creating unwanted products which can be separated by centrifugation. The centrifugation was conducted after bulky molecule ion-exchange (Figure 3.1 a). 40 mL of titanate nanosheet solution was put into a 50 mL centrifuge tube and rotated at 3800 rpm for a total 12 h (a 2 h centrifuge repeated 6 times). The supernatant solution was kept as purified titanate nanosheets.

3.1.2   Hydrothermal method for titanate synthesis

The work of Bavykin *et.al.* [24] has been adapted and modified as a methodology of scrolled titanate nanosheets (STiNS) and nanotubes (TiNT) synthesis by hydrothermal method. For STiNS, 20 g of TiO_2 (Degussa P25, Aeroxide) was refluxed with 10 mol L^{-1} NaOH (Sigma-Aldrich) in a PFA (perfluoroalkoxy polymer) round-bottom flask (Bohlender GmbH) for 2 weeks at 60 ^{o}C. Titanate nanotubes (TiNT) were made by refluxing 25 g TiO_2 (Degussa P25, Aeroxide) with 10 mol L^{-1} of KOH:NaOH 1:25 for 2 days at 100 ^{o}C. The resulting sodium titanate powders ($Na_2Ti_3O_7$) were filtered under vacuum and washed with distilled water until the washing solution reached pH 7. Then, the protonated titanate ($H_2Ti_3O_7$) was formed by washing sodium titanate with an excess of 0.1 mol L^{-1} HCl (Sigma-Aldrich) for more than 30 min until a stable pH value of 2 was reached, followed by distilled water washing to pH 5. Finally, 100 mL aqueous solution of 0.075 mol L^{-1} TBAOH or TMAOH or 0.1 mol L^{-1} CTAB were used to exfoliate 0.4 g of protonated titanate by stirring (200 rpm) at 22 ^{o}C for 2 weeks. Alternatively, 0.3 g of protonated titanate in 25 mL of dimethylacetamide (DMAc) or N,N'-dimethylformamide (DMF) were stirred for 2 weeks to induce an exfoliation of titanate.

3.1.3   Synthesis of titanate by sol-gel method

This method is based on the work of Tae *et.al.* [50] with modification on titanium precursor. 10 mL of titanium n-butoxide was added slowly to 150 cm^{-3} of aqueous solution of 0.273 mol L^{-1} TMAOH and stirred for 5 minutes at room temperature (20-25 ^{o}C). Then, the mixture was refluxed in argon at 100 ^{o}C for 24 h. The solution was turbid upon the addition of titanium n-butoxide. It slowly became transparent after 30 minutes. After 6 h, it became more opaque; the opacity remained after the reaction was finished.

3.1.4   Characterisation of titanate nanosheets

3.1.4.1   Field-emission scanning electron microscopy (FESEM) and Energy Dispersive X-ray Spectroscopy (EDX)

FESEM images were taken by a JEOL JSM 6500F microscope at an accelerating voltage of 5 kV or 15 kV with an ultimate resolution of 1.5 nm and a magnification range from 10 to 400.000 times. The elemental analysis of samples was done with an Oxford Inca 300 energy dispersive X-ray suite (detector resolution 133 eV) which integrated with FESEM. All of colloidal suspension samples were diluted and drop casted as 100 µL drops onto the silicon wafer which had been preclean with acetone.

3.1.4.2   Transmission electron microscopy (TEM)

TEM specimens were prepared by drop casting of diluted colloidal suspension on S147-3 copper grids with holey carbon film (diameter holes up to 100 µm) (Agar Scientific). TEM images were acquired using a JEOL 3010 transmission electron microscope with a point resolution of 0.17 nm, at an accelerating voltage of 300 kV and an exposure time of 1 second.

3.1.4.3   Measurement of titanate concentration using UV-vis spectroscopy

The concentration of titanate nanosheets and nanotubes in colloidal suspension was examined using a UV-vis spectrometer (Scinco Neosys 2000) by measuring the characteristic absorbance band at 280 nm. Samples were diluted to be determined and poured into 1 cm quartz cuvette (Perkin Elmer). Equation (3.1) was used for calculation of concentration of titanate.

$$A = \varepsilon \, l \, c \tag{3.1}$$

where A is absorbance of titanate solution at 280 nm. ε is molar absorptivity of a solution at 280 nm (5900 L mol^{-1} cm^{-1} for hydrothermal titanate nanostructures, 11170 L mol^{-1} cm^{-1} for Sasaki's flat titanate nanosheets, and 2184 L mol^{-1} cm^{-1} for sol-gel titanate nanosheets). l is the optical path length (1 cm). c is the concentration to be measured.

To get the molar absorptivity of titanate, the concentration of Ti^{4+} ions in the colloidal solution must be determined. For titanate nanotubes (TiNT), 5 mL of methanolic solution of titanate nanotubes were taken and evaporated. Dried titanate nanotubes powder were dissolved by 10 mL of 5 mol L^{-1} sulphuric acid at 100 °C for 3 hours. After spontaneously cooling down to 22 °C, 1 mL of H_2O_2 (30%) were added into the solution and stirred. The colour was changed from transparent into reddish yellow indicating the presence of Ti^{4+} ion complex in the presence of H_2O_2 [161]. The yellow coloured solution was diluted with a distilled water to the volume of 25 mL, and the absorbance was measured on a UV-vis spectrometer (Scinco Neosys 2000) at the wavelength of 420 nm against distilled water as reference. The concentration of Ti^{4+} ions were extracted based on the Beer-Lambert's law equation ($A = \varepsilon\, l\, c$, equation 3.1), where ε (molar absorptivity) of Ti^{4+} ions at a wavelength of 420 nm is 720 L mol^{-1} cm^{-1}. After normalising to the concentration of initial 5 mL methanolic solution of TiNT, it gave the value of 2.48 mmol L^{-1} of Ti^{4+} ions in the initial stock solution.

In Figure 3.1, a calibration curve were established at 280 nm wavelength using the same methanolic solution of titanate nanotubes, which can be used to determine the concentration of Ti^{4+} ions in titanate nanotubes. The value for molar absorptivity of TiNT was 5900 L mol^{-1} cm^{-1}, which obtained from the slope of the curve. By assuming complete dehydration of titanate nanotubes ($H_2Ti_3O_7$) into TiO_2, the number of moles of titanate nanotubes can be evaluated. The dehydration reaction can be described as $H_2Ti_3O_7 \rightarrow 3TiO_2 + H_2O$, where the moles of titanate nanotubes is one third of Ti^{4+} ions of dehydrated titanate nanotubes [162]. The mass of titanate nanotubes can be obtained by multiplying 1/3 moles of Ti^{4+} ions with 258 g mol^{-1}, which is the molecular weight of $H_2Ti_3O_7$. This calculation has also been applied for hydrothermal scrolled titanate nanosheets due to its similarity with titanate nanotubes.
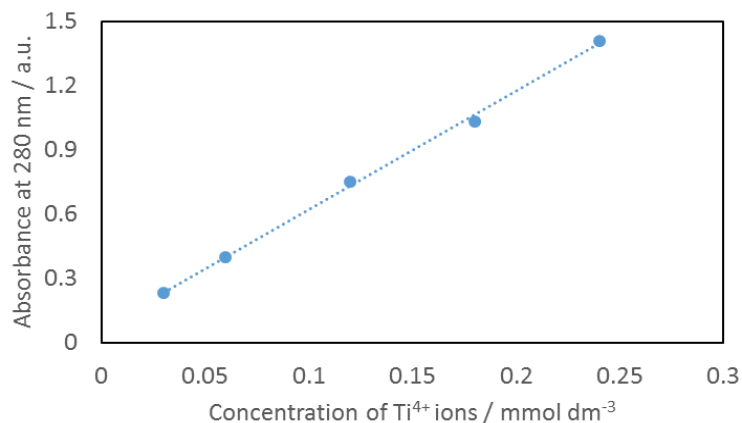
Figure 3.1. Calibration curve for Ti^{4+} ions concentration in titanate nanotubes versus absorbance at 280 nm.

For Sasaki's flat titanate nanosheets (TiNS), 5 mL of aqueous solution of titanate nanosheets were evaporated and the remaining powder was dissolved in 10 mL of 5 mol L^{-1} sulphuric acid at 100 ^{o}C for 3 hours. The colour was spontaneously changed from transparent to reddish yellow upon addition of 1 mL H$_2$O$_2$ (30%) implying the presense of Ti(IV) ion. The solution was diluted to 75 mL due to strong absorbance at 420 nm. Equation 3.1 was utilised to calculate the concentration of Ti^{4+} ions, using ε (molar absorptivity) of Ti^{4+} ions at a wavelength of 420 nm. The concentration of Ti^{4+} ions in initial 5 mL aqueous solution of TiNS was 20.65 mmol L^{-1}.

A calibration curve for determination of equivalent amount of Ti^{4+} ions in titanate nanosheets was prepared in Figure 3.2. The value of TiNS molar absorptivity was 11700 L mol^{-1} cm^{-1}, which obtained from the slope of the curve at the wavelength of 280 nm. Due to the similarities of titanate nanosheets (Ti$_{0.91}$O$_2$) crystal structure and TiO$_2$, the calculation of the mass of titanate nanosheets can be perfomed simply by multiplying the moles of Ti^{4+} ions with 80 g mol^{-1}, which is the molecular weight of TiO$_2$.
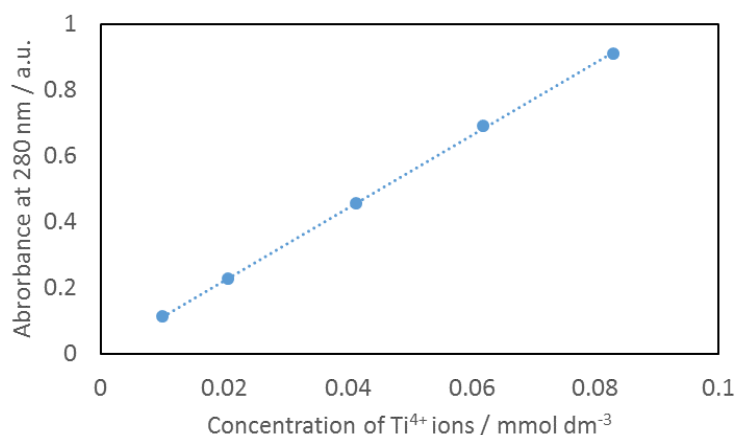
Figure 3.2. Calibration curve for Ti^{4+} ions concentration in Sasaki's titanate nanosheets versus absorbance at 280 nm.

The same procedure was applied to sol-gel titanate nanosheets, 5 mL of aqueous solution of sol-gel titanate nanosheets was evaporated and dissolved at 100 $^{\circ}$C for 3 hours in 5 mol L^{-1} sulphuric acid. After cooling down, 1 mL of H_2O_2 was added and the colour was turning into yellow. The solution was diluted and the concentration of Ti^{4+} ions was determined using the molar absorptivity of Ti^{4+} at 420 nm, which the obtained value was 208 mmol L^{-1}.

A calibration curve was established based on the concentration of Ti^{4+} ions and its absorbance at 280 nm in Figure 3.3. The molar absorptivity was obtained by calculating the slope of the curve, which is 2184 L mol^{-1} cm^{-1}. According to Tae *et.al.* [50], the chemical structure of sol-gel titanate nanosheets was similar to Sasaki's nanosheets ($Ti_{0.91}O_2$) which is close to TiO_2. The weight of titanates can be calculated by multiplying the moles of Ti^{4+} ions to 80 g mol^{-1}.
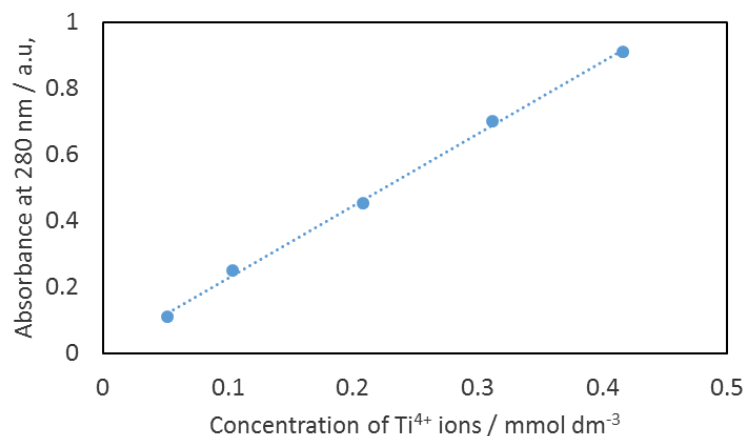
Figure 3.3. Calibration curve for Ti^{4+} ions concentration in sol-gel titanate nanosheets versus absorbance at 280 nm.

3.1.4.4   Images of titanate colloidal solution

Images of the colloidal suspension were taken by an 8 megapixel camera. The transparency of samples was qualitatively determined. Pictures were taken immediately after stopping the stirring process of the colloidal solution. Samples were left for one week and its images were retaken. The images of the samples that were stable for more than 6 months, without any differences in the appearance, were not recaptured.
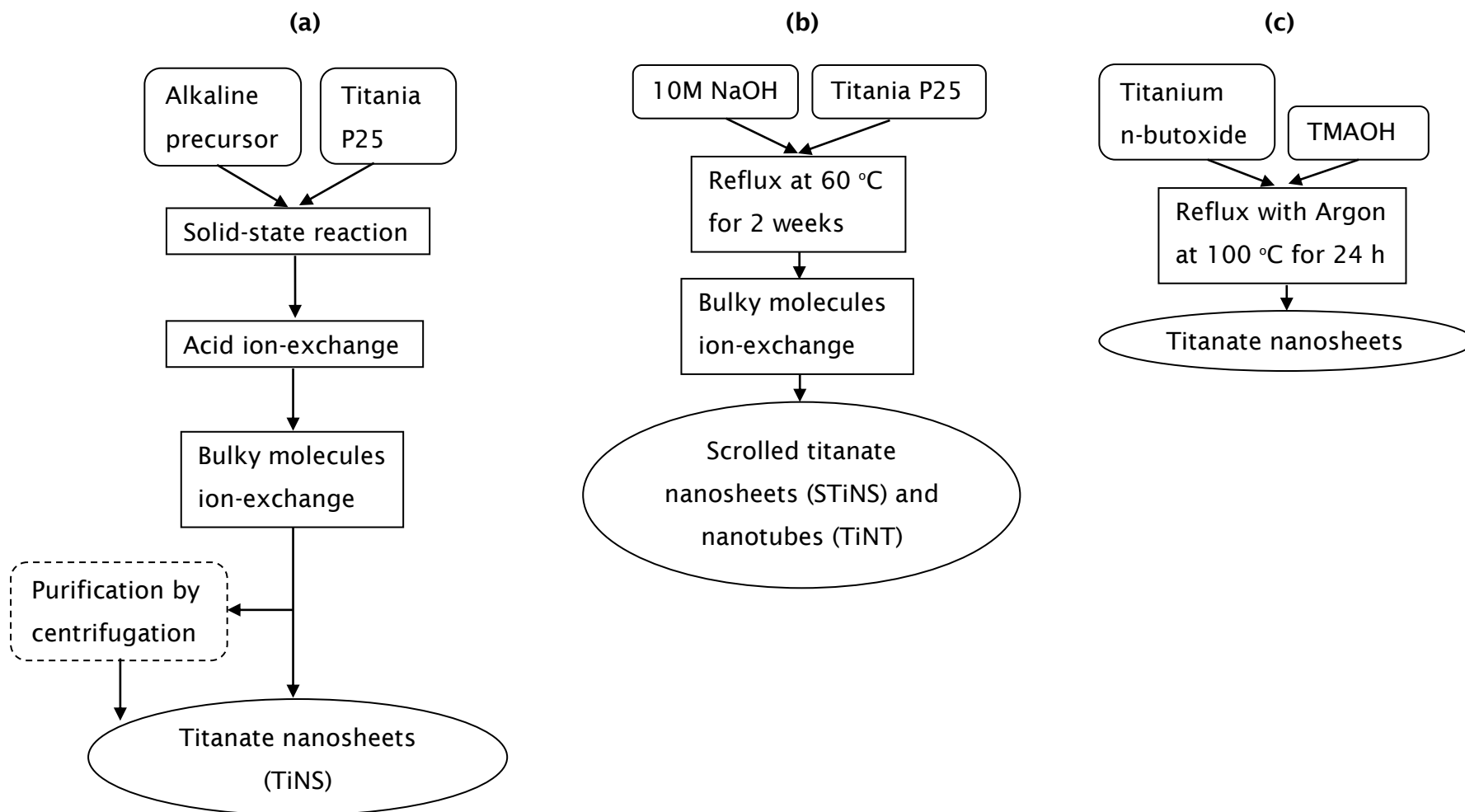
Figure 3.4. Scheme procedures of titanate nanostructures synthesis (a) Sasaki's method (--- = optional); (b) Hydrothermal method; (c) Sol-gel method.

3.2 Synthesis and characterisation of polyimide and polyimide nanocomposites

The procedure for classical two step polyimide synthesis is provided in section 3.2.1 while the use of electrospinning to synthesis polyimide is explained in section 3.2.2. The synthesis of polyimide nanocomposites is described in section 3.3.3. Methods to characterise polyimide and polyimide nanocomposites using FTIR, SEM, UV-vis spectroscopy, viscometry, and optical imaging are outlined in section 3.2.4.

3.2.1 Two step method of polyimide synthesis

The procedure of polyimide synthesis is divided into two parts which is polymerisation of polyamic acid and chemical imidization. The first step is a simple and convenient method that can be done at room temperature. An equimolar of two polyimide monomers, that is dianhydride and diamine, was dissolved and stirred in 250 mL 3 neck round bottom flask at 22 °C for 2 days under nitrogen atmosphere. One neck of the flask was used for nitrogen gas supply and as thermometer attachment. The rod of overhead stirrer was inserted through middle neck; air lock was connected to this neck as well to allow gas released while preventing air entering the flask. The last neck was used for addition of monomers and solvent, which was closed during polymerisation. The schematic representation of the setup was illustrated in Figure 3.5.
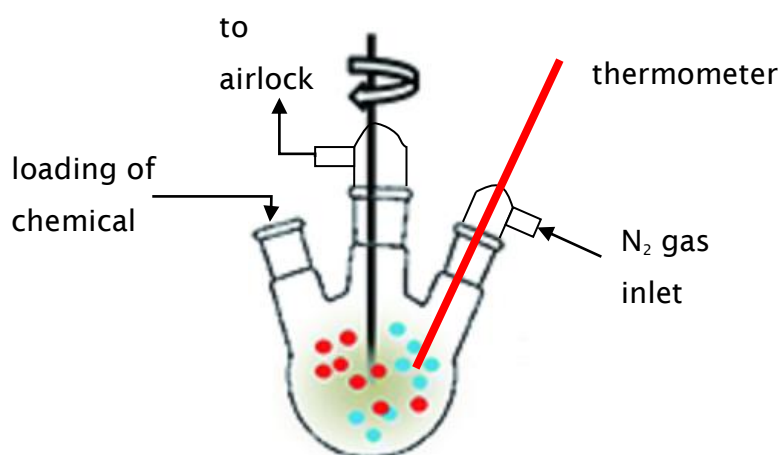
Figure 3.5. The schematic representation of the polymerisation setup.

Two types of polyimide were produced in this work. Firstly, an semi-alicyclic polyimide was synthesised using bicyclo[2.2.2]oct-7-ene-2,3,5,6-tetracarboxylic dianhydride (BOCA) and 4,4'-oxydianiline (ODA) as monomers and dimethylacetamide (DMAc) as a solvent. Secondly, an aromatic polyimide was prepared from pyromellitic dianhydride (PMDA) and 4,4'-oxydianiline (ODA) as monomers and N,N-dimethylformamide (DMF) as a solvent. As a typical example, a mixture of 2.392 g of ODA (1 mol) and 20 g of DMF was stirred inside 250 mL round bottom flask at 22 $^{\circ}$C. After ODA was dissolved, 2.608 g of PMDA (1 mol) was added to the solution and stirred for 1-3 days, yielding 20 wt% DMF solution of polyamic acid. All the reactions were undertaken under nitrogen atmosphere.

The second step was chemical imidization of polyamic acid and subdivided into 3 stages. Firstly, 1 mL of polyamic acid solution was dropped on a glass slide and was rolled with a glass rod that has 0.05 mm spacer from 2 rolls of polyester tape 3M^{TM}. For a low viscosity solution such as BOCA-ODA polyamic acid, 0.27-0.65 g solution was drop cast on the glass using a pressure sensitive adhesive (blu-tack, Bostik) as a cage to contain the liquid. Secondly, the glass slide with polyamic acid solution was immersed in a mixture of acetic anhydride and pyridine (mole ratio 4 : 3.5) for 1 minute to dehydrate the polyamic acid by capturing an excess of water. For a low viscosity solution, 500 µL of a mixture of acetic anhydride and pyridine (mole ratio 4 : 3.5) was added and stirred for 1 minute with the polyamic acid solution. Thirdly, the polyamic acid gel was heated in an oven at 120 $^{\circ}$C for 1 h. A schematic representation of chemical imidization is shown in Figure 3.6.
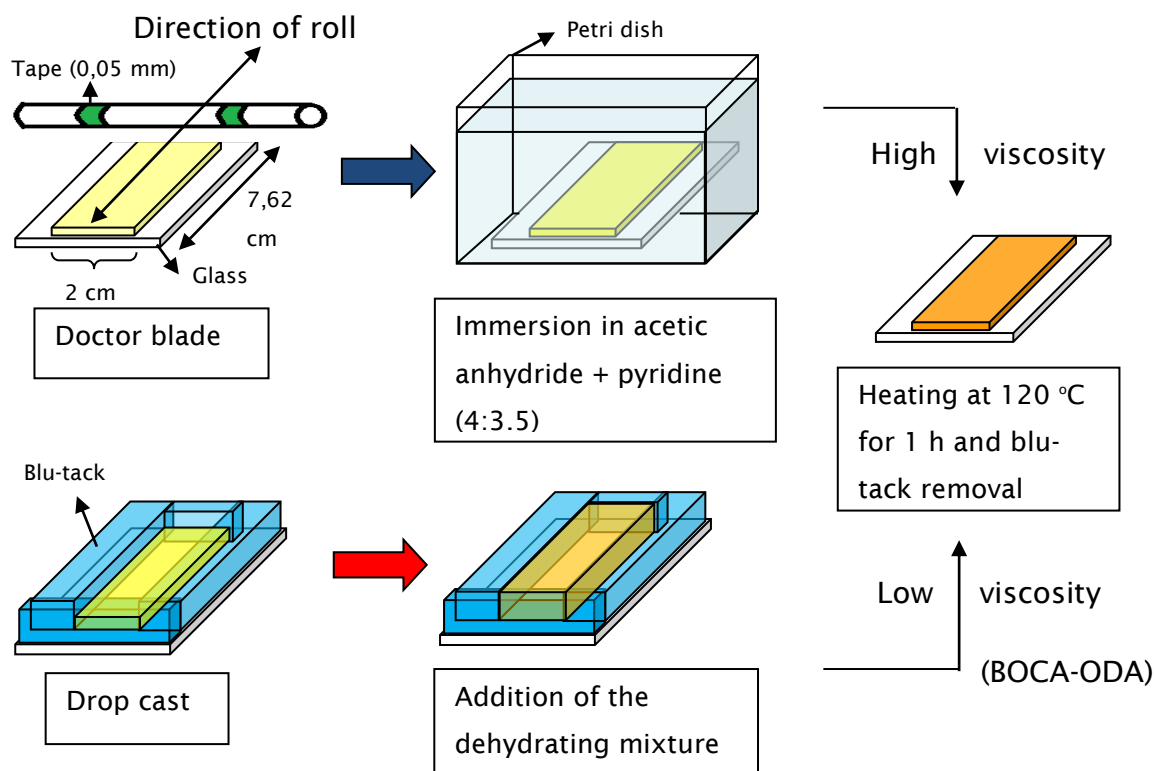
Figure 3.6. Schematic representation of chemical imidization of polyamic acid.

3.2.2 Electrospinning of polyimide

Some of the samples were spun to produce nanofibers. The electrospinning process was conducted before the chemical imidization by apparatus EC-DIG (IME technologies, the Netherlands). A mixture of 2.392 g of ODA (1 mol) and 20 g of DMF was stirred in a 250 mL round bottom flask at 22 ± 2.5 ºC. After the ODA had dissolved, 2.608 g of PMDA (1 mol) was added to the solution followed by stirring for 2 days, yielding 20 wt % DMF solution of polyamic acid. All the reactions were shielded by a nitrogen gas blanket. 1 mL polyamic acid solution was placed into a 2 mL syringe for electrospinning. A solution of polyamic acid in DMF was spun to an aluminum foil collector at a distance of 20, 25, 30, and 35 cm via a 20 kV DC voltage with a relative humidity level of $40 \pm 5\%$. For microscopy characterisation, silicon wafer for SEM (or cooper grid for TEM) with carbon tape was stuck on the aluminium foil. The nanofibers could be spun on the top of silicon wafer. After electrospinning, chemical imidization was conducted. Fibres and silicon wafer were immersed for 1 minute in a mixture of acetic anhydride and pyridine (mole ratio 4 : 3.5), followed by heating in oven at 120 ºC for 1 h.

3.2.3 *In-situ* and *ex-situ* synthesis of polyimide nanocomposites

Some of polyimide samples were reinforced with titanate nanostructures. Besides the pristine/uncoated titanate nanotubes and titania (Degussa P25), both coated with cetyl trimethylammonium bromide (CTAB) and used as the filler in the polyimide. 2.5 g of titanate nanotubes were stirred with 5 mL of 0.1 mol L^{-1} CTAB and 25 mL distilled water for 3 days. Titanate nanotubes were separated from the solution and dried at 22 $\pm$ 2.5 ^{o}C under vacuum. For preparation of the colloidal solution, 2 g of CTAB coated TiNT was stirred in 1 L DMF for 2 weeks at 600 rpm. The solution was allowed to settle for 48 h and the top of the liquid was collected yielding stable colloidal suspension (240 mg L^{-1}), measured by a gravimetric method.

For preparation of *in-situ* polyimide-titanate nanotube fiber, 2.391 g of 4,4'-oxydianiline (ODA) was mixed with 20 g of a stable colloidal suspension of CTAB-coated TiNT in DMF (240 mg L^{-1}) stirred at 22 $\pm$ 2.5 ^{o}C. After ODA had dissolved, 2.604 g of pyromellitic dianhydride (PMDA) (equimolar with ODA) were added to the solution and stirred for 2 days, yielding 20 wt % DMF solution of *in-situ* polyamic acid-titanate nanotube composite. All the polymerization reactions took place in a nitrogen atmosphere. The solution of PAA-TiNT was electrospun to the aluminum foil collector at a distance of 20 cm with a 20 kV DC voltage. The solution was supplied to the 0.8 mm needle using a syringe pump (IME Technologies, Netherlands) at a pumping rate 0.12 mL h^{-1}. In order to dehydrate the polyamic acid and convert it to polyimide, the electrospun PAA fibers were immersed in a mixture of acetic anhydride and pyridine (4: 3.5 volume ratio) for 1 min followed by heating in oven at 120 ^{o}C for 1 h.

For *ex-situ* polyimide-titanate nanotube fiber synthesis, 2.391 g of ODA was stirred in 10 g of DMF until complete dissolution. 2.604 g of pyromellitic dianhydride (PMDA) (equimolar with ODA) were added to the solution and stirred for 1 day, to produce a viscous solution of polyamic acid. 20 g of stable, colloidal suspension of CTAB-coated titanate nanotube in DMF (240 mg L^{-1}) was concentrated by rotary evaporation at 120 ^{o}C, yielding 10 g of concentrated stable colloidal suspension (480 mg L^{-1}). The concentrated solution was slowly poured into a viscous polyamic acid solution and stirred for 1 day. To produce the fiber, a solution of *ex-situ* synthesized polyamic acid-titanate nanotubes was spun onto an aluminum foil collector using a 20 kV DC voltage at a distance of 20 cm from the syringe tip. The solution was fed to the 0.8 mm needle

by a syringe pump (IME Technologies, Netherlands) at a pumping rate of 0.2 mL h^{-1}. Finally, the PAA/TiNT fiber was immersed in a mixture of acetic anhydride and pyridine (4:3.5 volume ratio) for 1 min followed by continued heating in air at 120 ^{o}C for 1 h.

3.2.4   Synthesis of water-soluble polyamic acid-titanate composite

The work of Lee, *et.al.* [163] has been used to synthesise a water-soluble polyamic acid salt. An aromatic polyamic acid salt was prepared from pyromellitic dianhydride (PMDA) and 4,4'-oxydianiline (ODA) as monomers and N,N-Dimethylacetamide (DMAc) as a solvent. All the reactions were shielded by nitrogen gas. As a typical example, a mixture of 1.201 g of ODA (1 mol) and 22.59 g of DMAc was stirred inside a 250 mL round bottom flask at 22 ^{o}C. After the ODA dissolved, 1.309 g of PMDA (1 mol) was added to the solution and stirred for 1 day, yielding a 10 wt% DMAc solution of polyamic acid. Then, 1.656 mL of triethylamine (TEA), equivalent to 2 mol of monomer, was added. Local white precipitation was visible upon addition of TEA into the solution as stated from Kreuz, *et.al.* [164] and disappeared after approximately 30 min. The resulting solution was poured into acetone and filtered with a nylon membrane (0.2 µm pore size) followed by washing with acetone twice. After drying at 22 ^{o}C for 24 hours, a light yellow PAAS powder was collected and stored at 22 ^{o}C and 40 ± 5% relative humidity. For the pure polymer film, 0.215 g of PAAS was stirred in 4 mL distilled water and 80 µL TEA to assist dissolution of PAAS, yielding 5 wt% of PAAS in aqueous solution. The solutions were stirred for 3 days and drop cast on glass. The drop cast solutions were kept at 22±2 ^{o}C and 40 ± 5% relative humidity for 4 days to achieve an equilibrium moisture content in the films.

0.08 g of titanate nanostructures such as TiNS, STiNS, and TiNT was sonicated for 9 h with 20 mL of distilled water and 400 µL triethylamine (TEA). The solution was kept for 4 days to separate non-dispersed agglomerates at the bottom. A known concentration (determined by UV-vis spectrometry) of titanate nanostructures (e.g., TiNS, STiNS, and TiNT) as stable colloidal suspensions was mixed with PAAS powder to make 5 wt% of a polyamic acid-titanate nanostructure composite (PAAS-TiO) aqueous solution with various concentrations of TiNS, STiNS, or TiNT (0.5, 1, 2, 3, and 5 wt% of solid). The

composite solutions were vigorously stirred for 3 days and drop cast on glass. The samples were allowed to dry at 22 ± 2 ^{o}C in $40 \pm 5\%$ relative humidity for 4 days.

3.2.5 Solution mixing of polyimide and titanate

A partially fluorinated polyimide (PI) was synthesised from 4,4'-(hexafluoroisopropylidene)diphthalic anhydride (6FDA) and 4,4′-Oxydianiline (ODA) as monomers using two step method which is polymerisation and imidization [86]. As a typical example, 1.553 g of ODA was dissolved in 20 g of N,N-Dimethylformamide (DMF) in a 250 mL round bottom flask. 3.447 g (equimolar) of 6FDA was slowly added to the solution and stirred for 2 days at 22.5 $\pm$2.5 ^{o}C yielding 20 wt% of 6FDA-ODA polyamic acid solution. The polymerisation reaction was shielded with nitrogen gas. A mixture of pyridine and acetic anhydride (3.5 : 4 volume ratio) was used for chemical imidization. 15 mL of imidization solution was poured slowly into 20 mL of polyamic acid solution and stirred for 1 day. The final solution was slowly precipitated in 250 mL methanol, filtered, and washed with methanol. The resulting yellowish powder was dried in vacuum at 22.5 ± 2.5 ^{o}C for 1 day. For pure polyimide film, 7.764 g of PI powder was dissolved in 40 mL dimethylsulfoxide (DMSO) by stirring for 2 weeks. 140 µL of the solution was taken and casted on top of the glass followed by drying at 120 ^{o}C for 1 h.

Composite solution was made by mixing 95 wt% of 6FDA-ODA PI solution and 5 wt% concentrated colloidal solution of titanate nanotubes. As an example, 7.376 g of PI powder stirred until dissolved in 38 mL DMSO over 2 weeks. A colloidal solution of titanate nanotubes was concentrated with rotary evaporator at 70 ^{o}C in vacuum to 2 mL containing 0.0745 g TiNT (1 wt% of total solid). The concentrated TiNT was poured to PI solution and stirred for 1 week. 140 µl of composite solution was immediately taken after stirring and casted on the glass followed by drying in a furnace at 120 ^{o}C for 1 h. The schematic representation of synthesis of polyimide nanocomposite film and fibre is shown in Figure 3.7.
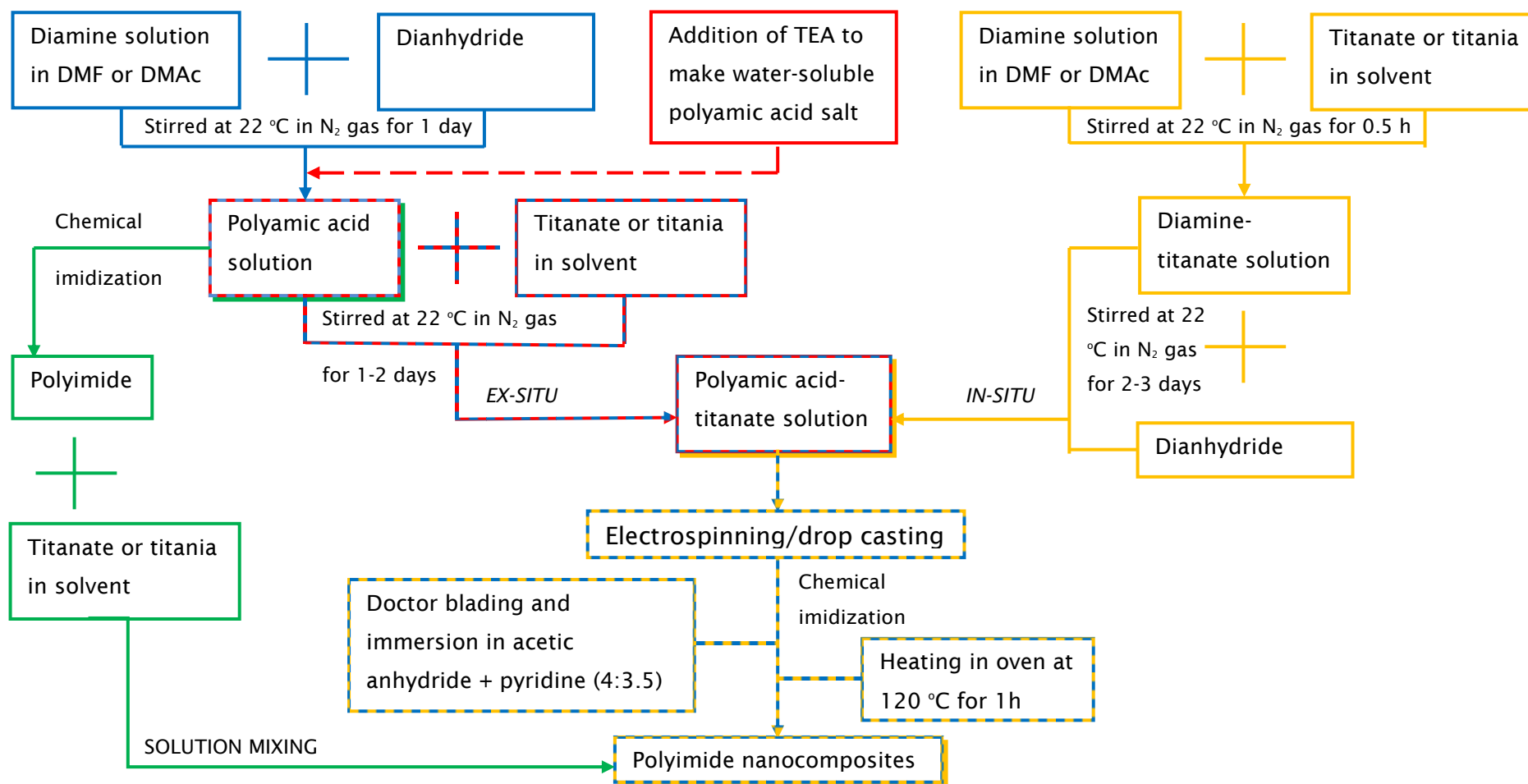
Figure 3.7. Synthesis scheme of polyimide nanocomposites. Blue, gold, red, and green colours represent *ex-situ*, *in-situ*, water-soluble, and solution mixing, respectively.

3.2.6 Characterisation of polyimide and polyimide nanocomposites

3.2.6.1 Small- and wide-angle X-ray scattering

Small- and Wide-angle X-ray scattering (SAXS and WAXS) data were collected on a Rigaku SmartLab diffractometer equipped with an in-plane arm and a 9 kW (45 kV, 200 mA) Cu target rotating anode generator. Symmetrical scans were measured in Bragg-Brentano configuration with 5 deg primary and secondary axial Soller slits and a 1D silicon strip D/teX Ultra 250 detector. In-plane measurements were made in parallel beam configuration with a 0.5 deg in-plane parallel slit collimator and in-plane parallel slit analyser with the detector operating in 0D mode.

3.2.6.2 Nanoindentation

The reduced modulus of elasticity and hardness were obtained with nanoindenter Nanotest Platform 3 (Micro Materials Ltd, UK). To prepare the samples, a small cut of the film (around 0.5 cm × 0.5 cm) was glued by epoxy glue to the soda-lime glass with the smoother surface (cast side) on top to be measured. Then, the glass was glued with acrylic glue to cylinder holder. The cylinder holder with glass and samples on top was put inside the nanoindenter to be measured. A Berkovich (3-side pyramidal) diamond tip was employed for nanoindentation test. A constant loading and unloading rate of 20 mN s^{-1} were applied with 30 seconds holding time after reaching the maximum depth. 20 indentations with 30 µm intervals at 0.5 to 1 mN loading ranges were set. The average values of modulus and hardness were calculated and its standard deviations were provided.

3.2.6.3 Differential scanning calorimetry

Thermal characterization of pure polyimide (PI) and PI/TiNT composite (14.2–20.5 mg) was performed by a Pyris 1 (Perkin Elmer) differential scanning calorimeter (DSC) under nitrogen atmosphere. Pristine polyimide and PI/TiNT composite films were cut to provide a snug fit into the holder. Each sample was held for 1 min at 50 °C then heated from 50 to 500 °C at the rate of 10 °C min^{-1}. The temperature was held at 500 °C for 1 min then allowed to cool to 30 °C before a sample was removed from the holder.

3.2.6.4   TEM, SEM, optical microscopy, and thickness measurement

The morphology and optical properties of samples were investigated by transmission electron microscopy (TEM) (JEOL-3010), field emission scanning electron microscopy (JEOL JSM 6500F) with accelerating voltage of 15-20 kV, TEM was employed to characterise the morphology of nanostructures and to study the dispersion of titanate nanostructures (e.g., TiNS, STiNS, and TiNT) in the polymer. Samples were dropped on top of a copper grid with a perforated carbon film and spin coated at 4300 rpm for 1 minute to achieve a very thin deposit for TEM. For electrospun fibre, the polymer or composite solution was spun on silicon wafer or copper grid containing a perforated carbon film for SEM and TEM characterisation, respectively. The photograph of 6FDA-ODA PI and PI-TiNT film was taken by 20.1 megapixels camera and Celestron™ LCD Digital Microscope II. LCD optical digital microscope with top and bottom illuminations (Celestron™ LCD Digital Microscope II). The optical image from the top illumination mode is captured by the light reflected from the surface of a specimen while bottom illumination is using transmission of light to the specimen form the bottom of specimen. The thickness of polyimide and polyimide nanocomposites films were measured by micrometre calliper (digital electronic micrometre, Mitutoyo, Japan).

3.2.6.5   UV-vis, FTIR, Raman spectroscopy, and viscosity measurement

The optical properties of polymer nanocomposites, pure polyimide, and concentration of methylene blue in solution (to study polymer degradation) were evaluated by UV-vis spectroscopy (Scinco Neosys 2000). A film with thickness around 100 microns was put inside the 1 cm quartz cuvette (Perkin Elmer) and was used to collect the transmission spectra of polymer film. A Fourier Transform Infrared Spectroscopy (Nicolet 380 FT-IR Spectrometer, Thermo Scientific) was used to characterise samples at a resolution of 4 cm^{-1}. For each sample, 32 successive scans were recorded to cover the wavenumber region of 500-4000 cm^{-1}. To smooth the FTIR spectra, Savitzky-Golay filtering algorithm that is provided by Origin 9.1 was used. Raman spectra were obtained using a Raman spectroscopy confocal microscope (Renishaw, RM 2000) using a light source of 632.8 nm wavelength. The exposure time was 10 seconds with a 1% intensity of laser radiation. The dynamic/absolute viscosity of titanate-polyamic acid solution was evaluated by a CAP 2000+ viscometer. A shearing force was applied to the solution

with the rate of 2500 s^{-1} for 40 seconds and the average value of the viscosity was taken. The viscosity of the diluted solution was measured by an Ostwald viscometer which held vertically at 22 $^{\circ}$C (Figure 3.8).

To measure the viscosity, the diluted solution was poured from the larger tube (left tube in Figure 3.8) up to X mark. Then, it was sucked until the solution reached the Y mark. Lastly, the solution was allowed to flow down through the capillary tube until Z mark. The stopwatch timer was used to measure the duration of the solution to travel from Y to Z. Later, this travel time was put into the calculation to calculate the kinematic viscosity via Equation (3.2).

$$v = C \text{ x } t \tag{3.2}$$

where v is kinematic viscosity (noted as cSt, where 1 cSt (centistoke) = 1 mm^2 s^{-1}), C is a calibration factor which is provided for the tube, t is duration of the solution to travel from Y to Z.
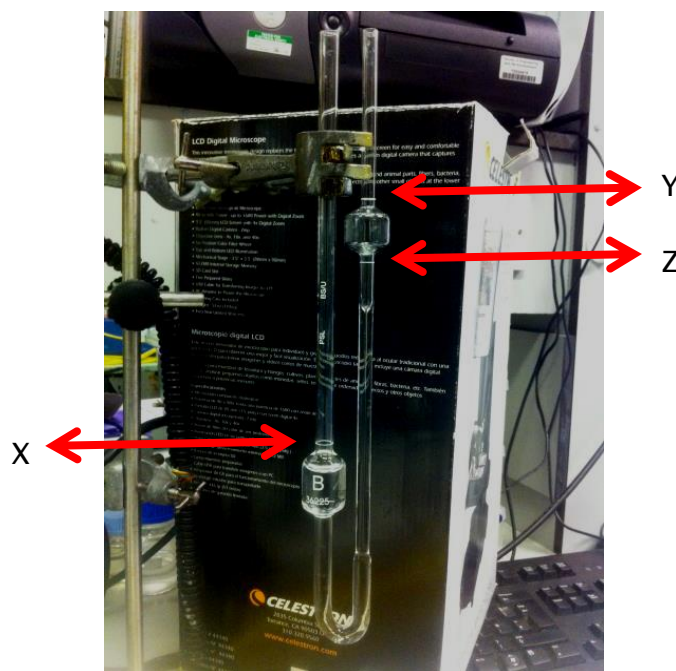
Figure 3.8. Ostwald viscometer setup

Kinematic viscosity measure the inherent viscosity of the fluid under influence of gravity while dynamic viscosity is the quantitative expression of a fluid's internal resistance to flow, which the unit of measure for dynamic viscosity is centipoise (cP) or

mPa s. Dynamic or shear viscosity (μ) is calculated by multiplying the kinematic viscosity (v) by density (ρ) of the solution:

$$\mu = v \text{ x } \rho \tag{3.3}$$

3.3 UV exposure testing of polyimide and polyimide nanocomposites

UV experiment was conducted to study the effect of UV irradiation on polyimide and polyimide nanocomposites. Polyimide and polyimide nanocomposites were exposed to UV light (xenon arc lamp) with 9.8 A current for different irradiation time (1-4 h). The distance between UV light and sample was 13.3 cm, yielding a light intensity of 15 W m^{-1}. The intensity of UV was measured using UV FASTCHECK^{TM} strips. The experiments were conducted at 22 ± 3 °C inside the fume hood covered with cardboard and aluminium foil.

Chapter 4: Synthesis and Characterisation of Titanate Nanosheets

4.1 Introduction

In this chapter, the synthesis of titanate nanosheets with three different method such as Sasaki's method [33], hydrothermal method [24], and sol-gel method [50] were studied and characterised using SEM, TEM, and XRD. For nanosheets made by Sasaki's method, different precursors were used creating caesium and potassium-lithium route titanate nanosheets. In the potassium-lithium route titanate, the solid-state reaction was performed in absence of an additive to enhance reaction rate (e.g., molten salt flux). Two types of crucibles were deployed such as aluminosilicate and platinum crucible to study its effect on the synthesis of titanate nanosheets. Intermediate hydrothermal temperature (60 $^\circ$C; between nanosheets and nanotubes formation [24]) was used to create titanate nanostuctures. Variation of sol-gel precursor (titanium n-butoxide instead of titanium isopropoxide) was used to synthesis sol-gel titanate nanosheets. The purpose of this chapter is to evaluate the morphology and concentration of the synthesised nanosheets which were used later to reinforce the polymer.

4.2 "Caesium" route to titanate nanosheet synthesis

The Sasaki's "caesium" route is a common and popular method to synthesise titanate nanosheets (TiNS). The Sasaki's three steps method was adapted with modification of the crucible [33]. Aluminosilicate (porcelain) and platinum crucible was used for heat treatment and its effect on solid-state reaction was studied.

First, the precursor (Cs_2CO_3 and TiO_2) was heat treated in the solid state for three heating process [33]. The first heating process of Cs_2CO_3 and TiO_2 was conducted at 800 $^\circ$C for 1 hour, aiming to remove carbon from Cs_2CO_3 according to the following reaction Cs_2CO_3 (s) $\rightarrow$ Cs_2O (s) + CO_2 (g). The second and third heating process was performed at 800 $^\circ$C for 20 hours each, and the resulting of the calcination process is

lepidocrocite-like titanate, which can be formulated as $Cs_x[Ti_{2-x/4}\square_{x/4}]O_4$, with $\square$ as titanium vacancy [33].

Second, acid ion-exchange was conducted and can be written as [160]:

$Cs_{0.7}Ti_{1.825}\square_{0.175}O_4$ (s) + 0.7 H^+ (aq) + H_2O (aq) $\rightarrow$ $H_{0.7}Ti_{1.825}\square_{0.175}O_4 \cdot H_2O$ (s) + 0.7 Cs^+ (aq).
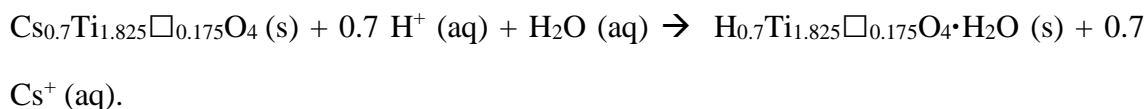
Three cycle of acid decantation has been done to remove the Cs^+ ions. Third, $H_{0.7}Ti_{1.825}\square_{0.175}O_4 \cdot H_2O$ was exfoliated by bulky molecules of tetrabutyl ammonium (TBA^+) ions [160]. The exfoliated titanate nanosheets were used to fabricate homogeneous dipersion of titanate within polyimide. As explained in Chapter 2.3.2, exfoliation of nanosheets is desireable to produce maximum enhancement of polymer due to high aspect ratio and surface area of the nanosheets providing more contacts with the polymer. Several characterizations such as SEM, EDX, TEM and UV-vis spectroscopy have been used to determine the characteristic of titanate in this work.

4.2.1   Characterisation of the "caesium" route to titanate nanosheets synthesis

The titanate nanosheets in TBAOH solution made by aluminosilicate (porcelain) crucible were examined by SEM and EDX. SEM images of the non-diluted samples show that there were sphere-like structure, which can be unreacted titania (Figure 4.1 a, shown in yellow circle), and sheet-like structure. In order to see the titanate nanosheets more clearly with less agglomerates, the sample was diluted 100 times (Figure 4.1 b, c, and d). In this sample, impurities such as aluminium compound (Figure 4.1 b, EDX results shows the elements on the red box) and agglomerates of unreacted titania in Figure 4.1 c were observed.

Element	Weight%
O K	29.20
Al K	5.64
Si K	57.94
Cl K	7.22
Totals	100.00
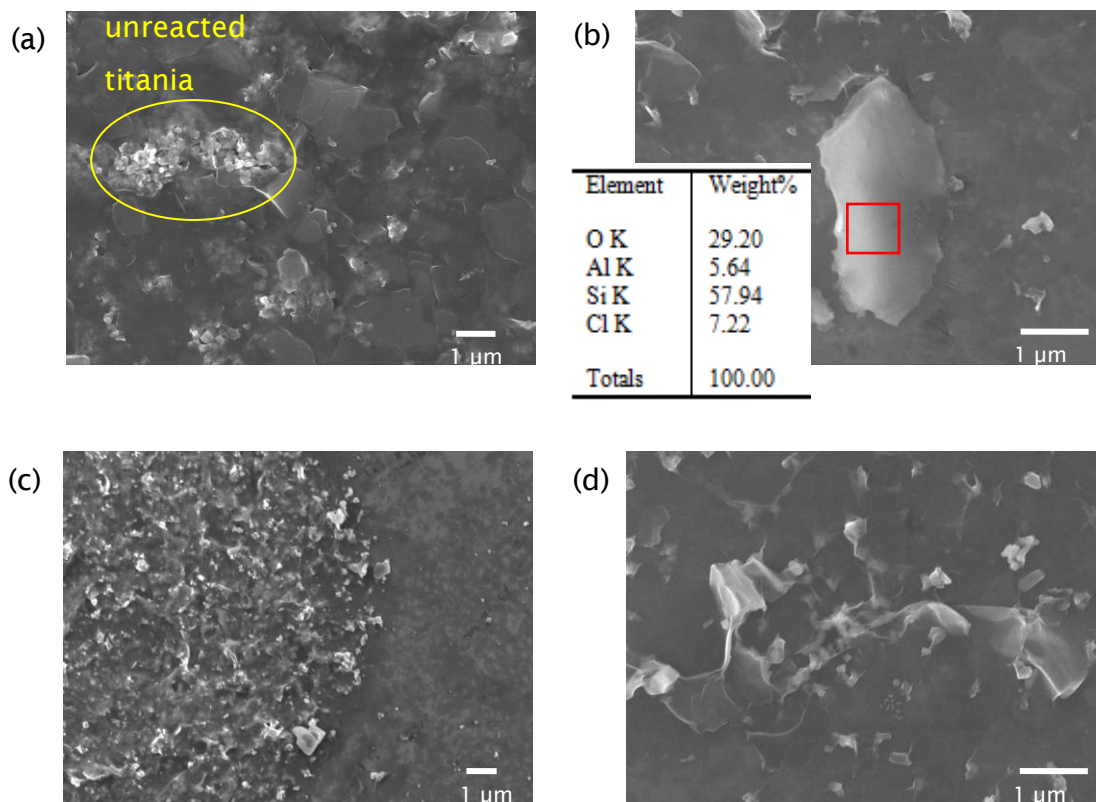
Figure 4.1. SEM images of several-layer nanosheets and impurities in TBAOH (a) non-diluted sample (yellow circle shown unreacted titania); (b) aluminium compound (EDX table shown the detection of elements in the red box); (c) agglomeration of layered nanosheets; (d) several-layer nanosheets (b,c,d = diluted 100 times).

The aluminium impurties may be due to reaction of caesium carbonate with the aluminosilicate crucible leaving some titania unreacted. The other elements such as silicon and oxygen which may be detected from silicon wafer substrate. The detection of chlorine may come from the reaction of aluminium compound with hydrochloric acid during acid ion-exchange.

Element	Weight%
O K	21.28
Si K	73.54
Ti K	5.18
Totals	100.00
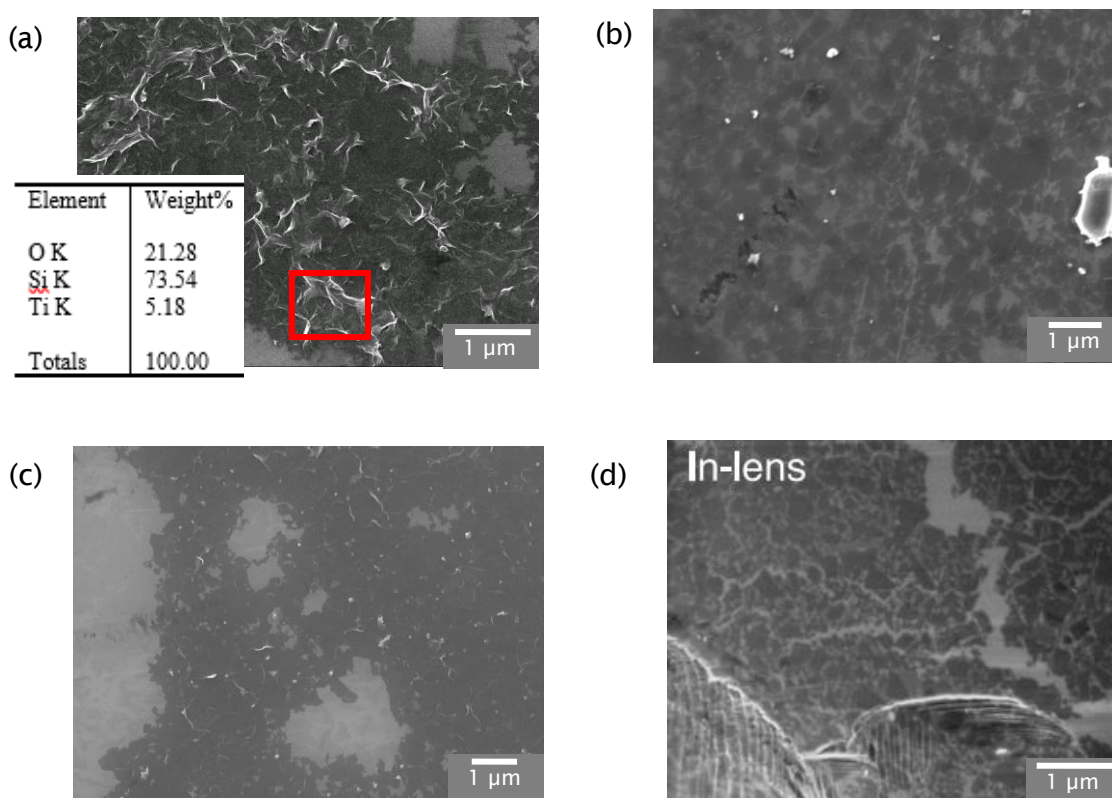
Figure 4.2. SEM images of single-layer nanosheets (a) non-diluted TiNS (EDX table shown the detection of elements in the red box); (b) diluted 100x; (c) diluted 400x; (d) single-layer nanosheets (dark island) of Sasaki's titanate in TBAOH (2.0 kV) (using in-lens detector which only detect lower energy secondary electron) [165].

Aluminium compound and unreacted titania did not appear in the sample which used platinum crucible in Figure 4.2. In non-diluted samples, the several-layer nanosheets were stand vertically on the top of silicon wafer due to attraction of adjacent nanosheets, and detected by EDX in Figure 4.2a. The single-layer nanosheets were seen as a dark island in the diluted 100 times samples (Figure 4.2 b) and for the sample diluted 400 times (Figure 4.2 c). These dark island of the single-layer nanosheets were akin to the literature in Figure 4.2d [165]. Furthermore, variation of bulky molecules (TBAOH and TMAOH) did not give a significant effect on the size of the nanosheets. Size of the nanosheets is similar for TBAOH and TMAOH samples which is 0.1-1 µm. Purification of nanosheets with 12 h centrifugation greatly reduced the impurities and several-layer nanosheets which are not completely exfoliated. However, the concentration of the

nanosheets is greatly reduced which proven by UV-vis spectroscopy (from 3.1 g L^{-1} to 0.768 g L^{-1}).
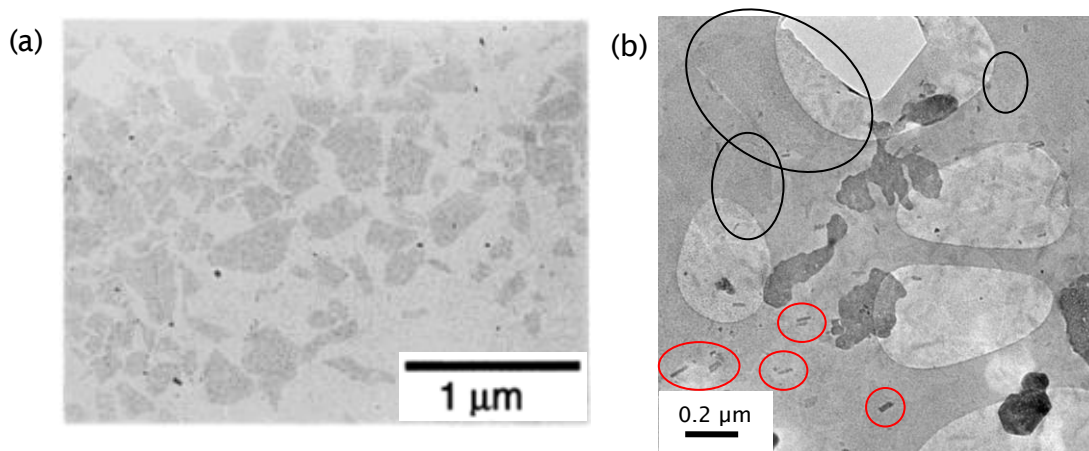
Figure 4.3. TEM images of titanate nanosheets in TBAOH (a) single-layer nanosheets from Sasaki's publication [166]; (b) single-layer nanosheets (black circle) and nanotubes (red circle) from this work.

TEM images of the sample (Figure 4.3 b, black circles) showed correlations with image in the literature (Figure 4.3 a). The extremely thin nanosheets resulted in a very feint contrast, making it hard to distinguish nanostructured material from the background substrate [166]. The very faint and low contrast of single-layer nanosheets indicated that these nanosheets are very thin. The thickness measurement was done by Sasaki, *et.al.* [166] with atomic force microscopy (AFM) which showed the value of 1.2-1.3 nm. Instead of single layers, some nanosheets stack horizontally on the substrate and become more prominent than single layer nanosheets. The colloidal suspension consists mainly of small, irregularly shaped nanosheet particles with a lateral size of *ca.* 100 nm. However, there are some large sheets with a lateral size of *ca.* 300 nm together with very small nanotubes (*ca.* 50 nm in length). According to Bavykin *et.al.* [167] titanate nanosheets tend to scroll into nanotubes in an alkaline environment. Such scrolling may also occur with very small nanosheets in alkali solution such as tetrabutyl ammonium hydroxide (TBAOH).

4.3 "Potassium-lithium" route to titanate nanosheets synthesis

The three steps procedure for synthesis of lepidocrocite-like titanate from potassium carbonate and lithium carbonate is attributed to the work of Sasaki *et.al.* [159]. This lepidocrocite-like titanate is crucial to synthesis single-layer nanosheets. First, solid-state reaction of titania, potassium carbonate, and lithium carbonate was performed to synthesis lepidocrocite-like titanate [38]. The first 30 min heating is for decarbonation by the following reactions: K_2CO_3 (s) → K_2O (s) + CO_2 (g) and Li_2CO_3 (s) → Li_2O (s) + CO_2 (g). Then, the following 20 h reaction created lepidocrocite-like potassium-lithium titanate ($K_xTi_{2-x/3}Li_{x/3}O_4$ with x ≈0.8).

Second, acid ion-exchange of this titanate was conducted and can be written as [160]:

$K_xTi_{2-x/3}Li_{x/3}O_4$ (s) + 4x/3 H^+ (aq.) + H_2O (aq.) →

$H_{4x/3}Ti_{2-x/3}O_4·H_2O$ (s) + x K^+ (aq.) + x/3 Li^+ (aq.).
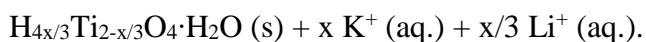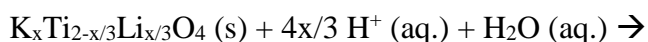
where x = 0.8 and the amount of water is independent of x. Ion exchange capacity of this titanate is higher than caesium titanate due to the exchange of two ions (i.e. K^+ and Li^+ ions) instead of only one ions (Cs^+) [160]. Three times acid decantation is enough to remove K^+ and Li^+ ions is similar to caesium titanate. Third, bulky molecules ion exchange of titanate was performed to exfoliate the layered titanate nanosheets. Due to higher ion exchange capacity, the amount of bulky ions needed for exfoliation is higher than caesium titanate (0.0165 mol L^{-1} and 0.025 mol L^{-1}, for caesium and potassium-lithium route respectively) [160]. The result of this process was examined by TEM and UV-vis spectroscopy.

4.3.1 Characterisation of "potassium-lithium" route to titanate nanosheets synthesis

Contrary to the Sasaki *et.al.* "potassium-lithium" single-layer nanosheets, which created very large sheet (≈30 µm diameter) [38], this work produced relatively small nanosheets (≈50 nm) (see Figure 4.4). Some titanate nanosheets were stacked on the top of each other on the edge of carbon film which is near the hole of carbon film in Figure 4.4 b.

This significant difference may caused by the molten K_2MoO_4 flux and slow cooling method (4 Kelvin per hour) that used by Sasaki. The molten flux, which created by reaction of K_2CO_3 and MoO_3, provided a good heat transfer medium promoting growth of the lepidocrocite-like titanate thus the resulting nanosheets were large.
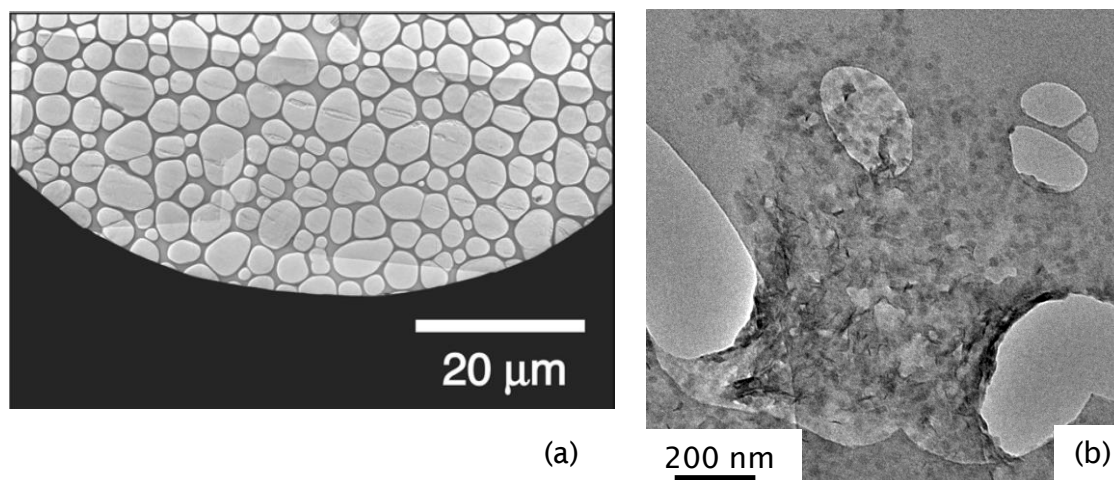
Figure 4.4. TEM images of "potassium-lithium" route of titanate nanosheets synthesis (a) Sasaki's nanosheets was grown using K_2MoO_4 flux and slow cooling method [38]; (b) the image of titanate in this work without flux and spontanaeously cooled in air.

4.4 Titanate synthesis by hydrothermal method

The hydrothermal route used for the synthesis of titanate in this work is based on the work of Bavykin *et.al.* [24]. This hydrothermal route of titanate synthesis was originally an alkaline hydrothermal method which proposed by Kasuga *et.al.* [168] and further developed toward reflux synthesis. The mechanism synthesis of this process is dissolution-recrystallization which metal oxides (e.g. TiO_2) is dissolved and oxidised with $OH^-_{(aq)}$ (e.g., NaOH) to precipitate micro- or nanosized particles amorphous $M(OH)_x \bullet nH_2O$ (M is metal and x is oxidation state of metal, e.g. $Al(OH)_3$, $Ti(OH)_4$) then converted to crystalline nanostructure during treatment. The shape and conversion amount of the nanostructure depend on the processing temperature [24]. Reflux of TiO_2 and NaOH for 4 days at 50 °C gives small amount of crystalline titanate nanosheets. At 70 °C, the mixture of titanate nanosheets and nanotubes are formed. At higher temperature, 90 °C and 110 °C, nanoparticles and nanotubes are formed instead of nanosheets.

The formation of nanotubes by hydrothermal synthesis at high temperature can be explained by scrolling process. The interaction of atoms between neighbouring layer of sheets must be smaller than the interaction of atoms in the same layer in order to induce the scrolling of sheets [60]. The imbalance in the rapid growth of each layer during spontaneous dissolution-crystallisation may creates bending of the layered nanosheets. In Sasaki's flat nanosheets, the lepidocrocite-like titanate nanosheets were made by solid-state reaction. In the cesium titanate nanosheets, the cesium, titanium, and oxygen atoms of the precursor were diffused through solid to the contact interface of the titania and cesium oxide grains [169]. Such mutual diffusion between two reacting solids created a new phase which is layered cesium titanate nanosheets. The contact area between grains of reacting solids determined the rate of cesium titanate synthesis thus the size of the cesium titanate may vary. In the most cases, the diffusion rate in solid is slower than the interfacial growth, giving a minimum possibility of scrolling to occur [170].

In the hydrothermal synthesis, high temperature creates favourable environment for scrolling process of the nanosheets [24]. Figure 4.5 show that 50 °C is not favourable for scrolling process thus favourable for the synthesis of nanosheets. However, the amount of converted materials is too low. On the other hand, though reaction at 70 °C yield a good amount of converted materials, some nanotubes are formed. Therefore, two weeks reflux of TiO_2 and NaOH at 60 °C was conducted to synthesis novel scrolled titanate nanosheets (STiNS).
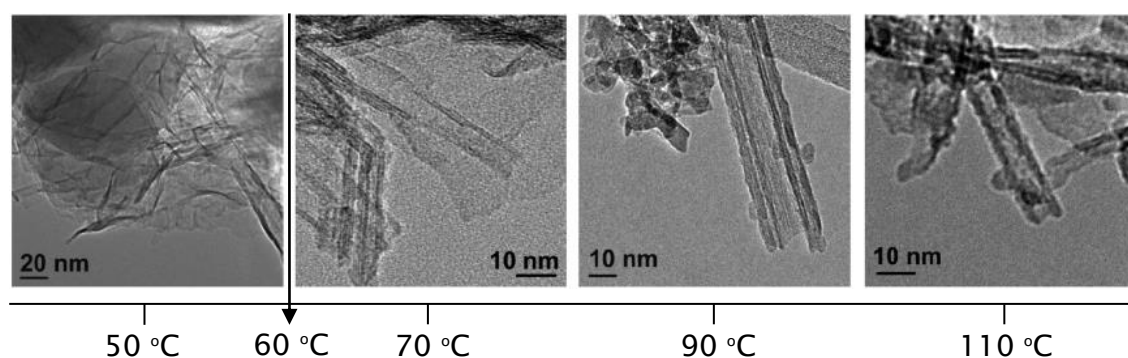
Figure 4.5. TEM images of titania and titanate nanostructures from TiO_2 (P25 Degussa) and 10 mol L^{-1} NaOH by alkaline hydrothermal method for 4 days at 50 °C, 70 °C, 90 °C, and 110 °C [16] (The 60 °C process is the focus of this work).

4.4.1 Characterisation of titanate nanosheets prepared through a novel hydrothermal route

SEM and TEM have been used to determine the shape and size of the samples. Figure 4.6 shows the distribution of titanate on the top of a silicon wafer. The morphology of titanate nanosheets created from hydrothermal synthesis is akin to nanotubes (Figure 4.6.). Such nanosheets are smaller than the nanotubes with a length of *ca.* 75 nm and diameter of *ca.* 10 nm.
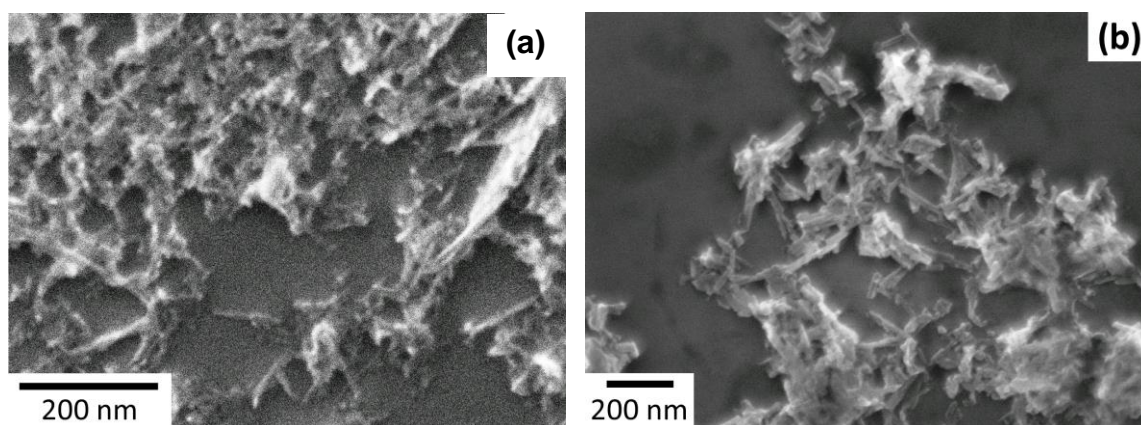
Figure 4.6. SEM images of (a) scrolled titanate nanosheets (STiNS) from TiO_2 (P25 Degussa) and 10 mol L^{-1} NaOH by reflux synthesis for 2 weeks at 60 °C; (b) titanate nanotubes made by refluxing TiO_2 (Degussa P25) with 10 mol L^{-1} of KOH:NaOH 1:25 for 2 days at 100 °C.
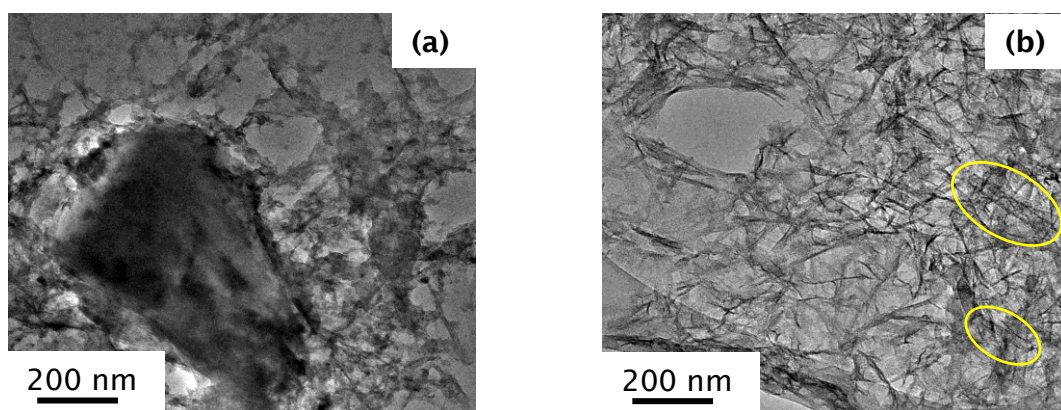
Figure 4.7. TEM images of titanate nanostructures from TiO_2 (P25 Degussa) and 10 mol L^{-1} NaOH by reflux synthesis for 2 weeks at 60 °C; (a) the unconverted materials (large particle); (b) the agglomeration of scrolled titanate nanosheets (STiNS), (Yellow circle showed traces of nanotubes).

Unconverted materials also spotted in TEM images in Figure 4.7 (a). The sample mostly consists of agglomeration of scrolled nanosheets with some traces of nanotubes in Figure 4.7 (b). The scrolled nanosheets did not have defined tubular structure. XRD profile in Figure 4.8 further support this statement.
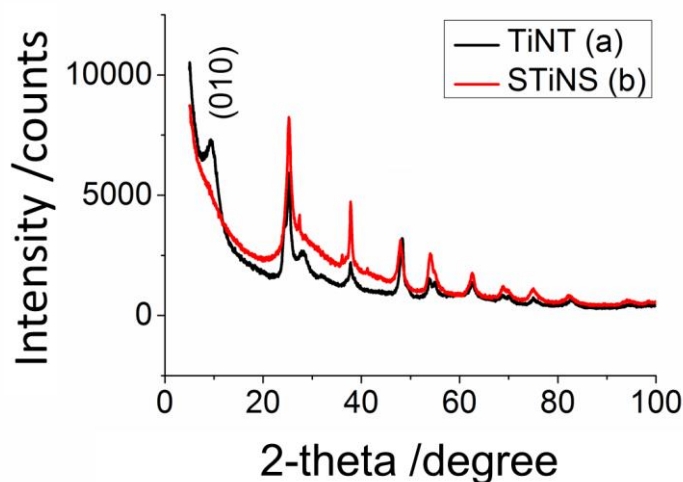
Figure 4.8. Combined SAXS and WAXS profile of (a) titanate nanotubes (TiNT) made by refluxing TiO_2 (Degussa P25) with 10 mol L^{-1} of KOH:NaOH 1:25 for 2 days at 100 °C; (b) scrolled titanate nanosheets (STiNS) from the reaction of TiO_2 (P25 Degussa) and 10 mol L^{-1} NaOH by reflux for 2 weeks at 60 °C. (010) peak is visible in titanate nanotubes sample.

The (010) peaks correspond to interlayer spacing of multi-layered nanotubes in the radial direction, which is not apparent in incomplete scrolling of nanosheets (scrolled titanate nanosheets which only scroll on the edges). This supports the scrolling mechanism of titanate nanotubes during synthesis which argues that nanotubes are formed from scrolling of sheets [171]. The characterisation of scrolled titanate nanosheets indicates that 60 °C of processing temperature was a favourable condition to synthesise scrolled sheets instead of nanotubes.

4.5   "Sol-gel" route to titanate nanosheets synthesis

Bottom-up approach was used in this work. Solution process, which involes hydrolysis and condensation, has been used hence the name "sol-gel" route for titanate synthesis. This method is a modification of the work of Tae *et.al.* [50], which used 33.4 µmol

titanium isopropoxide (TIP) and 273 mmol L^{-1} tetramethylammonium hydroxide (TMAOH). Tae's method is a large scale of Chemseddine *et.al.* [172] method, which used 1.14-11.4 µmol TIP and 0.26-11.6 mmol L^{-1}.TMAOH. An uniform size and shape of titanate nanosheets produces by Tae's method while Chemseddine's work leads to anatase nanoparticles. Such difference came from the concentration of tetramethyl ammonium hydroxide (TMAOH). In Tae's work excess of TMAOH stabilised the formation of titanate nanosheets. TMAOH is known as surfactant template and surface directing agent [173]. In Chemseddine's work, TMAOH acted as surfactant template of titania while in Tae's work TMAOH worked as surfactant template and surface directing agent of titanate nanosheets. The reactions (e.g., hydrolysis, condensation, and stabilisation) can be written as [50]:

Hydrolysis:
$$Ti(OR)_4 + 4\,H_2O \rightarrow Ti(OH)_4 + 4\,ROH$$

Condensation:
$$Ti - OH + XO - Ti \rightarrow Ti - O - Ti + XOH\ (X = H, R)$$

Base-catalyzed condensation
$$\begin{cases} Ti - OH + TMAOH \rightarrow Ti - O^- + TMA^+ + H_2O \\ Ti - OH + Ti - O^- \rightarrow Ti - O - Ti + OH^- \\ Ti - OH + OH^- \rightarrow Ti - O^- + H_2O \end{cases}$$

Stabilisation:
$$Ti_xO_yH_z + TMAOH \rightarrow TMA(Ti_xO_yH_{z-1}) + H_2O$$
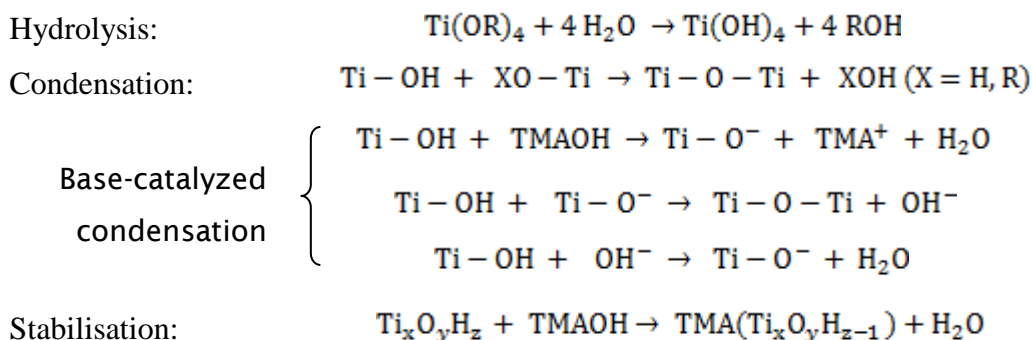
where the values of x and y depend on the concentration of TMAOH. Hydrolysis and condensation reactions are accelerated by TMAOH which created highly nucleophilic Ti-O$^-$. The resulting product of Tae's titanate is similar to lepidocrocite titanate which has chemical formula as $M_xTi_{2-x/4}\square_{x/4}O_4$ (M = monovalent cation and $\square$ is vacancy). Tae *et.al.* determined the value of x with elemental analysis and described his titanate as $TMA_x(Ti_{2-x/4}\square_{x/4}O_4)$ where x ≈0.7.

Titanium alkoxide precursor in Tae's work [108] is titanium isopropoxide (TIP) while in this work is $Ti[O(CH_2)_3CH_3]_4$ titanium n-butoxide ($Ti(OBu)_4$). Comparison between those two different titanium precursor, which are TIP and titanium n-butoxide, has been done by Chemseddine *et.al.* [172]. The type of titanium alkoxide affecting the size of the product (see Figure 4.9).
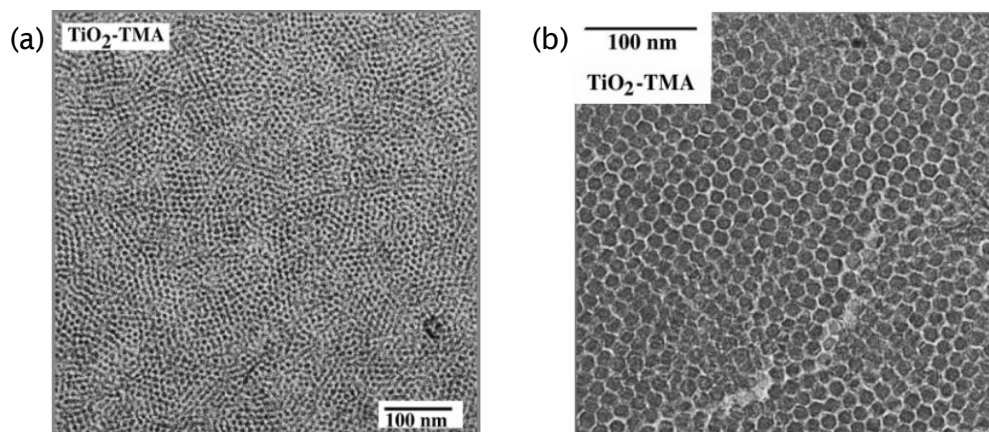
Figure 4.9. TEM images of Chemseddine titania/TMA⁺ nanocrystals self-assembled into a superlattice [172] using two different titanium alkoxide precursor (a) Titanium n-butoxide; (b) Titanium isopropoxide.

Titanium n-butoxide was used in this work and Tae procedure of titanate synthesis was followed. The morphology of the product was determined by TEM and compared to Tae's titanate.

4.5.1   Characterisation of titanate nanosheets via sol-gel method

TEM images with low and high magnification is used to examine the titanate in this work (see Figure 4.10). The majority of titanate in this work (33.4 mmol titanium n-butoxide and 273 mmol L^{-1} TMAOH; 24 h reflux) is diamond-shape titanate (Figure 4.10 a and b which noted in red circles) which is also similar in size to Tae's titanate in Figure 4.10 d (33.4 mmol TIP and 273 mmol L^{-1} TMAOH; 24 h reflux). However, there are small amount of impurities, which shown in yellow circle in Figure 4.9 b, that look like one of Chemseddine's titania in Figure 4.10 c (elongated slab; 11.4 µmol TIP and 11.6 µmol TMAOH; 6 h reflux). This may happens because the stirring speed was not sufficient enough to produce uniform titanate.
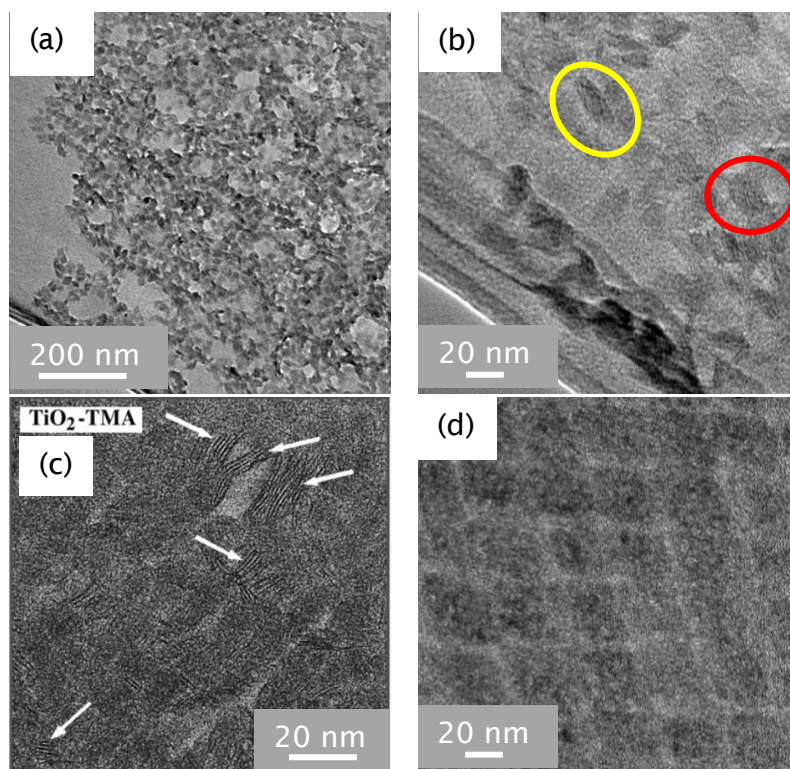
Figure 4.10. TEM images of "sol-gel" route titanate (a) titanate in this work; (b) high-magnification of titanate in this work (red circle similar to Tae's titanate; yellow circle similar to Chemseddine's titania); (c) Chemseddine titania (arrows indicate elongated slab with different length); (d) Tae's titanate.

The self-assembled feature of single layered titanate seems to be destroyed by high-magnification and prolong TEM observation (see Figure 4.10 a and b). Electron beam might decompose the organic cation (TMA$^+$) thus altering the self-assembled property of this titanate. Tae's argue that recrystallization of titanate may occur upon exposure of strong electron beam since the titanate is very thin ($\approx$1.12 nm detected by AFM) [50].

4.6   The concentration of titanate nanosheets in solution

In this thesis, the titanate nanosheets were later used as filler to reinforce the UV resistance, mechanical, and thermal properties of the polymer. It was important to

determine the concentration of titanate nanosheets in solution to add the exact amount of filler in polymer solution. All the titanate were dissolved in sulphuric acid and reacted with H_2O_2 creating Ti^{4+} ions complex. The calibration curve were plotted based on the concentration of Ti^{4+} ions and its absorbance at 280 nm in Chapter 3.1.4. The effect of centrifugation on concentration and the stability of titanate in organic solvent were determined.

4.6.1 The concentration and stability of Sasaki's titanate nanosheets in solution

The colloidal solution of titanate nanosheets was created after stirring 0.4 g protonated titanate nanosheets (TiNS) in 100 mL of aqueous solution of 0.0165 mol L^{-1} tetrabutylammonium hydroxide (TBAOH) or tetramethylammonium hydroxide (TMAOH) at 22 °C for 2 weeks. Hence, the initial concentration from the beginning of the stirring process is 4 g L^{-1}. In colloidal solution, the concentration was determined by taking the top solution from the bottle of colloidal solution.
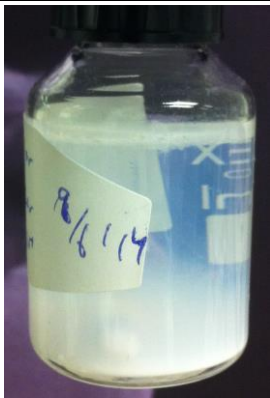
In caesium route titanate, the concentration of titanate nanosheets (TiNS), that has been synthesised using platinum crucible, was stable for more than 6 months in aqueous solution of TBAOH at 3.1 g L^{-1} in Table 4.1, sample 1. Some impurities and large nanosheets may settled at the bottom of the bottle. For samples that were made using porcelain (aluminosilicate) crucible, lower concentration (2.34 g L^{-1}) was observed directly after stirring and even less (1.22 g L^{-1}) after 1 week. Similar concentration was determined for the samples using TMAOH as a bulky molecules. The aluminium compound impurities in the samples may act as the counterions of the negatively charged titanate nanosheets, dragging the titanate to the bottom of the bottle [174].
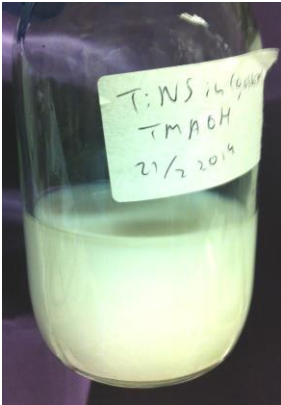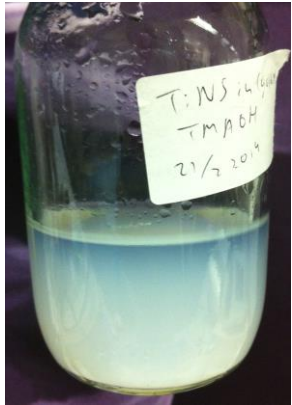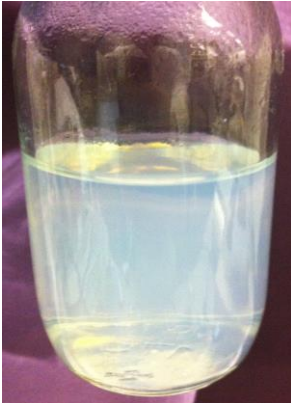
The effect of aluminium compound impurities was more observeable in titanate nanosheets made by potassium-lithium route. Table 4.1, sample 6, was shown three separate part of colloidal solution after the solution settled for 1 week. Whereas no titanate observed in the top part, the middle part has low concentration of titanate (0.46 g L^{-1}) and the bottom part has concentrated titanate (17.45 g L^{-1}). Contrary to the caesium route of titanate (≈100 nm lateral size), which the concentrated part was not observable in solution, smaller titanate (≈50 nm lateral size) made by potassium-lithium

route dragged slowly by aluminium compound impurities due to the less effect of gravity and less chance to interact with aluminium compounds.

Knowing the effect of gravity on the impurities, centrifugation was deployed to separate the impurities and the titanate nanosheets. After 12 hours of centrifugation at 3800 rpm, the stable colloidal solution of titanate nanosheets was achieved. However, the concentration was greatly reduced to 0.768 g L^{-1} and 0.5 g L^{-1} for TBAOH and TMAOH caesium route of titanate. The small remaining concentration indicated the strong interaction between aluminium compound and titanate nanosheets.

Table 4.1. Concentration and transparency of Sasaki's titanate nanosheets in solution.

No	Specimen	Concentration of nanosheets (g L^{-1})	Images of colloidal suspension of nanosheets	
			immediately after 2 weeks stirring	after 1 week sedimentation
1	Caesium route titanate in TBAOH (platinum crucible)	3.1		This solution is stable and visibly similar for more than 6 months after stirring
2	Caesium route titanate in TBAOH (aluminosilicate crucible)	as stir : 2.34 after 1 week: 1.22	as stir	after 1 week

No	Specimen	Concentration of nanosheets ($g\,L^{-1}$)	Images of colloidal suspension of nanosheets	
			immediately after 2 weeks stirring	after 1 week sedimentation
3	Caesium route titanate in TBAOH after 12 h centrifugation	0.768		this solution is stable for more than 16 months after stirring and centrifugation
4	Caesium route titanate in TMAOH (aluminosilicate crucible)	as stir : 2.01 after 1 week: 0.82	as stir	after 1 week
5	Caesium route titanate in TMAOH after 12 h centrifugation	0.50		this solution is stable for more than 16 months after stirring and centrifugation
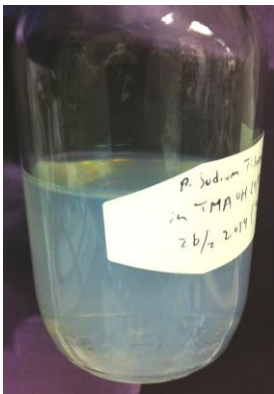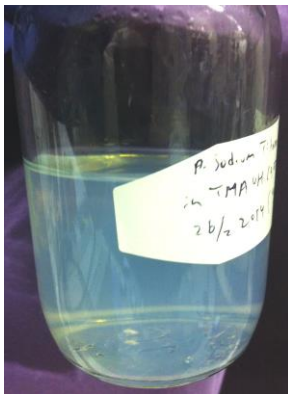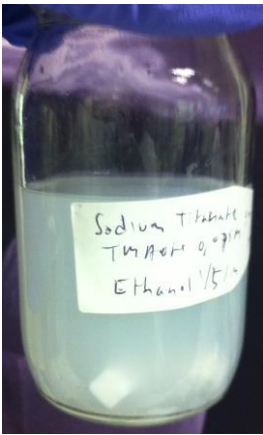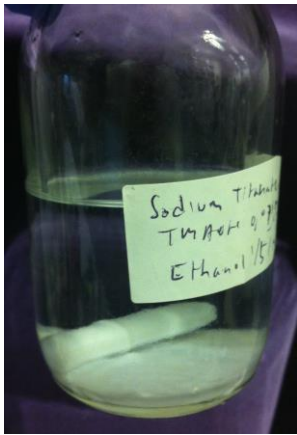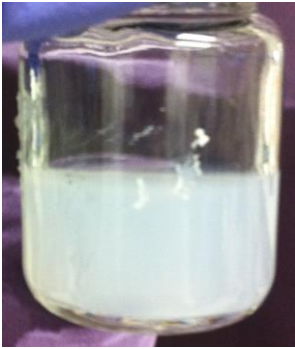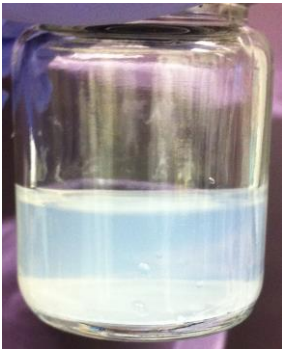
No	Specimen	Concentration of nanosheets (g L^{-1})	Images of colloidal suspension of nanosheets	
			immediately after 2 weeks stirring	after 1 week sedimentation
6	Potassium-lithium route titanate in TBAOH (aluminosilicate crucible)	as stir : 3.46 after 1 week top : 0 middle: 0.46 bottom : 17.45	 as stir	 after 1 week

4.6.2 The concentration and stability of the hydrothermal scrolled titanate nanosheets in several solvents

Choosing the right solvent is important to create stable colloidal suspension. Stable colloid will form if the colloidal particles have strong attraction with its solvent. This type of colloid is called lyophilic colloid or liquid loving colloid [174]. In Table 4.2, the scrolled titanate nanosheets (STiNS) was relatively stable in water while produced unstable colloidal suspension in ethanol. The titanate was completely settled down after 2 days leaving only the sediment in the sample. This may be caused by aggregation of titanate. Physical treatment such as sonication aided the dispersion of titanate improving stability in ethanol solution. However, sonication may shorten and broke the titanate nanostructures [175]. In dimethyl acetamide (DMAc), the scolled titanate nanosheets were even stable without bulky molecule exfoliating agent such as tetrabutylammonium hydroxide (TBAOH) or tetramethylammonium hydroxide (TMAOH). The hydroxyl groups of STiNS might interacted with DMAc by hydrogen bonding stabilising the STiNS in solvent. The concentration of titanate in DMAc was determined by taking 2 mL of the top solution, drying in air, and weighing the remaining solid.

Table 4.2. Concentration and transparency of scrolled titanate nanosheets in solution.

No	Specimen	Concentration of nanosheets (g L^{-1})	Images of colloidal suspension of nanosheets	
			immediately after 2 weeks stirring	after 1 week sedimentation
1	Scrolled titanate nanosheets (STiNS) in tetramethyl ammonium hydroxide (TMAOH)	as stir : 0.36 after 1 week : 0.488	 as stir	 after 1 week
2	Sodium route titanate in TMAOH with ethanol as a solvent	as stir : 0.072 after 2 days, there is no titanate on top	 as stir	 after 2 days

No	Specimen	Concentration of nanosheets (g L^{-1})	Images of colloidal suspension of nanosheets	
			immediately after 2 weeks stirring	after 1 week sedimentation
3	Sodium route titanate in TMAOH (1 d stirring + 1 h sonication) ethanolic solution	as stir : 0.2 after 1 week: 0.21	as sonicated	after 1 week
4	Sodium route titanate in DMAc	as stir: 0.24 after 2 days: 0.24 (characterised by gravimetric method)	` as stir	after 2 days

4.7   Conclusions

Titanate nanosheets had been synthesised successfully using "caesium", "potassium-lithium", hydrothermal and sol-gel route. Single layer nanosheets detected by SEM or TEM in caesium and potassium-lithium route titanate, and sol-gel titanate samples. Aluminium compound impurities spotted for aluminosilicate crucible samples due to reaction of alkali precursor with crucible, while for platinum crucible samples, the impurities did not observed. The impurities interacted with titanate nanosheets dragging

titanates to the bottom of solution, which can be separated by centrifugal force. This result showed that "caesium" titanate nanosheets could be produced using aluminosilicate crucible, although the final concentration was low (0.8 g L^{-1}) compared to the samples made by platinum crucible (3.1 g L^{-1}). The scrolled titanate nanosheets (STiNS), made by hydrothermal synthesis, were shown in TEM images and confirmed by SAXS. This sample also has some impurities which are unreacted material, non-homogeneous reaction may occur when the stirring stopped. The STiNS were stable in dimethyl acetamide (DMAc) without bulky molecules such as TBAOH or TMAOH, due to hydrogen bonding between hydroxyl group of titanate and DMAc. Sol-gel method produces diamond shape nanosheets similar with the literature. Nevertheless, there were some impurities, such as slab like structure which occurs maybe due to the reactants not mixing perfectly well.

Knowledge of the morphology and concentration of titanate nanosheets were used for composite fabrication, which is one of the aim of this thesis. Large nanosheets is more preferable since it have higher aspect ratio than small nanosheets providing more contacts with the polymer. The study of titanate stability in organic solvent such as DMAc was also usefull for *in-situ* or *ex-situ* synthesis of polymer composites, since the organic solvent was used in the polymerisation process of polyimide.

Chapter 5:   The Incorporation of Titanate Nanostructures in Water-Soluble Polyimide Precursor

5.1   Introduction

Polymer nanocomposite materials consist of a hybrid organic matrix containing dispersed nanostructure filler. The structures are widely varied from zero (sphere, cubes, and polyhedrons), one (rods, fibres, tubes), two (sheets, discs, plates) dimensional, and complex shapes (flower, leaf, etc.). These nanofillers provide significant improvement in the polymer properties at low filler loadings due to the large degree of contact between nanofiller and polymer. For example, the small addition of exfoliated clay (4.7 wt%) can increase the flexural modulus of nylon-6 by four times at 120 °C [176]. Successful application of clay filler to improve the mechanical properties of polymers requires further research on other nanostructure based polymer nanocomposites containing, e.g., metal oxides, hydroxides, nitrides, and chalcogenides. In the past decades, the synthesis method, chemical, and physical properties of titanium oxide with various structures (e.g., nanotubes and nanosheets) has been studied. Titanium oxide single layer nanosheets (TiNS), the graphene analogue, have been discovered by Sasaki, *et.al.* [33] towards 1998. These nanosheets can be obtained by a three-step process involving solid-state reaction, acid ion-exchange, and exfoliation [33]. The resulting product is a highly crystalline single layer sheet possessing unique properties which differ from bulk titanium oxide. This type of nanosheets has been applied in various functional nanocomposite polymers [177]. However, there is no systematic study on the mechanical reinforcement effects of titanate nanosheets on polymer nanocomposite.

In contrast to titanate nanosheets, titanate nanotubes (TiNT) only require a one-step alkaline hydrothermal treatment. Incorporation of elongated titanates into the polymers can improve the transport properties in nanofiltration membranes [178], gas sorption capacity [167], corrosion resistance [179], and thermal properties [146]. Instead of nanotubes, the alkaline hydrothermal method can also produce nanosheets with scrolled

morphology at lower processing temperatures [24]. The study of these scrolled nanosheets (STiNS) is still very limited. Titanate nanotubes and scrolled nanosheets due to the simplicity of their manufacturing and abundance of the precursors, can be useful low cost alternative to carbon nanostructures such as graphene and carbon nanotubes for certain applications (e.g., structural, thermal protection, gas and UV barrier).

In this work, titanate nanotubes (TiNT), scrolled titanate nanosheets (STiNS), and titanate nanosheets (TiNS) have been used as filler of the water soluble pyromelitic dianhydride-oxydianiline (PMDA-ODA) polyimide precursor (polyamic acid salt), which is made from the most common monomers of polyimide, PMDA and ODA. The effect of the incorporation of titanate nanostructures on mechanical and dielectric properties of polymer was evaluated. Nanoindentation has been used to study the reduced modulus (E_r) and hardness (H) of the composites. Experimental results are compared with theoretical models, such as those due to the modified rule of mixtures [132], Halpin-Tsai [180], and Halpin-Kardos [137], to study and evaluate the existing models. The dispersion of titanate nanosheets and nanotubes in polymer was studied by TEM to determine its correlation with mechanical properties and compared to that of the titanate nanostructures-polymer composite. Small-angle X-ray scattering (SAXS) was used to determine the interlayer spacing of nanosheets inside the polymer, to confirm incorporation of nanotubes within the polymer and investigate the degree and alignment of nanostructures.

5.2   Synthesis of water-soluble PMDA-ODA/titanate nanocomposites

Scrolled titanate nanosheets (STiNS), titanate nanosheets (TiNS) (from Chapter 4.2 and 4.4) and titanate nanotubes (TiNT) have been used to enhance the mechanical properties of water soluble polyimide precursors, namely, polyamic acid salt (PAAS). Titanate nanotubes, scrolled nanosheets, and nanosheets possess negative surface charges making them easily dispersed and stabilised in aqueous solvent, hence the choice of water-soluble polymers. The polyamic acid salt is a more stable form of polyamic acid which is the polyimide precursor [181]. Water-soluble polyamic acid salt was made by capping the carboxylic acid groups of polyamic acid (PAA) with triethylammonium

ions of triethylamine (TEA) which can be seen in Figure 5.1. To achieve high degree of salt formation, the mol ratio of trimethylamine and polyamic acid should be 2 to 1, where each mole of triethylamine capped two carboxylic acid groups in one mole of polyamic acid [182]. In water, polyamic acid ammonium salt was easily dissociates into carboxylate anions (R-COO$^-$) and triethylammonium cations (TEA$^+$).
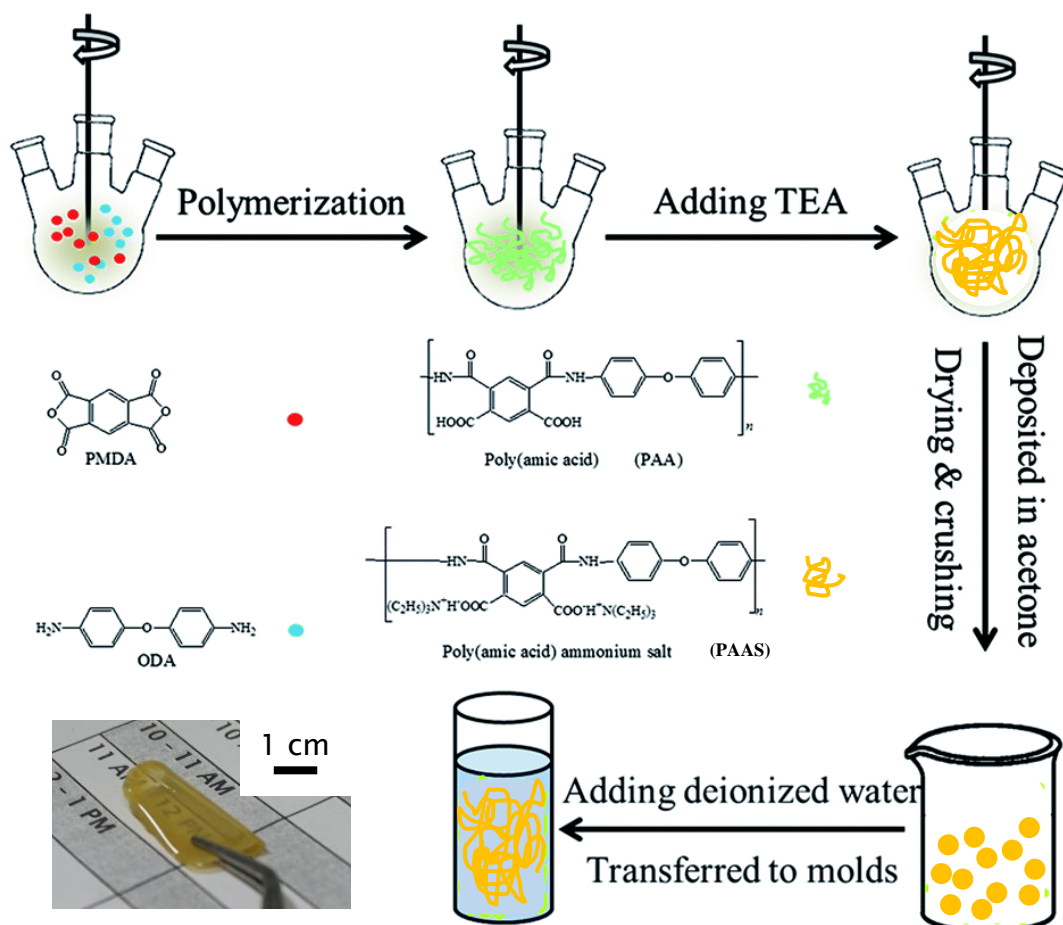
Figure 5.1. Illustration of the synthesis of polyamic acid salt film [183] and its photograph. Red and blue dots represent PMDA and ODA. Green and orange lines represent PAA and PAAS.

The water soluble PMDA-ODA polyamic acid salt is more flexible than non-water soluble PMDA-ODA polyimide (Kapton) while retaining its transparency and easily mouldable into flat film using drop casting method on glass slide. After thermal imidization at 150 °C for 1 hour in N_2 atmosphere, the polymer lost its flexibility and transparency. It was even more brittle than PMDA-ODA polyimide which made from

non-water soluble precursor. This might be due to void formation from volatilization of
ammonium compounds [182]. Therefore, the polymer nanocomposites were made from
water-soluble polyamic acid salt. Schematic representation of the incorporation of
nanostructures into polyamic acid salt is shown in Figure 5.2.
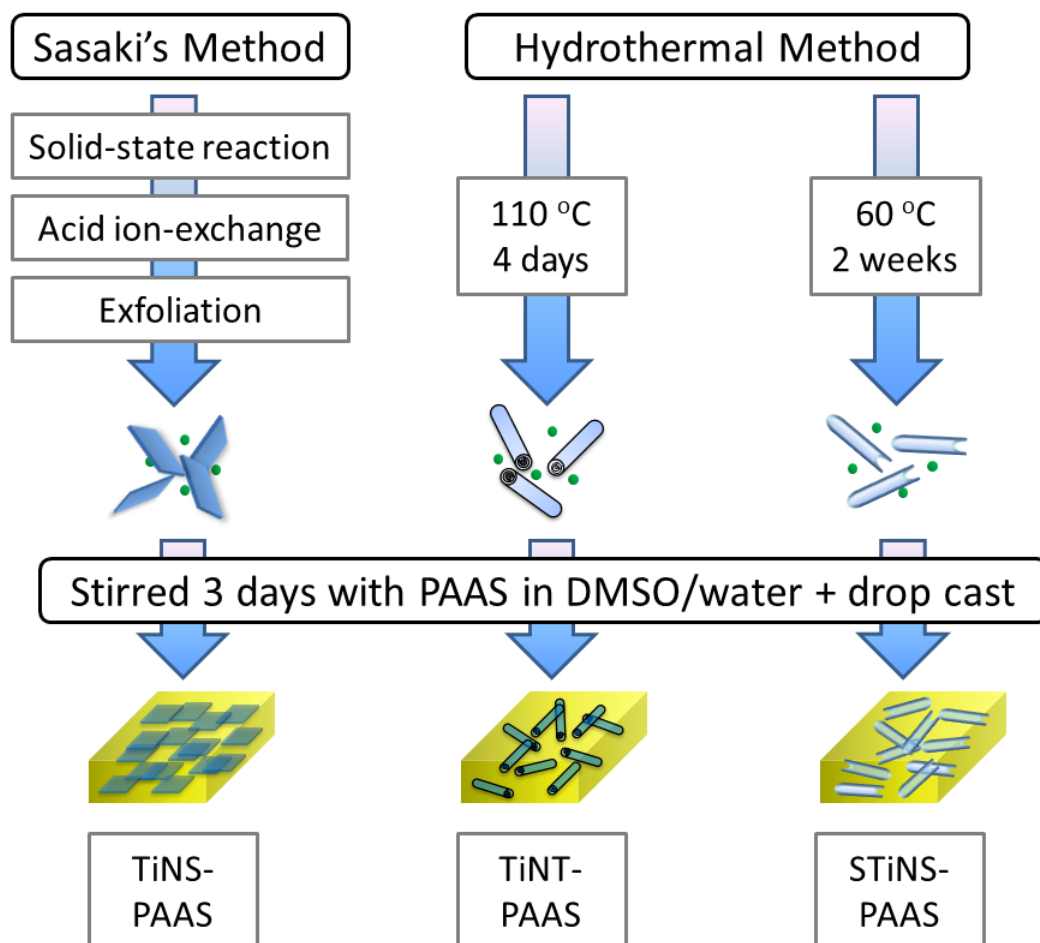
Figure 5.2. Schematic representation for the synthesis of titanate nanosheets (TiNS), titanate
nanotubes (TiNT), scrolled titanate nanosheets (STINS) and their composites with polyamic
acid salt (PAAS).

5.3   Effect of settling time (aging) of nanocomposites solution on its mechanical properties

The aging time of mixed aqueous solution of PAAS with nanostructured titanate may
affects the mechanical properties of final composite. The samples with longer settling

time can have inferior mechanical properties (e.g., modulus and tensile strength). During aging, the coagulation of nanostructures into large agglomerates occurs. In the case of carbon nanotubes, agglomeration may appear in the liquid epoxy resin during curing, even at a low filler content (0.05 wt%) [184]. In this work, the settling time to synthesise nanocomposites was varied. After stirring the composite mixture for 3 days, samples were either used immediately or settled for one week. Agglomeration occurred on the sample after one week settling time (Figure 5.3).
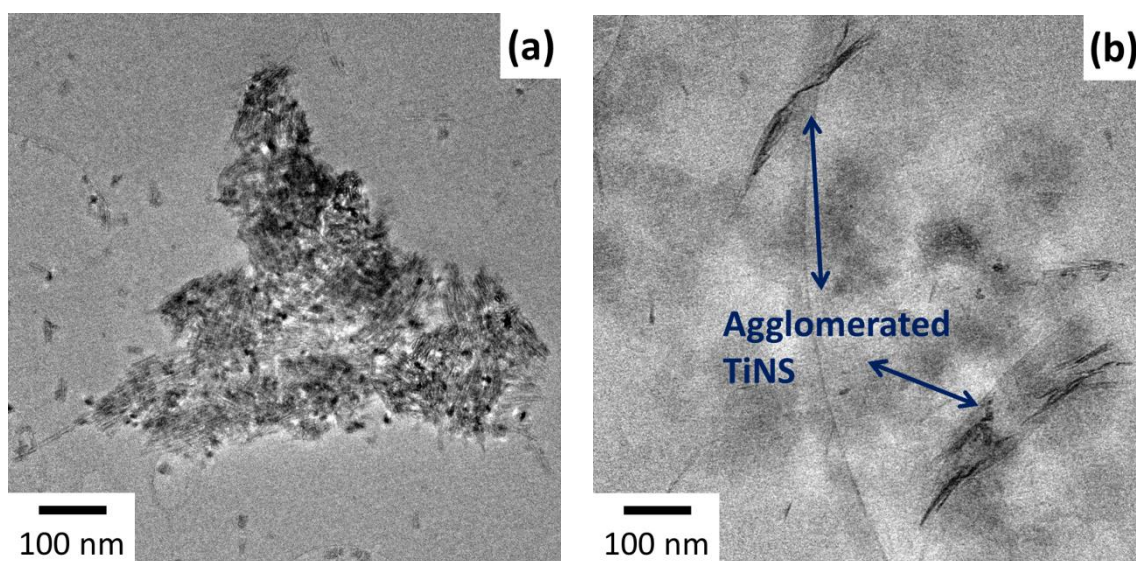
Figure 5.3. TEM images showing agglomeration of 1 wt% of (a) titanate nanotubes; (b) titanate nanosheets within the polyamic acid salt after settled for one week.

This agglomeration resulted in 27.35 % reduction of the modulus from 3.51 ± 0.20 GPa to 2.55 ± 0.12 GPa for TiNT samples with and without and with agglomerates respectively. For scrolled titanate nanosheets (STiNS) samples it reduced by 27.91 % from 3.26 ± 0.17 GPa to 2.35 ± 0.14 GPa. While for TiNS samples the modulus decreases by 22.83% from 4.03 ± 0.13 GPa to 3.11 ± 0.43 GPa. Thermodynamically, such a colloidal suspension is unstable since nanostructures (TiNS, TiNT, STiNS) [167,185] and polymer both have a negative surface charge [186]. However, the kinetic stability of the suspension allows a good dispersion of nanostructures within the polymer matrix, if a short aging time is used. This agglomeration also occurs when the filler concentration (e.g., TiNS, TiNT, STiNS) is more than 2 wt%, probably due to stronger van der Waals interaction in densely packed nanostructures.

5.4 Effect of titanate nanostructures on mechanical properties of water-soluble polymers

5.4.1 Theoretical predictions

In order to study the reinforcement behaviour of fillers in nanocomposites, comparison of experimental results with existing theoretical prediction is necessary. The theoretical models used in this particular research are models able to predict mechanical properties of composites containing matrix and filler as reinforcements with the basic assumptions of a void free matrix and no residual stress in composites (stress-free state). Some nanofiller such as titanate nanosheets have anisotropic mechanical properties [138]. Theoretical predictions might give an insight on filler orientation. Modified rule of mixtures, Halpin-Tsai, and Halpin-Kardos were chosen for this purpose.

The rule of mixtures or iso-strain model is a well-known model that is used to predict continuous unidirectional fibre composites. This model assumes the filler and matrix have the same elongation when a certain load is applied to the composite. However, it is not suitable for evaluating mechanical properties of some composites as it often overestimates the properties [130,131]. Hence, the modified rule of mixtures, which is a semi-empirical model, is applied [132]. The modified rule of mixtures considers the particle strengthening factor which is useful to compare different shape of filler.

The Halpin-Tsai equation is a model to estimate reinforcement of unidirectional oriented short fibres [133]. Halpin-Tsai model can also be adapted to predict the modulus of polymer nanocomposites with nanosheets (e.g., clay [134] and graphene [135]) as filler. The Halpin-Kardos equation was applied to randomly oriented short fibres with a quasi-isotropic laminate assumption involving the $[0/+45/90/-45]_n$ configuration [137]. Halpin-Kardos model can also be adapted for nanosheets (e.g., clay) up to 2 wt% in a polymer blend [134]. The authors argued that the tactoid phase of clay may act in a similar fashion to short fibres. The experimental results can be matched with Halpin-Tsai and Halpin-Kardos prediction to determine the orientation of filler within matrix.

The illustration of modified rule of mixture, Halpin-Tsai, and Halpin-Kardos model is given in Figure 5.4.
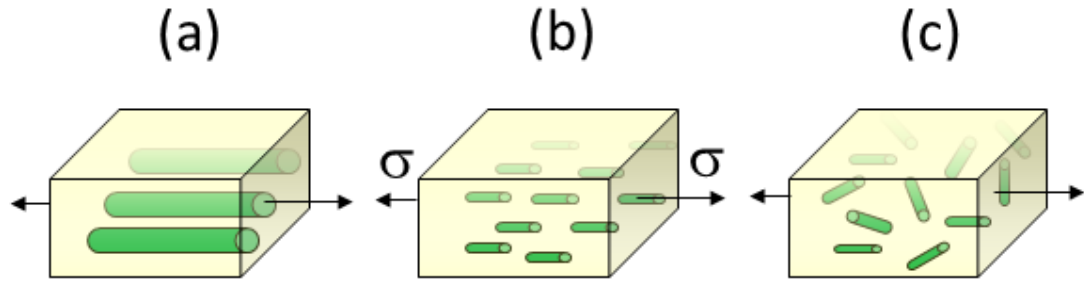
Figure 5.4. The schematic representation of (a) modified rule of mixture (continuous and unidirectional filler); (b) Halpin-Tsai model (short and unidirectional filler); (c) Halpin-Kardos model (short and random orientation filler). Arrows indicates stress (σ) direction.

The modified rule of mixtures is:

$$E_c = \chi_f E_f V_f + E_m (1 - V_m) \tag{5.1}$$

where E_c, E_f, and E_m are the moduli of composite, filler, and matrix, respectively. χ_f is a particle strengthening factor with values between 0 and 1. V_f and V_m are the volume fractions of filler and matrix obtained by converting the weight filler fractions, assuming the densities of TiO$_2$ (4.23 g cm^{-3}) and polyamic acid (1.04 g cm^{-3}). This equation can also be applied to estimate the hardness of the composite by substituting the modulus to hardness. The modulus and hardness of the filler is taken from CRC Materials Science and Engineering Handbook [187], which are 282.76 GPa and 10.99 GPa, respectively, considering TiNS, STiNS, and TiNT structures as TiO$_2$. The Young's modulus and hardness of the matrix are adapted from nanoindentation of the polyamic acid salt.

The Oliver-Pharr method [188] has been used to calculate Young's modulus from reduced modulus which obtained by nanoindentation

$$\frac{1}{E_r} = \frac{(1 - v_s^2)}{E_s} + \frac{(1 - v_i^2)}{E_i} \tag{5.2}$$

where E_r and E_s are respectively reduced modulus (obtained from nanoindentation) and Young's modulus of specimens. E_i is Young's modulus of indenter (for diamond tip 1140 GPa [125]). v_s and v_i are Poisson's ratio of specimen and indenter (for diamond tip 0.07 [125]), respectively.

Poisson's ratio of polymer nanocomposite can be obtained by the following formula [189]

$$\frac{1}{v_s} = \frac{\phi_f}{v_f} + \frac{1-\phi_f}{v_m} \tag{5.3}$$

where v_s, v_f, and v_m are Poisson's ratio of specimen, filler (for TiO_2 0.28 [187]), and polymer matrix (for polyamic acid 0.42 [86]), respectively. Φ_f is volume fraction of filler.

The Halpin-Tsai equation is:

$$\frac{E_c}{E_m} = \frac{1+2A_f\mu\phi_f}{1-\mu\phi_f} \tag{5.4}$$

where E_c and E_m are the moduli of the composite and matrix (PAAS), respectively. The Young's modulus of the matrix (PAAS) is adapted from nanoindentation measurements of pure PAAS. A_f is the filler aspect ratio (l/h), in this case (l) is the nanosheets (≈ 100 nm for TiNS) or nanotubes length (≈ 100 nm for TiNT; ≈ 75 nm for STiNS) and (h) is the nanosheets thickness (0.75 nm for TiNS) or nanotubes diameter (≈ 25 nm for TiNT; ≈ 10 nm for STiNS). Φ_f is the volume fraction of filler. μ is a geometric factor, given by:

$$\mu = \frac{(E_f/E_m)-1}{(E_f/E_m)+2A_f} \tag{5.5}$$

where E_f is the modulus of TiO_2 taken from literature [187]. The Halpin-Tsai equation is also able to predict the hardness of micro and nanocomposites by simply exchanging the modulus with hardness [136]. The hardness of the matrix (H_m) is determined by nanoindentation of pure PAAS while the hardness of TiO_2 (10.99 GPa) is taken from the literature [187].

The Halpin-Kardos equation is:

$$\frac{E_c}{E_m} = \frac{3}{8}\left[\frac{1+2A_f\eta_L\phi_f}{1-\eta_L\phi_f}\right] + \frac{5}{8}\left[\frac{1+2\eta_T\phi_f}{1-\eta_T\phi_f}\right] \tag{5.6}$$

where E_c and E_m are the moduli of the composite and matrix respectively. A_f is the
aspect ratio of the filler (l/h) where l is the nanosheets or nanotubes length and h is the
nanosheets thickness or nanotubes diameter. Φ_f is the filler volume fraction. η_L and η_T
can be determined from the following equations:

$$\eta_L = \frac{(E_f/E_m)-1}{(E_f/E_m)+2A_f} \tag{5.7}$$

$$\eta_T = \frac{(E_f/E_m)-1}{(E_f/E_m)+2} \tag{5.8}$$

where E_f is the modulus of TiO_2 [187]. To obtain the hardness, this equation was modified
by substituting the modulus for hardness.

5.4.2 Effect of titanate nanosheets (TiNS) on mechanical properties of water-soluble polymers

Here, we used titanate nanosheets (TiNS) as filler of polymer nanocomposites using
solution processing synthesis methods. Figure 5.5 a and 5.5 b shows experimental data
and theoretical predictions of the hardness and modulus of titanate nanosheets-polyamic
acid salt nanocomposites with different concentrations of TiNS (0, 0.5, 1, 2, 3, 5 wt%).

The addition of titanate nanosheets significantly enhanced the hardness and modulus of
the water-soluble polyamic acid salt. The hardness increased by 90% to 0.34 ± 0.02 GPa
with addition of 2% TiNS, while the modulus increased by 103% to 4.32 ± 0.17 GPa
compared to the pure polymer. The improvement in hardness matched the Halpin-Tsai
theory up to 2 wt% while, for the modulus, it followed up to 1 wt%. It also followed the
modified rule of mixtures with a 0.8 particle strengthening factor for hardness, which is
a factor determined empirically, up to 2 wt%. For the modulus, it corresponded up to 1
wt% to a 0.6 particle strengthening factor of modified rule of mixtures.

The reinforcement of PAAS by TiNS was comparable to the reinforcement of graphene oxide in polyvinyl alcohol (PVA) made by *in-situ* polymerisation [190]. The modulus and hardness in their work were shown much closer fit to Halpin-Tsai theory, which assume the filler aligned unidirectionaly parallel to the surface. However, the reinforcement of PVA was reached its plateau at 0.08 wt% of graphene oxide while in this work the modulus reinforcement started to decrease at 2 wt% of TiNS.
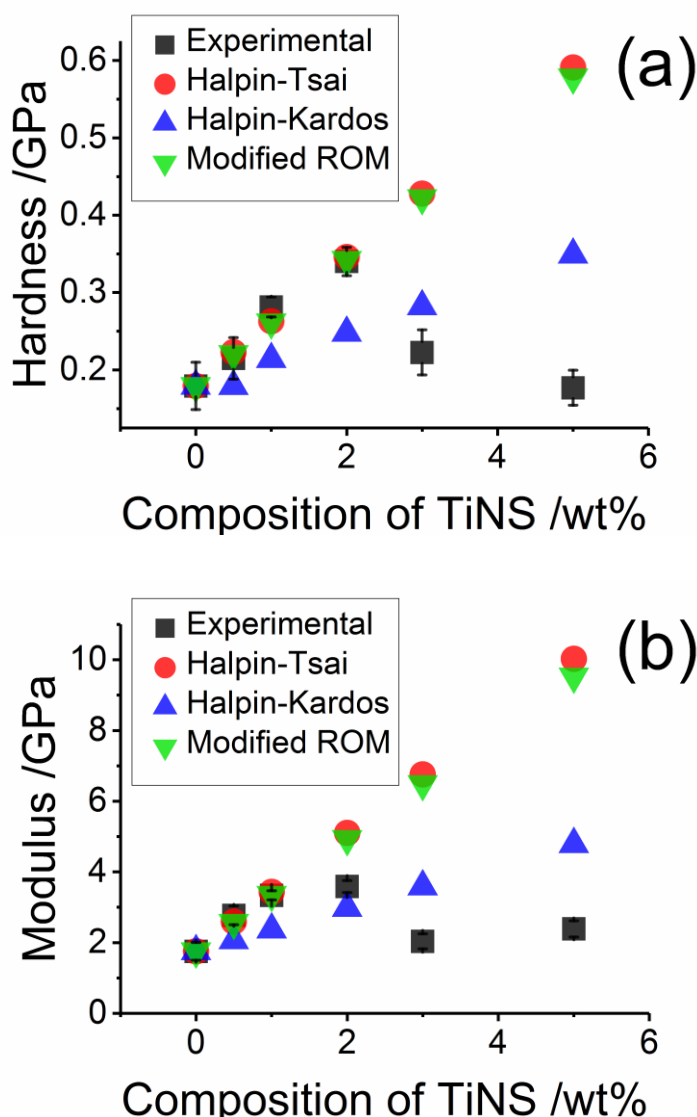
Figure 5.5. Nanoindentation data of titanate nanosheets-polyamic acid salt (TiNS-PAAS) nanocomposites compared to Halpin-Tsai, Halpin-Kardos, modified rule of mixture (ROM) theories; (a) hardness; (b) modulus.

Beyond the critical concentration (2 wt%), experimental results are not correlated with predictions. This might happen because at low filler concentrations the nanosheets are

fully exfoliated (Figure 5.6 a) maintaining the same aspect ratio and polymer-filler interactions. At higher filler loading, 'skewed' platelets or tactoid phases are created (Figure 5.6 b). Severe agglomerations may act as stress concentration sites [134]. (010) and (020) peaks shift to the left in small-angle and wide-angle X-ray scattering (SAXS and WAXS) patterns of TiNS sample and 5 wt% TiNS-PAAS (Figure 5.6 c). This shows that the interlayer distance of nanosheets is increased from 7.22 Å to 9.09 Å due to intercalation of the polymer. The disappearance of peaks at low concentration of TiNS (0.5 wt%) may be caused by exfoliation of TiNS within the polyamic acid.
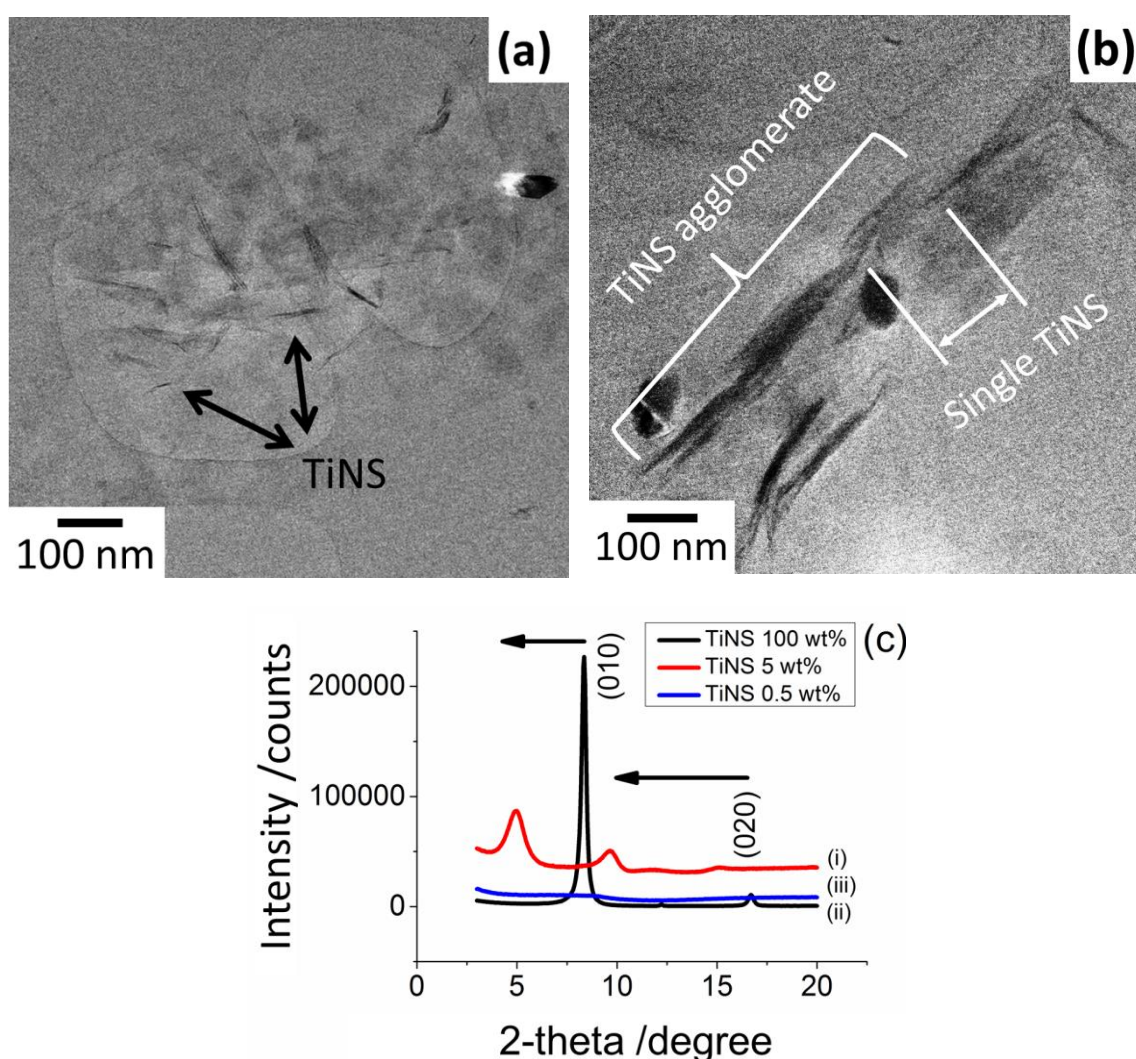
Figure 5.6. TEM images showing TiNS in PAAS; (a) exfoliated (1 wt% of TiNS); (b) agglomerated titanate nanosheets (3 wt% of TiNS); (c) combined SAXS and WAXS profile of (i) TiNS only, (ii) polymer intercalated TiNS at 5 wt% of TiNS (peaks shifted to the left), (iii) exfoliated TiNS at 0.5 wt% of TiNS (no peaks detected).

The number of stacked nanosheets and the correlation with the mechanical properties may also be predicted using the Brune-Bicerano model [191]. This model assumes the nanosheets are stacked in parallel and all platelets which contain the same number of stacks are dispersed unidirectionally within the polymer. The equation is as follows:

$$\frac{E_c}{E_m} = \frac{1 + 2A'_f \eta' \phi'}{1 - \eta' \phi'} \tag{5.9}$$

$$\eta' = \frac{E'_f - 1}{E'_f + 2A'_f} \tag{5.10}$$

$$A'_f = \frac{A_f}{N'} \left(\frac{1}{1 + (1 - 1/N') \frac{s}{t}} \right) \tag{5.11}$$

$$\phi' = \phi \left(1 + (1 - 1/N') \frac{s}{t} \right) \tag{5.12}$$

$$E'_f = E_f \left(\frac{1}{1 + (1 - 1/N') \frac{s}{t}} \right) + \frac{(1 - 1/N') \frac{s}{t}}{1 + (1 - 1/N') \frac{s}{t}} \tag{5.13}$$

$$N' = N + (1 - 1/N) \frac{s}{t} \left(\frac{\phi}{1 - \phi} \right) \tag{5.14}$$

where E_c, E_m, and E_f are moduli of the composite, the matrix and TiO_2 (taken from literature [187]) respectively. A_f is the aspect ratio of the filler (l/h) where l is the nanosheets length and h is the nanosheets thickness. Φ is the filler volume fraction and N is number of stacks. s/t is the ratio of spacing between nanosheets to thickness of a single nanosheet. The spacing is determined by SAXS measurements (9.09 Å, Figure 5c) and the geometry of the nanosheets (e.g., length and thickness) is evaluated by TEM (Figure 5a). Hardness is predicted by substituting the modulus with hardness.

Figure 5.7 shows the experimental and theoretical predictions of the modulus and hardness of nanocomposites for incomplete exfoliation. The modulus and hardness of nanocomposites fit the Brune-Bicerano model for 3 stacks at 2 wt% of TiNS. A 3 stack aggregate of nanosheets may impede the modulus and hardness improvement at 2 wt%

of TiNS. The Halpin-Tsai and Halpin-Kardos models cannot accurately predict the mechanical properties when there is incomplete exfoliation (Figure 5.5 a and 5.5 b). The Brune-Bicerano prediction is not accurate at relatively high filler content having a higher number of stacks. This model suggests that at 3 wt% and 5 wt% of TiNS, 50 stacks of TiNS may occur as fitted in the model, while TEM images in Figure 5.7 b show that the agglomerates have fewer than 50 stacks. At high content, the nanosheets agglomerate not only in parallel but also horizontally creating 'skewed' structures which are observed by TEM (Figure 5.6 b). This model should be evaluated taking into account the horizontal stacks.
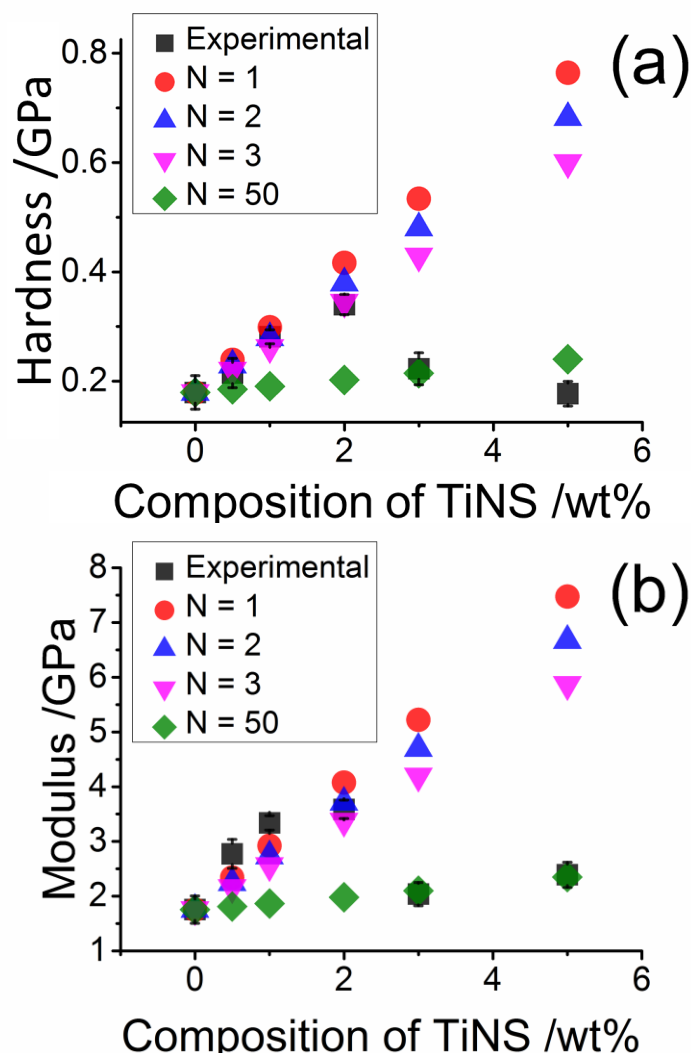
Figure 5.7. Comparison of nanoindentation data of titanate nanosheets-polyamic acid salt (TiNS-PAAS) with Brune-Bicerano model with various numbers of stacks (N); (a) hardness; (b) modulus.
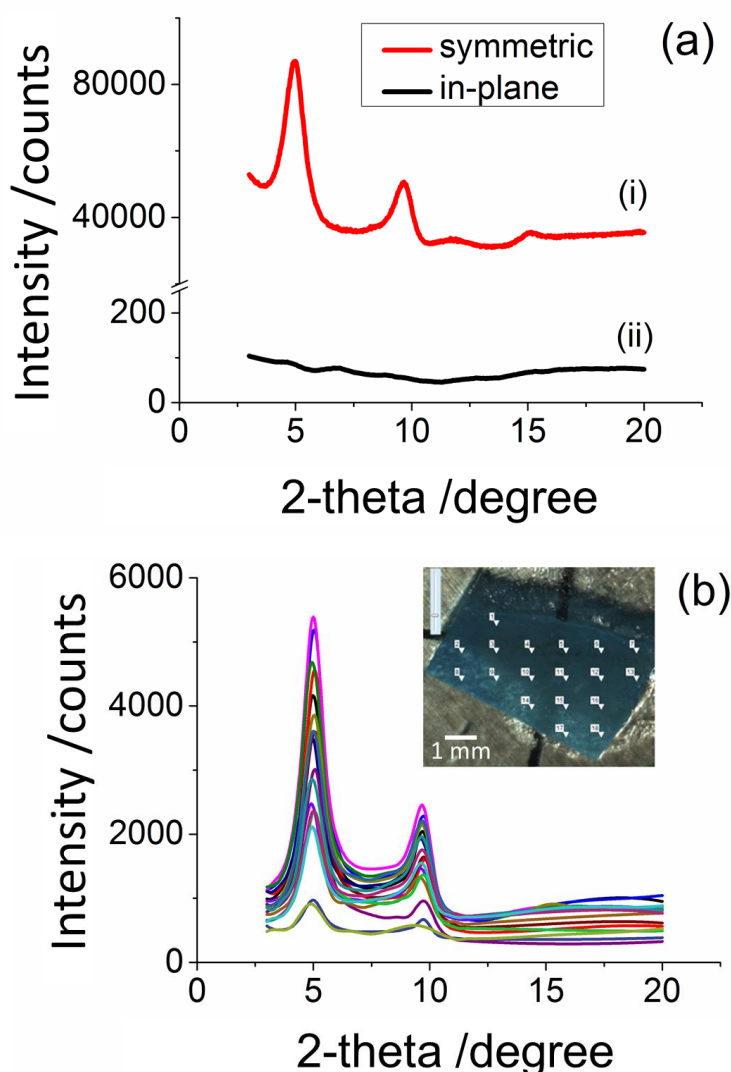
Figure 5.8. Combined SAXS and WAXS profile proving orientation of titanate nanosheets (TiNS) within polymer (a) TiNS peaks detected by symmetric scan (red, i) while it disappeared in in-plane scan (black, ii); (b) SAXS profile data of 18 samples symmetric scan with 1 mm apart (shown in inset) was provided, slight variation of peaks and intensity occur due to the sample was not perfectly flat.

In Figure 5.8, small-angle (SAXS) and wide-angle X-ray scattering (WAXS) shows that the (010) and (020) basal spacing of titanate nanosheets [56], which is 9.09 Å (d_{010}) and 17.88 Å (d_{020}), are not observed in the in-plane direction to the sample surface (in-plane scan) while in parallel direction (symmetric scan) these peaks are detected (Figure 5.8 a). A homogeneous preferred orientation is also observed in the nanocomposite film

proven by mapping across 18 spots on the sample (Figure 5.8 b). This proves that the titanate nanosheets were homogeneously aligned parallel to the surface inside the polymer (perpendicular to the indentation loading). This correlates with the Halpin-Tsai theory which assumes that the filler is unidirectional. This orientation is beneficial since titanate nanosheets have anisotropic reinforcement which is highest when the loading is perpendicular to the nanosheets [138]. In the case of clay, shearing (e.g., doctor blade) is required to induce preferred orientation of the clay within the polymer matrix [192]. For titanate nanosheets, simple drop casting produces oriented nanosheets within the polymer.

5.4.3 Effect of titanate nanotubes (TiNT) and scrolled titanate nanosheets (STiNS) on mechanical properties of water-soluble polymers

The hardness and modulus of the polyamic acid salt increased 91 % and 165 % by incorporation of 2 wt% titanate nanotubes respectively. This improvement was reduced and became stagnant after 2 wt% loading of titanate nanotubes. At 3 and 5 wt% TiNT, the improvement for the modulus was 104% and 108% respectively. This reinforcement tendency is similar to that in previously reported studies [193] also using ultrasonication to disperse the nanotubes. Shorter nanotubes are formed due to sonication leading to reduction of their mechanical properties [194]. It may also accelerate the dispersion of the nanotubes [195] and hence the mechanical properties of TiNT-PAAS nanocomposites were increased. However, aggregation of nanotubes may happen at high concentrations reducing the reinforcement effect of nanotubes. Figure 5.9 a and b show experimental data and theoretical predictions of hardness and modulus of the titanate nanotubes-polyamic acid salt (TiNT-PAAS) nanocomposites with different concentrations of TiNS (0, 0.5, 1, 2, 3, 5 wt%).
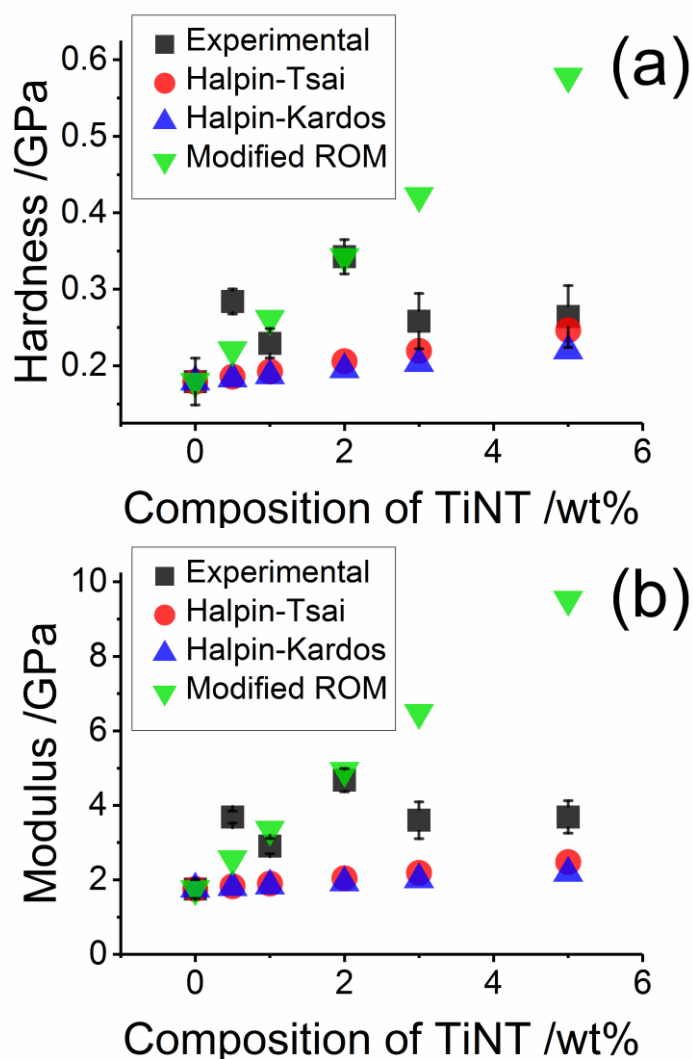
Figure 5.9. Nanoindentation data of titanate nanotubes-polyamic acid salt (TiNT-PAAS) nanocomposites compared to Halpin-Tsai, Halpin-Kardos, modified rule of mixture (ROM) theories; (a) hardness; (b) modulus.

There was no difference in SAXS profile when the film was measured in either out-of-plane or in-plane directions (Figure 5.10). This proves that titanate nanotubes were dispersed randomly with no preferred orientation.
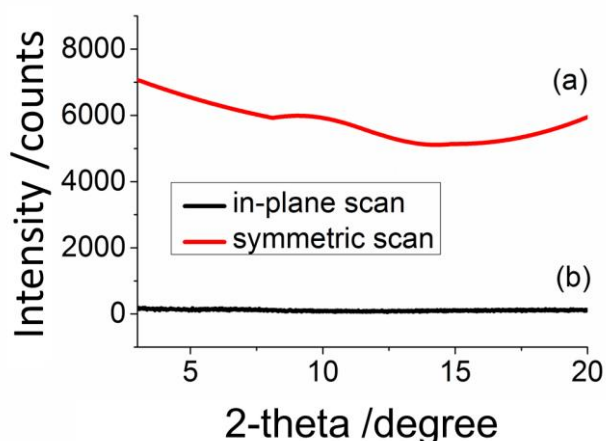
Figure 5.10. Combined SAXS and WAXS measurement for 5 wt% titanate nanotubes within polymer by (a) symmetric scan (red); (b) in-plane scan (black). Neither shows any significant peaks due to alignment. In-plane scans are always of much lower intensity.

At low TiNT content (<3 wt%), the experimental data correspond to the modified rule of mixtures with a 0.8 particle strengthening factor for hardness and 0.6 for the modulus. Halpin-Tsai and Halpin-Kardos predictions, using TiO_2 filler properties, underestimated the mechanical properties of nanocomposites which may indicate that hydrothermal titanate nanotubes structure, which is akin to $H_2Ti_3O_7$ [196,197], is stronger than bulk TiO_2. Currently, studies on the mechanical properties of titanate nanotubes mainly focus on anodized titanate nanotubes [198,199] which are single nanotubes with moduli ranging from 2.2 to 9.4 GPa. This number is much lower than the modulus of TiO_2 (282.76 GPa). Therefore, comprehensive studies on the mechanical properties of hydrothermally synthesised titanate nanotubes are needed in the future.

Figure 5.11 a and b give the nanoindentation results and predictions of scrolled titanate nanosheets-polyamic acid salt (STiNS-PAAS) nanocomposites with controlled concentrations of STiNS (0, 0.5, 1, 2, 3, 5 wt%).
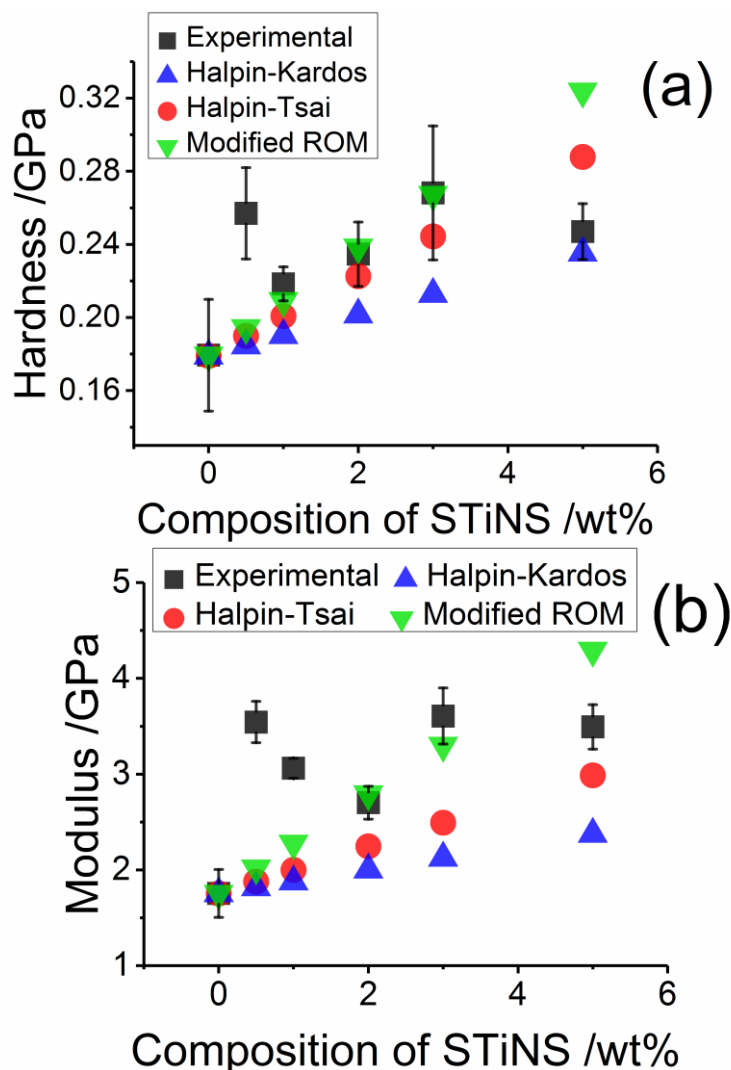
Figure 5.11. Nanoindentation data of scrolled titanate nanosheets-polyamic acid salt (STiNS-PAAS) nanocomposites compared to Halpin-Tsai, Halpin-Kardos, modified rule of mixture (ROM) theories; (a) hardness; (b) modulus.

Although STiNS and TiNT have the same structures (Chapter 4.4, Figure 4.6), their reinforcement behaviour is different. The mechanical improvement of nanocomposites skewed until it reached 3 wt%. The modulus improved by 104 % and 97 % for 3 and 5 wt% of STiNS respectively. This skewed improvement is probably caused by the less defined structured of STiNS which is an intermediate structure between sheet and tube. The experimental results were also higher than Halpin-Tsai and Halpin-Kardos

predictions, which using TiO_2 as filler properties, proving that hydrothermal titanate has higher mechanical properties than TiO_2. It followed the modified rule of mixtures with a 0.3 particle strengthening factor for the hardness and 0.2 for the modulus. Higher reinforcement behaviour of nanostructures (TiNS, TiNT, and STiNS) reflected in higher number of the hardness particle strengthening factors which are 0.8, 0.8, 0.3 for TiNS, TiNT, and STiNS respectively. The high reinforcement ability of TiNS may be due to preferred orientation of nanosheets within matrix thus optimizing the reinforcement. Unlike TiNS, hydrothermal TiNT and STiNS have random orientation. Their reinforcement may be caused by high mechanical properties of hydrothermally synthesised titanate nanostructures. However, scrolled titanate nanosheets (STiNS) may also have anisotropic mechanical properties like TiNS [138], that significantly lowering the mechanical properties of STiNS-PAAS nanocomposite, which has random orientation instead of arranged unidirectionally.

5.5   Conclusions

Titanate nanosheets, titanate nanotubes, and scrolled titanate nanosheets are used in this work to improve the mechanical properties of the polyamic acid salt. Settling time in nanocomposite processing is also studied and shorter settling time is preferable to avoid agglomeration. Addition of titanate nanosheets to water soluble polyamic acid significantly enhances the hardness and modulus of the polymer. The hardness increases by 90 % on addition of 2 wt% TiNS while the modulus increases by 103 % compared to the pure polymer. This proves that triethylamine (TEA) can be used as a bulky molecule instead of tetrabutyl ammonium hydroxide (common chemical for titanate nanosheets exfoliation) to exfoliate titanate nanosheets. A high aspect ratio (l/h = 133.33) and uniform distribution of titanate nanosheets provides significant reinforcement of polymer. Dispersed nanosheets aligned within the polymer matrix (parallel to the surface) were observed by SAXS. This reinforcement behaviour matches well with Halpin-Tsai theory [180] at low filler content (up to 1 wt%) assuming the filler has a unidirectional orientation. At 2 wt% of TiNS it followed the Brune-Bicerano model with 3 stacks of nanosheets agglomerates. At high filler loadings (>2 wt%), the mechanical properties of the composites did not fit established theories due to 'skewed' agglomeration of the titanate nanosheets. These sheets are stacked on each other,

creating several layers of elongated agglomerates. This causes poor distribution of nanosheets and might disturb the stress distribution between nanosheets and the polymer. This elongated agglomerate suggests improvement of the Brune-Bicerano model [191] which only considers sheets stacking in a parallel direction.

Although titanate nanotubes have a lower aspect ratio ($l/h = 4$) and random orientation, titanate nanotubes have a higher reinforcement ability. The hardness and modulus of the polyamic acid salt increased 91 % and 165 % by addition of 2 wt% titanate nanotubes respectively. This indicates that titanate nanotubes made by hydrothermal synthesis may have higher mechanical properties than bulk TiO_2. However, the mechanical properties of nanocomposites reached a plateau after 2 wt% of TiNT due to aggregation of TiNT. Higher reinforcement effectiveness of the nanostructures can be represented by higher value of the hardness particle strengthening factors of the nanostructures (TiNS, TiNT, and STiNS), which are 0.8, 0.8, 0.3 for TiNS, TiNT, and STiNS respectively. Whereas having different structure, it is possible that the hydrothermally synthesised scrolled titanate nanosheets (STiNS) have anisotropic mechanical properties such as titanate nanosheets (TiNS) made by exfoliation of solid state reaction [138], lowering the reinforcement ability on the polymer matrix when dispersed randomly within the matrix.

Chapter 6:   Synthesis and Characterisation of Polyimide/Titanate Nanocomposite Films and Fibres

6.1   Introduction

Polyimide is a high performance polymer having excellent heat and chemical resistance combined with relatively facile processability, enabling it to be used in electronic devices, hot gas filtration applications for spacecraft and in satellites [2,4]. A new functional composite material can be created by incorporating nanofiller into polymer. For example, addition of Fe–FeO nanoparticles into polyimide induces magnetic properties [200]. In this work, the preparation of semi-aromatic and aromatic polyimide was studied. Several strategies for incorporation of titanate nanostructures were examined. The effect of the added titanate nanotube on thermal and mechanical properties of polyimide composite film was also discussed.

The range of its applications can be expanded by the formation of micro and nanofibers of the polymer. Electrospinning is a facile and low-cost method to efficiently produce ultrathin fibers ranging from submicron to nanometer diameter. Such fine fibers can be tailored into the mat to achieve a tuneable volumetric porosity with a large surface to volume ratio. Studies incorporating titanate nanotube into electrospun fiber are still very limited. Bajsić *et.al.* [201] have embedded titanate nanotubes and TiO_2 nanospheres into electrospun polycaprolactone. However, the work mainly considered the effect of added filler on the UV stimulated degradation of the polymer composite fibers, without detailed investigation of the distribution of filler within the polymer. Good uniformity of filler dispersion in the polymer can strongly affect its properties. We have studied the electrospinning of polyamic acid mixed with suspended cetyltrimethylammonium bromide (CTAB) coated titanate nanotubes in dimethylformamide (DMF) solution with the aim of producing TiNT reinforced polyamide composite nanofibers. Both *ex-situ* and *in-situ* approaches have been investigated. Inside the body of these microfibers,

embedded titanate nanotubes were evenly distributed within the polymer matrix and, to
an extent oriented parallel to the fibre direction, as observed by SEM and TEM.

6.2   Synthesis of PMDA-ODA/titanate nanocomposites

6.2.1   Preparation of PMDA-ODA polyimide

Aromatic polyimide was synthesised using pyromellitic dianhydride (PMDA) and 4,4'-
oxydianiline (ODA) as monomers. Transparent yellow viscous solutions of polyamic-
acid in dimethylacetamide (DMAc) was synthesised at 22 ± 2.5 °C for 1, 2, and 3 days
with 20 wt% concentration. Afterwards, chemical imidization using acetic anhydride
and pydridine at 120 °C for 1 hour was applied to synthesise the polyimide. The
formation of polyimide was confirmed by the FTIR (Figure 6.1).

FTIR spectrum of PMDA-ODA polyimide shows the characteristic of chemical bonds
of polyimide (Figure 6.1 b) and is also supported by FTIR spectrum from literature
(Figure 6.1 a). The peaks of 1775 cm^{-1}, 1720 cm^{-1}, 1375 cm^{-1}, 723 cm^{-1} belong to
asymmetric C=O stretch, symmetric C=O stretch, C-N stretch, and deformation of
imide ring, respectively.

116
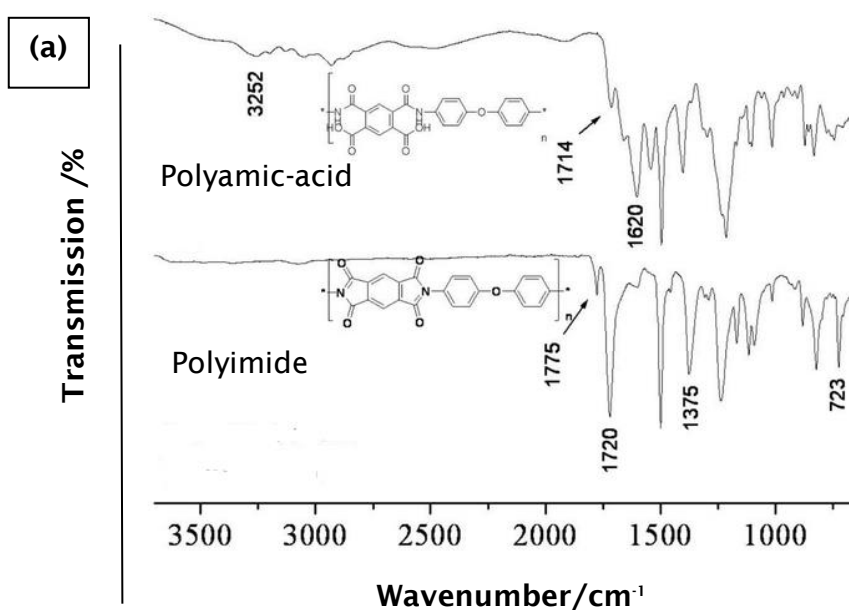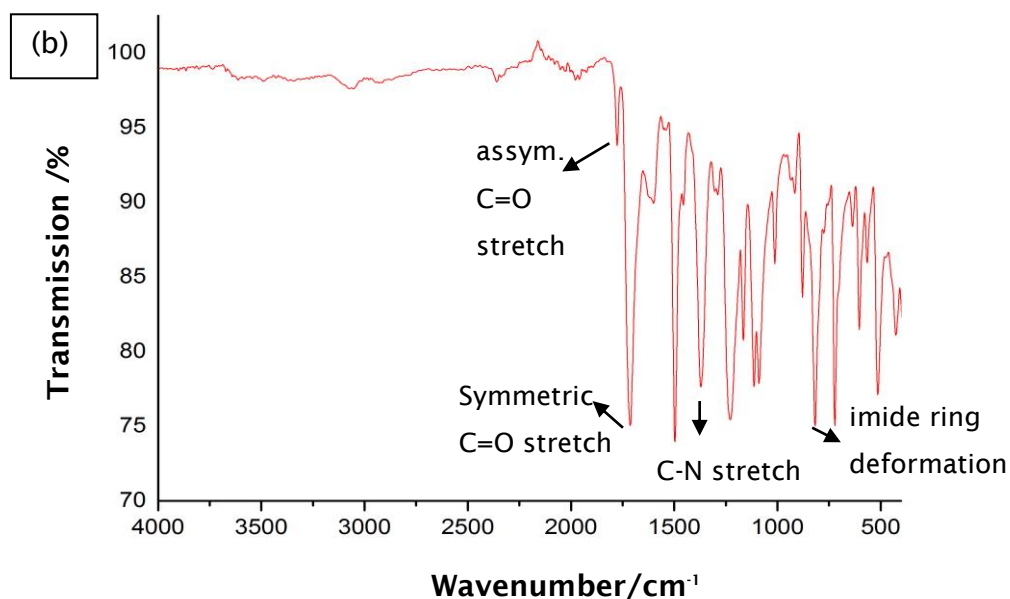
Figure 6.1. FTIR spectra of PMDA-ODA polyimide: (a) FTIR spectra of polyamic-acid and polyimide [202], (b) PMDA-ODA polyimide spectrum.

The doctor blade technique has often been employed to create polyimide film. The images of polyimide films are provided in Figure 6.2. The resulting polyimide films which deposited on 1×1 inch surface were folded and wrapped upon evaporation of the solvent in Figure 6.2 a. This may be caused by non-uniform packing of the polyamic-acid chain inside the solution. 65.5 g and 85.5 g of weight were applied upon last step of chemical imidization (heating in the furnace at 120 °C for 1 h) to prevent the film folding and delamination. Wrinkles were observed in polyimide film which has been applied a load of 65.5 g. On the other hand, applying load of 85.5 g produced flat polyimide film after heating in Figure 6.5 b. The flat film was rolled after 1 day left at room temperature (20-25 °C) due to internal residual stress in Figure 6.2 c. By applying doctor blade on large surface (3×1 inches), the polyimide film remained flat on the glass surface in Figure 6.2 d. Large contact area between polyimide and glass increased the mechanical interlock retaining the shape of the film. The polyimide film can be peeled off easily from the glass surface by immersing the film in DI water.
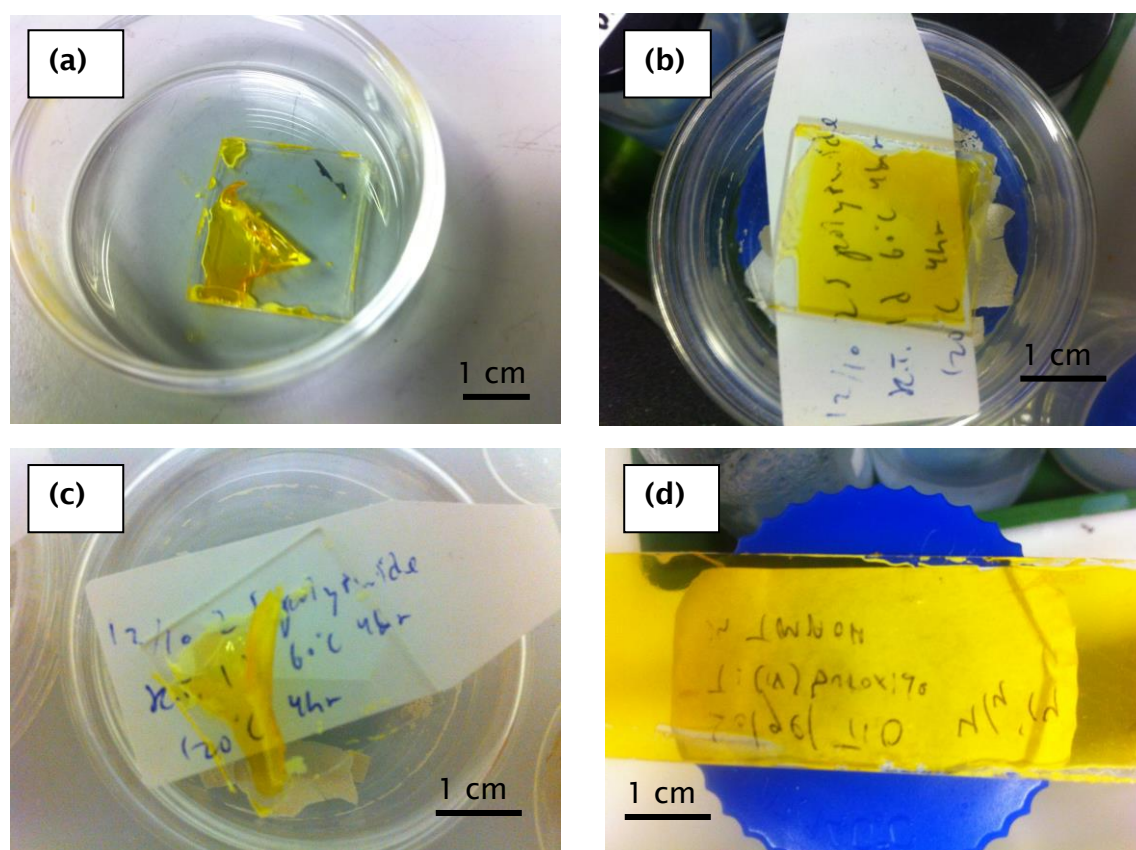
Figure 6.2. Images of PMDA-ODA polyimide films by doctor blading: (a) polyimide film doctor bladed on 1×1 inch surface without applied weight (wrinkle), (b) polyimide film fabricated with 85.5 g of applied weight, immediately after heating (flat), (c) polyimide film fabricated with 85.5 g of applied weight, after 1 day left (rolled), (d) polyimide film fabricated by doctor blading on large area (3 inches $\times$ 1 inch).

6.2.2   Effect of polyimide processing on polyimide properties

The effect of several parameters in polyimide processing (duration of polyamic-acid polymerisation) on polyimide properties is studied and discussed in this section. Duration of polymerisation affects the length of polymer chain which is expressed as average molecular weight of polymer. In macro-mechanic, average molecular weight is not affecting the modulus of the polymer [203]. However, average molecular weight exerts influence on nano-tribological properties. High molecular weight improves creep resistance of polymer [204]. Creep is defined as a time-dependent deformation at constant stress and temperature. It can occur even at room temperature. This creep behaviour has an impact on reduced modulus since creep stress is applied in reduced modulus testing

118

during holding time. Consequently, higher reduced modulus is achieved by increasing the average molecular weight of polymer.

Three samples from 1-3 days polymerisation are investigated by nano-indentation (Table 6.1).

Table 6.1. Reduced modulus and hardness of several polyimide films at various polymerisation times.

Sample	Applied load	Average nano-modulus	Average nano-hardness
Polyimide (1 day polymerisation)[a]	0.5-1 mN	6.64 ± 0.69 GPa	0.48 ± 0.03 GPa
Polyimide (2 days polymerisation)[a]	0.5 mN*	8.84 ± 0.54 GPa	0.78 ± 0.06 GPa
Polyimide (3 days polymerisation)[a]	0.5-1 mN	4.79 ± 0.28 GPa	0.36 ± 0.02 GPa

[a] = 30 seconds holding time, each load containing 20 indentation with retraction distance 30 µm and at 30 µm interval; * = an error occurred when 1 mN applied

From this data (Table 6.1), polyimide that is synthesised with 2 days polymerisation has higher reduced modulus and hardness than polyimide with 1 day polymerisation. The improvement of reduced modulus and hardness can be caused by the increase in chain length of polyimide. The chain length may be reduced after 3 days polymerisation due to the degradation of polyimide precursor (polyamic-acid) at room temperature (20-25 $^{\circ}$C) thus the reduced modulus and hardness are decreased after 3 days polymerisation of the polyimide sample. Two days polymerisation is the best condition to synthesise polyimide with high nano-tribological properties However, 3 days polymerisation gives the smallest deviation of measurement which probably due to more uniform chain length after 3 days stirring.

6.2.3   Preparation of polyimide fibres

Several parameters to synthesis polyimide fibre by electrospinning such as polymer concentration [205], humidity [206], and applied voltage [205] have been studied previously. Polymer concentration must be higher than 10 wt% to maintain stable jet creating bead-free uniform smooth and continuous fibre. Water molecules in the air influence the discharge rate and conductivity of fibre surface. Reducing humidity produces smaller fibre diameter. As a result, ultrafine polymer fibre ≈100 nm can be produced in 5% humidity. Stronger electrical field by increasing applied voltage induces more uniform and smooth fibre due to stretching of the polymer jet. However, the effect of working distance is still vague. There was no significant change in fibre morphology on changing the working distance from 10 cm to 20 cm [205]. In this thesis, a systematic study on the effect of modifying the working distance from 20 cm to 35 cm is provided.

Pure polyimide fibres were prepared with working distance of 20, 25, 30, and 35 cm while constant value has been applied to other parameters (20 kV applied voltage, 0.1 mL h^{-1} feed rate, 20 wt% polymer solution, humidity 40 ± 5%) (Figure 6.2 and 6.3).

Generally, increasing the distance from the needle tip to collector yields polymer fibre with smaller diameter [207]. Enlarging the gap between tip and collector gives more room for fibre stretching, resulting in a smaller fibre diameter. Bead formation can occur beyond a certain distance due to instability of the polymer jet. However, this phenomenon does always occur. In polyimide solution, changing the working distance from 10 to 20 cm gave no significant effect on the fibre diameter and morphology [205]. Further expansion of the working distance (>25 cm) can induce inhomogeneity of the fibre (shown by large error bar) which may arise from jet instability (Figures 6.6 and 6.7). The diameter of the fibre also improved at 35 cm opposed to the effect of increasing working distance. A larger fibre diameter was also observed in a previous experiment using a relatively high polycaprolactone concentration (7.5 and 10 wt%) in acetone solution at a low flow rate (0.05 mL min^{-1}) [208]. Increasing the distance between the tip and collector may weaken field strength, lowering the importance of jet stretching.
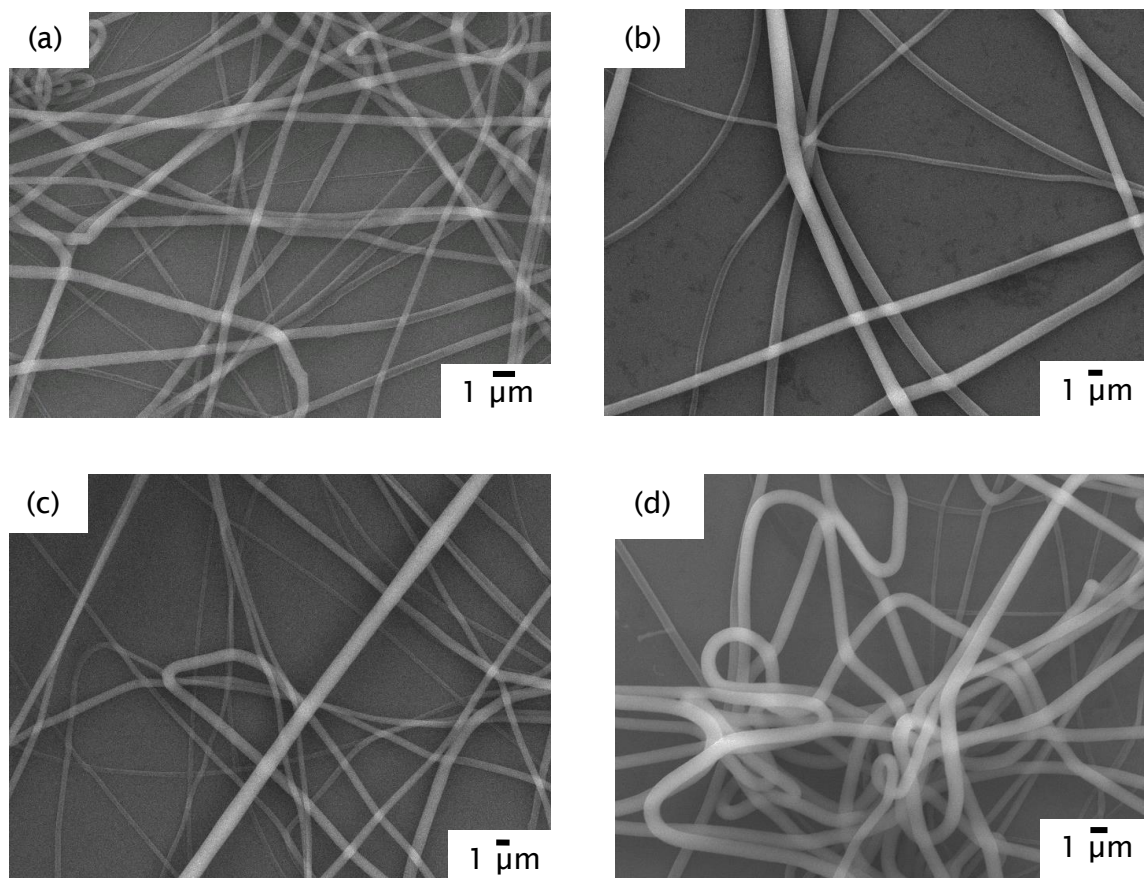
Figure 6.3. SEM images of pure polyimide fibres with varied working distance (at 20 kV applied voltage, 0.1 mL h^{-1} feed rate, 20 wt% polymer solution, humidity 40 ± 5%), (a) 20 cm; (b) 25 cm; (c) 30 cm; (d) 35 cm.
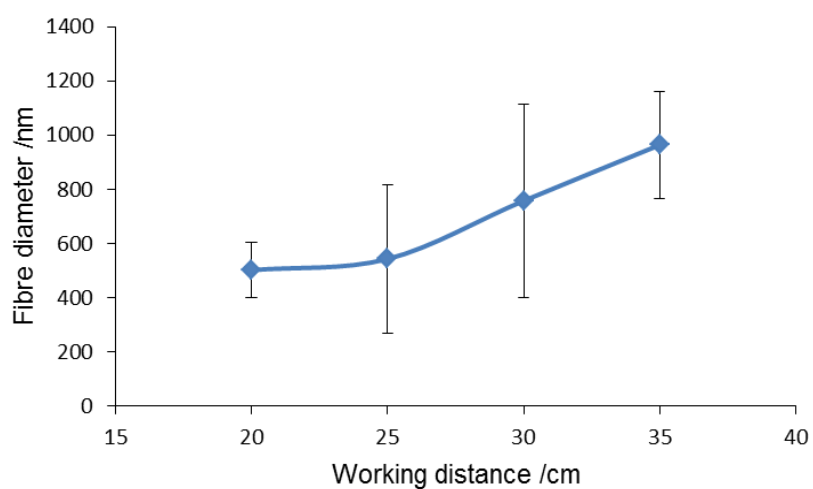
Figure 6.4. The effect of working distance on fibre diameter (at 20 kV applied voltage, 0.1 mL h^{-1} feed rate, 20 wt% polymer solution, humidity 40 ± 5%).

The effect of chemical imidization on the morphology of electrospun fibres is shown in Figure 6.5. Unlike the thermal imidization at which the fibres usually shrink decreasing their average diameter, we have found that, during chemical imidization, the average diameter increased from 210 ± 75 nm to 502 ± 101 nm (see Figure 6.5), probably due to swelling caused by the dehydrating agents.
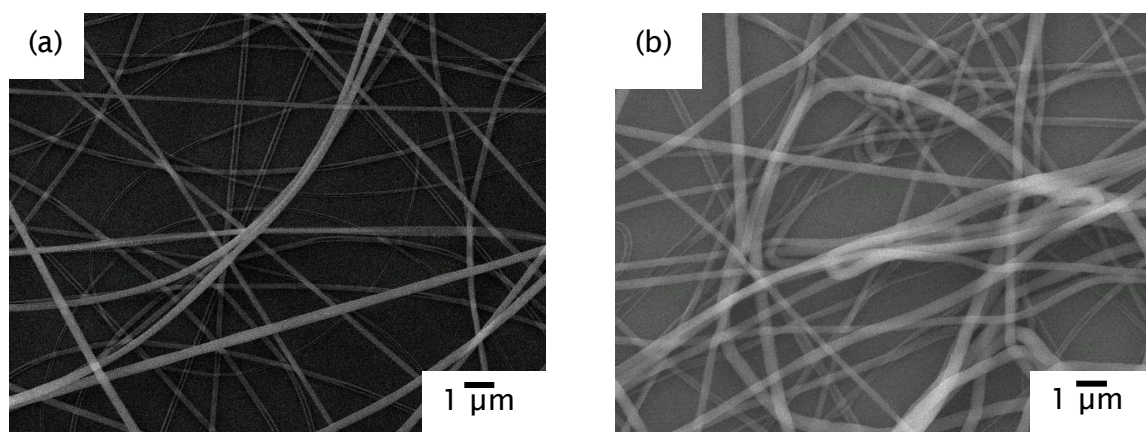
Figure 6.5. SEM images of (a) polyamic acid fibre; (b) polyimide fibre (20 cm working distance, 20 kV applied voltage, 0.1 mL h^{-1} feed rate, 20 wt% polymer solution, humidity $40 \pm 5\%$).

Neat polymer fibres tended to kink and intertwine with each other after chemical imidization. The reasons for such deformations of the fibres during imidization, according to Nishino *et.al* [209], are internal mechanical stress arising due to chemical processes and inability of long polymer chains, to effectively allow relaxation and stress relief.

6.2.4   Preparation and properties of titanate-polyimide nanocomposites

In-situ and *ex-situ* approaches were applied to synthesise 0.5 wt% uncoated titanate scrolled nanosheets (STiNS)-polyimide nanocomposite. A thick film of polyimide could not be achieved by *in-situ* approach. On the other hand, a relatively thick film was be

obtained by *ex-situ* approach. The images of *in-situ* and *ex-situ* uncoated titanate
nanosheets-polyimide nanocomposites is provided in Figure 6.6.
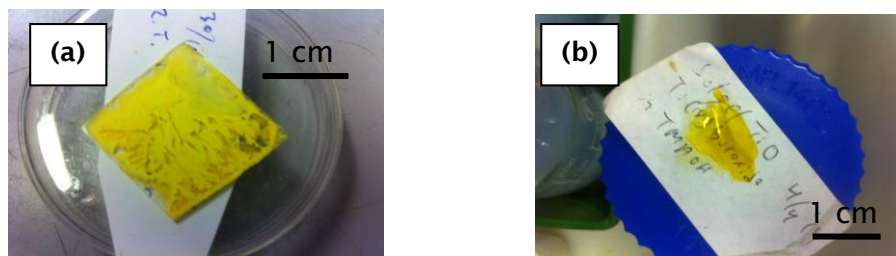
Figure 6.6. The images of 0.5 wt% uncoated scrolled titanate nanosheets (STiNS)-polyimide
nanocomposites with different fabrication method: (a) *in-situ*, (b) *ex-situ.*

A thin and yellow powdery coating was formed by *in-situ* method instead of a film. This
occurrence induced by very low viscosity of polyimide precursor, namely polyamic-
acid. Hydroxyl group of STiNS hindered the polymerisation of polyimide precursor
fabricating short chain of polyamic-acid [98]. In *ex-situ* approach, polyamic-acid was
polymerised for 1 day. Hence, longer polymer chain was achieved. However, the
addition of titanate nanosheets lowered the viscosity of polyamic-acid although it was
still higher compared to polyamic-acid produced by *in-situ* method. Similar result also
occurred in polyimide film embedded with titanate nanotubes.

Cetyltrimehylammonium bromide (CTAB) has been used to coat the surface of titanate
nanotubes (TiNT). 2.5 g of titanate nanotubes were stirred with 5 mL of 0.1 mol L^{-1}
CTAB and 25 mL distilled water for 3 days. Titanate nanotubes were separated from the
solution and dried at 22 ± 2.5 °C under vacuum. For preparation of the colloidal
solution, 2 g of CTAB-coated TiNT was stirred in 1 L DMF for 2 weeks at 600 rpm.
The solution was allowed to settle for 48 h and the top of the liquid (2 mL) was
collected, dried, and weighed to measure the concentration (240 mg L^{-1}, measured by a
gravimetric method).

By coating with CTAB, a thick film was able to be produced even from *in-situ* method.
However, it was found that addition of titanate nanotubes into polyamic acid solution
significantly reduces its dynamic viscosity. For example, the measured viscosity of the
20 wt% solution of PAA in DMF was ≥ 10000 mPa.s at room temperature, whereas

small addition of TiNT (only 0.1 wt% of total solid) has resulted in a decrease in the viscosity to 3840 mPa s and 2870 mPa s for *ex-situ* and *in-situ* TiNT-polyamic acid, respectively. This reduction also occurred in diluted samples which measured at 0.5 g dL^{-1}. It was 2.4, 1.9, and 1.4 mPa s for polyamic acid, *ex-situ,* and *in-situ* samples.

Usually, addition of nanostructured materials to the diluted solution of polymer results in linear (in respect to concentration of added nanoparticles) growth of its dynamic viscosity [210]. However, deviation from that tendency has been also widely observed recently [211–214]. Jain's selective adsorption hypothesis [211] is probably the most relevant here. It is possible that long and high molecular mass polyamic acid chains are selectively absorbed on the surface of titanate nanotube leading to reduction in entanglement between polymer chains in the solutions lowering apparent dynamic viscosity. Due to the fact that both *in-situ* and *ex-situ* composite mixtures showed a reduction in viscosity, we can also rule out the possibility that such a reduction is due to inhibition of the polymerisation in presence of TiNT. Indeed, for the *ex-situ* case, the polyamic acid is fully formed before the addition of nanotubes.

The thermal properties of PI-TiNT have been further investigated using differential scanning calorimetry (DSC), which is a common method to determine the glass transition temperature (T_g) of polymers. Usually, T_g can be detected by the baseline shift (red dashed line in Figure 6.7) or a peak in the DSC curve indicating an endothermic processes linked to rapid change in polymer mobility from glassy to rubbery state. The DSC curve of pure, neat polyimide shows a characteristic endothermic peak at 407 ºC of relatively narrow width, which can be associated with glass transition (Figure 6.7 a). The reported T_g for pure ODA-PMDA polyimide is within that range of temperatures [215].

Addition of nanostructures into the polymer matrix can either increase or decrease the T_g of the polymer composite depending on the mechanism of interactions between nanoparticles and polymeric chain [216]. We have found that small addition of titanate nanotubes (0.1 wt %) to the PI matrix, obtained by both *in-situ* and *ex-situ* methods, has increased its T_g by *ca.* 69 ºC from 407 ºC to 476 ºC (Figure 6.7). Such a dramatic shift in T_g is not unusual for PI polymers. Recently it has been reported 50 ºC shift of T_g temperatures in polyimide–graphene composite [217]. The mechanism involved in the

change of glass transition is probably related to the strong interaction between nanostructured titanate and polyimide resulting in more restriction in polymer chains mobility via steric hindrance. Also, strong covalent bond may occur between hydroxyl group on the surface of titanate nanotube and amino group of polyamic acid during imidization resulting in branching the polymer chain and leading to crosslinking, which usually increases the glass transition temperature in polyimide [218]. Addition of nanostructured material to the monomers during polymerization can affect the degree of polymerization of the final polymer to such a degree that the T_g of polymer nanocomposite is altered [219]. However, we have found that the T_g is the same in both *in-situ* and *ex-situ* composites (Figure 6.7 b, c) proving that addition of titanate nanotube does not affect the degree of PAA polymerization.
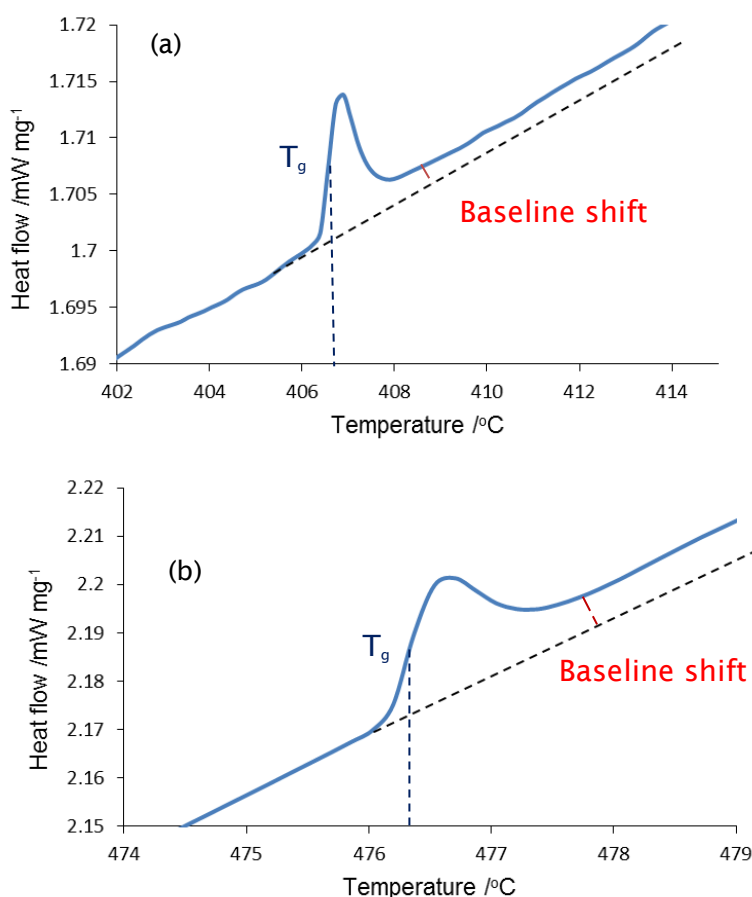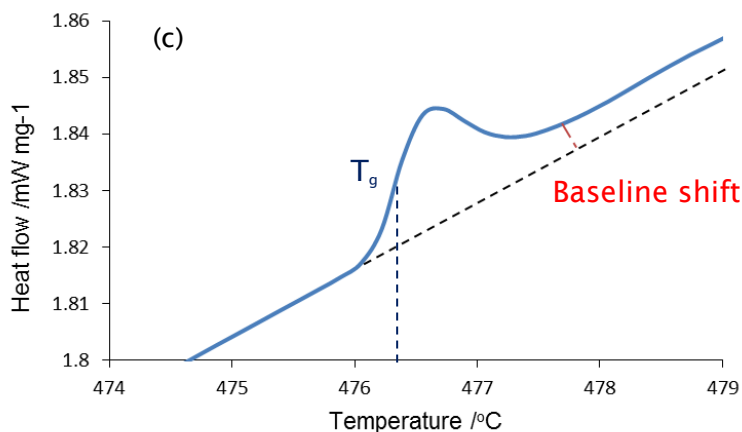
Figure 6.7. Differential scanning calorimetry (DSC) curve of (a) pure polyimide; and polyimide incorporated with 0.1 wt% titanate nanotubes (TiNT) by (b) *in-situ* synthesized polyimide/titanate nanotube composite; (c) *ex-situ* synthesized polyimide/titanate nanotube composite.

The effect of the incorporation of CTAB coated titanate nanotubes on the mechanical properties of polyimide (2 days polymerisation) nanocomposites is shown in Table 6.2. The incorporation of titanate within polyimide was done in two ways which are direct mixing as stir TiNT and mixing of stable colloidal suspension of TiNT. Direct mixing of TiNT slightly improved the modulus of polyimide. However, the standard of deviation of TiNS-polyimide samples is very high due to poor dispersion of titanate nanosheets inside polyimide matrix. By using stable colloidal suspension, the deviation of measured properties was reduced indicating good dispersion of TiNT. Although nanotubes were stable in DMF colloidal suspension, the concentration was very low (≈ 0.16 g L^{-1}). There was no significant difference between the mechanical properties of nanocomposite and pure polyimide by addition of 0.1 wt% stable colloidal suspension of TiNT.

Table 6.2. The effect of the incorporation of titanate nanotubes on the mechanical properties of polyimide.

Samples	Incorporation method	Reduced modulus (GPa)	Hardness (GPa)
polyimide	-	8.84 ± 0.54	0.78 ± 0.06
0.5 wt% TiNT-polyimide	directly mix after stirring of TiNT	10.02 ± 9.56	0.41 ± 0.32
in-situ 0.1 wt% TiNT-polyimide	mixing with stable colloidal suspension of TiNT	8.19 ± 0.92	0.68 ± 0.13
ex-situ 0.1 wt% TiNT-polyimide	mixing with stable colloidal suspension of TiNT	8.46 ± 0.19	0.70 ± 0.02

Instead of CTAB, titanate nanotubes were functionalized with branched polyethyleneimine (PEI, Mw $\approx$25000, Sigma-Aldrich) to increase the number of functional groups such as amine group. Hypothetically, PEI coated TiNT might be more stable in polar protic solvent such as DMF due to hydrogen bonding [220]. Titanate nanotubes were coated using wet impregnation method [221]. 4 g of TiNT was added into methanol solution (40 mL) of PEI (4 g) and stirred at 20 °C for 2 h and another 6 h at 60 °C allowing the volatilization of solvent. The residue was heated in an oven at 100 °C overnight. There was no significant difference in the stability of TiNT-PEI in DMF solution. A few agglomerates were spotted in diluted samples by SEM which was akin to TiNT-CTAB samples in Figure 6.8. This might be due to inhomogeneous coating of relatively high molecular weight polyethyleneimine. Chen *et.al.* [222] reported similar case in functionalization of multi-walled carbon nanotubes (MWCNT) with various molecular weight poly(L-lactic acid) (PLLA). By increasing the molecular weight of PLLA from 1000 to 3000, the PLLA coating became thicker and more uniform. On the other hand, the amount of PLLA coating lowered when the molecular weight further increased to 11.000 and 15.000. A squid leg-like morphology forming blobs of PLLA on MWCNT surface leaving much of the MWNT surface bare.
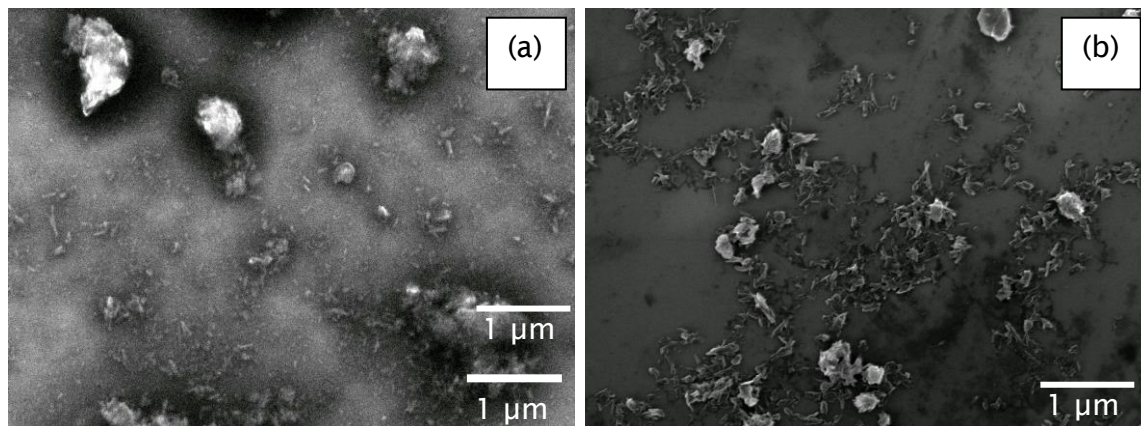
Figure 6.8. SEM images of (a) PEI coated TiNT; (b) CTAB coated TiNT drop casted on the top of silicon wafer (both samples diluted to the same concentration).

6.2.5   Synthesis of *in-situ* and *ex-situ* polyimide/titanate nanotube composite nanofibre

Besides film and plate, composites can be tailored into fibrous form by electrospinning. The one-dimensional filler (multiwalled carbon nanotubes) within the polymer can be aligned along the direction of the fibre by electrostatic force in the electrospinning process [157]. Herein, titanate nanotubes bearing one-dimensional morphology is suitable as filler in polyimide fibre. Based on the literature review and experimental results of pure polyimide fibre synthesis, polyimide/titanate nanotube composite was made with certain electrospinning parameters which are 20 kV of applied voltage, 20 cm working distance, 40 ± 5 % of humidity, and 20 wt% of solid in solution. The *in-situ* and *ex-situ* approaches were deployed to fabricate the composites. In the *in-situ* samples, a colloidal solution of known concentration of titanate nanotubes was added to the ODA solution before the polymerisation of PMDA and ODA while for *ex-situ* samples, the colloidal solution of titanate nanotubes was added after 1 day polymerisation of PMDA-ODA. The schematic of electrospinning procedure of *in-situ* and *ex-situ* polymer nanocomposite is depicted in Figure 6.9.
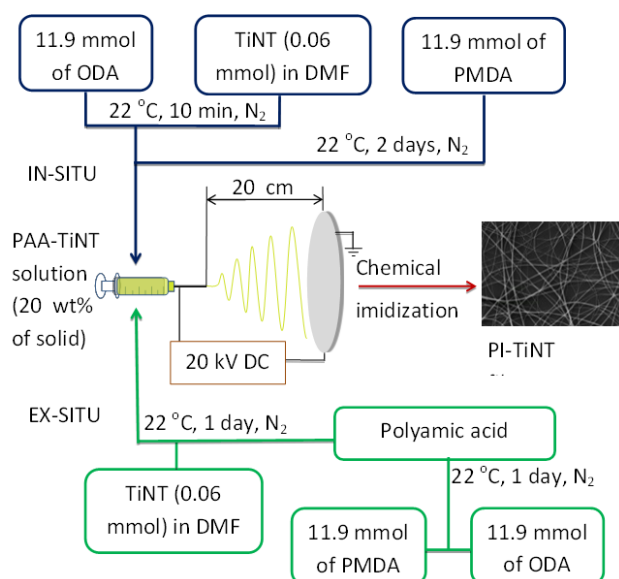
Figure 6.9. Schematic illustration of electrospinning of *in-situ* and *ex-situ* polyamic acid-titanate nanotube (PAA-TiNT) nanofibres. For chemical imidization, the PAA-TiNT fibres collected on the aluminium foil (grey disc on the right side) and immersed in acetic anhydride and pyridine (4: 3.5 volume ratio) for 1 min followed by heating at 120 °C for 1 hour.

It was found that addition of 0.1 wt% titanate nanotube into polyamic acid solution significantly reduces its dynamic viscosity. Generally, for efficient electrospinning of polymer solutions into the desired quality nanofibres the rheological properties of the solutions (such as viscosity, surface tension, electric conductivity, volumetric charge density, etc.) could vary only within the certain limits extending of which may result in instability of the electrically charged jet leading to formation of beads or wide distribution in nanofibres diameters. [223] However, the observed reduction in viscosity after addition of TiNT has facilitated the pumping of the dissolved polymer mixture during electrospinning.

It was found that viscosity differences between *in-situ* and *ex-situ* synthesis also affected the morphology of the composite fibre. Figure 6.10 b shows frequent occurrence of the polymer beads with typical size 188 ± 82 nm in the nanofibrous with typical diameter 57 ± 20 nm PAA-TiNT composite prepared by the in-situ method in which viscosity of the electrospinning fluid was 2870 mPa s. In contrast, electrospinning of the PAA-TiNT solution of the same concentration prepared by ex-

situ methods with 3840 mPa s viscosity results in larger diameter of composite nanofibres (328 ± 93 nm) with no beads formation (see Figure 6.10 a).
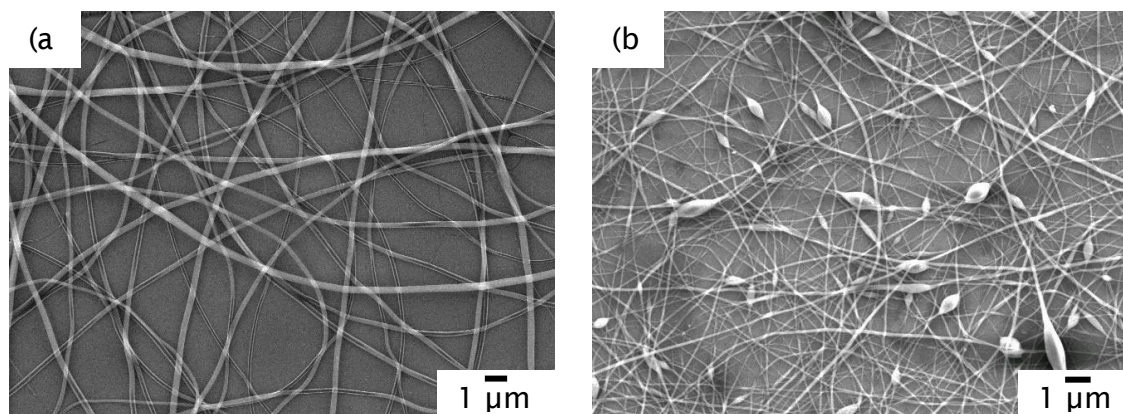
Figure 6.10. SEM images of polyamic acid-titanate nanotube fibre (0.1 wt% TiNT in PAA). (a) *ex-situ* synthesised sample (thick fibre without bead); (b) *in-situ* synthesised sample (thin fibre with beads).

These observations are in agreement with previously observed effect of viscosity of electrospinning fluids on the probability of beads formation [224]. At low viscosity, beaded fibre is usually formed by capillary break-up of the jet during electrospinning. Since increase in concentration of polymer in solution results in an increase of its viscosity, [225] the quality of the *in-situ* synthesised fibres could be improved by increasing the concentration of PAA.

In order to determine the distribution of nanostructured TiNT within the polymer fibres HR-TEM was employed. Our early samples in which colloidal solution of nanotubes was prepared by 1 day stirring of the TiNT powder in DMF show poor dispersion of nanotubes which remain aggregated in original unbroken particles (see Figure 6.11 a) resulting in appearance of random swellings in the uniform nanofibre in SEM images. Despite poor dispersion, TEM image confirms good interaction between TiNT and polyimide seeing as efficient wetting of the nanotubes by polymer. It appears that all of the nanotubes are covered by polymer materials meaning that poor dispersion is mainly due to the presence of initial TiNT agglomerates in the colloidal solution.
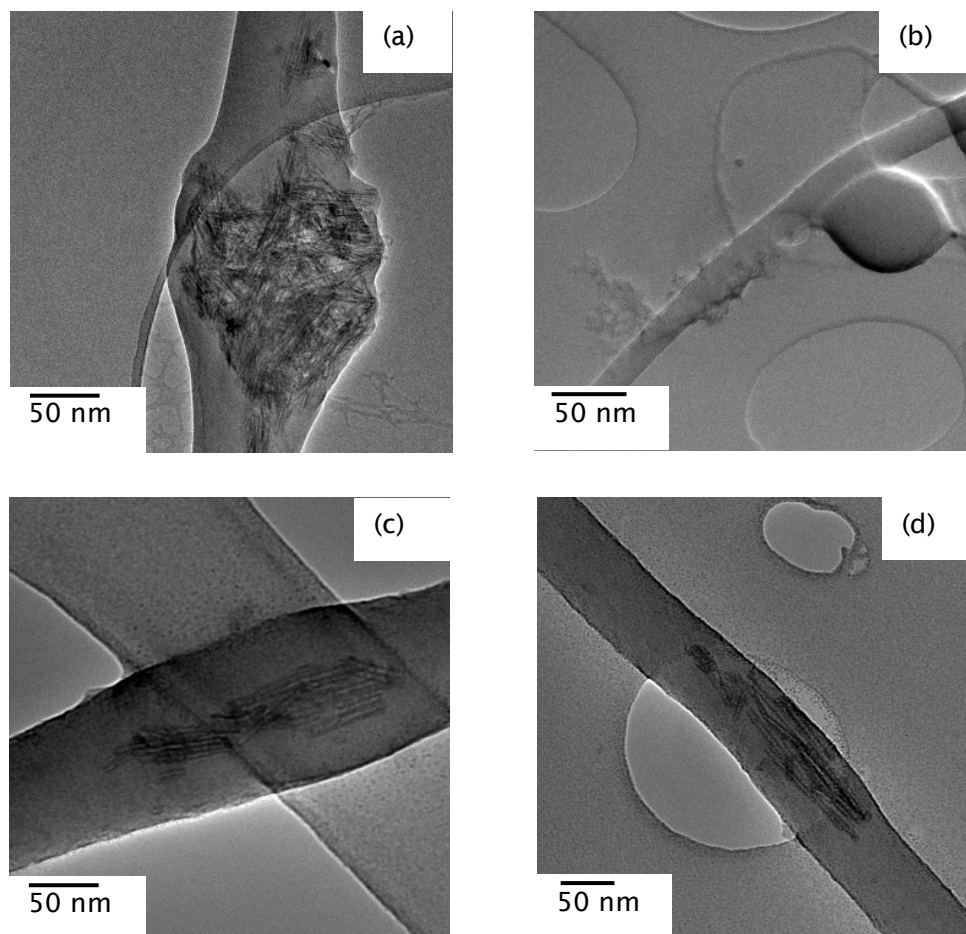
Figure 6.11. TEM images of electrospun PI-TiNT (0.1 wt% TiNT in PAA) composite nanofibres (a) agglomerate of nanotubes within polyimide fibre (from 1 day mechanical stirring sample); (b) empty bead of polyimide (from 2 weeks mechanical stirring sample); (c) aligned nanotubes within polyimide fibre (from *ex-situ* PAA-TINT stable colloidal suspension); (d) aligned nanotubes within polyimide fibre (from *in-situ* PAA-TiNT stable colloidal suspension).

Using our previously established method of untangle nanotubes agglomerates without shortening of their length by long term stirring [175], the colloidal solution of isolated TiNT obtained by 2 weeks stirring was used for preparation of PI/TiNT composite nanofibres. Figures 6.11 c and 6.11 d shows TEM image of polyimide nanofibres reinforced by titanate nanotubes prepared by *ex-situ* and *in-situ* respectively. Both samples show appearance of nanotubes oriented along the length of the fibre. From the

analysis of many TEM images it was concluded that (i) despite absence of large agglomerates of TiNT, the observed nanotubes are mostly found assembled into small bundles, (ii) there are long fragments of the fibres completely free from the nanotubes and (iii) in case of low viscosity *in-situ* solution, there are appearance of spheroidal beads without embedded nanotubes (see Figure 6.11 b). Since the quantity of the added nanotubes is still relatively low, bearing in mind not fully uniform distribution of TiNT, it resulted in the appearance of nanofibres without nanotubes. Also, the low fluid viscosity induced polymer beads formation rather than the presence of large agglomerates of TiNT as Figure 6.11 a. Usually, an *in-situ* approach to dispersion gives better results compared to *ex-situ* methods [226]. In the present work, both approaches resulted in satisfactory distribution of nanotubes in the polymer, allowing greater flexibility in production.

6.3 Synthesis of semi-aromatic polyimide

Instead of aromatic polyimide (e.g., PMDA-ODA, 6FDA-ODA), the preparation of semi-aromatic polyimide based on bicyclo-[2.2.2]oct-7-ene-2-exo,3-exo,5-exo,6-exo-2,3:5,6-dianhydride (BOCA) and 4,4'-oxydianiline (ODA) was also studied. Two-step method was used to synthesis this polyimide. In the first step, BOCA was reacted with ODA at 22 ± 2.5 °C for 2 days in dimethyl acetamide (DMAc) resulting low viscosity, clear, and transparent solution of 25 wt% polyamic-acid (BOCA-ODA). Subsequently, the polyamic acid was chemically imidized by acetic anhydride and pyridine at 120 °C for 1 hour in air.

The chemical structure of polyimide (BOCA-ODA) was confirmed by FTIR, which has similar peaks compared to literature [227]. The spectrum were provided in Figure 6.12.
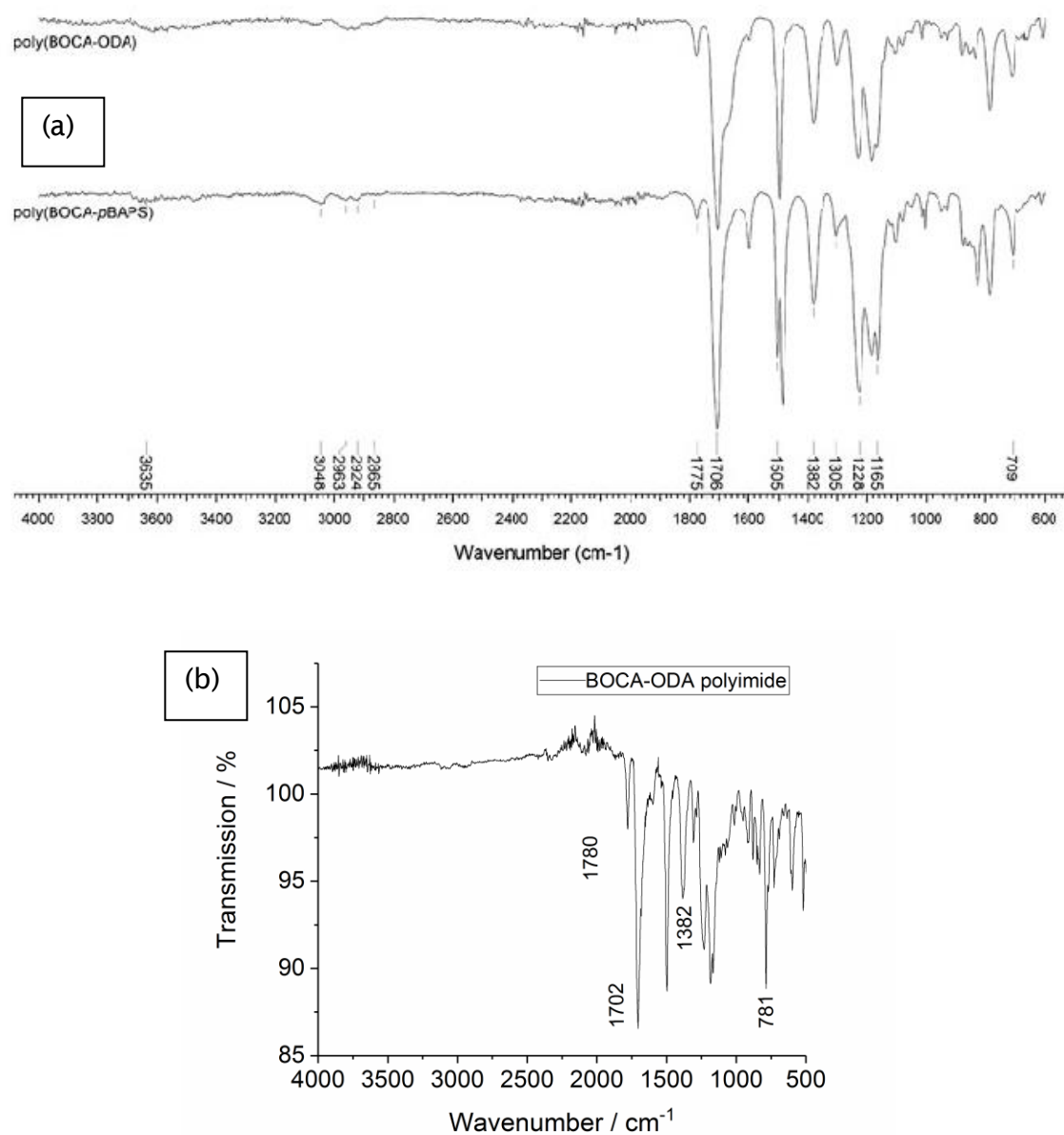
Figure 6.12. FTIR spectrum of polyimide from BOCA and ODA; (a) from literature (the top spectra of the graph) [227], (b) from this experiment.

The peaks of 1702 cm^{-1} and 1780 cm^{-1} associate to C=O symmetric and asymmetric stretching of amide, respectively. The 1382 cm^{-1} corresponds to C-N stretching vibration of imide ring while absorption band at 781 cm^{-1} is due to deformation of imide ring. This FTIR spectrum indicated that polyimide has been successfully synthesised.

133

The resulting polyimide film (fabricated by drop casting 0.27 g of 25 wt% polyamic-acid solution) was very brittle and could easily destroy by tweezers although it is transparent to visible light in Figure 6.13 a. An attempt to make thick film using 0.65 g of 25 wt% polyamic-acid solution produced thick solid white coloured film in Figure 6.13 b which was also very brittle. This phenomenon is presumably caused by short chain formation of polyamic-acid precursor. Matsumoto *et.al.* argue that dianhydrides monomer with bicyclo-octane structure have low reactivity thus high temperature is needed to obtain long chain polyamic-acid [228]. High molecular weight polyamic-acid have been successfully synthesised at 90 ℃ for 2 days using bicyclo[2.2.2]octane-2-exo,3exo,5-exo,6-exo-2,3:5,6-dianhydride (BODA), which is similar to dianhydride monomer that is used in this work. The polymerisation temperature in this work was increased to 95 ℃ for 2 days. Nonetheless, a solid white precipitates appeared after imidization at 120 ℃ for 1 hour in Figure 6.13 c. It was found that this type of polyimide was vulnerable to water (non-solvent) precipitation [227,229]. Low temperature evaporation (80 ℃) and vacuum environment needed to cast this polyimide film.
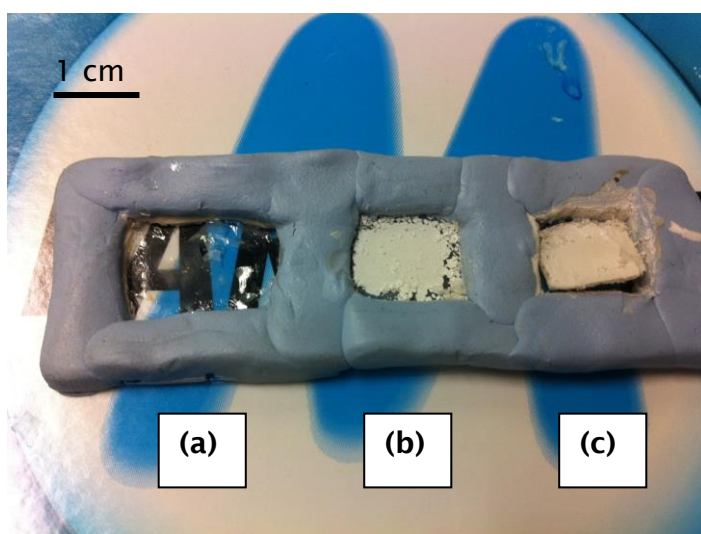
Figure 6.13. The images of polyimide films made by drop casting and imidization of 25 wt% BOCA-ODA polyamic acid with different weight and polymerisation temperature: (a) thin polimide film (0.27 g of polyamic acid), (b) thick polyimide film (0.65 g of polyamic acid), (c) thick polyimide film (0.65 g of polyamic acid). Sample a and b were polymerised at 22 ± 2.5 ℃ for 2 days while sample c was at 95 ℃ for 2 days (all imidization were conducted in air).

6.4   Conclusions

A thick and relatively flexible aromatic polyimide (PMDA-ODA) film was successfully synthesised by two-step method while semi-aromatic (BOCA-ODA) polyimide created thin and very brittle film. BOCA-ODA polyimide has very low viscosity and vulnerable to water precipitation making it difficult to synthesise a thick film. Two days PMDA-ODA polymerisation gave the best nanotribological properties compared to 1 and 3 days which may indicates optimum polymerisation duration. To ensure the synthesis of polyimide-titanate nanocomposites film, hydroxyl group of titanate should be coated to prevent it from inhibiting the polymerisation. CTAB coating of the nanotubes was essential in preparing polymer nanocomposites samples. However, the addition of CTAB coated titanate nanotubes still decreased the viscosity of polyamic acid (as a polyimide precursor) which similar reduction observed by Jain *et.al.* [211]. This viscosity reduction caused by selective absorption of high molar mass polyamic acid on titanate nanotubes, leading to a reduction in entanglement density and an improvement in chain mobility. The reduction of viscosity reduces the production of kinked and intertwined fibre after chemical imidization. However, beads occur on the composite fibre at very low viscosity (2870 mPa s) suggesting that higher viscosity is beneficial to creation of bead-free nanofibres.

The incorporation of titanate nanotubes (0.1 wt %) to the PI matrix, obtained by both *in-situ* and *ex-situ* methods, has increased its T_g by *ca.* 69 °C from 407 °C to 476 °C. which due to strong interaction between nanostructured titanate and polyimide resulting in more restriction in polymer chains mobility via steric hindrance. Strong covalent bonding may occur between hydroxyl groups on the surface of titanate nanotubes and the polyamic acid during imidization. The same T_g in both *in-situ* and *ex-situ* composites implied that addition of titanate nanotube did not affect the degree of PAA polymerization. There was no significant effect on modulus and hardness of polyimide by addition of 0.1 wt% titanate nanotubes. Optimal functionalization by using certain molecular weight of polyethyleneimine (PEI) might be needed to increase the concentration of stable colloidal suspension of TiNT in organic solvent such as DMF.

Several approaches have been employed to prepare aligned titanate nanotube within polyimide fibres. This work recommends the use of stable colloidal suspension over

135

direct mixing of TiNT solution, whether concentrated (as used in *ex-situ* samples) or not (as used for *in-situ* samples), to synthesise an aligned titanate nanotube within polyimide fibre. By using stable colloidal suspension, dispersion of titanate nanotubes within polyimide fibres was also improved.

Chapter 7:   Effect of UV Irradiation on Polyimide and Polyimide Nanocomposites

7.1   Introduction

Polyimide is a common polymer that is used for outer space applications such satellite and spacecraft. A satellite moves in a circular orbit around the earth at certain distance and gravitationally bounds to each other. Many important satellites such as those for weather, communication, spacecraft for scientific and military observation, and International Space Station are located in low earth orbit [230]. Low earth orbit (LEO) is the closest orbit of earth with a distance of 200-2000 km above earth's surface. Ultraviolet, solar-flare X-rays, solar wind electrons, thermal cycling, atomic oxygen, and debris are able to degrade such polymer in space [231]. In this thesis, protection of polyimide and characterisation method of UV degraded polymer nanocomposites was discussed. Titanate nanostructures are used as UV absorber or screener. Titanium oxide, often in the anatase TiO_2 form, is commonly used as a photocatalyst. Not all crystallographic phases of titanium oxide act as a catalyst. Rutile TiO_2 can be used as a UV screener for poly(L-lactide) [232]. The structure of titanium oxide used in this paper is akin to $H_2Ti_3O_7$ and is made by hydrothermal synthesis using sodium hydroxide and P25 Degussa reactants. Alkali solution significantly reduces the catalytic properties of hydrothermal titanate by introducing defects on its structure which lead to a recombination site of electron and hole [60]. The effectiveness of hydrothermal titanate nanostructures as UV screener is studied by Raman spectroscopy, nanoindentation, optical microscopy.

Ultraviolet degradation of polymer can be detected by physical or chemical characterisation. Some physical changes such as roughness, micro cracks and pores can be seen by atomic force microscopy [233], scanning electron microscopy [232], fluorescence microscopy [234], or optical microscopy. Contact angle measurement may indicate the effect of UV on roughness. Melt rheology of the polymer is also changed due to scission of polymer chain. Destructive test such as tensile test can elucidate the effect of UV on elasticity, strength, and modulus of bulk polymer [235]. Most recent physical tests (e.g.,

nanoindentation) are able to pinpoint mechanical properties through thickness direction. However, most nanoindentation studies on the effect of UV mainly focused on epoxy materials [236,237]. Since the effect of UV varies among diverse polymers, further work is needed.

Chemical characterisation can provide early detection of UV degradation. Electron spin resonance is able to detect free radicals within the polymer [238] and retardation of UV degradation by carbon nanotubes in polymer [239]. X-ray diffraction spectroscopy (XRD) and differential scanning calorimetry (DSC) can discern changes in crystallinity of crystalline or semi-crystalline polymer. Crystallinity is known to increase upon UV irradiation since amorphous parts of the polymer may degrade [240]. X-ray photoelectron spectroscopy (XPS) can sense the difference in binding energy on the polymer surface up to 5-10 nm and is usually coupled with time-of-flight secondary ion mass spectrometry (TOF-SIMS) which can provide imaging based on mass spectral data up to 1-2 nm [241]. Chromatography can detect volatile organic compounds that may escape from the polymer during UV irradiation [242]. Oxidised polymer may emit light when heated in an inert atmosphere, giving rise to chemiluminescence. Such luminescence might indicate the presence of carbonyl compounds and hydroperoxides in the polymer [243,244]. Infrared spectroscopy and Raman spectroscopy may detect changes in the chemical bonding in the polymer. Carbonyl index, which is the ratio of carbonyl bond intensity over reference bond that is not affected by UV, is often used as an indication of UV degradation in the polymer [245,246]. However, Rouillon, *et.al.* [247] argue that carbonyl index may not be the best indicator of UV degradation. An integrated combination of characterisation methods may be the best way to study the UV degradation of polymer.

In this chapter, a characterisation method is proposed which is based on methylene blue (MB) adsorption on moieties created by polyimide photodegradation [248]. Polyimide film, which is used, e.g., for space applications and electronics, was irradiated by UV light producing moieties with several functional groups that may adsorb methylene blue dye. Methylene blue or methylthioninium chloride is a cationic dye which is positively charged in aqueous solution. The changes in methylene blue concentration were measured by UV-vis spectroscopy.

7.2 Effect of UV irradiation on 6FDA-ODA/TiNT nanocomposites

There are two types of polyimide used in this work, which are pyromelitic dianhydride-oxydianiline (PMDA-ODA) and 4,4'-(hexafluoroisopropylidene)diphthalic anhydride-oxydianiline (6FDA-ODA) polyimide. Those polyimides has differences in optical properties and UV stability. PMDA-ODA polyimide has the characteristic of yellow colour, while 6FDA-ODA is colourless due to the bulky flouro-containing anhydride resulting in less intermolecular bonding [249]. Upon UV irradiation, PDMA-ODA generates more free radicals than 6FDA-ODA [104]. However, 6FDA-ODA degrades faster due to the spontaneous conversion of the radicals into the degradation products. The inhibition of UV degradation of 6FDA-ODA polyimide is needed, for example by incorporating titanate nanostructures within the polymer.

The polymer nanocomposites were made by solution mixing of 6FDA-ODA polyimide with titanate nanotubes (TiNT) creating 1 wt% titanate nanotubes-polyimide composite. The inhibition of UV degradation of 6FDA-ODA polyimide by hydrothermal titanate nanotubes was studied by Raman spectroscopy, nanoindentation, transmission electron microscopy (TEM), optical microscopy, and calculation of MB adsorption on irradiated polymer.

7.2.1 Effect of UV irradiation on the amount of chemical bonds

Monitoring photodegradation by detecting chemical bonding using infrared or Raman spectroscopy is one of the oldest methods that is extensively used [247,250]. The carbonyl group (C=O bond) is the most common indicator of UV degradation [245,246]. However, Rouillon, *et.al.* [247] argue that carbonyl index may not be the best indicator of UV degradation in polypropylene. It takes a long time to see changes in this index which makes it unsuitable for early detection of UV degradation. Unlike polypropylene, fluorinated polyimide has several functional groups such as C-F and C-N including carbonyl groups that can be a good indicator of UV damage [251].Raman spectra of 6FDA-ODA PI and PI-TiNT in Figure 7.1 show some functional groups (e.g., C=C, C=O, C-N, C-F) which was used to study photodegradation.
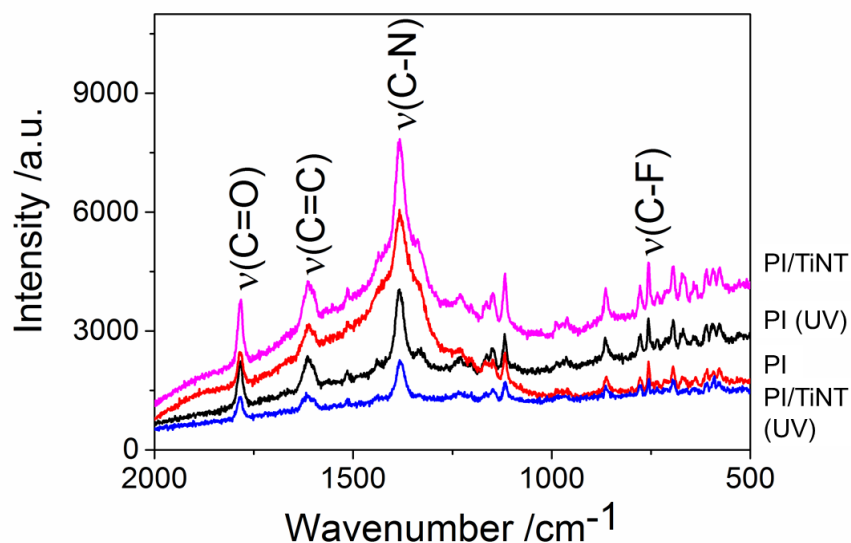
Figure 7.1. Raman spectra of PI and PI-TiNT before and after UV exposure: (PI, red) PI non-irradiated; (PI (UV), black) PI irradiated for 3 h; (PI/TiNT, purple) PI-TiNT non-irradiated; (PI/TiNT (UV), blue) PI-TiNT irradiated for 3 h.

Raman spectra were obtained using a Raman spectroscopy confocal microscope (Renishaw, RM 2000) using a light source of 632.8 nm wavelength. The exposure time was 10 seconds with a 1 % intensity of laser radiation. The stretching vibration (ν) at wavenumbers of 1783 cm^{-1}, 1618 cm^{-1}, 1380 cm^{-1}, and 756 cm^{-1} represent C=O, C=C from phenyl, C-N, and C-F from CF$_3$, respectively. C-N bond in 6FDA-ODA polyimide overlapped with neighbouring peaks, making it difficult to calculate the area for photodegradation study. Therefore, C-N was excluded from the study. Phenyl C=C bonding in 6FDA-ODA polyimide is less susceptible to breakdown upon UV irradiation, rendering it useful as a reference peak. The change in absorbance of C=O and C-F was monitored for UV degradation.

To quantify the spectral changes of polyimide exposed to UV radiation, the peak area A_g related to unstable functional group such as C=O or C-F was referenced against peak area A_{ph} of stable functional group, which in case of polyimide is aromatic C=C bond at wavenumber of ≈1618 cm^{-1} using equation suggested elsewhere [251]:

$$\Delta A = \frac{A_g / A_{ph} - A_g^0 / A_{ph}^0}{n \times A_g^0 / A_{ph}^0}$$

(7.1)

where A_g^0 and A_g are initial (prior UV exposure) and current (after UV exposure) peak areas of specific functional group affected by photodegradation respectively, A_{ph}^0 and A_{ph} are initial and current peak areas the areas from aromatic C=C bond respectively, n is the number of specific functional groups in one repeating unit of 6FDA-ODA polyimide. (e.g., 4 for C=O, 6 for C-F). The relative area change (ΔA) evaluated from Equation (7.1) shows the number of degrading specific functional groups under UV irradiation. The more negative ΔA value, the more groups from the polymer chain has been cleaved.

Table 7.1. Effect of 3 h UV irradiation on the intensity of C-F and C=O bonds.

Group index	ΔA_{PI}	$\Delta A_{PI/TiNT}$
C=O index	-0.0787	0.0088
C-F index	-0.0540	-0.0350

It is shown in Table 7.1 that the C-F and C=O bond were decreased significantly after 3 h during UV irradiation of the pure polyimide sample. The C=O bond absorbance was decreased to a value of 0.079 while C-F was 0.054, demonstrating that the C=O bond was more prone to breakdown by UV irradiation. This result agrees with a previous study [251]. PI/TiNT composite film still retained C=O bonding after 3 h ($\Delta A = 0.009$) while the C-F bond did not reduce as much as pure polyimide. Positive value may come from inaccuracy due to background noise. The absorption was decreased to 0.035 and 0.054 for PI/TiNT and pure polyimide, respectively. This indicates that non-calcined hydrothermally synthesised titanate nanotubes protect the most vulnerable bond (e.g., C=O) to UV attack and also reduce the damage of C-F bonding in 6FDA-ODA polyimide. Titanate nanotubes show an absorbance peak at a wavelength of 280 nm [60], protecting the C=O bond (which might be prone to UV attack) at wavelength of *ca.* 280 nm. Degradation of the C-F bond might be due to irradiation at a longer wavelength above $\approx$280 nm.

7.2.2 Estimation of polymer chain scission rate by sorption of methylene blue

UV irradiation may cause chain scission leading to structural changes of polymer and release of volatile compounds. For example, Vectran® produces chemical moieties with several functional groups such as hydroxyl and carboxylic acid groups which detected by FTIR after 96 h of UV exposure [252]. FTIR can be useful to detect changes in chemical bonds. Using FTIR, long-time exposure is needed to be detected. Physical changes may occur even before detected by FTIR [247]. Presence of volatile compound such as carbon dioxide can be detected after a few minutes UV exposure on anatase-polyethylene composite by FTIR [253]. However, a complex arrangement is required. A new method to give early detection degradation products is needed.

It is important to note that appearance of polar functional groups at the ends of the broken chains of photodegraded polymer may result in change in its affinity to various probe molecules. Therefore, the degree of photodegradation can be monitored by ability of polymer to sorb various charged dye molecules in the polymer matrix. We have found that neat 6FDA-ODA have relatively low capacity to sorb methylene blue (MB) dye from aqueous solutions, whereas samples irradiated by UV are characterised by higher capacity (see Figure 7.2 a (right) and Figure 7.2 b (right)). This phenomenon is consistent with the above mechanism of polyimide photodecomposition and can be used as a method for estimation of the quantity of such broken chains in the polymer assuming that it is proportional to the quantity of generated adsorption sites for the MB.
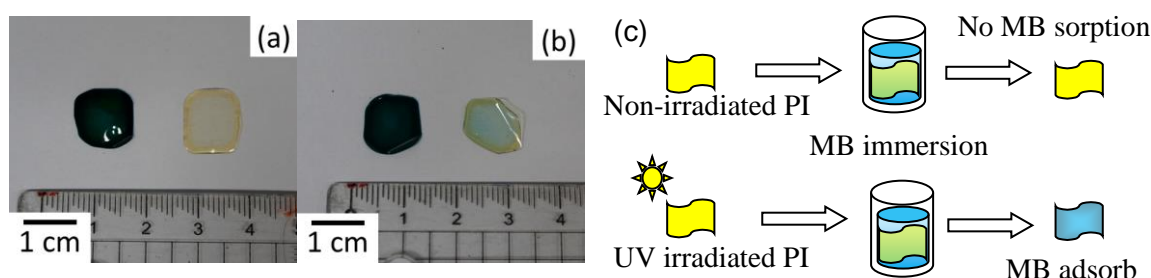
Figure 7.2. The photograph of 6FDA-ODA PI and PI/TiNT samples after 24 h immersion in methylene blue (a) PI/TiNT (left) and PI (right) of non-irradiated sample; (b) PI/TiNT (left) and PI (right) after 4 h UV exposure; (c) Illustration of the estimation of PI chain scission by methylene blue sorption.

We have found that incorporation of TiNT into polyimide matrix has resulted in significant increase in the sorption capacity of the obtained composited towards MB in Figure 7.2 a (left) and 7.2 b (left). Due to the anionic nature of titanate nanotubes, the capability of the PI/TiNT composite to sorb the cationic dyes such as methylene blue was siginificantly increased. To detect moieties generated in PI/TiNT composite due to UV light, the adsorbance of PI/TiNT composite was subtracted from the adsorbance of TiNT.

The adsorption was distributed homogenously over polyimide implying good distribution of titanate nanotubes in polyimide. Dispersion of titanate nanotubes proved to be adequate by TEM in Figure 7.3 a. However, few agglomerates also appeared in the PI/TiNT nanocomposite sample in Figure 7.3 b.
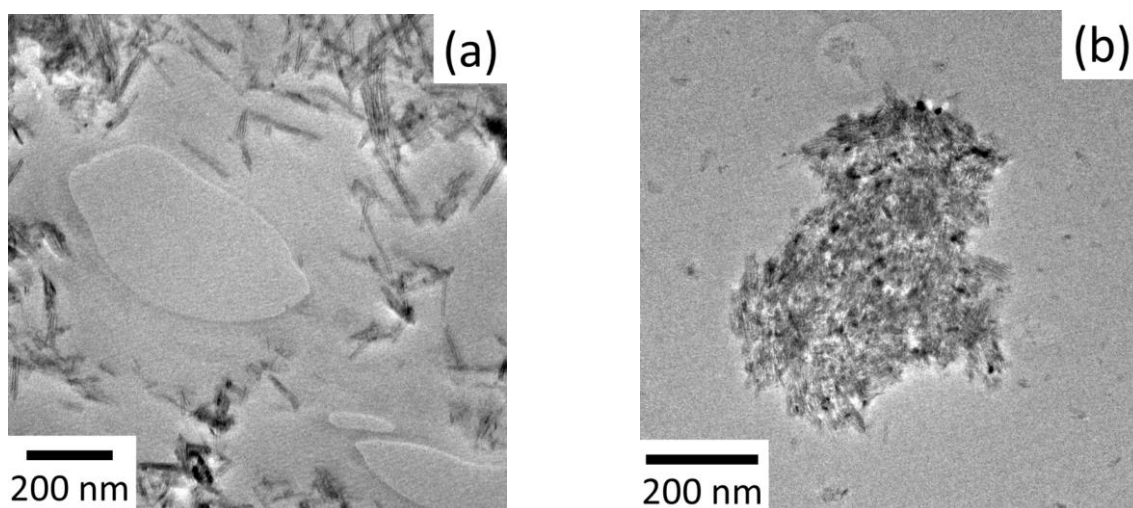
Figure 7.3. TEM images showing (a) distribution of titanate nanotubes in polyimide matrix; (b) titanate nanotube agglomerates were spotted in polyimide.

After 4 h UV irradiation, some methylene blue remained on the surface of irradiated polyimide in Figure 7.2 b. Methylene blue might be adsorbed on functional groups from irradiated 6FDA-ODA polyimide. Polyimide created radicals when irradiated [104] and its termination may create some functional groups which able to adsorb methylene blue. For example, similar polyimide, irradiated PMDA-ODA polyimide produces phenyl isocyanate [103], phenol, amine groups [6], and volatile gases (e.g., CO, CO_2) [103]. Reduction of C=O and C-F bond exhibited by Raman in Figure 7.1 and Table 7.1. Considering

high dissociation energy of C=O (178 kcal mol^{-1}) and C-F (116 kcal mol^{-1}) bond [254,255], the reduction of those bonds might come from cleavage of neighbouring C-C (83 kcal mol^{-1}) bond releasing gas such as CO, CO_2, and CHF_3. Scission of other weak bond such as C-N (73 kcal mol^{-1}), C-O (85.5 kcal mol^{-1}), and N-CO (86 kcal mol^{-1}) bonds may create functional group such as phenol, amine, isocyanate, and carboxylic acid. Based on literature and Raman spectra (Figure 7.1 and Table 7.1), proposed photodegradation mechanism of 6FDA-ODA is shown in Figure 7.4.
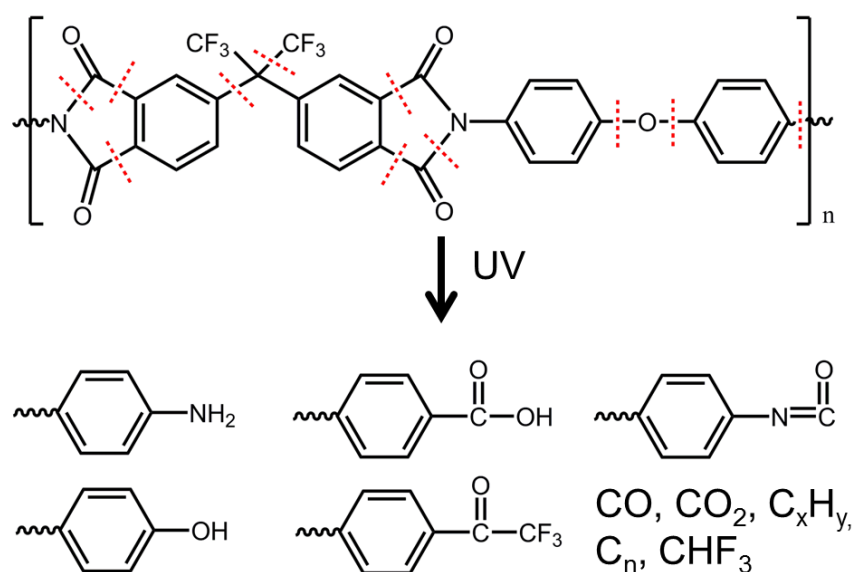
Figure 7.4. Proposed photodegradation mechanism of 6FDA-ODA polyimide by UV irradiation.

The phenol, amine, isocyanate, and carboxylic acid groups attracted methylene blue forming chemical bonds by hydrogen bonding. Hence, adsorption of methylene blue indicated UV damage on polyimide samples. To study the kinetic of degradation, pure polyimide and polyimide nanocomposites were irradiated with controlled duration of UV exposure and were stained by methylene blue (MB) solutions.

In order to estimate the amount of broken polymer chains after exposure of PI to UV light, its capacity to adsorb MB cations has been determined using following procedure. A film sample, 1 cm × 1 cm by size was weighed and immersed in to 5 mL of 1×10^{-6} mol L^{-1} methylene blue (MB) aqueous solution for 24 h at 22 ± 2 °C. The concentration

of MB before (c_0) and after (c) sorption was determined using UV-Vis spectrometer Neosys-2000 (Scinco). A molar extinction coefficient of 708 L mol^{-1} cm^{-1} was used at a wavelength of 667 nm. Each sample was measured twice and the average was taken to determine the concentration. The amount of methylene blue (α^{PI}) absorbed by neat 6FDA-ODA PI sample was calculated using:

$$\alpha^{PI} = \frac{(c_0 - c)V}{m}$$

(7.2)

where V is the volume of methylene blue solution and m is the mass of the film sample. When PI composite with TiNT was used, the amount of MB sorbed by the sample ($a^{PI/TiNT}$) has two contributions, from pure polymer (a^{PI}) and from titanate nanotubes (a^{TiNT}):

$$a^{PI/TiNT} = a^{PI} + a^{TiNT}$$

(7.3)

The value a^{TiNT} depends mostly on the surface charge and specific area of titanate nanotubes and is not affected by UV radiation [256] therefore that value can be determined by comparisons $a_0^{PI/TiNT}$ and a_0^{PI} measured at dark conditions (prior UV exposure) for composite and neat polymer respectively.

$$a^{TiNT} = a_0^{TiNT} = a_0^{PI/TiNT} - a_0^{PI}$$

(7.4)

The amount of MB sorbed by photodegrading polymer (a^{PI}) for neat and composite polymer material after their UV exposure was calculated using combination of Equations (7.2), (7.3) and (7.4):

$$a^{PI*}(\text{the amount of PI degraded in composite}) = a^{PI/TiNT} - a^{TiNT}$$

(7.5)

Figure 7.5 showed the amount of MB sorbed by photodegraded PI in neat PI (a^{PI}) and by the degraded PI in PI-TiNT (a^{PI*}) composites after the certain duration of their UV exposure.
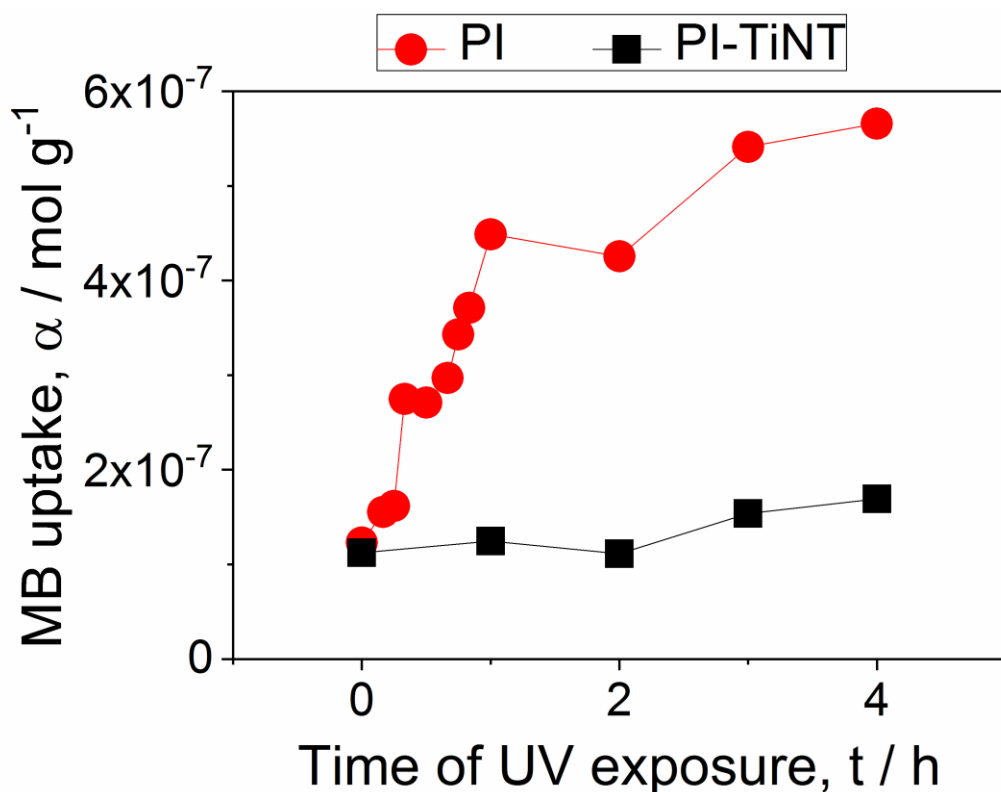
Figure 7.5. Methylene blue (MB) uptake studies of in PI (a^{PI}) (●) and PI-TiNT (a^{PI*}) (■) samples after a certain duration of UV irradiation on the samples.

The absorption of MB in pure polyimide sample significantly increased after UV irradiation while PI-TiNT composite absorption only slightly increased suggesting inhibition of polyimide photodegradation by titanate nanotubes. In the case of the pure polyimide sample, the kinetic curve was characterised by rapid 4 fold increase in concentration of adsorption sites in polymer within 1 hour of UV exposure, followed by plateau after 4 hours [104]. On the contrary, PI-TiNT exhibited only a small increment, even after 4 hours. This result was consistent with Raman spectra (Table 7.1) which implied TiNT protection on chemical bond (C=O bond) of polyimide. The reduction of C-F bond did not produce functional group that can adsorb methylene blue. Thus, no significant changes occurred with or without UV irradiation upon PI-TiNT on the adsorption of methylene blue. However, some stable radical might remained in the sample and reacted with methylene blue leading to discolouration of dye [248,257].

MB adsorption study can be used to identify the majority of moeites created by UV degradation. Based on Raman spectra and literature, the degradation moieties may contain phenol, amine, isocyanate, and carboxylic acid groups. However, large MB adsorption in irradiated polyimide indicated that the degradation moieties dissociated into anion which can be adsorb by cationic dye such as methylene blue. To further confirm the charge of degradation moeites in water, methyl orange has been used as anionic dye instead of cationic dye. The methyl orange uptake in polyimide before irradiation and after 3 hours of irradiation gave no changes implying no attraction between anionic dye and degradation moieties. Phenol, carboxylic acid, and isocyanate were indicated to be the majority of moieties since those groups were able to dissociate into anion in water.

7.2.3 Effect of UV irradiation on physical properties of the film

The effect of UV degradation on the physical properties of the polymer is very dependent on the type of polymer. Moreover, each polymer has several bonds that will produce various type of macro-radical depending on its dissociation energy [258]. Such a large number of possibilities create diverse physical changes such as reduced ductility [259], crosslinking [260], decolouration or yellowing [261], loss of transparency, reduction in toughness [262], cracking, and chalking due to erosion of the polymer surface, exposing filler [263]. In this work, digital microscopy and nanoindentation were used to monitor physical changes of irradiated polyimide (PI) and its nanocomposites (PI/TiNT). Photographs of pure PI and PI/TiNT samples are provided in Figure 7.6.
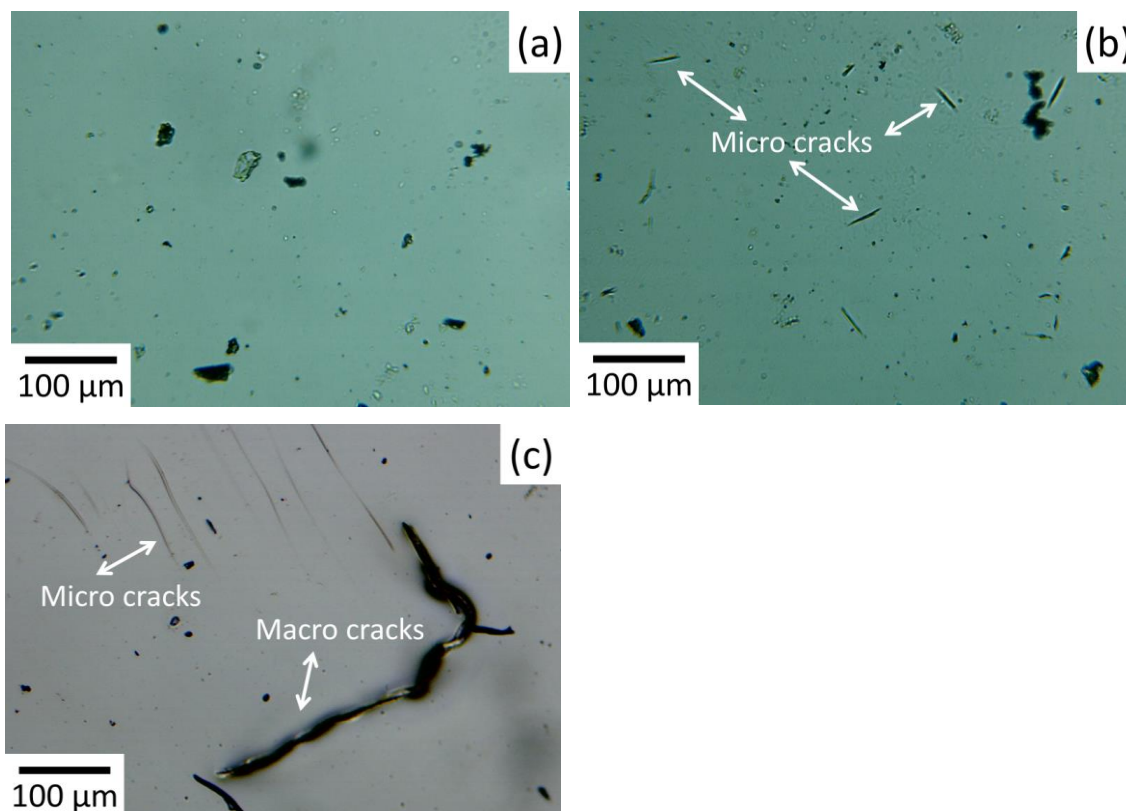
Figure 7.6. Digital optical microscopy images for (a) non-irradiated PI; (b) PI/TiNT after 3 hours irradiation; (c) PI after 3 hours UV exposure.

No crack is shown in pure polyimide without UV irradiation (Figure 7.6 a) whereas, after 3 h irradiation, both PI (Figure 7.6 c) and PI/TiNT in Figure 7.6 b show visible cracks. Absence of chemical bonds such as C=O and C-F bonds produced shorter polymer chain (Table 7.1, Figure 7.1 and 7.5) triggering the formation of cracks. Irradiated PI/TiNT nanocomposite has shorter cracks than irradiated PI which is ≈40 µm and >100 µm for PI/TiNT and PI, respectively. Both micro and macro cracks appeared in irradiated polyimide (Figure 7.6 c). TiNT protected the C=O bond from degradation, as confirmed by Raman spectra in Table 7.1, preventing further propagation of cracks.
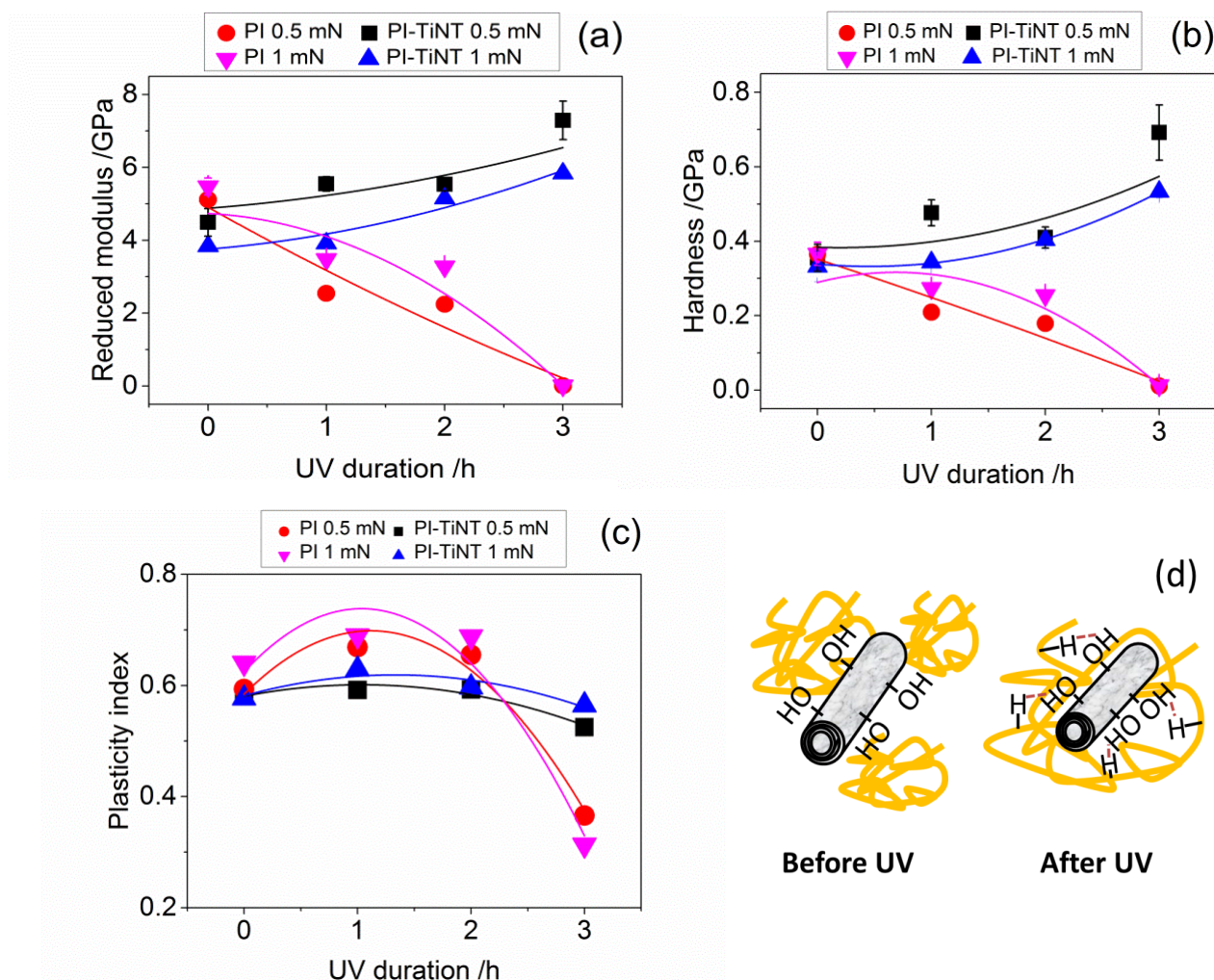
Figure 7.7. Nanoindentation studies of PI and PI/TiNT with 0.5 mN and 1 mN applied load; (a) reduced modulus, (b) hardness, (c) plasticity index as a function of UV exposure time, (d) illustration of the crosslinking between TiNT and irradiated PI by hydrogen bonds.

A nanoindentation study was conducted to examine the effect of UV irradiation on mechanical properties of pure PI and PI/TiNT nanocomposite. The effect of UV light on modulus, hardness, and plasticity index of PI and PI/TiNT is shown in Figure 7.7. The effect of UV on the hardness and the modulus of pure PI contrasted from PI-TiNT nanocomposite. UV irradiation increased hardness and modulus of PI/TiNT while reduced the hardness and modulus of PI. The effect became more prominent after 3 hours of irradiation. It is known that amorphous part of polymer is more susceptible than crystalline part to UV degradation. 6FDA-ODA polyimide is an amorphous polymer with low chain packing order due to the presence of bulky

hexafluoroisopropylidene group [264]. Chain cleavage on such amorphous polyimide may cause direct reduction on hardness and modulus in Figure 7.7 a and b. In contrast, the increase in hardness and modulus was observed in PI/TiNT nanocomposite sample. Crosslinking between titanate nanotube and polyimide may occur via hydrogen bonding which illustrated in Figure 7.7 d. Crosslinking of filler and polymer matrix was known to strengthen interfacial bond between filler and matrix leading to higher mechanical properties of composite [265].

Brittleness is also one of the physical changes that may occur due to UV attack. Instead of hardness and modulus, plasticity index has more correlation with brittleness. Plasticity index is a dimensionless property measuring the ability of material to plastically deform before breaks [266]. The formula can be expressed by:

$$Plasticity\ index = W_p/(W_p + W_e) \tag{7.9}$$

where W_p and W_e is plastic work and elastic work done during nanoindentation, respectively. The value of plasticity index is varied from 0 to 1, where 0 for the most brittle material and 1 for the most ductile material. Plasticity index for PI and PI/TiNT can be seen in Figure 7.7 c. For 0.5 mN applied load, the plasticity index of pure polyimide sample reduced significantly after 3 hours of UV irradiation (38 %) while only slight decreased observed for PI/TiNT (10 %) compared to non-irradiated samples. This also indicated that titanate nanotubes may protect the polyimide from UV attack. The shielding effect of titanate nanotubes is more prominent at 1 mN applied load. Plasticity index reduced by 51 % and 2 % for PI and PI/TiNT, respectively after 3 h UV irradiation indicating that titanate nanotubes protected the polyimide underneath from further damage.

7.3   Effect of UV irradiation on PMDA-ODA/TiNT nanocomposites

7.3.1   Effect of UV exposure on PMDA-ODA polyimide

Instead of 6FDA-ODA based polyimide, the effect of UV exposure was also tested for PMDA-ODA, which was made by the pyromelitic anhydride and oxydianiline as monomers. Pure polyimide (PI) sample (PMDA-ODA with 3 days polymerisation of 20 wt% of polyamic acid) was exposed to UV radiation for 2 days. Then, FTIR, digital microscope, digital camera, and UV-vis spectrometer were used to investigate the sample. There are significant changes in transparency which are shown in Figure 7.8.
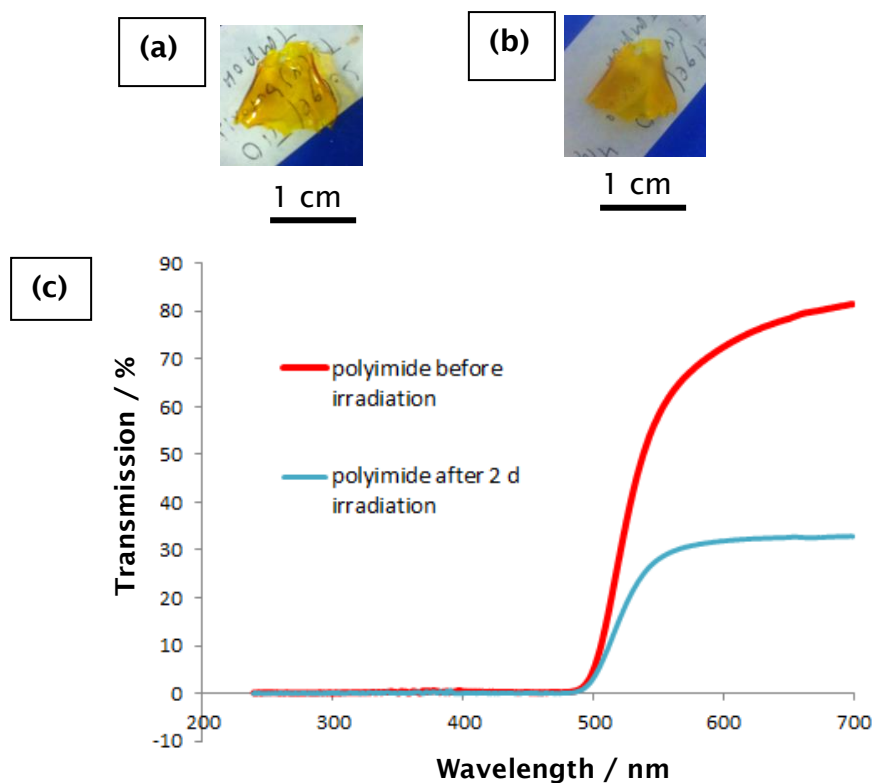
Figure 7.8. Effects of UV irradiation on transparency of polyimide (3 days polymerisation of 20 wt% polyamic acid): (a) image of polyimide before UV irradiation, (b) image of polyimide after UV irradiation, (c) UV-vis spectra of polyimide before and after UV irradiation (thickness ≈100 microns).

After UV irradiation, some transmitted visible light (from 500-700 nm) through polyimide was reduced more than half which proven by digital images and UV-vis

spectra. This phenomenon was caused by light scattering which is induced by bubbles and surface roughness. The bubbles and surface roughness were investigated by digital microscope (Figure 7.9).
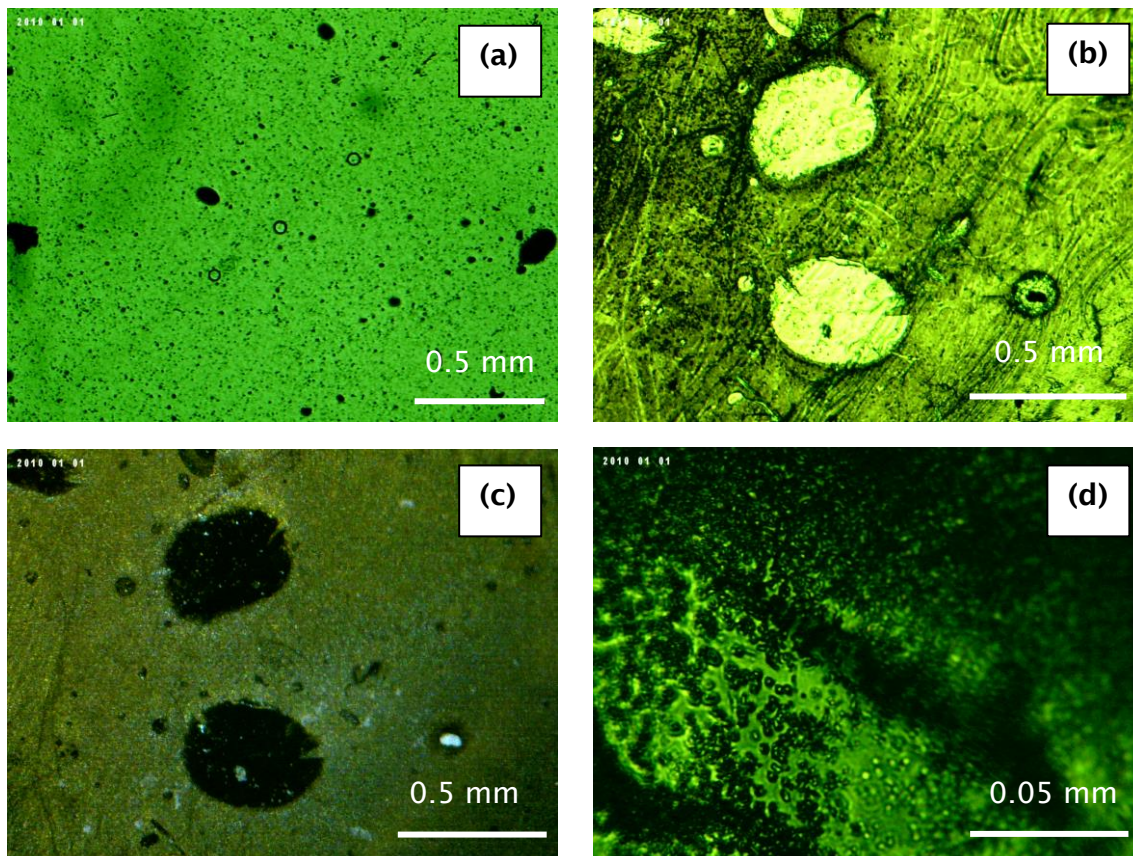
Figure 7.9. Images of polyimide films by digital microscope: (a) polyimide before UV irradiation, (b) polyimide after 2 days UV irradiation, (c) reflective image of polyimide after 2 days UV irradiation, (d) polyimide after 2 days UV irradiation.

There was no reflective image of non-radiated polyimide because the majority of light is transmitted through the sample. Moreover, only few of bubbles and some dirt spotted in the polyimide film before UV irradiation (Figure 7.9 a). After 2 days UV irradiation, most of the surfaces were able to reflect the light thus giving a reflective image of polyimide (Figure 7.9 c). However, some regions in irradiated polyimide were still transparent to the visible light (black holes in Figure 7.9 c). The reflective parts of polyimide after UV exposure were caused by a lot of tiny bubbles that induce light refraction and scattering (Figure 7.9 d). These bubbles and surface roughness were presumably produced by chain scissions of polyimide thus generating some radicals and

new compounds. FTIR was used to evaluate the differences in chemical bonds of polyimide before and after radiation (Figure 7.10).
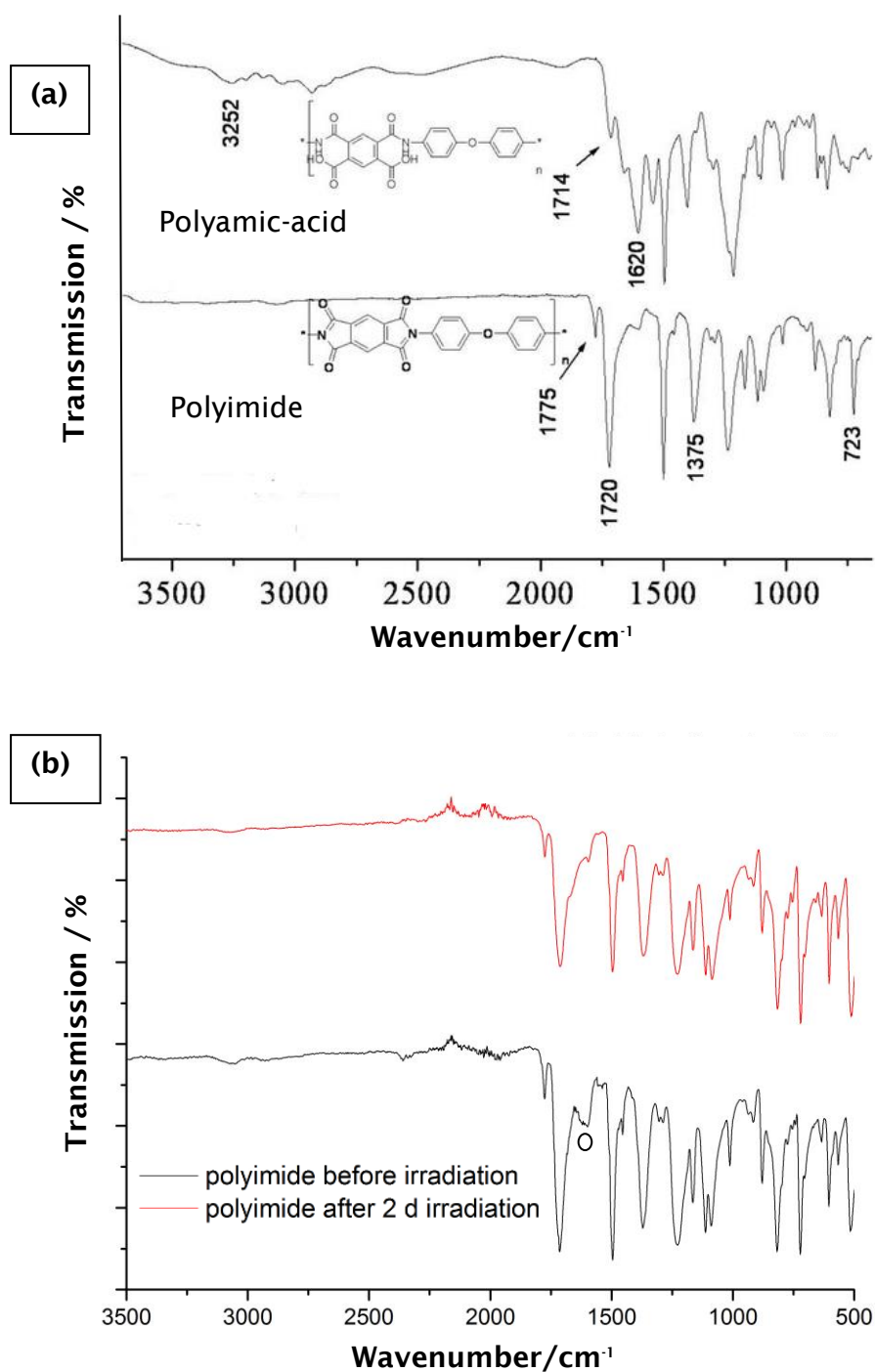
Figure 7.10. FTIR spectra of PMDA-ODA polyimide: (a) FTIR spectra of polyamic-acid and polyimide from literature [202], (b) FTIR spectra of polyimide before and after irradiation in this work.

There was no significant difference in the FTIR spectra of polyimide before and after irradiation. Nevertheless, there was a small peak around 1620 cm^{-1}, which resemble the N-H bend of polyamic-acid (see Figure 7.10 a and 7.10 b (white dot)). This peak showed that the imidization process in the polyimide sample was not complete. It was known that imidization can also occur by UV exposure [267]. Hence, the disappearance of polyamic-acid peak after UV irradiation was caused by UV imidization. However, the hydrogen bond of water as a by-product of imidization did not appear in polyimide sample after 2 days UV irradiation. The water was evaporated and become bubbles thus its chemical bond was more difficult to detect by FTIR.

The large amount of bubbles were probably produced by the photo-oxidation process that created water vapour. The water vapour was generated in the chain propagation process of photo-oxidation.

Initial step : Polyimide (PH) → P● + P●

Chain propagation :   P● + O_2 → POO●

POO● + PH → POOH + P●

POOH → PO● + ●OH

2POOH → PO● + POO● + H_2O

PH + ●OH → P● + H_2O
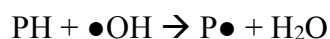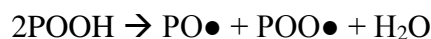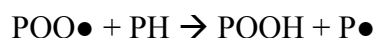
The origin of bubbles and surface should be investigated further by other characterisation methods such as electron paramagnetic resonance (EPR) or electron spin resonance (ESR) spectroscopy, and X-ray photoelectron spectroscopy (XPS).

7.3.2   Incorporation of scrolled titanate nanosheets and its effect on UV degradation of PMDA-ODA polyimide

0.5 wt% scrolled titanate nanosheets (STiNS, fabricated by hydrothermal method) was used to synthesis titanate-polyimide nanocomposites by *ex-situ* method, where the titanate added after 1 day polymerisation of PMDA-ODA. All the titanate were coated

by CTAB to prevent the hydrolysis of polyamic acid by hydroxyl groups of titanate. The effect of UV irradiation on scrolled titanate nanosheets-polyimide (STiNS-PI) nanocomposite was investigated by digital microscope, digital camera, and UV-vis spectrometer. The changes in transparency of STiNS-PI nanocomposite and its comparison with pure PI were shown in Figure 7.11.
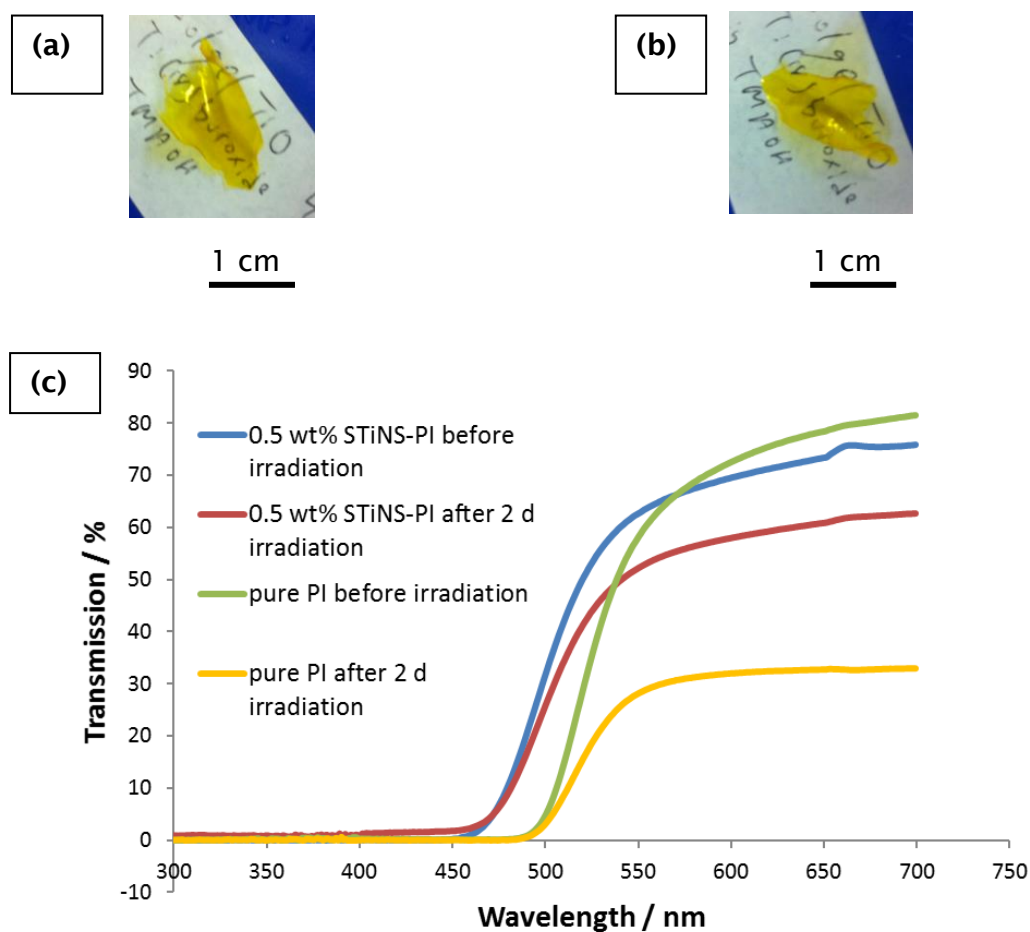
Figure 7.11. Effects of UV irradiation on transparency of 0.5 wt% STiNS-PI nanocomposites (3 days polymerisation of 20 wt% polyamic acid): (a) image of STiNS-PI nanocomposite before UV irradiation, (b) image of STiNS-PI nanocomposite after UV irradiation, (c) UV-vis spectra of STiNS-PI nanocomposites before and after UV irradiation (thickness ≈100 microns).

The incorporation of 0.5 wt% STiNS within polyimide (PI) slightly affected the transparency of the film in the visible region, due to the scattering of light by dispersed STiNS within the composite film. Interestingly, the colour of polyimide also affected by STiNS, which the absorbance of wavelength around 500 nm shifted to 450 nm by

addition of STiNS shown in Figure 7.11 c. Hasegawa *et.al.* concluded that there are three factors which affected the visible light absorption of polyimide [83]. These three factors has been discussed in Chapter 2.2.4, which are the charge transfer in the chain sequence, the use of fluorinated monomers, and the use of aliphatic monomers [83].

Same monomers were used which eliminated the possibility of the absorption shifting due to the choice of monomers. Charge transfer complex (CTC) of polyimide is related to electron-accepting characteristic of dianhydride and electron-donating properties of diamine. The electron accepting and donating properties influence the intra and intermolecular interaction of chains. The visible light absorbance improves as the intra and intermolecular interaction increases. Disturbance in chains such as steric hindrance is needed to lowered the intra and intermolecular interaction. According to Jeneke *et.al.* the glass transition (T_g) of polymer increased as the intermolecular interaction decreased [268]. It was shown in Chapter 6.2.4, that the incorporation of 0.5 wt% of titanate dramaticly increased the T_g of polyimide. During the imidisation process, crosslink may occur between titanate and polyimide causing complexation of forces in polyimide, which ultimately decreased the intermolecular interaction in polymer chains resulting in lower visible light absorption.

The transparency of STiNS-PI nanocomposite was slightly decreased after 2 days UV irradiation. The transmittance of STiNS-PI nanocomposites was reduced from 70 % to 58 % at a wavelength of 600 nm. This reduction was relatively small compare to pure polyimide samples. The transmittance of pure polyimide sample was decreased from 73 % to 32 % at a wavelength of 600 nm. Nonetheless, bubbles were still generated which observed by digital microscope. The images of STiNS-PI nanocomposites before and after 2 days UV irradiation were shown in Figure 7.12.
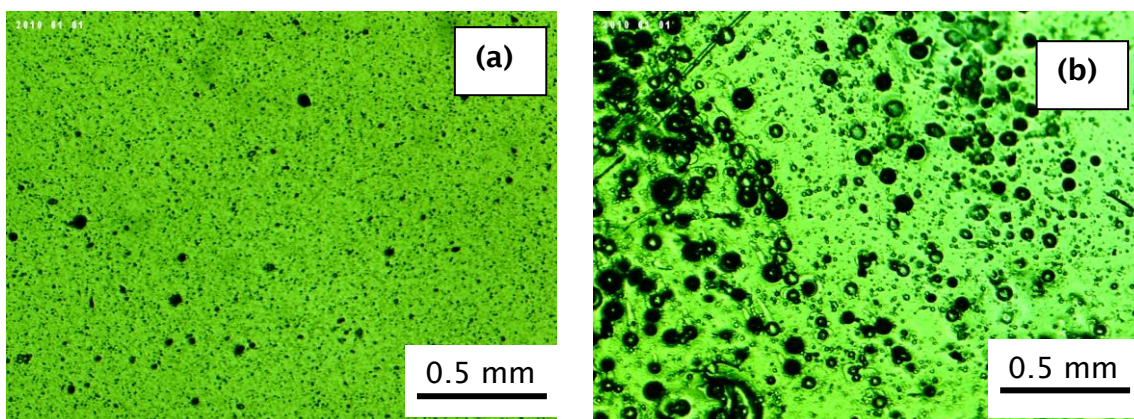
Figure 7.12. Images of 0.5 wt% STiNS-PI nanocomposite films by digital microscope: (a) STiNS-PI nanocomposite before UV irradiation, (b) STiNS-PI nanocomposite after 2 days UV irradiation.

As shown in Figure 7.12 b, bubbles of the size of ≈5 microns were formed after 2 days of UV exposure. Though the size of the bubbles was bigger than 2 days irradiated pure polyimide sample (≈0.35 microns), the number of bubbles was greatly reduced. This showed that the titanate nanosheets covered some part of polyimide nanocomposites. Therefore, the generation of bubbles was focused on the spot that are not covered by titanate nanosheets. However, the protection of UV degradation was not highly reproducible (1 out of 3) which may be due to imperfect dispersion of nanosheets on the polymer surface.

7.4 Conclusions

The effect of UV exposure on 6FDA-ODA polyimide (PI) and polyimide-titanate nanotubes (PI/TiNT) nanocomposite was also studied. To monitor chemical changes, Raman spectroscopy was used and MB adsorption method was adapted to detect degradation moieties. Raman spectra proved that UV light was able to eliminate some C=O and C-F bonds in polyimide. In PI/TiNT nanocomposites, there were no changes in C=O bonding and the reduction of C-F bonding was less than in pure PI, implying the protection of polyimide by titanate nanotubes. Based on Raman spectra and existing literature [103,254,255,269], UV degradation mechanism of 6FDA-ODA was proposed. Functional group such as phenol, amine, and carboxylic acid might be created and adsorbed methylene blue by hydrogen bonding. In PI sample, a significant increment of

MB absorption was observed after a few minutes and reached its plateau after 1 h due to more liberation of gas and rearrangement of chemical groups. In PI/TiNT sample, the absence of degradation moieties, that can adsorb methylene blue, yielded no significant change on PI/TiNT sample even after 4 h of UV irradiation.

Physical changes of PI and PI/TiNT samples were studied by digital microscope and nanoindentation. Shorter cracks ($\approx$40 μm) appeared in PI/TiNT samples while >100 μm long cracks were visible in PI after 3 hours of UV exposure. The cleavage of C=O bonds in PI samples initiated a large crack. UV irradiation increased hardness and modulus of PI/TiNT but reduced the hardness and modulus of PI. Backbone chain of 6FDA-ODA polyimide, which is an amorphous polymer, might prone to UV light reducing its hardness and modulus. Whereas for PI/TINT, crosslinking of titanate nanotube and polyimide via hydrogen bonding may strengthen interface between TiNT and PI. Brittleness was studied by comparing plasticity index which varied from 0 to 1 (0 corresponding to the most brittle material and 1 for the most ductile one). Compared to non-irradiated samples, plasticity index at 1 mN applied load reduced by 51% and 2% for PI and PI/TiNT, respectively after 3 h UV exposure indicating that titanate nanotubes protected the polyimide underneath from further damage.

Two days UV irradiation of pure PMDA-ODA polyimide sample greatly reduced the transparency of polyimide (from 73 % to 32 % at a wavelength of 600 nm) due to the formation of large amount of tiny bubbles. These bubbles were induced by photo-oxidation and imidization of polyamic-acid residue. The addition of 0.5 wt% scrolled titanate nanosheets reduced the number of bubbles thus the transparency only slightly decreases (70% to 58% at a wavelength of 600 nm) compared to un-irradiated nanocomposite sample. However, the inhibition of PMDA-ODA polyimide UV degradation was not highly reproducible (1 out of 3) which may be due to poor dispersion of nanosheets on the polymer surface of unprotected samples.

Chapter 8:   Conclusions and Suggestions for Further Work

8.1   Conclusions

The work presented in this thesis was addressed to elucidate the effect of incorporation of titanate nanostructures, namely titanate nanosheets (TiNS), titanate nanotubes (TiNT), and scrolled titanate nanosheets (STiNS), on the properties of polyimide based nanocomposites with focus on its ultraviolet (UV) resitance. In addition of polymer nanocomposites film, the preparation of polyimide-titanate fibres was also discussed.

In the first part of this project, all the synthesis methods for titanate nanosheets such as Sasaki's method, hydrothermal method, and sol-gel were performed. For titanate nanosheets (TiNS) made by Sasaki's method, aluminium compound impurities was observed due to reaction of alkali precursor with aluminosilicate crucible, while for platinum crucible samples, there were no such impurities. The number of aluminium impurities was reduced by centrifugal force although the concentration of TiNS was also decreased by 3 times. The stability of colloidal suspension is influenced by surface charge (alumina impurities affected surface charge of samples) and the type of the solvent (water and DMAc were better than ethanol) for scrolled titanate nanosheets (STiNS). The study of the titanate morphology, its concentration, and the titanate stability in solvent were used as a base knowledge to synthesis the polymer nanocomposite.

In the Chapter 5, the effect of incorporation of titanate nanostructures such as titanate nanosheets (TiNS), titanate nanotubes (TiNT), and scrolled titanate nanosheets (STiNS) on the mechanical properties of water-soluble polyimide precursor (polyamic acid salt) was studied. One must note that in unstable suspension, shorter settling time is necessary to avoid agglomeration. The hardness increases by 90 % on addition of 2 % TiNS while the modulus increases by 103% compared to the pure polymer. Preffered orientation of dispersed nanosheets within the polymer matrix (parallel to the surface) was observed by SAXS. This reinforcement behaviour corresponded well with Halpin-Tsai theory [180] at low filler content (up to 1 wt%)   assuming the filler has a

unidirectional orientation. Brune-Bicerano model, a prediction for incomplete exfoliation of nanosheets within polymer, was matched with TiNS reinforcement at 2 wt% of TiNS with 3 stacks of nanosheets agglomerates. 'Skewed'/elongated agglomerates were observed at high filler loadings (>2 wt%), and made nanocomopsites properties lower than established theories. These agglomerates may disturb the stress distribution between nanosheets and the polymer. The morphology of the elongated agglomerate did not match with the Brune-Bicerano model [191] which only considers sheets stacking in a parallel direction thus revision of the model is recommended.

Unexpectedly, titanate nanotubes have a higher reinforcement ability although it have a lower aspect ratio ($l/h = 4$) and random orientation. The hardness and modulus of the polyamic acid salt increased 91 % and 165 % by addition of 2 wt% titanate nanotubes respectively. Titanate nanotubes made by hydrothermal synthesis may have higher mechanical properties than bulk TiO_2 which was used as an assumption in theoretical predictions. However, the reinforcement reached a plateau after 2 wt% of TiNT due to aggregation of TiNT. The effectivity of the reinforcement can be reflected by value of the hardness particle strengthening factors of the nanostructures (TiNS, TiNT, and STiNS), which are 0.8, 0.8, 0.3 for TiNS, TiNT, and STiNS respectively. The low reinforcement ability of scrolled titanate nanosheets (STiNS) may be caused by its random orientation, while it is possible that STiNS might have anisotropic mechanical properties such as titanate nanosheets (TiNS) made by exfoliation of solid state reaction [138].

Three types of polyimide matrix were synthesised in this work, which are semi-aromatic polyimide (BOCA-ODA), fully aromatic polyimide (PMDA-ODA) and fully aromatic fluorinated polyimide (6FDA-ODA). A thick and relatively flexible aromatic polyimide (PMDA-ODA) film was successfully synthesised by two-step method. However, semi-aromatic (BOCA-ODA) polyimide created thin and very brittle film which possibly due to very low viscosity and prone to water precipitation. The polymerisation duration for PMDA-ODA was varied from 1 to 3 days and it was found that 2 days polymerisation gave the best nanotribological properties indicating optimum polymerisation before it started to degrade. CTAB coating of the nanotubes was essential to prevent hydrogyl group of titanate from inhibiting the polymerisation. However, the the viscosity of polyimide precursor solution was still reduced by the addition of CTAB coated titanate

nanotubes. This reduction was caused by selective absorption of high molar mass polyamic acid on TiNT, leading to a reduction in entanglement density and an improvement in chain mobility. The reduction of viscosity reduced the production of kinked and intertwined fibre after chemical imidization. However, the formation of beads was observed at a very low viscosity (2870 mPa s) suggesting that higher viscosity is beneficial to creation of bead-free nanofibres.

The glass transition temperature (T_g) was increased from 407 ºC to 476 ºC by the incorporation of titanate nanotubes (0.1 wt %) to the PI matrix either by *in-situ* and *ex-situ* method. Strong covalent bonding may occur between hydroxyl groups on the surface of titanate nanotubes and the polyamic acid during imidization which restricted the polymer chain mobility. The same T_g in both *in-situ* and *ex-situ* composites implied that addition of titanate nanotube did not affect the degree of PAA polymerization. The addition of 0.1 wt% titanate nanotubes had no significant effect on modulus and hardness of polyimide. However, the attempt to increase the concentration of stable colloidal suspension of TiNT in organic solvent such as DMF using PEI (Mw 25000 g mol^{-1}) yielded no siginificant effect suggesting another approach or using lower molecular weight PEI. To fabricate aligned titanate nanotube within polyimide fibres, the use of stable colloidal suspension was recommended, whether concentrated (as used in *ex-situ* samples) or not (as used for *in-situ* samples). Dispersion of titanate nanotubes within polyimide fibres was also improved using stable colloidal solution.

In the Chapter 7, the effect of incorporating titanate within polyimide on its resistance to UV degradation was evaluated. Two days UV irradiation upon PMDA-ODA polyimide significantly decreased its transparency (from 73 % to 32 % at a wavelength of 600 nm) due to the formation of large amount of tiny bubbles, which might be induced by photo-oxidation and imidization of polyamic-acid residue. The addition of 0.5 wt% scrolled titanate nanosheets reduced the number of tiny bubbles yielding only slightly decreased of transparency (70 % to 58 % at a wavelength of 600 nm) compared to un-irradiated nanocomposite sample. However, the inhibition of PMDA-ODA polyimide UV degradation was not highly reproducible which may be due to inhomogenous dispersion of nanosheets on the polymer surface of unprotected samples.

Lastly, the effect of titanate nanotubes (TiNT) on UV resistance of 6FDA-ODA polyimide (PI) was also studied. 6FDA-ODA polyimide was the most prone polyimide

to UV exposure, which may spontaneously created degradation products upon UV irradiation. Raman spectroscopy and MB adsorption method was adapted to monitor chemical changes. Raman spectra indicated that UV exposure was able to eliminate some C=O and C-F bonds in polyimide. Whereas in PI/TiNT, there were no significant changes in C=O bonding and the C-F bonding only slightly reduced compared to pure PI, implying the protection of polyimide by titanate nanotubes. Based on Raman spectra and literature [103,254,255,269], UV degradation mechanism of 6FDA-ODA was proposed. Functional group such as phenol, amine, and carboxylic acid might be created and adsorbed methylene blue by hydrogen bonding. A significant increment of MB absorption was observed after a few minutes in PI samples and reached its plateau after 1 h which probably due to liberation of gas and rearrangement of chemical groups. In PI/TiNT sample, there was no significant change even after 4 h of UV irradiation possibly due to the absence of degradation moieties that can adsorb methylene blue.

Physical changes of PI and PI/TiNT samples were examined by digital microscope and nanoindentation. Long cracks (>100 µm) were observed in PI while shorter cracks (≈40 µm) were visible in PI/TiNT samples after 3 hours of UV exposure indicating the C=O bonds cleavage, which occurred only in pure PI, took part in cracks formation. UV irradiation improved hardness and modulus of PI/TiNT but reduced the hardness and modulus of PI. 6FDA-ODA polyimide, which is an amorphous polymer, might prone to UV damage reducing its mechanical properties. In PI/TINT samples, slight degradation on polyimide (indicated by Raman) may help to strengthen interface between TiNT and PI by crosslinking of titanate nanotube and polyimide via hydrogen bonding may. Brittleness, which is an indicator of UV damage, was evaluated by comparing plasticity index (0 corresponding to the most brittle material and 1 for the most ductile one). Plasticity index at 1 mN applied load reduced by 51 % and 2 % for PI and PI/TiNT, respectively, after 3 h UV exposure compared to non-irradiated samples indicating inhibition of UV degradation of polyimide by incorporation of titanate nanotubes.

To sum up, titanate nanostructures have been synthesised by Sasaki's, hydrothermal, and sol-gel methods, which inhibits photodegradation of aromatic fluorinated polyimide (6FDA-ODA). The degradation rate and moieties were estimated by cationic and anionic dye immersion. The titanate has also improved the mechanical properties of water-based polyimide precursor and the thermal properties of PMDA-ODA polyimide.

8.2 Suggestions for Further Work

8.2.1 Synthesis of titanate nanosheets

Titanate nanosheets were successfully synthesised using Sasaki's method, hydrothermal method, and sol-gel method based on literature. An attempt of using cheaper crucible such as aluminosilicate crucible was performed. However, some impurities were appeared (e.g., unreacted titania, aluminium compound). Centrifugation was applied to separate titanate nanosheets with aluminium compound. However, the concentration reduced by 3 times. Other approaches are recommended such as dissolution of aluminium compound without damaging titanate nanosheets by controlling acidity or basicity.

8.2.2 Incorporation of titanate nanostructures into water-soluble polyamic acid salt

The effect of incorporation of titanate nanostructures within water-soluble polymer was studied systematically. It was found that the addition of titanate nanostructures were able to significantly improves the mechanical and dielectric properties of polymer. Preffered orientation of nanosheets within polymer was observed for titanate nanosheets while titanate nanotubes and scrolled titanate nanosheets were dispersed randomly. The scope of this work can be extended through investigation of the following:

- Experiment with different polymer matrix which has positive zeta potential in aqueous solution is necessary to strengthen the bond between negatively charged titanate and the polymer.

- Investigation on the mechanical properties of titanate nanotubes made by hydrothermal method is needed as our result has shown that the mechanical properties of TiNT might higher than bulk TiO_2. It can be studied experimentaly, using atomic force spectroscopy [270], thermal observation by micro-raman [271] and TEM [272], or theoreticaly [273].

- Doping of titanate nanotubes might be needed to reduce the dielectric loss of titanate nanotubes. The study can be further extended to application of doped titanate nanotubes reinforced dielectric elastomer.

8.2.3   Synthesis of titanate-polyimide nanocomposites

The novel research about incorporation titanate nanostructures into non-soluble PMDA-ODA polyimide was done by *in-situ* and *ex-situ* approaches in Chapter 6. It was found that the addition of even small amount of titanate (0.1 wt%) significantly increased glass transition temperature of polyimide by *ca.* 69 °C. Microfibres of polyimide-titanate nanocomposites were achieved with aligned titanate within the fibres. The effect of titanate on physical properties of polymer such as viscosity and mechanical properties was also studied. However, more concentrated titanate nanostructures are needed to improve the mechanical properties of polyimide. Further work is needed to systematically study several approaches (e.g., functionalization, mechanical treatments) to improve the concentration of titanate nanotubes in organic solvent such as DMF while maintaining highly homogenous dispersion.

8.2.4   Inhibition of polymer UV degradation by incorporation of titanate nanotubes

The protection of 6FDA-ODA polyimide from UV damage by titanate nanotubes was presented. Novel method to characterise the chemical changes of polyimide by cationic and anionic dye immersion was also explored. Calculation using adsorption isotherm at equilibrium concentration might as well be perform to eliminate the possible reaction from the radical left in the samples. Comparison with exsisting characterisation which is able to give early detection of chemical changes such as electron spin resonance (ESR) is recommended.

Appendix A : Insertion of Titanate Nanosheets and Nanotubes in Anodized Titania Nanotubes Array

A.1 Preparation of TiNT, TiNS, and TiO$_2$NT

A method to insert titanate nanotubes (TiNT) and nanosheets (TiNS) into anodized titania nanotubes (TiO$_2$NT) array using mechanical stimulated electrophoretic deposition was developed under collaboration with Alysson S. Martins. TiNT were prepared by the alkaline hydrothermal method [274]. 10 mol L^{-1} of KOH:NaOH 1:25 was mixed with 25 g TiO$_2$ (Degussa P25). The solution was stirred and kept under reflux for 2 days at 100 $^{\circ}$C. To convert the TiNT to their protonated form, the resulting powder was washed with 0.1 mol L^{-1} HCl until it reached pH 2. The powder was washed with water to achieve the pH 5 then it was dried under vacuum. TiNS were made by sol-gel method as describes in Chapter 3.1.3 and Chapter 4.5.

The titanium (Ti) foils (99 % purity, 1 mm thickness and 2.4 × 2.4 cm^2 area) was used for growth of TiO$_2$NT which were previously polished with SiC paper of successively finer particle sizes of 320, 400, 800 and 1200 grit. The foils were cleaned in isopropyl alcohol, acetone and ultrapure water (1.3 μS cm^{-1}) respectively in an ultrasonic bath for 5 minutes then dried under N$_2$ gas. Anodising was performed in a cell containing a titanium plate anode and a planar stainless steel cathode at a distance of 1 cm. The electrolyte used was 0.3 % HF and 1 mol L^{-1} NaH$_2$PO$_4$ in aqueous solution. The applied potential was increased by 1 V every 30 seconds until it reached 20 V then held constant for 2 hours using a DC power supply [275]. The electrodes were washed with ultrapure water, dried with N$_2$ gas and calcined at 450 °C for 2 hours at a linear heating rate of 2 °C min^{-1}. The morphologies of TiNT, TiNS, and TiO$_2$NT are provided in Figure A.1.
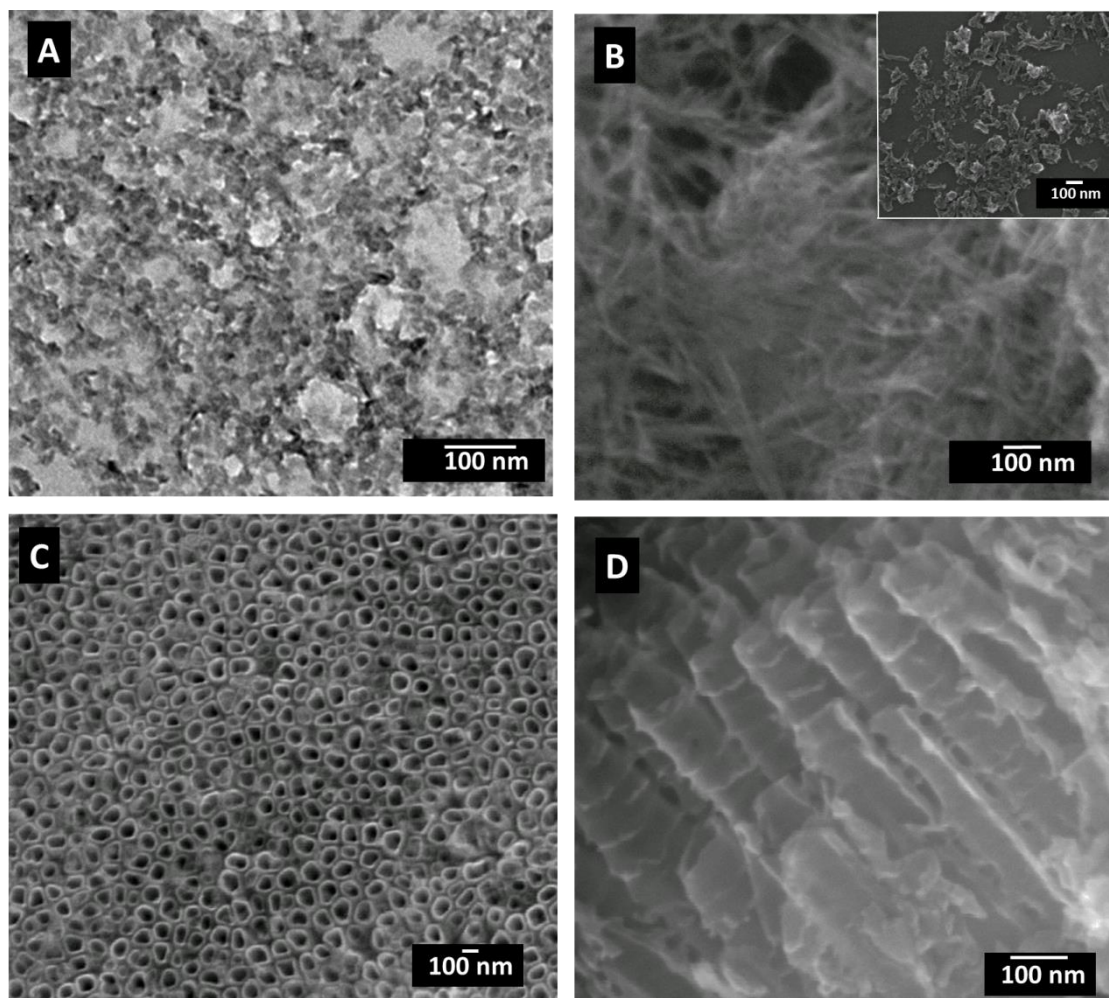
Figure A.1. SEM images of TiNS (A); TiNT (B); top view (C) and cross section (D) of TiO$_2$NT.

A.2 Insertion of TiNT or TiNS into TiO$_2$NT

The mechanically stimulated insertion was done as follows. A suspension of 100 mg L^{-1} TiNT was sonicated for 3 hours to decrease the average nanotube length; this procedure reduced the size of TiNT to ≈100 nm (inset in Figure A.1 b) facilitating the insertion into TiO$_2$NT. The EPD was carried out onto the surface of TiO$_2$NT (2.4 × 2.4 cm^2) where was added 1 cm^3 of the electrolyte containing 5 vol% of the titanate suspension (TiNS or TiNT) dispersed in a mixture of methanol and water (50:50 vol%); the conductivity resultant was 859 and 5 μS cm^{-1} for TiNS and TiNT electrolyte, respectively. The TiO$_2$-NT Ti anode and the stainless steel cathode were kept parallel at distance of 0.5 mm to maintain a thin-film electrolyte thickness of 0.5 mm on the surface. The anodic potential applied to the cell was 20 V for 20 minutes at 25 °C. To

avoid blocking the surface of TiO_2-NT with titanates, a modified brush, which consists of nylon bristles, was used near the counter electrode. Figure A.2 shows a schematic of the arrangement and the expected behaviour; the brush of the counter electrode swept excess TiNT or TiNS in electrolyte preventing a compact layer of titanates on the surface of TiO_2NT. The linear movements of the brush (indicated by arrow in Figure A.1 c and d) were controlled manually by hand at a rate approximately 1 cm s^{-1}. The titanates can then be incorporated within anodized nanotubes in the presence of the potential gradient.
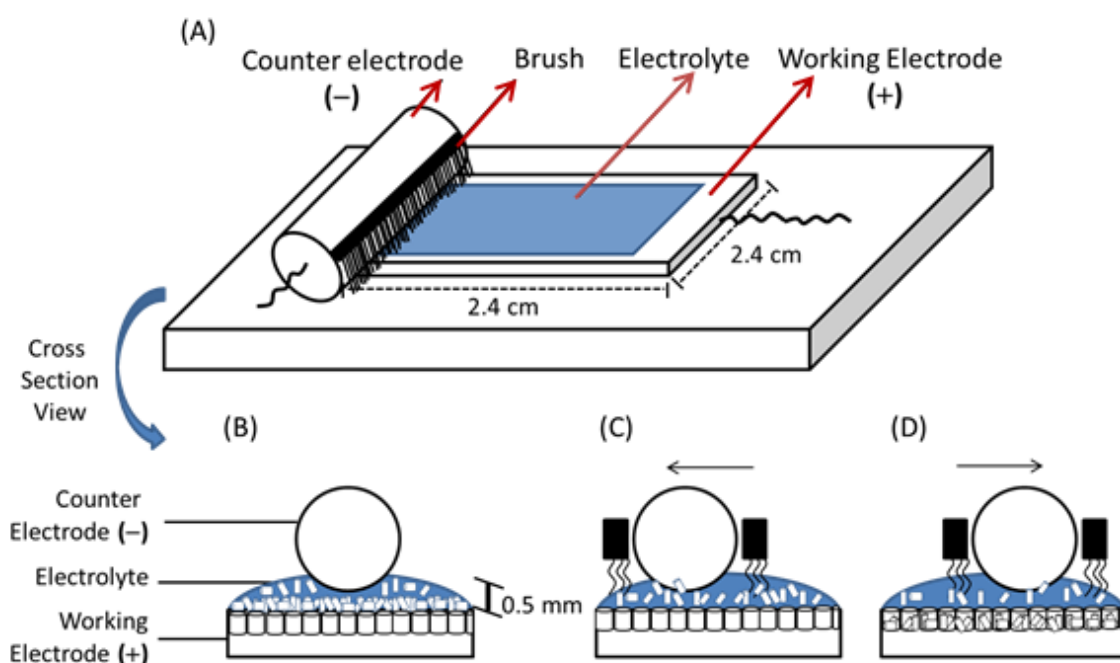
Figure A.2. Schematic of electrophoretic deposition of titanates into the pores of TiO_2-NT using a brush modified surface treatment (A); generating compact layer of titanates in the substrate of TiO_2 nanotubes (B); brush moving the titanates in the surface (C) and incorporation of titanates inside of pores of the TiO_2 substrate (D).

The mechanically stimulated electrophoretic deposition of TiNT and TiNS into TiO_2NT was compared with drop casting method. The 1 cm^3 suspension of TiNT or TiNS (5 vol%) in a mixture of methanol and water (50:50 vol%) was drop casted ($\approx$1 mL) on the surface of TiO_2NT (2.4 × 2.4 cm^2). The resulting depositions were examined by SEM in Figure A.3. It was shown in drop casting samples TiNT and TiNS did not properly inserted into the inner pores of TiO_2NT but covering the top of TiO_2NT. On the other

hand, insertions using mechanically stimulated EPD yielded incorporation of TiNT or TiNS into the inner pores of TiO$_2$NT besides the top of TiO$_2$NT were laid bare.
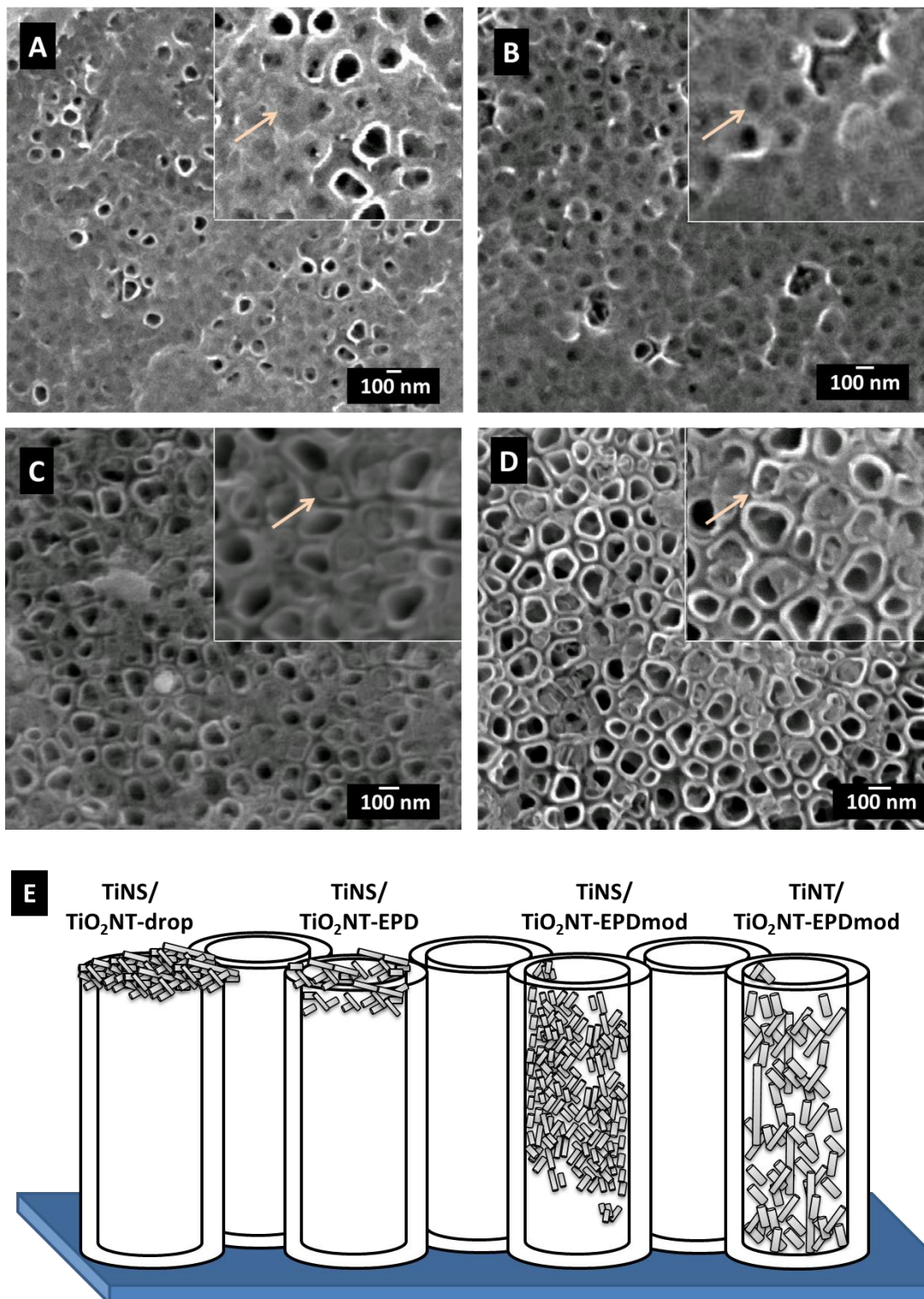
Figure A.3. SEM images of (A) TiNS/TiO$_2$NT-drop; (B) TiNS/TiO$_2$NT-EPD; (C) TiNS/TiO$_2$NT-EPDmod and (D) TiNT/TiO$_2$NT-EPDmod. The pores indicated by the arrows in the insets are schematically represented in (E).

Appendix B : The effect of titanate nanotubes on the polyamic acid salt dielectric

Titanate nanotubes are known to have a huge dielectric constant (ε' >10^4 at frequency lower than 10^3 Hz) which is comparable to other dielectric materials such as $CaCu_3Ti_4O_{12}$, Li and Ti doped NiO [276]. Dielectric constant or relative permittivity (ε') is the ability of material to be polarised under influence of an applied electric field. This indicates the capacity of the material to store the electric energy by means of polarisation. The effect of incorporation of titanate nanotubes within polyamic acid salt on its dielectric properties was studied.

B.1 Dielectric measurement

Dielectric spectroscopy was performed in Electronic and Computer Science, University of Southampton using a Solatron 1296 dielectric interface along with a Schlumberger SI 1260 impedance/phase gain analyser on specimens 10 mm in diameter. Before testing, an area of a circle with diameter of 1 cm of the film samples was sputter coated with gold on both sides to provide a better sample/electrode contact. Alternative current (AC) impedance measurements were performed at room temperature ($\approx$23 ^{o}C) over the frequency (f) range 0.1 Hz - 1 MHz. The real ($Z'(\omega)$) and imaginary ($Z''(\omega)$) parts of impedance were denoted as a function of angular frequency (ω), where $\omega = 2\pi f$. The complex impedance can be extracted based on the relation of $Z^*(\omega) = Z'(\omega) - iZ''(\omega)$, where $i = \sqrt{-1}$. These impedance parameters were deployed to obtain the value of the complex dielectric permittivity.

The complex dielectric permittivity ($\varepsilon^*(\omega)$), which consists of real ($\varepsilon'(\omega)$) and imaginary permittivity ($\varepsilon''(\omega)$), were calculated as

$$\varepsilon^*(\omega) = \varepsilon'(\omega) - i\varepsilon''(\omega) = 1/i\omega C_o\, Z^*(\omega) \tag{B.1}$$

where $C_o = \varepsilon_o\, S/L$ represents the vacuum capacitance of an empty cell capacitor with an area of S and a thickness of L. The real part of permittivity ($\varepsilon'(\omega)$) is a measure of the amount of energy from an external electric field stored in a material [277]. The imaginary part of permittivity ($\varepsilon'(\omega)$) is called the loss factor, which is a measure of the dissipation of energy to an external electric field. Dissipation factor, D, can be expressed as loss

tangent or tan δ, which is a ratio of the energy lost to the energy stored, and can be formulated as

$$\tan \delta = \varepsilon''(\omega) \, / \, \varepsilon'(\omega) \qquad\qquad\qquad (B.2)$$

B.2 The effect of titanate nanotubes on the polyamic acid salt relative permittivity and dielectric loss

. The relative permittivity and dielectric loss measurement was shown in Figure B.1.
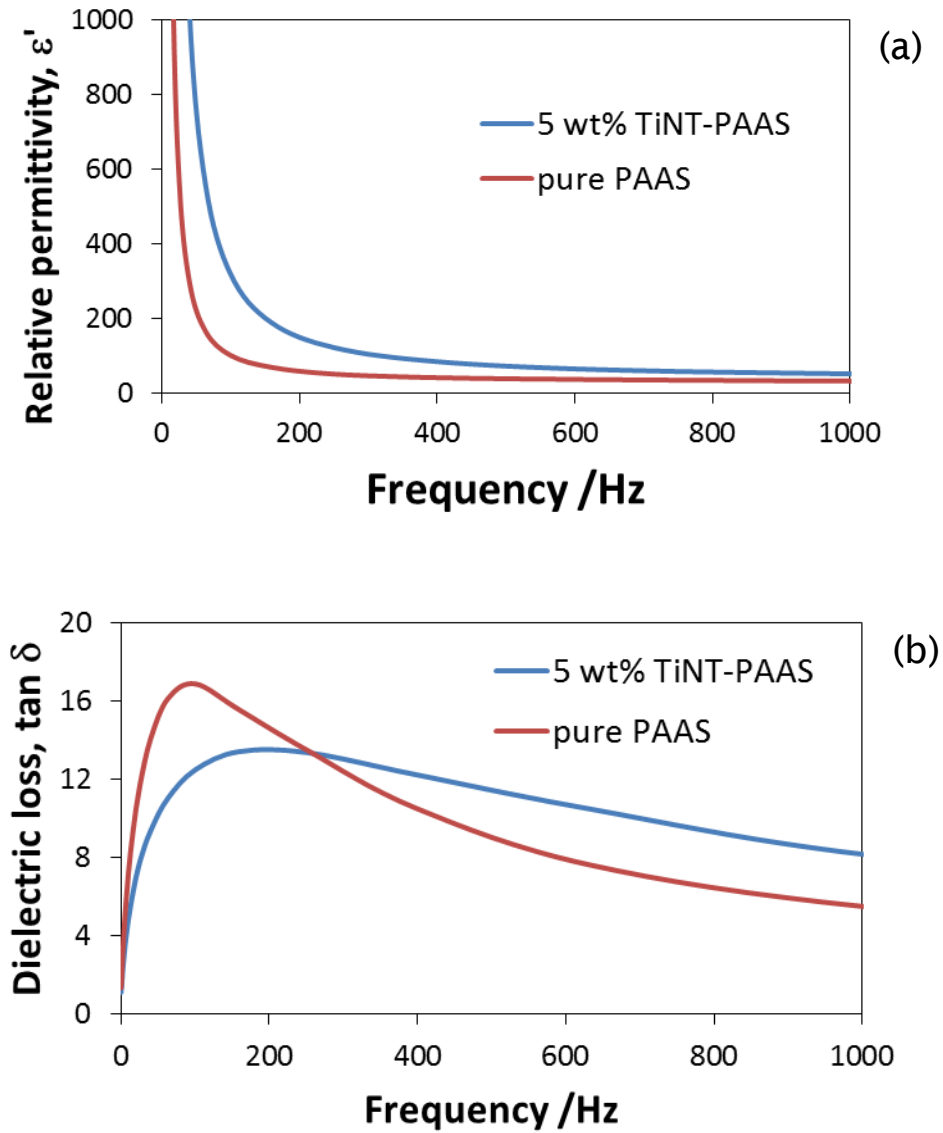
Figure B.1. Frequency dependency of (a) the relative permittivity; (b) dielectric loss of pure PAAS and TiNT-PAAS

The addition of 5 wt% of titanate nanotubes significantly increased relative permittivity of polyamic acid salt from 101 to 318 at 100 Hz. However, the dielectric loss at high frequency (>300 Hz) was also improved. The dielectric loss is the loss of electromagnetic energy propagating inside a dielectric material which is not desirable. Kasian *et.al.* [278] successfully reduced the dielectric loss of titanate nanotubes by cobalt doping although its relative permittivity was slightly decreased. Further research is required on doped titanate nanotubes as filler to enhance dielectric properties of polymer nanocomposites. The possibilities of doped titanate nanotubes-polymer nanocomposites as charge-storage capacitor, electro-caloric cooling, and actuator needs to be explored.

List of References

1. Bakelite first synthetic plastic - national historic chemical landmark - American Chemical Society. *National Historic Chemical Landmark* (1993). Available at: https://www.acs.org/content/acs/en/education/whatischemistry/landmarks/bakelite.html. (Accessed: 3rd October 2017)

2. Liaw, D. J. *et al.* Advanced polyimide materials: syntheses, physical properties and applications. *Prog. Polym. Sci.* **37,** 907–974 (2012).

3. Paşahan, A. *High performance polymers - polyimides based - from chemistry to applications.* (InTech, 2012). doi:10.5772/2834

4. Watson, K. A., Palmieri, F. L. and Connell, J. W. Space environmentally stable polyimides and copolyimides derived from [2,4-bis(3-aminophenoxy)phenyl] diphenylphosphine oxide. *Macromolecules* **35,** 4968–4974 (2002).

5. Ghosh, M. *Polyimides: fundamentals and applications.* (Marcel Dekker, Inc., 1996).

6. Wu, J. *et al.* Effects of ultraviolet irradiation and atomic oxygen erosion on total electron emission yield of polyimide. *IEEE Trans. Plasma Sci.* **42,** 191–198 (2014).

7. Gouzman, I., Girshevitz, O., Grossman, E., Eliaz, N. and Sukenik, C. N. Thin film oxide barrier layers: protection of kapton from space environment by liquid phase deposition of titanium oxide. *ACS Appl. Mater. Interfaces* **2,** 1835–1843 (2010).

8. Tomczak, S. J. *et al.* Properties and improved space survivability of poss (polyhedral oligomeric silsesquioxane) polyimides. in *MRS Proceedings* **851,** NN9.1-NN9.12 (Cambridge University Press, 2004).

9. Brunsvold, A. L., Minton, T. K., Gouzman, I., Grossman, E. and Gonzalez, R. An investigation of the resistance of polyhedral oligomeric silsesquioxane polyimide to atomic-oxygen attack. *High Perform. Polym.* **16,** 303–318 (2004).

10. Jeong, M. S. *et al.* Methodological considerations of electron spin resonance spin trapping techniques for measuring reactive oxygen species generated from metal oxide nanomaterials. *Sci. Rep.* **6,** 26347 (2016).

11. Jun, Y., Choi, J. and Cheon, J. Shape control of semiconductor and metal oxide nanocrystals through nonhydrolytic colloidal routes. *Angew. Chem. Int. Ed. Engl.* **45,** 3414–39 (2006).

12. White, R. D. Metal oxide and silicate nanotubes: synthesis and hydrogen storage applications. (University of Southampton, 2012).

13. Xi, G. and Ye, J. Synthesis of bismuth vanadate nanoplates with exposed {001} facets and enhanced visible-light photocatalytic properties. *Chem. Commun.* **46,** 1893 (2010).

14. Sajan, C. P., Wageh, S., Al-Ghamdi, A. A., Yu, J. and Cao, S. TiO_2 nanosheets with exposed {001} facets for photocatalytic applications. *Nano Res.* **9,** 3–27 (2016).

15. Iida, M., Sasaki, T. and Watanabe, M. Titanium dioxide hollow microspheres with an extremely thin shell. *Chem. Mater.* **10,** 3780–3782 (1998).

16. Feng, Q., Kajiyoshi, K. and Yanagisawa, K. Topotactic preparation of preferentially oriented $BaTiO_3$ and TiO_2 thin films on polycrystalline substrate. *Chem. Lett.* **32,** 48–49 (2003).

17. Sato, T., Yamamoto, Y., Fujishiro, Y. and Uchida, S. Intercalation of iron oxide in layered $H_2Ti_4O_9$ and $H_4Nb_6O_{17}$: visible-light induced photocatalytic properties. *J. Chem. Soc. Faraday Trans.* **92,** 5089 (1996).

18. Yanagisawa, M., Uchida, S., Yin, S. and Sato, T. Synthesis of titania-pillared hydrogen tetratitanate nanocomposites and control of slit width. *Chem. Mater.* **13,** 174–178 (2001).

19. Nakano, S., Sasaki, T., Takemura, K. and Watanabe, M. Pressure-induced intercalation of alcohol molecules into a layered titanate. *Chem. Mater.* **10,** 2044–2046 (1998).

20. Ogawa, M. and Takizawa, Y. Intercalation of alkylammonium cations into a layered titanate in the presence of macrocyclic compounds. *Chem. Mater.* **11,** 30–32 (1999).

21. Wang, J., Yin, S. and Sato, T. Characterization of $H_2Ti_4O_9$ with high specific surface area prepared by a delamination/reassembling process. *Mater. Sci. Eng. B* **126,** 53–58 (2006).

22. Sasaki, T., Komatsu, Y. and Fujiki, Y. Protonated pentatitanate: preparation, characterizations, and cation intercalation. *Chem. Mater.* **4,** 894–899 (1992).

23. Wen, P., Itoh, H., Tang, W. and Feng, Q. Single nanocrystals of anatase-type TiO_2 prepared from layered titanate nanosheets: formation mechanism and characterization of surface properties. *Langmuir* **23,** 11782–11790 (2007).

24. Bavykin, D. V., Kulak, A. N. and Walsh, F. C. Metastable nature of titanate nanotubes in an alkaline environment. *Cryst. Growth Des.* **10,** 4421–4427 (2010).

25. Huang, J., Cao, Y., Deng, Z. and Tong, H. Formation of titanate nanostructures under different NaOH concentration and their application in wastewater treatment. *J. Solid State Chem.* **184,** 712–719 (2011).

26. Wang, C. *et al.* Hydrothermal growth of layered titanate nanosheet arrays on titanium foil and their topotactic transformation to heterostructured tio 2 photocatalysts. *J. Phys. Chem. C* **115,** 22276–22285 (2011).

27. Wang, F. *et al.* Hydrothermal synthesis of highly crystallized lepidocrocite nanosheets of TiO_2 under low temperature. *Chem. Lett.* **34,** 418–419 (2005).

28. Pavasupree, S., Ngamsinlapasathian, S., Suzuki, Y. and Yoshikawa, S. Use of high surface area TiO_2 nanosheet in dye-sensitized solar cell. *MRS Proc.* **951,** (2011).

29. Liu, J., Chen, J. S., Wei, X., Lou, X. W. and Liu, X.-W. Sandwich-like, stacked ultrathin titanate nanosheets for ultrafast lithium storage. *Adv. Mater.* **23,** 998–1002 (2011).

30. Tsai, M. C., Chang, J. C., Sheu, H. S., Chiu, H. T. and Lee, C. Y. Lithium ion intercalation performance of porous laminal titanium dioxides synthesized by sol-gel process. *Chem. Mater.* **21,** 499–505 (2009).

31. Nguyen-Phan, T.-D., Oh, E.-S., Chhowalla, M., Asefa, T. and Shin, E. W. Hierarchical macrochanneled layered titanates with 'house-of-cards'-type titanate nanosheets and their superior photocatalytic activity. *J. Mater. Chem. A* **1,** 7690–

References

7701 (2013).

32. Hoa, N. T. Q. and Kim, E.-T. Self-catalytic growth of $TiO_{[2-\delta]}$ nanobelts and nanosheets using metallorganic chemical vapor deposition. *Electrochem. Solid-State Lett.* **11,** K1 (2008).

33. Sasaki, T. and Watanabe, M. Osmotic swelling to exfoliation. exceptionally high degrees of hydration of a layered titanate. *J. Am. Chem. Soc.* **120,** 4682–4689 (1998).

34. Grey, I. E., Li, C., Madsen, I. C. and Watts, J. a. The stability and structure of $Cs_x[Ti_{2-x/4}\square_{x/4}]O_4$, 0.61<x<0.65. *J. Solid State Chem.* **66,** 7–19 (1987).

35. West, A. R. *Solid state chemistry and its applications*. (John Wiley and Sons, 1987).

36. Allen, M. R. *et al.* Evolution of physical and photocatalytic properties in the layered titanates $A_2Ti_4O_9$ (A = K, H) and in nanosheets derived by chemical exfoliation. *Chem. Mater.* **22,** 1220–1228 (2010).

37. Sasaki, T. *et al.* Preparation and acid-base properties of a protonated titanate with the lepidocrocite-like layer structure. *Chem. Mater.* **7,** 1001–1007 (1995).

38. Tanaka, T., Ebina, Y., Takada, K., Kurashima, K. and Sasaki, T. Oversized titania nanosheet crystallites derived from flux-grown layered titanate single crystals. *Chem. Mater.* **15,** 3564–3568 (2003).

39. Choy, J.-H. and Han, Y.-S. A combinative flux evaporation–slow cooling route to potassium titanate fibres. *Mater. Lett.* **34,** 111–118 (1998).

40. Yokoyama, M., Ota, T. and Yamai, I. Preparation of potassium hexatitanate long fibres by the flux evaporation method. *J. Mater. Sci.* **24,** 3787–3790 (1989).

41. Ma, R., Bando, Y. and Sasaki, T. Nanotubes of lepidocrocite titanates. *Chemical Physics Letters* **380,** 577-582 (2003).

42. Ma, R., Fukuda, K., Sasaki, T., Osada, M. and Bando, Y. Structural features of titanate nanotubes/nanobelts revealed by raman, x-ray absorption fine structure and electron diffraction characterizations. *J. Phys. Chem. B* **109,** 6210–6214 (2005).

43. Gao, T., Fjellvåg, H. and Norby, P. Protonic titanate derived from $Cs_xTi_{2-x/2}Mg_{x/2}O_4$ (x = 0.7) with lepidocrocite-type layered structure. *J. Mater. Chem.* **19,** 787–794 (2009).

44. Sasaki, T., Watanabe, M., Michiue, Y., Iida, M. Fine hollow powder, thin flaky titanium oxide powder obtained by pulverization of the fine hollow powder and processes for producing the same. Patent US 20080003176 A1 (2011).

45. Miyamoto, N., Kuroda, K. and Ogawa, M. Exfoliation and film preparation of a layered titanate, Na2Ti3O7, and intercalation of pseudoisocyanine dye. *J. Mater. Chem.* **14,** 165–170 (2004).

46. Ma, R., Liu, Z., Li, L., Iyi, N. and Sasaki, T. Exfoliating layered double hydroxides in formamide: a method to obtain positively charged nanosheets. *J. Mater. Chem.* **16,** 3809 (2006).

47. Omomo, Y., Sasaki, T., Wang, L., and Watanabe, M. Redoxable nanosheet crystallites of MnO_2 derived via delamination of a layered manganese oxide. *J. Am. Chem. Soc.* **125,** 3568–3575 (2003).

48. Hu, G., Yi, L. and Liu, C. Supercritical N,N-dimethylformamide exfoliation of the layered bulk titanate material into titania nanosheets. *J. Supercrit. Fluids* **72,** 59–67 (2012).

49. Sukpirom, N. and Lerner, M. M. Rapid exfoliation of a layered titanate by ultrasonic processing. *Mater. Sci. Eng. A* **333,** 218–222 (2002).

50. Tae, E. L., Lee, K. E., Jeong, J. S. and Yoon, K. B. Synthesis of diamond-shape titanate molecular sheets with different sizes and realization of quantum confinement effect during dimensionality reduction from two to zero. *J. Am. Chem. Soc.* **130,** 6534–6543 (2008).

51. Kim, G. *et al.* TiO_2 nanodisks designed for Li-ion batteries: a novel strategy for obtaining an ultrathin and high surface area anode material at the ice interface. *Energy Environ. Sci.* **6,** 2932–2938 (2013).

52. Orzali, T., Casarin, M., Granozzi, G., Sambi, M. and Vittadini, A. Bottom-up assembly of single-domain titania nanosheets on (1×2)-Pt(110). *Phys. Rev. Lett.* **97,** 1–4 (2006).

53. Funatsu, A. *et al.* Mass production of titanium oxide ($Ti_2O_5^{2-}$) nanosheets using a soft, solution process. *RSC Adv.* **3,** 21343 (2013).

54. Nakamura, K., Oaki, Y. and Imai, H. Monolayered nanodots of transition metal oxides. *J. Am. Chem. Soc.* **135,** 4501–4508 (2013).

55. Ban, T., Nakagawa, T. and Ohya, Y. Bottom-up synthesis of titanate nanosheets in aqueous sols and their morphology change by the addition of organic ligands and dialysis. *Cryst. Growth Des.* **15,** 1801–1807 (2015).

56. Kim, T. W. *et al.* Highly stable nanocontainer of APTES-anchored layered titanate nanosheet for reliable protection/recovery of nucleic acid. *Sci. Rep.* **6,** 21993 (2016).

57. Sakai, N., Ebina, Y., Takada, K. and Sasaki, T. Electronic band structure of titania semiconductor nanosheets revealed by electrochemical and photoelectrochemical studies. *J. Am. Chem. Soc.* **126,** 5851–5858 (2004).

58. Sasaki, T. and Watanabe, M. Semiconductor nanosheet crystallites of quasi-TiO_2 and their optical properties. *J. Phys. Chem. B* **101,** 10159–10161 (1997).

59. Ma, R. and Sasaki, T. Nanosheets of oxides and hydroxides: ultimate 2D charge-bearing functional crystallites. *Adv. Mater.* **22,** 5082–5104 (2010).

60. Bavykin, D. V. and Walsh, F. C. *Titanate and titania nanotubes*. (Royal Society of Chemistry, 2009). doi:10.1039/9781849730778

61. Zhang, S. *et al.* Formation mechanism of $H_2Ti_3O_7$ nanotubes. *Phys. Rev. Lett.* **91,** 256103 (2003).

62. Pandiyarajan, C., Pandikumar, A. and Ramaraj, R. Photoelectrocatalytic performance of a titania-keggin type polyoxometalate-gold nanocomposite modified electrode in methanol oxidation. *Nanotechnology* **24,** 435401 (2013).

63. Du, G. H., Chen, Q., Che, R. C., Yuan, Z. Y. and Peng, L.-M. Preparation and structure analysis of titanium oxide nanotubes. *Appl. Phys. Lett.* **79,** 3702–3704 (2001).

64. Chen, Q., Du, G. H., Zhang, S. and Peng, L.-M. The structure of trititanate nanotubes. *Acta Crystallogr. Sect. B Struct. Sci.* **58,** 587–593 (2002).

References

65. Bavykin, D., Friedrich, J., Lapkin, A., and Walsh, F., Stability of aqueous suspensions of titanate nanotubes. *Chem. Mater.* **18,** 1124-1129 (2006).

66. Bavykin, D. V, Gordeev, S. N., Moskalenko, A. V, Lapkin, A. A. and Walsh, F. C. Apparent two-dimensional behavior of TiO_2 nanotubes revealed by light absorption and luminescence. *J. Phys. Chem. B* **109,** 8565–8569 (2005).

67. Mital, M. and Scott, E. P. Thermal design methodology for an embedded power electronic module using double-sided microchannel cooling. *J. Electron. Packag.* **130,** 31003 (2008).

68. 1" × 36 yds roll polymide kapton tape insulation for tattoo coils. Available at: http://www.monstersteel.com/tattoo-supplies/1-x-36yds-Roll-Polymide-Kapton-Tape-Insulation-for-Tattoo-Coils-nid-712663.html,. (Accessed: 8th September 2014)

69. Bender, T. P. and Wang, Z. Y. Polyimide thin films produced by direct solid-state polymerization of an amino anhydride monomer. *Macromolecules* **33,** 9477–9479 (2000).

70. Abadie, M. J. and Rusanov, A. L. *Practical Guide to Polyimides*. (Smithers Rapra Technology, 2007).

71. Kaneda, T., Katsura, T., Nakagawa, K., Makino, H. and Horio, M. High-strength–high-modulus polyimide fibers I. one-step synthesis of spinnable polyimides. *J. Appl. Polym. Sci.* **32,** 3133–3149 (1986).

72. Georgiev, A. *et al. High performance polymers - polyimides based - from chemistry to applications*. (InTech, 2012). doi:10.5772/2834

73. Georgiev, A., Spassova, E., Assa, J. and Danev, G. *Preparation of polyimide thin films by vapour deposition and solid state reactions. polymer thin films* (InTechOpen, 2010).

74. Luyben, W. L. and Chien, I.-L. *Design and control of distillation systems for separating azeotropes -*. (John Wiley and Sons, 2011).

75. Inoue, H., Sasaki, Y. and Ogawa, T. Comparison of one-pot and two-step polymerization of polyimide from BPDA/ODA. *J. Appl. Polym. Sci.* **60,** 123–131 (1996).

76. Nelson, A., Guerra, G., Williams, D. J., Karasz, F. E. and MacKnight, W. J. Catalytic activity of benzimidazole in the imidization of polyamic acids. *J. Appl. Polym. Sci.* **35,** 243–248 (1988).

77. Hasanain, F. and Wang, Z. Y. New one-step synthesis of polyimides in salicylic acid. *Polym. Commun.* **49,** 831–835 (2008).

78. Matsumoto, T. Aliphatic polyimides derived from polyalicyclic monomers. *High Perform. Polym.* **13,** S85–S92 (2001).

79. Watanabe, Y. *et al.* Synthesis of wholly alicyclic polyimides from N-silylated alicyclic diamines and alicyclic dianhydrides. *Macromolecules* **35,** 2277–2281 (2002).

80. Mathews, A. S., Kim, I. and Ha, C. S. Fully aliphatic polyimides from adamantane-based diamines for enhanced thermal stability, solubility, transparency, and low dielectric constant. *J. Appl. Polym. Sci.* **102,** 3316–3326 (2006).

81.   DUPONT ™ KAPTON ® Summary of properties. 3 Available at: http://www.dupont.com/content/dam/dupont/products-and-services/membranes-and-films/polyimde-films/documents/DEC-Kapton-summary-of-properties.pdf. (Accessed: 13th February 2017)

82.   Park, J.-H., Lee, J.-H. and Soon, A. Organics on oxidic metal surfaces: a first-principles DFT study of PMDA and ODA fragments on the pristine and mildly oxidized surfaces of Cu(111). *Phys. Chem. Chem. Phys.* **18,** 21893–21902 (2016).

83.   Hasegawa, M. and Horie, K. Photophysics, photochemistry, and optical properties of polyimides. *Prog. Polym. Sci.* **26,** 259–335 (2001).

84.   Yang, Y., Jung, Y., Cho, M. D., Lee, S. G. and Kwon, S. Transient color changes in oxidative-stable fluorinated polyimide film for flexible display substrates. *RSC Adv.* **5,** 57339–57345 (2015).

85.   Yen, H.-J., Tsai, C.-L., Wang, P.-H., Lin, J.-J. and Liou, G.-S. Flexible, optically transparent, high refractive, and thermally stable polyimide–TiO_2 hybrids for anti-reflection coating. *RSC Adv.* **3,** 17048 (2013).

86.   Ghosh, M. K. and Mittal, K. L. *Polyimides : fundamentals and applications.* (Marcel Dekker, Inc., 1996).

87.   Hasegawa, M. and Horii, S. Low-CTE polyimides derived from 2,3,6,7-naphthalenetetracarboxylic dianhydride. *Polym. J.* **39,** 610–621 (2007).

88.   Diaham, S., Locatelli, M.-L. and Khazak, R. in *High performance polymers - polyimides based - from chemistry to applications* (ed. Abadie, M.) (InTech, 2012). doi:10.5772/53994

89.   Chuang, K. C., Criss, J. M. and Mintz, E. A. Polyimide composites based on asymmetric dianhydrides (a-ODPA vs a-BPDA). in *54th International SAMPE Symposium* (2009).

90.   Devasahayam, S., Hill, D. J. T. and Connell, J. W. Effect of electron beam radiolysis on mechanical properties of high performance polyimides. a comparative study of transparent polymer films. *High Perform. Polym.* **17,** 547–559 (2005).

91.   Hougham, G. G. *Fluoropolymers 2: properties.* (Springer Science and Business Media, 2006).

92.   Chen, X. Y., Vinh-Thang, H., Ramirez, A. A., Rodrigue, D. and Kaliaguine, S. Membrane gas separation technologies for biogas upgrading. *RSC Adv.* **5,** 24399–24448 (2015).

93.   Matsumoto, T. Aliphatic polyimides derived from polyalicyclic monomers. *High Perform. Polym.* **13,** S85–S92 (2001).

94.   Matsumoto, T. Semiaromatic polyimides based on bis(aminomethyl)bicyclo[2.2.1]heptane. *High Perform. Polym* **11,** 367–377 (1999).

95.   Zhai, L., Yang, S. and Fan, L. Preparation and characterization of highly transparent and colorless semi-aromatic polyimide films derived from alicyclic dianhydride and aromatic diamines. *Polymer.* **53,** 3529–3539 (2012).

96.   Mathews, A. S., Kim, I. and Ha, C.-S. Fully aliphatic polyimides from adamantane-based diamines for enhanced thermal stability, solubility,

References

transparency, and low dielectric constant. *J. Appl. Polym. Sci.* **102,** 3316–3326 (2006).

97. Rabilloud, G. *High-performance polymers: chemistry and applications*. (Editions Technip, 1999).

98. Kreuz, J. A. Hydrolyses of polyamic-acid solutions. *J. Polym. Sci. Part A Polym. Chem.* **28,** 3787–3793 (1990).

99. Cai, D. *et al.* Synthesis, characterization and hydrolytic stability of poly (amic acid) ammonium salt. *Polym. Degrad. Stab.* **96,** 2174–2180 (2011).

100. Miller, S. B., Lappin, G. R. and Tholstrup, C. E. *Modern plastics encyclopedia*. (McGraw-Hill Inc., 1968).

101. Deanin, R. D., Orroth, S. A., Eliasen, R. W. and Greer, T. N. Mechanism of ultraviolet degradation and stabilization in plastics. *Polym. Eng. Sci.* **10,** 228–234 (1970).

102. Commereuc, S. *et al.* About the end life of novel aliphatic and aliphatic-aromatic (co)polyesters after UV-weathering: structure/degradability relationships. *Polym. Degrad. Stab.* **98,** 1321–1328 (2013).

103. Peng, G., Hao, W., Yang, D. and He, S. Degradation of polyimide film under vacuum ultraviolet irradiation. *J. Appl. Polym. Sci.* **94,** 1370–1374 (2004).

104. Hill, D. J. T. *et al.* Effect of simulated low earth orbit radiation on polyimides (UV degradation study). *J. Appl. Polym. Sci.* **58,** 1847–1856 (1995).

105. Yousif, E. and Haddad, R. Photodegradation and photostabilization of polymers, especially polystyrene: review. *Springerplus* **2,** 398 (2013).

106. Gupta, R. K., Kennel, E. and Kim, K.-J. *Polymer nanocomposites handbook*. (CRC Press, 2009).

107. Sun, X., Sun, H., Li, H. and Peng, H. Developing polymer composite materials: carbon nanotubes or graphene? *Adv. Mater.* **25,** 5153–5176 (2013).

108. Anandhan, S. and Bandyopadhyay, S. *Polymer nanocomposites: from synthesis to applications*. (InTech, 2011). doi:10.5772/1548

109. Ma, P.-C., Siddiqui, N. A., Marom, G. and Kim, J.-K. Dispersion and functionalization of carbon nanotubes for polymer-based nanocomposites: a review. *Compos. Part A Appl. Sci. Manuf.* **41,** 1345–1367 (2010).

110. Pavlidou, S. and Papaspyrides, C. D. A review on polymer-layered silicate nanocomposites. *Prog. Polym. Sci.* **33,** 1119–1198 (2008).

111. Liu, H., Wang, T. and Wang, Q. Tribological properties of thermosetting polyimide/TiO_2 nanocomposites under dry sliding and water-lubricated conditions. *J. Macromol. Sci. Part B* **51,** 2284–2296 (2012).

112. Paul, D. R. and Robeson, L. M. Polymer nanotechnology: nanocomposites. *Polymer (Guildf).* **49,** 3187–3204 (2008).

113. Yano, K., Usuki, A., Okada, A., Kurauchi, T. and Kamigaito, O. Synthesis and properties of polyimide-clay hybrid. *J. Polym. Sci. Part A Polym. Chem.* **31,** 10 (2003).

114. Tyan, H.-L., Wei, K.-H. and Hsieh, T.-E. Mechanical properties of clay-polyimide (BTDA-ODA) nanocomposites via ODA-modified organoclay. *J. Polym. Sci. Part B Polym. Phys.* **38,** 2873–2878 (2000).

115. Chen, B. *et al.* A critical appraisal of polymer-clay nanocomposites. *Chem. Soc. Rev.* **37,** 568–594 (2008).

116. Tsai, M. H., Tseng, I. H., Liao, Y. F. and Chiang, J. C. Transparent polyimide nanocomposites with improved moisture barrier using graphene. *Polym. Int.* **62,** 1302–1309 (2013).

117. Huang, T. *et al.* Modi fi ed Graphene / polyimide nanocomposites : reinforcing and tribological effects. *Appl. Mater. Interfaces* **5,** 4878–4891 (2013).

118. Hu, N. T. *et al.* Graphene oxide reinforced polyimide nanocomposites via in situ polymerization. *J. Nanosci. Nanotechnol.* **12,** 173–178 (2012).

119. Kong, J. Y. *et al.* Preparation and properties of polyimide/graphene oxide nanocomposite films with Mg ion crosslinker. *Eur. Polym. J.* **48,** 1394–1405 (2012).

120. Zhang, L. Bin *et al.* Preparation, mechanical and thermal properties of functionalized graphene/polyimide nanocomposites. *Compos. Part A Appl. Sci. Manuf.* **43,** 1537–1545 (2012).

121. Heo, C. and Chang, J.-H. Polyimide nanocomposites based on functionalized graphene sheets: Morphologies, thermal properties, and electrical and thermal conductivities. *Solid State Sci.* **24,** 6–14 (2013).

122. Yoonessi, M. *et al.* Graphene polyimide nanocomposites; thermal, mechanical, and high-temperature shape memory effects. *ACS Nano* **6,** 7644–7655 (2012).

123. Longun, J., Walker, G. and Iroh, J. O. Surface and mechanical properties of graphene-clay/polyimide composites and thin films. *Carbon N. Y.* **63,** 9–22 (2013).

124. Du, J.-H., Bai, J. and Cheng, H.-M. The present status and key problems of carbon nanotube based polymer composites. *Express Polym. Lett.* **1,** 253–273 (2007).

125. Fischer-Cripps, A. C. *Nanoindentation*. (Springer New York, 2011). doi:10.1007/978-1-4419-9872-9

126. Fischer-Cripps, A. C. *Introduction to contact mechanics*. (Springer US, 2007). doi:10.1007/978-0-387-68188-7

127. Briscoe, B. J., Fiori, L. and Pelillo, E. Nano-indentation of polymeric surfaces. *J. Phys. D Appl. Phys.* **31,** 2395–2405 (1998).

128. Hibbeler, R. C. *Mechanics of materials*. (Pearson, 2013).

129. Voigt, W. Ueber die Beziehung zwischen den beiden elasticitätsconstanten isotroper körper. *Ann. Phys.* **274,** 573–587 (1889).

130. Nielsen, L. E. and Landel, R. F. *Mechanical properties of polymers and composites*. (M. Dekker, 1994).

131. Lewis, T. B. and Nielsen, L. E. Dynamic mechanical properties of particulate-filled composites. *J. Appl. Polym. Sci.* **14,** 1449–1471 (1970).

132. Fu, S.-Y., Xu, G. and Mai, Y.-W. On the elastic modulus of hybrid particle/short-fiber/polymer composites. *Compos. Part B Eng.* **33,** 291–299 (2002).

133. Bokobza, L. Multiwall carbon nanotube elastomeric composites: a review. *Polymer.* **48,** 4907–4920 (2007).

References

134. Ebadi-Dehaghani, H., Khonakdar, H. A., Barikani, M. and Jafari, S. H. Experimental and theoretical analyses of mechanical properties of PP/PLA/clay nanocomposites. *Compos. Part B Eng.* **69,** 133–144 (2015).

135. Wan, C. and Chen, B. Reinforcement and interphase of polymer/graphene oxide nanocomposites. *J. Mater. Chem.* **22,** 3637–3646 (2012).

136. Goyal, R. K., Tiwari, A. N. and Negi, Y. S. Microhardness of PEEK/ceramic micro- and nanocomposites: correlation with Halpin–Tsai model. *Mater. Sci. Eng. A* **491,** 230–236 (2008).

137. Halpin, J. C. and Kardos, J. L. The Halpin-Tsai equations: a review. *Polym. Eng. Sci.* **16,** 344–352 (1976).

138. Liu, M. *et al.* Photolatently modulable hydrogels using unilamellar titania nanosheets as photocatalytic crosslinkers. *Nat. Commun.* **4,** 743–756 (2013).

139. Jellison, G. E., Boatner, L. A., Budai, J. D., Jeong, B.-S. and Norton, D. P. Spectroscopic ellipsometry of thin film and bulk anatase (TiO_2). *J. Appl. Phys.* **93,** 9537–9541 (2003).

140. Gaya, U. I. and Abdullah, A. H. Heterogeneous photocatalytic degradation of organic contaminants over titanium dioxide: a review of fundamentals, progress and problems. *J. Photochem. Photobiol. C Photochem. Rev.* **9,** 1–12 (2008).

141. Kudo, A. and Miseki, Y. Heterogeneous photocatalyst materials for water splitting. *Chem. Soc. Rev.* **38,** 253–78 (2009).

142. M. Schaller, C. Synergy in the sunlight. *Eur. Coatings J.* **1,** 1–11 (2010).

143. Huang, Z.-M., Zhang, Y.-Z., Kotaki, M. and Ramakrishna, S. A review on polymer nanofibers by electrospinning and their applications in nanocomposites. *Compos. Sci. Technol.* **63,** 2223–2253 (2003).

144. Ding, Y., Hou, H., Zhao, Y., Zhu, Z. and Fong, H. Electrospun polyimide nanofibers and their applications. *Prog. Polym. Sci.* **61,** 67–103 (2016).

145. Nah, C., Han, S. H., Lee, M.-H., Kim, J. S. and Lee, D. S. Characteristics of polyimide ultrafine fibers prepared through electrospinning. *Polym. Int.* **52,** 429–432 (2003).

146. Harito, C., Porras, R., Bavykin, D. V. and Walsh, F. C. Electrospinning of in situ and ex situ synthesized polyimide composites reinforced by titanate nanotubes. *J. Appl. Polym. Sci.* **133,** 44641 (2016).

147. Jiang, S., Hou, H., Agarwal, S. and Greiner, A. Polyimide nanofibers by 'green' electrospinning via aqueous solution for filtration applications. *ACS Sustain. Chem. Eng.* **4,** 4797–4804 (2016).

148. Karube, Y. and Kawakami, H. Fabrication of well-aligned electrospun nanofibrous membrane based on fluorinated polyimide. *Polym. Adv. Technol.* **21,** 861–866 (2010).

149. Cheng, C. *et al.* High-strength and high-toughness polyimide nanofibers: synthesis and characterization. *J. Appl. Polym. Sci.* **116,** 1581–1586 (2010).

150. Yao, J., Pantano, M. F., Pugno, N. M., Bastiaansen, C. W. M. and Peijs, T. High-performance electrospun co-polyimide nanofibers. *Polymer (Guildf).* **76,** 105–112 (2015).

151. He, Y. *et al.* Highly strong and highly tough electrospun polyimide/polyimide

composite nanofibers from binary blend of polyamic acids. *RSC Adv.* **4,** 59936–59942 (2014).

152.   Huang, C., Chen, S., Reneker, D. H., Lai, C. and Hou, H. High-strength mats from electrospun poly(p-phenylene biphenyltetracarboximide) nanofibers. *Adv. Mater.* **18,** 668–671 (2006).

153.   Chen, S. *et al.* Electrospun nanofiber belts made from high performance copolyimide. *Nanotechnology* **19,** 15604 (2008).

154.   Xiaoang, W., Ying, Y. and Xidong, L. Preparation of bead-free PMDA-ODA polyimide nanofiber fabrics from electro-spinning. in *Proceedings of the XIX International Conference on Gas Discharges and Their Applications* (2012).

155.   Beachley, V. and Wen, X. Effect of electrospinning parameters on the nanofiber diameter and length. *Mater. Sci. Eng. C. Mater. Biol. Appl.* **29,** 663–668 (2009).

156.   Jayaram, S. and Cherney, E. A. Electrospinning as a new method of preparing nanofilled silicone rubber composites. *IEEE Trans. Dielectr. Electr. Insul.* **19,** 777–785 (2012).

157.   Biji; P.; G. R. Rakesh; G. S. Ranjit; Karthikeyan; K. K.; Radhakrishnan. A facile route for controlled alignment of carbon nanotube-reinforced, electrospun nanofibers using slotted collector plates. *Express Polym. Lett.* **9,** 105 (2015).

158.   Mazinani, S., Ajji, A. and Dubois, C. Morphology, structure and properties of conductive PS/CNT nanocomposite electrospun mat. *Polymer (Guildf).* **50,** 3329–3342 (2009).

159.   Sasaki, T. *et al.* A mixed alkali metal titanate with the lepidocrocite-like layered structure. preparation, crystal structure, protonic form, and acid−base intercalation properties. *Chem. Mater.* **10,** 4123–4128 (1998).

160.   Maluangnont, T. *et al.* Osmotic swelling of layered compounds as a route to producing high-quality two-dimensional materials. a comparative study of tetramethylammonium versus tetrabutylammonium cation in a lepidocrocite-type titanate. *Chem. Mater.* **25,** 3137–3146 (2013).

161.   Singh, R. S. and Singh, S. P. Spectrochemical studies on charge transfer bands due to d0, d5 and d10 ions in a sodium silicate glass. *J. Mater. Sci.* **36,** 1555–1562 (2001).

162.   Bela, S., See, A., Wong, W. and Ho, G. W. Hydrolysis and ion exchange of titania nanoparticles towards large-scale titania and titanate nanobelts for gas sensing applications. *J. Phys. D Appl. Phys.* **43,** 35401 (2010).

163.   Lee, T. *et al.* Preparation and characterization of polyimide/mesoporous silica hybrid nanocomposites based on water-soluble poly(amic acid) ammonium salt. *Eur. Polym. J.* **45,** 19–29 (2009).

164.   Kreuz, J. A., Endrey, A. L., Gay, F. P. and Sroog, C. E. Studies of thermal cyclizations of polyamic acids and tertiary amine salts. *J. Polym. Sci. Part A-1 Polym. Chem.* **4,** 2607–2616 (1966).

165.   Kumagai, K., Sekiguchi, T., Fukuda, K. and Sasaki, T. Secondary electron imaging of monolayer titania nanosheets. *Appl. Phys. Express* **2,** 2–5 (2009).

166.   Sasaki, T., Ebina, Y., Kitami, Y., Watanabe, M. and Oikawa, T. Two-dimensional diffraction of molecular nanosheet crystallites of titanium oxide. *J. Phys. Chem. B* **105,** 6116–6121 (2001).

References

167. Bavykin, D. V., Friedrich, J. M. and Walsh, F. C. Protonated titanates and TiO_2 nanostructured materials: synthesis, properties, and applications. *Adv. Mater.* **18,** 2807–2824 (2006).

168. Kasuga, T., Hiramatsu, M., Hoson, A., Sekino, T. and Niihara, K. Formation of titanium oxide nanotube. *Langmuir* **14,** 3160–3163 (1998).

169. Hagenmuller, P. *Preparative methods in solid state chemistry*. (Elsevier, 1972).

170. Frade, J. R. and Cable, M. Theoretical solutions for mixed control of solid state reactions. *J. Mater. Sci.* **32,** 2727–2733 (1997).

171. Bavykin, D. V. *et al.* The effect of hydrothermal conditions on the mesoporous structure of TiO_2 nanotubes. *J. Mater. Chem.* **14,** 3370 (2004).

172. Chemseddine, A. and Moritz, T. Nanostructuring titania: control over nanocrystal structure, size, shape, and organization. *Eur. J. Inorg. Chem.* **2,** 235–245 (1999).

173. Yang, H., Xu, R., Xue, X., Li, F. and Li, G. Hybrid surfactant-templated mesoporous silica formed in ethanol and its application for heavy metal removal. *J. Hazard. Mater.* **152,** 690–698 (2008).

174. Lyklema, J. *Fundamentals of interface and colloid science: particulate colloids*. (Morgan Kaufmann, 2005).

175. Porras, R., Bavykin, D. V, Zekonyte, J., Walsh, F. C. and Wood, R. J. Titanate nanotubes for reinforcement of a poly(ethylene oxide)/chitosan polymer matrix. *Nanotechnology* **27,** 195706 (2016).

176. Yoshitsugu, K. *et al.* Mechanical properties of nylon. 6-clay hybrid. *J. Mater. Res.* **8,** 1185–1189 (1993).

177. Wang, L. and Sasaki, T. Titanium oxide nanosheets: graphene analogues with versatile functionalities. *Chem. Rev.* **114,** 9455–9486 (2014).

178. Sumisha, A. *et al.* Functionalized titanate nanotube–polyetherimide nanocomposite membrane for improved salt rejection under low pressure nanofiltration. *RSC Adv.* **5,** 39464–39473 (2015).

179. Herrasti, P., Kulak, A., Bavykin, D., Ponce De Léon, C., Zekonyte, J., Walsh, F., Electrodeposition of polypyrrole–titanate nanotube composites coatings and their corrosion resistance. *Electrochim. Acta* **56,** 1323–1328 (2011).

180. Halpin, J. C. Stiffness and expansion estimates for oriented short fiber composites. *J. Compos. Mater.* **3,** 732–734 (1969).

181. Cai, D. *et al.* Synthesis, characterization and hydrolytic stability of poly (amic acid) ammonium salt. *Polym. Degrad. Stab.* **96,** 2174–2180 (2011).

182. Yang, J. and Lee, M.-H. A water-soluble polyimide precursor: synthesis and characterization of poly(amic acid) salt. *Macromol. Res.* **12,** 263–268 (2004).

183. Zhang, L., Wu, J., Sun, N., Zhang, X. and Jiang, L. A novel self-healing poly(amic acid) ammonium salt hydrogel with temperature-responsivity and robust mechanical properties. *J. Mater. Chem. A* **2,** 7666–7668 (2014).

184. Ma, P.-C., Mo, S.-Y., Tang, B.-Z. and Kim, J.-K. Dispersion, interfacial interaction and re-agglomeration of functionalized carbon nanotubes in epoxy composites. *Carbon N. Y.* **48,** 1824–1834 (2010).

185. Osada, M. and Sasaki, T. Nanosheet architectonics: a hierarchically structured assembly for tailored fusion materials. *Polym. J.* **47,** 89–98 (2015).

186. Ding, F., Tong, Y., Luo, X., Guan, H. and Hu, B. Preparation, characterization, and properties of polyamic acid nano-emulsion. *Polym. Adv. Technol.* **22,** 2633–2637 (2011).

187. Shackelford, J. F. . and Alexander, W. in *CRC materials science and engineering handbook, third edition* (eds. Shackelford, J. F. and Alexander, W.) (CRC Press, 2000). doi:doi:10.1201/9781420038408.ch6

188. Oliver, W. C. and Pharr, G. M. An improved technique for determining hardness and elastic modulus using load and displacement sensing indentation experiments. *J. Mater. Res.* **7,** 1565 (1992).

189. Kubát, J., Rigdahl, M. and Welander, M. Characterization of interfacial interactions in high density polyethylene filled with glass spheres using dynamic-mechanical analysis. *J. Appl. Polym. Sci.* **39,** 1527–1539 (1990).

190. Ma, J. *et al.* Poly(vinyl alcohol)/graphene oxide nanocomposites prepared by in situ polymerization with enhanced mechanical properties and water vapor barrier properties. *RSC Adv.* **6,** 49448–49458 (2016).

191. Brune, D. A. and Bicerano, J. Micromechanics of nanocomposites: comparison of tensile and compressive elastic moduli, and prediction of effects of incomplete exfoliation and imperfect alignment on modulus. *Polymer.* **43,** 369–387 (2002).

192. Malwitz, M. M., Lin-Gibson, S., Hobbie, E. K., Butler, P. D. and Schmidt, G. Orientation of platelets in multilayered nanocomposite polymer films. *J. Polym. Sci. Part B Polym. Phys.* **41,** 3237–3248 (2003).

193. Porras, R. *et al.* Titanate nanotubes for reinforcement of a poly(ethylene oxide)/chitosan polymer matrix. *Nanotechnology* **27,** 195706 (2016).

194. Arash, B. *et al.* Mechanical properties of carbon nanotube/polymer composites. *Sci. Rep.* **4,** 6479 (2014).

195. Qian, D., Dickey, E. C., Andrews, R. and Rantell, T. Load transfer and deformation mechanisms in carbon nanotube-polystyrene composites. *Appl. Phys. Lett.* **76,** 2868–2870 (2000).

196. Chen, Q., Du, G. H., Zhang, S. and Peng, L.-M. The structure of trititanate nanotubes. *Acta Crystallogr. B.* **58,** 587–93 (2002).

197. Du, G. H., Chen, Q., Che, R. C., Yuan, Z. Y. and Peng, L.-M. Preparation and structure analysis of titanium oxide nanotubes. *Appl. Phys. Lett.* **79,** 3702 (2001).

198. Kang, S.-H. *et al.* Size effect on mechanical properties of TiO_2 capped nanotubes investigated using in situ transmission electron microscopy. *Microsyst. Technol.* **20,** 515–520 (2014).

199. Shokuhfar, T., Arumugam, G. K., Heiden, P. A., Yassar, R. S. and Friedrich, C. Direct compressive measurements of individual titanium dioxide nanotubes. *ACS Nano* **3,** 3098–3102 (2009).

200. Zhu, J. *et al.* Positive and negative magnetoresistance phenomena observed in magnetic electrospun polyacrylonitrile-based carbon nanocomposite fibers. *J. Mater. Chem. C* **2,** 715–722 (2014).

201. Bajsić, E. G. *et al.* The effect of UV irradiation on the electrospun PCL/TiO_2 composites fibers. *J. Appl. Polym. Sci.* **133,** 43539 (2016).

202. Kim, S. *et al.* Porous polyimide membranes prepared by wet phase inversion for

References

use in low dielectric applications. *Int. J. Mol. Sci.* **14,** 8698–707 (2013).

203.	Perkins, W. G., Capiati, N. J. and Porter, R. S. The effect of molecular weight on the physical and mechanical properties of ultra-drawn high density polyethylene. *Polym. Eng. Sci.* **16,** 200–203 (1976).

204.	O'Connell, P. A., Bonner, M. J., Duckett, R. A. and Ward, I. M. Effect of molecular weight and branch content on the creep behavior of oriented polyethylene. *J. Appl. Polym. Sci.* **89,** 1663–1670 (2003).

205.	Liu, J. *et al.* Hydrophobic electrospun polyimide nanofibers for self-cleaning materials. *Macromol. Mater. Eng.* **300,** 358–368 (2015).

206.	Fukushima, S., Karube, Y. and Kawakami, H. Preparation of ultrafine uniform electrospun polyimide nanofiber. *Polym. J.* **42,** 514–518 (2010).

207.	Mazoochi, T., Hamadanian, M., Ahmadi, M. and Jabbari, V. Investigation on the morphological characteristics of nanofiberous membrane as electrospun in the different processing parameters. *Int. J. Ind. Chem.* **3,** 2 (2012).

208.	Bosworth, L. A. and Downes, S. Acetone, a sustainable solvent for electrospinning poly(ε-caprolactone) fibres: effect of varying parameters and solution concentrations on fibre diameter. *J. Polym. Environ.* **20,** 879–886 (2012).

209.	Nishino, T., Kotera, M., Inayoshi, N., Miki, N. and Nakamae, K. Residual stress and microstructures of aromatic polyimide with different imidization processes. *Polymer (Guildf).* **41,** 6913–6918 (2000).

210.	Hughes, A. J. The einstein relation between relative viscosity and volume concentration of suspensions of spheres. *Nature* **173,** 1089–1090 (1954).

211.	Jain, S. *et al.* Strong decrease in viscosity of nanoparticle-filled polymer melts through selective adsorption. *Soft Matter* **4,** 1848 (2008).

212.	Mackay, M. E. *et al.* Nanoscale effects leading to non-Einstein-like decrease in viscosity. *Nat. Mater.* **2,** 762–766 (2003).

213.	Tuteja, A., Mackay, M. E., Hawker, C. J. and Horn†, B. Van. Effect of ideal, organic nanoparticles on the flow properties of linear polymers: non-Einstein-like behavior. *Macromolecules* **38,** 8000–8011 (2005).

214.	Kalathi, J. T., Grest, G. S. and Kumar, S. K. Universal viscosity behavior of polymer nanocomposites. *Phys. Rev. Lett.* **109,** 198301 (2012).

215.	Bershtein, V. A. *et al.* Relationship of processing conditions to structure and properties in PMDA-ODA polyimide. *J. Macromol. Sci. Part B* **44,** 613–639 (2005).

216.	Corcione, C. and Frigione, M. Characterization of nanocomposites by thermal analysis. *Materials (Basel).* **5,** 2960–2980 (2012).

217.	Marashdeh, W. F., Longun, J. and Iroh, J. O. Relaxation behavior and activation energy of relaxation for polyimide and polyimide-graphene nanocomposite. *J. Appl. Polym. Sci.* **133,** 43684 (2016).

218.	Kim, K., Yoo, T., Kim, J., Ha, H. and Han, H. Effects of dianhydrides on the thermal behavior of linear and crosslinked polyimides. *J. Appl. Polym. Sci.* **132,** 41412 (2015).

219.	Lanciano, G., Greco, A., Maffezzoli, A. and Mascia, L. Effects of thermal history

in the ring opening polymerization of CBT and its mixtures with montmorillonite on the crystallization of the resulting poly(butylene terephthalate). *Thermochim. Acta* **493,** 61–67 (2009).

220. Papa, A.-L. *et al.* Dispersion of titanate nanotubes for nanomedicine: comparison of PEI and PEG nanohybrids. *Dalt. Trans.* **44,** 739–746 (2015).

221. Liu, J. *et al.* Polyethyleneimine functionalized protonated titanate nanotubes as superior carbon dioxide adsorbents. *J. Colloid Interface Sci.* **386,** 392–397 (2012).

222. Guang-Xin Chen, Hun-Sik Kim, Park, B. H. and Yoon, J.-S. Controlled functionalization of multiwalled carbon nanotubes with various molecular-weight poly(l-lactic acid). *J. Phys. Chem. B* **109,** 22237–22243 (2005).

223. Reneker, D. H., Yarin, A. L., Fong, H. and Koombhongse, S. Bending instability of electrically charged liquid jets of polymer solutions in electrospinning. *J. Appl. Phys.* **87,** 4531–4547 (2000).

224. Fong, H., Chun, I. and Reneker, D. . Beaded nanofibers formed during electrospinning. *Polymer (Guildf).* **40,** 4585–4592 (1999).

225. Chisca, S., Barzic, A. I., Sava, I., Olaru, N. and Bruma, M. Morphological and rheological insights on polyimide chain entanglements for electrospinning produced fibers. *J. Phys. Chem. B* **116,** 9082–9088 (2012).

226. Sain, S. *et al.* A comparative study of polymethylmethacrylate/cellulose nanocomposites prepared by in situ polymerization and ex situ dispersion techniques. *J. Reinf. Plast. Compos.* **32,** 147–159 (2013).

227. Barzic, A. I. *et al.* An insight on the effect of rubbing textile fiber on morphology of some semi-alicyclic polyimides for liquid crystal orientation. *Polym. Bull.* **70,** 1553–1574 (2013).

228. Matsumoto, T. and Kurosaki, T. Soluble and colorless polyimides from bicyclo[2.2.2]octane-2,3,5,6-tetracarboxylic 2,3:5,6-dianhydrides 1. *Macromolecules* **30,** 993–1000 (1997).

229. Baker, R. W. *Membrane technology and applications*. (John Wiley and Sons, 2004).

230. Yang, J. C. and De Groh, K. K. Materials issues in the space environment. *MRS Bull.* **35,** 12–16 (2010).

231. Shimamura, H. and Yamagata, I. Degradation of mechanical properties of polyimide film exposed to space environment. *J. Spacecr. Rockets* **46,** 15–21 (2009).

232. Wang, W.-W. *et al.* Stability of poly(l-lactide)/TiO_2 nanocomposite thin films under UV irradiation at 254 nm. *Polym. Degrad. Stab.* **98,** 885–893 (2013).

233. Kowalonek, J. Surface studies of UV-irradiated poly(vinyl chloride)/poly(methyl methacrylate) blends. *Polym. Degrad. Stab.* **133,** 367–377 (2016).

234. Norrman, K., Larsen, N. B. and Krebs, F. C. Lifetimes of organic photovoltaics: Combining chemical and physical characterisation techniques to study degradation mechanisms. *Sol. Energy Mater. Sol. Cells* **90,** 2793–2814 (2006).

235. Volkmer, T., Arietano, L., Plummer, C., Strautmann, J. and Noël, M. Loss of tensile strength in cellulose tissue on the surface of spruce (Picea abies) caused

by natural photodegradation and delignification. *Polym. Degrad. Stab.* **98,** 1118–1125 (2013).

236. Gu, X. *et al.* Probing photodegradation beneath the surface: a depth profiling study of UV-degraded polymeric coatings with microchemical imaging and nanoindentation. *J. Coatings Technol. Res.* **4,** 389–399 (2007).

237. Delobelle, P., Guillot, L., Dubois, C. and Monney, L. Photo-oxidation effects on mechanical properties of epoxy matrixes: Young's modulus and hardness analyses by nano-indentation. *Polym. Degrad. Stab.* **77,** 465–475 (2002).

238. Motyakin, M. V., Gerlock, J. L. and Schlick, S. Electron spin resonance imaging of degradation and stabilization processes: behavior of a hindered amine stabilizer in UV-exposed poly(acrylonitrile−butadiene−styrene) polymers. *Macromolecules* **32,** 5463–5467 (1999).

239. Nielsen, K. L. C. *et al.* The radiation degradation of a nanotube–polyimide nanocomposite. *Polym. Degrad. Stab.* **93,** 169–175 (2008).

240. Cogulet, A., Blanchet, P. and Landry, V. Wood degradation under UV irradiation: a lignin characterization. *J. Photochem. Photobiol. B Biol.* **158,** 184–191 (2016).

241. Jørgensen, M., Norrman, K. and Krebs, F. C. Stability/degradation of polymer solar cells. *Sol. Energy Mater. Sol. Cells* **92,** 686–714 (2008).

242. Philippart, J.-L., Posada, F. and Gardette, J.-L. Mass spectroscopy analysis of volatile photoproducts in photooxidation of polypropylene. *Polym. Degrad. Stab.* **49,** 285–290 (1995).

243. Blakey, I., Goss, B. and George, G. Chemiluminescence as a probe of polymer oxidation. *Aust. J. Chem.* **59,** 485 (2006).

244. Collin, S., Bussière, P.-O., Therias, S. and Lacoste, J. The role of hydroperoxides in the chemiluminescence of oxidized polymers reconsidered. *Eur. Polym. J.* **76,** 122–134 (2016).

245. Allen, N. S. and Edge, M. *Fundamentals of polymer degradation and stabilisation*. (Elsevier Applied Science, 1992).

246. Subowo, W. S., Barmawi, M. and Liang, O. B. Growth of carbonyl index in the degradation of polypropylene by UV irradiation. *J. Polym. Sci. Part A Polym. Chem.* **24,** 1351–1362 (1986).

247. Rouillon, C. *et al.* Is carbonyl index a quantitative probe to monitor polypropylene photodegradation? *Polym. Degrad. Stab.* **128,** 200–208 (2016).

248. Das, N. K. and Mandal, B. M. Methylene blue as a retarder of free radical polymerization: 1. polymerization of acrylonitrile, methyl methacrylate and styrene. *Polymer.* **23,** 1653–1658 (1982).

249. Ando, S., Matsuura, T. and Sasaki, S. Coloration of aromatic polyimides and electronic properties of their source materials. *Polym. J.* **29,** 69–76 (1997).

250. Mellor, D. C., Moir, A. B. and Scott, G. The effect of processing conditions on the u.v. stability of polyolefins. *Eur. Polym. J.* **9,** 219–225 (1973).

251. Devasahayam, S., Hill, D. J. T. and Connell, J. W. FT-Raman studies of a range of polyimides subjected to high-energy radiations at room and elevated temperatures. *J. Appl. Polym. Sci.* **101,** 1575–1582 (2006).

252. Liu, Y. *et al.* Structural evolution and degradation mechanism of Vectran® fibers upon exposure to UV-radiation. *Polym. Degrad. Stab.* **98,** 1744–1753 (2013).

253. Jin, C., Christensen, P. A., Egerton, T. A., Lawson, E. J. and White, J. R. Rapid measurement of polymer photo-degradation by FTIR spectrometry of evolved carbon dioxide. *Polym. Degrad. Stab.* **91,** 1086–1096 (2006).

254. Sanderson, R. T. *Chemical bonds and bond energy*. (Academic Press, 1971).

255. Sanderson, R. T. *Polar covalence*. (Academic Press, 1983).

256. Bavykin, D. V, Redmond, K. E., Nias, B. P., Kulak, A. N. and Walsh, F. C. The effect of ionic charge on the adsorption of organic dyes onto titanate nanotubes. *Aust. J. Chem* **63,** 270–275 (2010).

257. Satoh, A. Y., Trosko, J. E. and Masten, S. J. Methylene blue dye test for rapid qualitative detection of hydroxyl radicals formed in a fenton's reaction aqueous solution. *Enviromental Sci. Technol.* **41,** 2881–2887 (2007).

258. David, C., Geuskens, G., Rabek, J. F., Bamford, C. H. and Tipper, C. F. H. *Degradation of polymers*. (Elsevier Scientific Pub. Co, 1975).

259. Briassoulis, D. Analysis of the mechanical and degradation performances of optimised agricultural biodegradable films. *Polym. Degrad. Stab.* **92,** 1115–1132 (2007).

260. Sabir, M. I., Xu, X. and Li, L. A review on biodegradable polymeric materials for bone tissue engineering applications. *J. Mater. Sci.* **44,** 5713–5724 (2009).

261. Varley, R. J., Simmonds, E. K., Seebergh, J. E. and Berry, D. H. Investigation of factors impacting the in-service degradation of aerospace coatings. *Prog. Org. Coatings* **74,** 679–686 (2012).

262. Briassoulis, D. The effects of tensile stress and the agrochemical Vapam on the ageing of low density polyethylene (LDPE) agricultural films. Part I. Mechanical behaviour. *Polym. Degrad. Stab.* **88,** 489–503 (2005).

263. Lu, T., Solis-Ramos, E., Yi, Y.-B. and Kumosa, M. Synergistic environmental degradation of glass reinforced polymer composites. *Polym. Degrad. Stab.* **131,** 1–8 (2016).

264. Lee, C., Seo, J., Shul, Y. and Han, H. Optical properties of polyimide thin films. effect of chemical structure and morphology. *Polym. J.* **35,** 578–585 (2003).

265. Deng, S. H., Zhao, J. J., Lin, Q. F., Fan, C. J. and Zhou, X. D. Formation of interfacial network structure via photo-crosslinking in carbon fiber/epoxy composites. *eXPRESS Polym. Lett.* **8,** 505–516 (2014).

266. Beake, B. D., Harris, A. J. and Liskiewicz, T. W. in *Materials characterization : modern methods and applications* (ed. Ranganathan, N.) 17–18 (CRC Press, 2016).

267. Toirov, A. and Tashrifov, K. Thermal cyclodehydration of polyamic acid initiated by UV-irradiation. *Iran. Polym. J.* **1,** 16–22 (1995).

268. Jenekhe, S. A. and Roberts, M. F. Effects of intermolecular forces on the glass transition of polymers. *Macromolecules* **26,** 4981–4983 (1993).

269. Wu, J. *et al.* Effects of ultraviolet irradiation and atomic oxygen erosion on total electron emission yield of polyimide. *IEEE Trans. Plasma Sci.* **42,** 191–198 (2014).

References

270. Salvetat, J.-P. *et al.* Mechanical properties of carbon nanotubes. *Appl. Phys. A* **69,** 255–260 (1999).

271. Lourie, O. and Wagner, H. D. Evaluation of young's modulus of carbon nanotubes by micro-Raman spectroscopy. *J. Mater. Res.* **13,** 2418–2422 (1998).

272. Treacy, M. M. J., Ebbesen, T. W. and Gibson, J. M. Exceptionally high Young's modulus observed for individual carbon nanotubes. *Nature* **381,** 678–680 (1996).

273. Ding, F. Theoretical study of the stability of defects in single-walled carbon nanotubes as a function of their distance from the nanotube end. *Phys. Rev. B* **72,** 245409 (2005).

274. Bavykin, D. V., Kulak, A. N. and Walsh, F. C. Metastable nature of titanate nanotubes in an alkaline environment. *Cryst. Growth Des.* **10,** 4421–4427 (2010).

275. Ghicov, A., Schmidt, B., Kunze, J. and Schmuki, P. Photoresponse in the visible range from Cr doped TiO_2 nanotubes. *Chem. Phys. Lett.* **433,** 323–326 (2007).

276. Hu, W., Li, L., Tong, W. and Li, G. Water–titanate intercalated nanotubes: fabrication, polarization, and giant dielectric property. *Phys. Chem. Chem. Phys* **12,** 12638–12646 (2010).

277. Scaife, B. K. P. *Principles of dielectrics.* (OUP Oxford, 1998).

278. Kasian, P. *et al.* Co-doped titanate nanotubes: Synthesis, characterization, and properties. *Jpn. J. Appl. Phys.* **53,** 06JG12 (2014).